

# **Multiscale Variability Associated with the Intraseasonal Oscillation over the Western Pacific Warm Pool**

by  
Xin Lin

Department of Atmospheric Science  
Colorado State University  
Fort Collins, Colorado

Research supported by the National Oceanic and Atmospheric Administration under Grants NA90RAH00077 and NA37RJ0202, and by a NASA Graduate Fellowship on Global Change under Grant NGT-30190.



**Department of  
Atmospheric Science**

**MULTISCALE VARIABILITY ASSOCIATED WITH THE  
INTRASEASONAL OSCILLATION OVER THE  
WESTERN PACIFIC WARM POOL**

by

Xin Lin

Department of Atmospheric Science  
Colorado State University  
Fort Collins, CO 80523

Spring 1997

Atmospheric Science Paper No. 635

## ABSTRACT

### MULTISCALE VARIABILITY ASSOCIATED WITH THE INTRASEASONAL OSCILLATION OVER THE WESTERN PACIFIC WARM POOL

A 4-dimensional gridded dataset is generated based on sounding data collected during the Tropical Ocean Global Atmosphere (TOGA) Coupled Ocean Atmosphere Response Experiment (COARE) over the tropical western Pacific. Along with surface and satellite data, we document mean and transient behavior of the atmosphere, and investigate multiscale variability associated with the Intraseasonal Oscillation (ISO) over the Pacific warm pool. In particular, the behavior of the atmosphere and the response of the ocean surface before, during, and after the passages of westerly wind bursts are quantitatively examined.

Three prominent westerly wind bursts occurred over the Intensive Flux Array (IFA) during the four-month Intensive Observing Period in association with the ISOs. Heavy precipitation usually fell 1 to 3 weeks prior to the peak westerly wind bursts. Subsidence dominated when the westerly winds prevailed. The tropospheric vertical wind shear associated with tropical low-frequency oscillations strongly modulated convective heating and moistening. SSTs reached their maximum during the undisturbed phase of the ISOs, gradually decreased as convection intensified, and reached their minimum during the periods of peak westerly winds when deep convection was generally suppressed over the IFA. A descriptive model of the kinematic and thermodynamic characteristics of a westerly wind burst is proposed. Evidence has been found against certain popular ISO theories.

The vertical distributions of heating and moistening at different phases of the ISO are determined for different areas within the warm pool, with specific attention to the periods of westerly wind bursts. They agree very well with observations from surface, Doppler radar

and satellites. Large-scale rainfall rates are calculated from the moisture budget and surface observations, and are compared with remote sensing and operational model forecasts. Some deficiencies of remote sensing and model forecasts are pointed out.

There are striking differences between long-term mean profiles along the equator and those in the ITCZ bands, suggesting great care should be exercised in generalizing divergence, vertical motion, heating, and moistening profiles from one region to another over the western Pacific warm pool.

Cloud spectral model results indicate that the western Pacific warm pool boundary layer outside the ITCZ frequently develops tradewind-like characteristics with abundant shallow cumulus during suppressed and undisturbed periods. These episodic trade-like regimes are prominent enough to impact the seasonal distributions of boundary-layer heating and moistening.

Xin Lin  
Department of Atmospheric Science  
Colorado State University  
Fort Collins, Colorado 80523  
Spring 1997

## ACKNOWLEDGEMENTS

I would like to express my sincere gratitude to my advisor, Professor Richard H. Johnson, for his constant encouragement and strong support in the past few years. His insightful suggestions for my research, his stimulating guidance on my work, and his patient help in improving my English, were not only needed for me to finish this dissertation, they are also beneficial to my future career.

I would also like to thank my other committee members, Prof. Steve Rutledge, Prof. Dave Randall, and Prof. Bogusz Bienkiewicz, for many constructive comments and assistance. Professor Rutledge and his group provided invaluable help to understanding of ISO-modulated tropical convection from Doppler radar perspective. Stimulating discussions with Professor Randall and taking his classes greatly increased my knowledge in tropical circulation and cloud modelings.

I also wish to gratefully acknowledge the unselfish assistance of and numerous discussions with Paul Ciesielski and Rick Taft concerning research data, programming, and software packages during my Ph.D. study. Many thanks to my officemate Jason Knievel for serving as the "Grammar Police" for my dissertation and many other papers. Many others assisted this research at different points during the last four years, and they also deserve to be thanked. They include Jim Bresch, Bill Gallus, Gail Cordova, Tom Rickenbach, Charlotte DeMott, Walt Petersen, Kuanman Xu, and Pat Haertel.

I would like to give my special thanks to my parents and my wife Hui for their continuous support and patience in the past few years.

This research was supported by a NASA Graduate Fellowship on Global Change under Grant NGT-30190 and by the National Oceanic and Atmospheric Administration under Grants NA90RAH00077 and NA37RJ0202.

DEDICATION

To my parents and my wife

## CONTENTS

<b>1 INTRODUCTION</b>	<b>1</b>
<b>2 BACKGROUND</b>	<b>6</b>
2.1 Studies on the Intraseasonal Oscillations . . . . .	6
2.1.1 <i>Overview of observational studies</i> . . . . .	6
2.1.2 <i>Overview of theoretical and simple modeling studies</i> . . . . .	14
2.1.3 <i>Overview of GCM studies</i> . . . . .	18
2.2 Studies on heat and moisture budgets . . . . .	19
2.2.1 <i>Heat and moisture budget analyses</i> . . . . .	20
2.2.2 <i>Diagnosis of cloud effects</i> . . . . .	24
2.3 Summary . . . . .	26
<b>3 DATA AND ANALYSIS METHODS</b>	<b>29</b>
3.1 The TOGA COARE field experiment . . . . .	29
3.2 Data and analysis methods . . . . .	30
3.2.1 <i>Rawinsonde data</i> . . . . .	30
3.2.2 <i>Satellite data</i> . . . . .	35
3.2.3 <i>Surface data</i> . . . . .	36
3.2.4 <i>Operational model analyses</i> . . . . .	36
<b>4 BASIC KINEMATIC AND THERMODYNAMIC FEATURES</b>	<b>39</b>
4.1 Observations from OLR and IR data . . . . .	39
4.1.1 <i>Mean distributions</i> . . . . .	39
4.1.2 <i>Intraseasonal variabilities</i> . . . . .	41
4.2 Basic kinematic features . . . . .	44
4.2.1 <i>Zonal wind</i> . . . . .	44
4.2.2 <i>Meridional wind</i> . . . . .	51
4.2.3 <i>Divergence</i> . . . . .	54
4.2.4 <i>Vertical motion</i> . . . . .	57
4.3 Basic thermodynamic features . . . . .	65
4.3.1 <i>Humidity</i> . . . . .	65
4.3.2 <i>Temperature perturbations</i> . . . . .	68
4.4 Synthesis of observations . . . . .	70
4.5 Summary and discussions . . . . .	73

<b>5 HEATING, MOISTENING, AND RAINFALL</b>	<b>76</b>
5.1 Surface heat fluxes . . . . .	76
5.2 Broad scale considerations . . . . .	84
5.3 Rainfall analysis . . . . .	85
5.3.1 <i>Mean distribution of rainfall</i> . . . . .	85
5.3.2 <i>Comparison of rainfall rates</i> . . . . .	90
5.3.3 <i>Components of the moisture budget</i> . . . . .	92
5.4 Heat and moisture budgets . . . . .	92
5.4.1 <i>Monthly time series</i> . . . . .	94
5.4.2 <i>Mean profiles</i> . . . . .	102
5.5 Summary and discussions . . . . .	106
<b>6 DIURNAL VARIATION IN CONVECTION</b>	<b>112</b>
6.1 Introduction . . . . .	112
6.2 Clear-sky, light-wind conditions . . . . .	116
6.3 Cloudy-sky, strong-wind conditions . . . . .	126
6.4 Conclusions and discussion . . . . .	135
<b>7 DIAGNOSIS OF SHALLOW CUMULUS EFFECTS</b>	<b>137</b>
7.1 The cloud spectral diagnostic model . . . . .	138
7.2 Data and numerical methods . . . . .	142
7.3 Observed heating and moistening distributions . . . . .	144
7.4 Diagnostic model results . . . . .	156
7.4.1 <i>Late-December/early-January westerly wind burst</i> . . . . .	156
7.4.2 <i>Early-February westerly wind burst</i> . . . . .	162
7.4.3 <i>November-early December undisturbed period</i> . . . . .	164
7.4.4 <i>Discussion</i> . . . . .	167
7.5 Summary . . . . .	172
<b>8 SUMMARY AND FUTURE WORK</b>	<b>174</b>
8.1 Summary . . . . .	174
8.2 Future work . . . . .	177
8.2.1 <i>Diagnose the effect of a midlevel stable layer</i> . . . . .	178
8.2.2 <i>Compare and validate modeling results</i> . . . . .	178
<b>REFERENCES</b>	<b>179</b>

## LIST OF FIGURES

2.1	Schematic depiction of the time and space (zonal plane) variations of the disturbance associated with the intraseasonal oscillation. Dates are indicated symbolically by the letters at the left of each chart and correspond to dates associated with the oscillation in Canton's station pressure. The letter A refers to the time of low pressure at Canton and E is the time of high pressure there. The other letters represent intermediate times (taken from Madden and Julian 1972). . . . .	8
2.2	Schematic describing the details of the large-scale eastward propagating cloud complexes [slanting ellipses marks ISV (intraseasonal variability) on the left-hand side]. Slanting heavy lines represent super cloud clusters (SCC) within the larger complexes or ISV. The right-hand side illustrates the fine structure of the SCC with smaller westward-moving cloud cluster that develop, grow to maturity, and decay in a few days (from Nakazawa 1988). . . . .	12
2.3	Conceptual illustration of the 30-60 day wave as an air-sea interaction instability (from Emanuel 1987). Anomalously strong easterlies at right give rise to anomalous heat fluxes from the sea surface; the moist entropy is then rapidly redistributed aloft by convection. The resulting temperature anomaly leads the surface convergence by one quarter cycle, leading to wave growth and eastward propagation. . . . .	17
2.4	The mean apparent heat source $Q_1$ (solid) and moisture sink $Q_2$ (dashed) (from Yanai et al. 1973). On the left is the radiative heating profile given by Dopplick (1970). . . . .	21
2.5	Partitioning of the normalized apparent heat source $Q_1$ into convective-scale (cumulus) and mesoscale components for $f=0.2$ ; $f$ is the fraction of the total rainfall produced by mesoscale anvils (from Johnson 1984). . . . .	23
3.1	The TOGA COARE sounding network. The solid circles indicate ISS stations and the open circles represent other sounding stations. . . . .	31
3.2	Locations of moorings in COARE domain. . . . .	37
4.1	IOP-mean and monthly mean brightness temperatures over the Large Scale Array. Contour intervals 2.5 K and areas with temperature less than 265 K are shaded. (a) IOP mean, (b) November, (c) December, (d) January, (e) February. . . . .	40
4.2	(a) Hovmöller diagram of pentad OLR values averaged between 5°S and 5°N for September 1992 - March 1993 (from Gutzler et al. 1994). Vertical axis labels indicated initial month-day of each pentad average. The longitude of the LSA are bracketed at the top of the figure and the approximate longitudinal extent of the IFA is delineated by vertical lines running down the plot. Contour intervals 20 $W m^{-2}$ . Shading denotes OLR greater than 200 $W m^{-2}$ . . . . .	42

4.2	Continued. (b) Time-longitude section of OLR (left) and GMS IR (right) averaged between the equator and $5^\circ$ during the TOGA COARE IOP from November 1, 1992 to February 28, 1993 (from Nakazawa 1995). . . . .	43
4.3	(a) Time series of zonal U component ( $\text{m s}^{-1}$ ) at 0000 UTC averaged over the Intensive Flux Array (5-day running mean). Contour intervals $4 \text{ m s}^{-1}$ and westerlies are shaded. (b) The IOP-mean vertical profile of zonal U component over the IFA (solid curve), and daily-averaged U profiles on December 11 and January 1. Positive values indicate westerlies. . . . .	45
4.4	(a) Time-latitude cross section of zonal component of the wind at 1000 hPa. Westerlies are shaded. The intervals are $2 \text{ m s}^{-1}$ . (b) Time-latitude cross section of GMS brightness temperature (in unit of K). The regions with T less than 260 K are shaded. . . . .	47
4.4	Continued. (c) Frequency distribution of zonal wind component at 1000 hPa over the IFA during COARE IOP. Ordinate values are numbers of 1000 hPa zonal wind component during the COARE IOP at 6-hour intervals. Positive values indicate westerlies. . . . .	48
4.4	Continued. (d) Time series of the surface latent heat flux (solid line) from WHOI IMET buoy ( $\text{W m}^{-2}$ ). Superimposed is surface wind speed (dashed line) from the IMET buoy ( $\text{m s}^{-1}$ ). Mean latent heat flux of $117 \text{ W m}^{-2}$ is indicated. (e) Time series of the surface sensible heat flux (solid line) from WHOI IMET buoy ( $\text{W m}^{-2}$ ). Superimposed is GMS brightness temperature (dashed line) over the IFA. Mean sensible heat flux is indicated. (The IMET buoy data courtesy of Drs. Robert Weller and Steve Anderson, WHOI). . . .	50
4.5	The IOP-mean zonal wind component at (a) 850 hPa, (b) 150 hPa over the Large Scale Array. Solid lines indicate westerlies, while dashed lines represent easterlies. The intervals are $1 \text{ m s}^{-1}$ . . . . .	52
4.6	(a) Time series of daily-mean meridional V component ( $\text{m s}^{-1}$ ) averaged over the Intensive Flux Array (5-day running mean). Contour intervals $2 \text{ m s}^{-1}$ and southerlies are shaded. (b) Vertical profiles of meridional wind (in $\text{m s}^{-1}$ ) averaged over the IFA. The solid line represents the IOP-mean, and dashed lines are for Dec. 11 and Jan. 1 cases. . . . .	53
4.7	The north-south cross section of horizontal divergence averaged between $150^\circ\text{E}$ and $160^\circ\text{E}$ ( $10^{-6} \text{ s}^{-1}$ ). Positive regions, indicative of divergence, are shaded. . . . .	55
4.8	The IOP averaged vertical profiles of horizontal divergence over the Intensive Flux Array and the double-ITCZ bands ( $4^\circ\text{N}$ and $7^\circ\text{S}$ ) ( $10^{-6} \text{ s}^{-1}$ ). . . . .	56
4.9	(a) Time series of the IFA-averaged GMS brightness temperature (Deg C). (b) Time series of the IFA-averaged vertical motion ( $\text{mb h}^{-1}$ ) throughout the COARE IOP. Areas with $\omega \leq -1.0 \text{ mb h}^{-1}$ are shaded. (c) Time series of 1000 hPa wind speed over the IFA. (5-day running mean). . . . .	58
4.10	Scatter plots of brightness temperature and vertical motion over the IFA. (a) $\omega$ at 300 hPa, (b) $\omega$ at 700 hPa. . . . .	60
4.11	North-south cross section of $\omega$ ( $\text{mb h}^{-1}$ ) between $150^\circ\text{E}$ and $160^\circ\text{E}$ . Regions of upward motion are shaded. (a) IOP mean, (b) November, (c) December, (d) January, (e) February. Contour interval is $0.5 \text{ mb h}^{-1}$ . . . . .	62
4.12	(a) East-west cross section of IOP-mean $\omega$ averaged between $5^\circ\text{N}$ and $5^\circ\text{S}$ . Shaded regions indicate upward motion. (b) East-west variation of NCEP SST averaged between $5^\circ\text{N}$ and $5^\circ\text{S}$ (Deg C). . . . .	64

4.13 (a) Time series of the daily-mean relative humidity (%) over the Intensive Flux Array. Shaded area indicates RH > 64%. (b) Time series of the IFA-mean wind speed ( $\text{m s}^{-1}$ ) at 700 hPa. (5-day running mean). . . . .	66
4.14 IOP-mean profiles of relative humidity over the IFA. Solid lines are from the COARE analysis, with respect to liquid water and ice. Dashed lines are from ECMWF and NCEP model assimilated analyses. . . . .	67
4.15 (a) Time series of temperature perturbation (deviation from the COARE mean) over the IFA. Contour interval 0.8 K and anomalous warming is shaded. (b) Time series of the IFA-averaged GMS brightness temperature (Deg C). . . . .	69
4.16 A descriptive model of the kinematic, thermodynamic and surface properties of the December-early-January westerly wind burst as it passed the IFA. Day 0 is time of maximum low-level westerlies, with earlier times indicated by negative days (placed to the right so that the left portion of the diagram is to the west: see caution in text, however, about fully interpreting diagram as west-east section). Letters in figure refer to anomalies: W = warm, C = cool, M = moist and D = dry. Heavy arrows indicate strong vertical motion, light arrows weak vertical motion. Clouds are schematic, horizontal scales exaggerated. Temperatures corresponding to pressure levels are indicated on right. . . . .	71
5.1 Comparisons of surface latent heat flux ( $\text{W m}^{-2}$ , 5-day running mean) (a) from IMET buoy ( $1^{\circ}45'S$ , $156^{\circ}E$ ) and three TOGA TAO buoys (mt163a: $5^{\circ}S$ , $156^{\circ}E$ ; mt165a: $2^{\circ}S$ , $156^{\circ}E$ ; mt166a: $0^{\circ}S$ , $157^{\circ}E$ ). (b) from IMET buoy, R/V Shiyang #3, R/V Kexue #1, and the ECMWF IFA-mean. A time series of surface wind speed over the IFA ( $\text{m s}^{-1}$ ) is superimposed in (b) for comparison. . . . .	77
5.1 Continued. . . . .	78
5.2 Comparisons of surface sensible heat flux ( $\text{W m}^{-2}$ , 5-day running mean) (a) from IMET buoy ( $1^{\circ}45'S$ , $156^{\circ}E$ ) and three TOGA TAO buoys (mt163a: $5^{\circ}S$ , $156^{\circ}E$ ; mt165a: $2^{\circ}S$ , $156^{\circ}E$ ; mt166a: $0^{\circ}S$ , $157^{\circ}E$ ). (b) from IMET buoy, R/V Shiyang #3, R/V Kexue #1, and the ECMWF IFA-mean. . . . .	80
5.2 Continued. . . . .	81
5.3 (a) The IOP-mean surface latent heat flux ( $\text{W m}^{-2}$ ) over the Large Scale Array. Contour intervals $10 \text{ W m}^{-2}$ and areas with values $> 120 \text{ W m}^{-2}$ are shaded. (b) The IOP-mean surface sensible latent heat flux ( $\text{W m}^{-2}$ ) over the Large Scale Array. Contour intervals $1.0 \text{ W m}^{-2}$ and areas with values $> 9 \text{ W m}^{-2}$ are shaded. . . . .	83
5.4 The IOP-mean NCEP SST (Deg C) over the LSA. Contour intervals $0.2^{\circ}$ and areas with SST $> 29.0^{\circ}$ are shaded. . . . .	84
5.5 Time series of daily-mean zonal U component ( $\text{m s}^{-1}$ ), precipitation and evaporation ( $\text{mm day}^{-1}$ ) averaged over the Intensive Flux Array (5-day running mean). Contour intervals $4 \text{ m s}^{-1}$ and westerlies are shaded. . . . .	86
5.6 Comparison of the IOP-mean rainfall distributions over the LSA ( $\text{mm day}^{-1}$ ): (a) Budget determination, (b) ECMWF forecast result, (c) SSM/I measurements, (d) GPI estimation. Contour intervals $2 \text{ mm day}^{-1}$ and areas with rainfall rate $> 6 \text{ mm day}^{-1}$ are shaded. . . . .	87
5.6 Continued. . . . .	88

5.7	Comparison of daily-mean rainfall rates ( $\text{mm day}^{-1}$ ) over the IFA from moisture budget, SSM/I retrievals, GPI and ECMWF model forecast result (5-day running mean). . . . .	91
5.8	Comparison of components of the moisture budget: precipitation, evaporation, storage and moisture convergence over the IFA ( $\text{mm day}^{-1}$ , 5-day running mean). . . . .	93
5.9	Monthly time series of the IFA-mean apparent heat source $Q_1$ ( $\text{K day}^{-1}$ ), the apparent moisture source $Q_2$ ( $\text{K day}^{-1}$ ), SST (Deg C), surface wind speed ( $\text{m s}^{-1}$ ), GMS brightness temperature (Deg C), surface latent and net longwave radiative heat fluxes ( $\text{W m}^{-2}$ ). November, December, January, and February. The contour intervals for $Q_1$ and $Q_2$ are $3 \text{ K day}^{-1}$ and areas $> 1.0 \text{ K day}^{-1}$ are shaded. Dotted lines above the $Q_1$ figures indicate periods during the COARE IOP when both ships Kexue #1 and Shiyan #3 were out of the IFA. . . . .	95
5.9	Continued. . . . .	96
5.9	Continued. . . . .	99
5.9	Continued. . . . .	101
5.10	Comparison of rainfall-normalized apparent heat source $Q_1$ (in units of $\text{K day}^{-1}/1 \text{ cm day}^{-1}$ ) from the IFA, the OSA, the Marshall Islands region (Yanai et al. 1973) and the GATE region (Thompson et al. 1979). . . . .	103
5.11	Comparison of rainfall-normalized apparent heat source $Q_2$ (in units of $\text{K day}^{-1}/1 \text{ cm day}^{-1}$ ) from the IFA, the OSA, the Marshall Islands region (Yanai et al. 1973) and the GATE region (Thompson et al. 1979). . . . .	105
5.12	North-south cross sections of (a) $Q_1$ and (b) $Q_2$ ( $\text{K day}^{-1}$ ) between $150^\circ\text{E}$ and $160^\circ\text{E}$ . Contour intervals are $1 \text{ K day}^{-1}$ and areas with positive values are shaded. . . . .	107
5.12	Continued. . . . .	108
6.1	Time series of near-surface meteorological observables measured at the WHOI buoy (taken from Weller and Anderson 1996). Two-hour averages of, from top to bottom, the wind component toward the north, the wind component toward the east, barometric pressure, specific humidity, incoming longwave radiation, incoming shortwave radiation, air temperature, and sea surface temperature (0.45 m depth). . . . .	114
6.2	Time series of unfiltered apparent heat source $Q_1$ ( $\text{K day}^{-1}$ ), the apparent moisture source $Q_2$ ( $\text{K day}^{-1}$ ), 1000 hPa wind speed ( $\text{m s}^{-1}$ ), GMS brightness temperature (Deg C) over the IFA, along with SST (Deg C) and surface latent heat fluxes ( $\text{W m}^{-2}$ ) from the IMET buoy between 11 November and 10 December, 1992. The contour intervals for $Q_1$ and $Q_2$ are $3 \text{ K day}^{-1}$ and areas $> 1.0 \text{ K day}^{-1}$ are shaded. Dotted lines above the SST figure indicate periods during the COARE IOP when the clear-sky, light-wind condition prevailed. . . . .	117
6.3	(a) Time series of total rainrate (thick solid line) and non-convective rainrate (thin solid line) in $\text{mm day}^{-1}$ for Cruise 1 (taken from Rickenbach and Rutledge 1996a). The time intervals when events of each types were present are also shown. . . . .	119
6.3	Continued. (b) A radar reflectivity map at a height of 2 km for a sub-MCS scale non-linear event on 1 December 1992 (from TCIP0 TOGA COARE Operations Summary). . . . .	120

6.4	Diurnal variations (1-h intervals) in surface latent and sensible heat fluxes ( $W m^{-2}$ , SST (Deg C), and near surface air temperature (Deg C) under the clear-sky, light-wind condition. (IMET buoy data courtesy of Drs. Weller and Anderson, WHOI).	121
6.5	Diurnal variations in divergence ( $10^{-6} s^{-1}$ ), vertical motion ( $mb h^{-1}$ ), $T'$ (Deg C), and $Q_2$ ( $K day^{-1}$ ) over the IFA under the clear-sky, light-wind condition. Shaded regions indicate divergence, upward motion, positive T deviation, and drying, respectively.	123
6.6	Time series of (a) relative humidity (%) profiles; (b) precipitable water (in g, 400-1000 hPa; 500-1000 hPa; 600-1000 hPa) over the IFA between 11 November and 10 December, 1992.	125
6.7	Diurnal variation in MIT Doppler radar rainfall for sub-MCS non-linear events under the clear-sky, light-wind condition (courtesy of Drs. Tom Rickenbach and Steve Rutledge, CSU).	127
6.8	Histograms of the fraction of convective features occurring in 1 km convective feature height bins, for each event type and for all events combined under the clear-sky, light-wind condition (courtesy of Drs. Tom Rickenbach and Steve Rutledge, CSU).	128
6.9	Time series of unfiltered apparent heat source $Q_1$ ( $K day^{-1}$ ), the apparent moisture source $Q_2$ ( $K day^{-1}$ ), 1000 hPa wind speed ( $m s^{-1}$ ), GMS brightness temperature (Deg C) over the IFA, along with SST (Deg C) and surface latent heat fluxes ( $W m^{-2}$ ) from the IMET buoy between 11 December and 10 January, 1992. The contour intervals for $Q_1$ and $Q_2$ are $3 K day^{-1}$ and areas $> 1.0 K day^{-1}$ are shaded. Dotted lines above the SST figure indicate periods during the COARE IOP when the cloudy sky strong wind condition prevailed.	129
6.10 (a)	Time series of total rainrate (think solid line) and non-convective rainrate (thin solid line) in $mm day^{-1}$ for Cruise 2 (taken from Rickenbach and Rutledge 1996a). The time intervals when events of each types were present are also shown.	130
6.10	Continued. (b) A radar reflectivity map at a height of 2 km for a MCS scale linear event on 24 December 1992.	131
6.11	Diurnal variations (1-h intervals) in surface latent and sensible heat fluxes ( $W m^{-2}$ , SST (Deg C), and near surface air temperature (Deg C) under the cloudy sky strong wind condition. (IMET buoy data courtesy of Drs. Weller and Anderson, WHOI).	133
6.12	Diurnal variations in divergence ( $10^{-6} s^{-1}$ ), vertical motion ( $mb h^{-1}$ ), $T'$ (Deg C), and $Q_2$ ( $K day^{-1}$ ) over the IFA under the cloudy sky strong wind condition. Shaded regions indicate divergence, upward motion, positive T deviation, and drying, respectively.	134
7.1	Profiles of $Q_1$ and $Q_2$ normalized by precipitation rate for Intensive Flux Array (IFA), Outer Sounding Array (OSA) and Marshall Islands (from Yanai et al. 1973).	145
7.2	$Q_1$ and $Q_2$ profiles for convectively disturbed period (11-17 December 1992).	146
7.3	IOP time series of $Q_2$ (top panel, positive values shaded) and precipitation rate $P_0$ and evaporation rate $E_0$ (bottom panel) for Outer Sounding Array.	148

7.4	IOP time series of $Q_2$ (top panel, positive values shaded) and precipitation rate $P_0$ and evaporation rate $E_0$ (bottom panel) for Intensive Flux Array. Also, surface wind speed has been added to bottom panel. . . . .	149
7.5	$Q_1$ , $Q_2$ , $Q_R$ , and $Q_1 - Q_R$ profiles for two westerly wind burst periods (27 December-3 January and 2-10 February) and an undisturbed ISO phase (14 November-5 December). . . . .	151
7.5	Continued. . . . .	152
7.5	Continued. . . . .	153
7.6	(Left) The observed $Q_1$ , $Q_2$ , $Q_R$ , and $Q_1 - Q_R$ for the undisturbed BOMEX period 22-26 June 1969 (From Nitta and Esbensen 1974). (Center) schematic of tradewind cumulus layer showing effects of condensation $\bar{c}$ and evaporation $\bar{e}$ on the heat and moisture budgets. (Right) Mean vertical $p$ -velocity $\bar{\omega}$ over budget area. . . . .	154
7.7	Vertical profiles of saturation moist static energy of the environment $\bar{h}^*$ and moist static energy of the clouds at the detrainment level $h_D$ during 27 December-3 January westerly wind burst. . . . .	157
7.8	A photograph taken from the R/V <i>Vickers</i> (2.1°S 156.3°E) around 0100 UTC on 26 December 1992 (Courtesy Tom Rickenbach). The photograph shows shallow cumulus with tops near 2-2.5 km (assuming a cloud base of ~0.5 km) and higher clouds above. . . . .	158
7.9	(a) Mean, environmental and cumulus mass fluxes and (b) entrainment and detrainment for 27 December-3 January westerly wind burst. . . . .	160
7.10	(a) Heat and (b) moisture balances for 27 December-3 January westerly wind burst. . . . .	161
7.11	As in Fig. 7.7, except for 2-10 February westerly wind burst. . . . .	162
7.12	A photograph taken from the R/V <i>Vickers</i> (2.1°S 156.3°E) in the evening of 6, 7 or 8 February 1992 (Courtesy Rob Cifelli). The photograph shows shallow cumulus with tops near 1.5 km (assuming a cloud base of ~0.5 km). . . . .	163
7.13	As in Fig. 7.9, except for 2-10 February westerly wind burst. . . . .	165
7.14	As in Fig. 7.10, except for 2-10 February westerly wind burst. . . . .	166
7.15	A photograph taken from the <i>Xiangyanghong #5</i> (2.0°S 155.8°E) on 21 November 1992). The photograph shows shallow cumulus with tops near 2-2.5 km (assuming a cloud base of ~0.5 km). . . . .	168
7.16	As in Fig. 7.7, except for 14 November-5 December undisturbed period. . . . .	169
7.17	As in Fig. 7.9, except for 14 November-5 December undisturbed period. . . . .	170
7.18	As in Fig. 7.10, except for 14 November-5 December undisturbed period. . . . .	171

## LIST OF TABLES

2.1	Spatial and temporal scales of hierarchic structure of ISOs (taken from Nakazawa 1988). . . . .	11
3.1	Some characteristics of sounding stations within Large Scale Array during COARE IOP. . . . .	32
5.1	The IOP-mean surface latent and sensible heat fluxes ( $\text{W m}^{-2}$ ) from different sources. . . . .	79
6.1	Some characteristics of the ocean and the atmosphere during undisturbed and disturbed periods. . . . .	115

## Chapter 1

### INTRODUCTION

Tropical convection, especially over the western Pacific warm pool, plays a significant role in global redistribution of heat, moisture, and momentum. This region is characterized not only by the warmest sea surface in the open oceans, but also by the largest annual rainfall and latent heat release in the atmosphere (Webster and Lukas 1992), implying a strong coupling between the ocean and atmosphere. Latent heat released by condensation of water vapor in the tropical atmosphere and surface heat fluxes from the tropical ocean have been considered to act as major heat sources for the global circulation (e.g., Riehl 1954; Riehl and Malkus 1958; Emanuel et al. 1994).

Among the broad temporal and spatial scales of tropical oscillation, the most prominent large-scale feature is the 30-60 day eastward propagating oscillation (hereafter referred to as the intraseasonal oscillation or ISO), which was first detected by Madden and Julian (1971) in the zonal wind and surface pressure in the tropical Pacific. While this oscillation is evident in circulation fields throughout the tropics (Madden and Julian 1972; Knutson and Weickmann 1987), its signature in convection is generally limited to the eastern Indian and western Pacific Oceans (Madden and Julian 1972, 1994). Strong low-level westerlies usually appear near the equator following the convectively active phase of this oscillation (e.g., Lau et al. 1989; Sui and Lau 1992; Madden and Julian 1994). These anomalous winds, referred to as westerly wind bursts (Luther et al. 1983; Nitta and Motoki 1987), can last from a few days to several weeks, and usually have a large impact on tropical deep convection and the ocean surface. Although not all westerly wind bursts are associated with the ISO, there is evidence to suggest that the ISO modulates both the frequency and amplitude of

higher-frequency convection and westerly burst events (Lau et al. 1989; Gutzler 1991; Sui and Lau 1992; Hendon and Liebmann 1994).

In recent years, the ISO and westerly wind bursts in the tropical Pacific have received renewed interest since they may serve as triggering mechanisms to the El Niño-Southern Oscillation (ENSO), which can affect both interannual and intraannual variabilities of the global climate system (Harrison and Schopf 1984; Lau and Chan 1986, 1988). Connections have also been noted with the Indian and East Asian monsoon (Yasunari 1979; Chang and Lau 1980, 1982; Krishnamurti and Subrahmanyam 1982; Lau et al. 1983), the Australian monsoon (Holland 1986; Hendon and Liebmann 1990a, b), tropical storms (Gray 1979), and weather patterns in middle latitudes (e.g., Lau and Chan 1986; Magaña and Yanai 1991). Nakazawa (1988) using Geostationary Meteorological Satellite (GMS) IR data, showed that the ISO in the tropical western Pacific is associated with one or more eastward-moving super cloud clusters, with successive formation of new individual cloud clusters east of the mature stage cloud clusters. Individual cloud clusters embedded within super cloud clusters move westward.

Several theories have been proposed to explain the origin and characteristics of the ISO: wave-CISK (e.g., Chang 1977; Lau and Peng 1987; Chang and Lim 1988; Wang 1988a), forcing-response (e.g., Yamagata and Hayashi 1984; Hu and Randall 1994), Wind-Induced Surface Heat Exchange (WISHE) (Emanuel 1987; Neelin et al. 1987; Yano and Emanuel 1991) (see the review by Hayashi and Golder 1993), and feedback between local SST gradient and convection (Flatau et al. 1997). However, most of these ideas have not been tested and proven by observations, and many remain unexplored due to insufficient surface and upper air records over the tropical western Pacific, particularly over open oceans. Outgoing long wave radiation (OLR) data are not able to provide the basic kinematic and thermodynamic features, which are essential to understanding the dynamics of the ISO. Its relationship with surface rainfall rates and vertical heating profiles is still not well understood. Model output analyses, although they can provide high temporal and spatial resolution datasets, are sensitive to different physical parameterization schemes (e.g., Emanuel 1988; Chao and Lin 1994) and assimilation constraints.

Determination of convective heating and moistening is essential to studies on tropical oscillations at various scales. Modeling studies have suggested that the short-term changes in climate and the variability of global circulations are very sensitive to the details of the vertical heating profiles from convection and low-level heating from boundary-layer processes (Hartmann et al. 1984; Lau and Peng 1987). However, the knowledge of tropical vertical heating and moistening distributions, mesoscale and cloud-scale processes, and precipitation is very limited except for several well-instrumented and short-duration field experiments such as GARP Atlantic Tropical Experiment of 1974 (GATE) and Equatorial Mesoscale Experiment (EMEX) of 1987. In the western Pacific, several heat and moisture budget studies have been undertaken near the Marshall Islands (Reed and Recker 1971; Nitta 1972; Yanai et al. 1973); however, this region is centered off the equator ( $5 - 10^{\circ}\text{N}$ ) and we do not know if these results can be extended to the equatorial warm pool. Also, little is known about the primary heating and moistening distributions in the western Pacific warm pool that occur in connection with the ISOs (Nakazawa 1988; Lau et al. 1989). The importance of the feedback between the ocean surface and the tropical low-frequency oscillations is still mysterious. Several modeling studies of the 30–60-day oscillation have illustrated that their propagation speeds are very sensitive to the vertical distribution of heating (Lau and Peng 1987; Chang and Lim 1988) and zonal SST gradients (Flatau et al. 1997).

The western Pacific is a region of net fresh-water input into the ocean (Lukas 1990; Webster and Lukas 1992). Mass and buoyancy fluxes can significantly affect the dynamics and thermodynamics of the ocean's mixed layer (Ostapoff et al. 1973; Miller 1976), and direct thermal effects associated with precipitation may act as a negative feedback on convection (Greenhut 1978). The distribution of precipitation and evaporation over the warm pool has long been subject to considerable uncertainty due to sparse traditional land-based gauge measurements and shipboard estimates, and possible unrepresentative observations (Legates and Willmott 1990). One of the most important objectives of meteorological satellites is to monitor climate change and estimate energy transport by accurately determining surface rainfall using remote sensing devices. Furthermore, general circulation models

require accurate rainfall information over tropical oceans to improve their cumulus parameterizations. Several methods using satellite data have been developed to estimate tropical rainfall rates (Spencer 1986; Arkin and Meisner 1987). To fulfill these objectives requires comparing satellite estimates to surface and budget-derived determinations.

The November 1992 – February 1993 TOGA COARE (Tropical Ocean Global Atmosphere/Coupled Ocean-Atmosphere Response Experiment) (Webster and Lukas 1992) was designed to improve understanding of the role of the western Pacific warm pool in the mean and transient state of the tropical ocean/atmosphere system. Various meteorological and oceanographic observations were taken in order to describe and understand the principal processes responsible for the coupling of the ocean and the atmosphere in the warm pool system. A sounding network enabled determination of the four-dimensional structure of atmospheric heating and moistening and budget-derived rainfall distribution. Surface fluxes were measured over the warm pool over a wide range of scales using a variety of platforms from the microscale (e.g., ships and aircrafts) to the mesoscale (with aircraft and radars) to the large scale (using satellite and sounding data). Several westerly wind bursts occurred over the TOGA COARE domain during the four-month Intensive Observing Period (IOP) providing a unique opportunity to investigate the mean and transient behavior and horizontal variability of the atmosphere and the ocean over the warm pool.

Given that the western Pacific warm pool is a focal point for deep convection as well as the highest amplitude of tropical intraseasonal variability, including westerly wind bursts, the objective of this study has been to (1) document the basic kinematic and thermodynamic features of the atmosphere and its convective variability over the period of TOGA COARE, in particular, the interactions among the ISOs, convection and surface fluxes; (2) determine heating, moistening, evaporation, and rainfall distribution over the western Pacific pool; (3) study different cloud population and oceanic response under disturbed and undisturbed weather conditions. In particular, several questions are investigated:

- How do convection, surface heat and radiative fluxes, and SSTs evolve before, during and after the passage of an ISO-related westerly wind burst? Are they similar to those predicted by some ISO theories? This information has never been documented

in tropical oceans, and will be very essential for cloud-resolving and single column modeling and theoretical studies.

- What are the representative heating and moistening profiles over the western Pacific warm pool? How well do remote sensing rainfall estimations compare with budget-type determination and operational model forecasts?
- What controls the population of shallow and deep convection under disturbed and undisturbed weather conditions? What are the diurnal variabilities of the atmosphere and ocean surface under the clear-sky, light-wind and cloudy-sky, strong-wind conditions?

## Chapter 2

### BACKGROUND

#### 2.1 Studies on the Intraseasonal Oscillations

##### *2.1.1 Overview of observational studies*

In the 1960s and 1970s, although there was a general lack of surface and upper air data over tropical oceans, both theoretical and observational studies on tropical waves made considerable progress. Almost at the same time that Matsuno (1966) published his pioneering theoretical work on classification of tropical waves, Yanai and Maruyama (1966) discovered the mixed Rossby-gravity wave. Later Wallace and Kousky (1968), using spectrum analysis methods, identified Kelvin waves in the lower stratosphere.

Madden and Julian (1971) applied spectral and cross-spectral analysis methods to analyze nearly ten years of daily rawinsonde data from Canton Island. A prominent 40-50 day oscillation was detected in the zonal wind and surface pressure in the tropical Pacific. They found that the oscillation in the lower tropospheric zonal wind is in phase with surface pressure oscillation, and out of phase with the upper tropospheric zonal wind. Low surface pressures were usually associated with strong 850 hPa easterlies and high surface pressures associated with weak 850 hPa easterlies or westerlies. The tropospheric temperatures exhibited a similar peak and were found to be highly coherent with the surface pressure oscillation. However, no signs of the oscillation were evident in the mixing ratio data at 850 hPa and the meridional wind component.

Madden and Julian (1972) extended their work to more stations and meteorological variables to investigate the spatial extent of the low-frequency oscillation. Their cross-spectral analysis suggests that the oscillation is of global scale but restricted to the tropics.

It features a baroclinic vertical structure and a wavenumber one wave propagation. The lower tropospheric oscillation is confined to the tropical Pacific and Indian Oceans while that of the upper troposphere can affect the entire circumference of the globe. Figure 2.1 is a schematic taken from Madden and Julian (1972) which approximately depicts the time and space evolution of a disturbance associated with the ISO. The ISO-related disturbance can be seen as an eastward movement of large-scale circulation cells oriented in the equatorial plane. It usually originates in the eastern Indian Ocean (near  $80^{\circ}\text{E}$ ), gradually moves across the maritime continent and into the western Pacific Ocean, and then weakens and dissipates as it continues to propagate eastward to the central and eastern Pacific. It was speculated by Madden and Julian (1972) that these zonally propagating 30-60 day oscillations might be equatorial Kelvin waves.

Following Madden and Julian's discovery, many observational and diagnostic studies have been undertaken to describe the general features of the ISO and its possible relationship with other phenomena, in particular: the initialization mechanism of the ISOs, the global extent of the ISOs, the propagating features of the ISOs, and the ISO-related multiscale variabilities in the atmosphere and the ocean.

Since the ISOs are usually observed to originate in the tropical Indian Ocean, there is a strong possibility that they are closely related with the monsoonal convection which is resulted from the unique large land-sea contrast in this region. Yasunari (1979) was among the first to directly relate eastward propagation of the ISO disturbance along the equator to the northward propagating cloud bands during the Indian summer monsoon. Based on satellite cloud data, he found that the northward movement of monsoonal clouds was initiated by eastward-propagating low-frequency disturbances developing over the equatorial Indian Ocean. These northward-propagating bands also have a prominent spectral peak at 30-60 day period. The active and break phases of the monsoon could be related to the fluctuation of this period range. Several later studies on monsoonal cloud bands, precipitation, and 850 hPa wind anomalies (Yasunari 1980, 1981; Krishnamurti and Subrahmanyam 1982; Murakami 1983; Lau and Chan 1986; Knutson et al. 1986; Hartmann and Michelson 1989) confirmed the relevance of the ISOs to the northward propagation of the break-active phases of Indian monsoon.

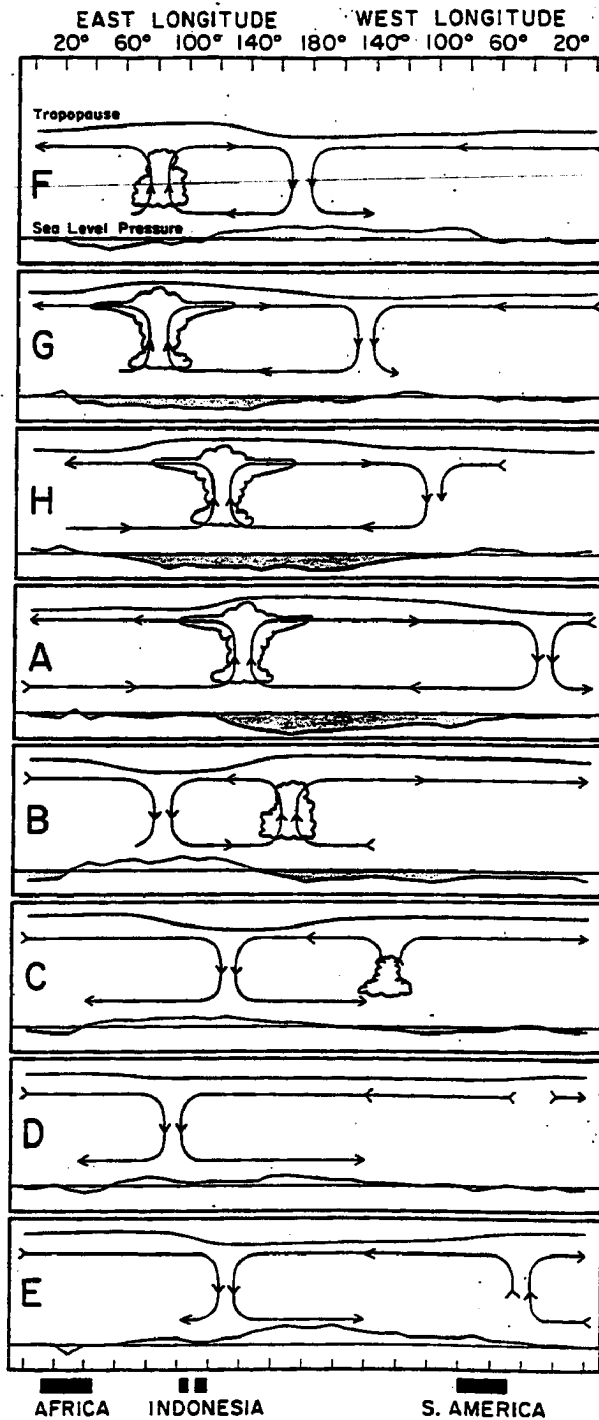


Figure 2.1: Schematic depiction of the time and space (zonal plane) variations of the disturbance associated with the intraseasonal oscillation. Dates are indicated symbolically by the letters at the left of each chart and correspond to dates associated with the oscillation in Canton's station pressure. The letter A refers to the time of low pressure at Canton and E is the time of high pressure there. The other letters represent intermediate times (taken from Madden and Julian 1972).

Is it possible that the active and break phases of Indian monsoon provoke the low-frequency oscillation? Wang and Rui (1990) investigated synoptic climatology of transient tropical intraseasonal convection anomalies from 1975 to 1985. They identified 122 events during this period and classified them into three categories: eastward (77), independent northward (27), and westward (18) propagation. They found that the eastward propagation occurs more frequently in boreal winter than in summer, while the independent northward propagation, which is not associated with equatorial eastward propagation, occurs in boreal summer from May to October. Furthermore, Wang and Rui (1990) noticed that a majority of strong events occur during boreal winter from November to April, whereas weak events most frequently occur from May to August. Similar seasonally variational features have also been noticed by Madden (1986) and Gutzler and Madden (1989). This evidence appears to imply that the Indian summer monsoon might not initiate the ISOs in the equatorial Indian Ocean. Rather, the break and active phases of Indian summer monsoon are heavily modulated by the low-frequency oscillation. Several GCM studies (Hayashi and Sumi 1986; Hayashi and Golder 1986) with ocean-covered earth have suggested that the intraseasonal oscillations could be simulated in a model without land-sea interactions. These modeling results support Wang and Rui (1990)'s finding and exclude the Indian Ocean monsoonal convection as a major mechanism for initializing the tropical low-frequency oscillation.

Although some composite analyses (e.g., Rui and Wang 1990) have shown some intraseasonal convective anomalies over equatorial Africa during early developing phase of the ISOs, there has been no solid evidence indicating that the ISOs can originate over equatorial Africa, and composite methods are not well suited to identified the source regions. Yasunari (1981) and Murakami (1987) noted that occurrence of strong cold surges from southern midlatitude Indian Ocean usually accompany the eastward propagation of the ISO-related disturbances. They hypothesized that the origin of clouds over equatorial Indian Ocean could be related to these midlatitude cold-air outbreaks. To date, however, where the ISOs are preferentially initiated and how they are initiated still remain as a mystery.

Operational model analyses and outgoing longwave radiation (OLR) data have been extensively used to describe the global-scale aspects and the propagation features of the ISO

and related tropical deep convection. Lorenc (1984) studied the large-scale divergence and mean velocity potential fields during the First GARP Global Experiment (FGGE) year. His work based on model assimilated analyses clearly described an eastward propagating wave in the upper-level divergence field with zonal wavenumber one and period of 30-60 days, which was deduced indirectly from sounding data by Madden and Julian (1971, 1972). By analyzing ten years of OLR and eight years of 250 hPa circulation data, Weickmann et al. (1985) statistically investigated evidence for links between the intraseasonal fluctuations of tropical OLR and the global 250 hPa streamfunction. They found that the strongest OLR fluctuations at intraseasonal periods are located from the equator to 15°S and extended from 60° to 160°E and in the vicinity of the South Pacific Convergence Zone (SPCZ). By applying empirical orthogonal function analysis, Lau and Chan (1986) noticed that the most dominant mode of the intraseasonal variability of tropical convection consists of an east-west oriented 30-60 day dipole that propagates eastward at a speed of 4 – 5 m s<sup>-1</sup>. An inverse relationship can be observed between OLR time series over these two dipole centers. Extratropical OLR anomalies evolved coherently with the 40-60 day tropical oscillation. Based on the evidence that the 1982-1983 ENSO event appeared to have been preceded by an outburst of 40-50 day wave activity originating from the Indian Ocean, they hypothesized that the 40-50 day oscillation may have acted as a trigger to the ENSO event, thus relating the sub-seasonal variability in the Tropics to global climate changes.

Knutson and Weickmann (1987) examined the composited life cycles of the 30-60 day oscillation using NMC global wind analyses and OLR data. They found that convection anomalies are smaller over tropical Africa and South America than over the Indian and western Pacific oceans. Anomalies of OLR are nearly negligible over cooler tropical sea surface. Rui and Wang (1990) composited intraseasonal OLR anomalies for 36 cases, and documented the development and dynamic structure of tropical 30-60 day oscillation. The intraseasonal convection anomalies were shown to have a four-stage development process: initiation over equatorial Africa, rapid intensification when passing through the Indian Ocean, mature evolution characterized by weakening in the maritime continent and redevelopment over the western Pacific, and dissipating after passing the date line.

Since high-resolution satellite IR data became available, considerable attention has been switched to the fine structure of the ISOs. During the active phase of intraseasonal variations, Nakazawa (1986, 1988, 1995), using 3-hourly GMS IR data, found that there exists a hierarchic structure of convective activities in the tropical western Pacific: planetary scale ISO, eastward moving synoptic scale super cluster, and westward moving meso-scale cloud cluster. Table 2.1 lists the spatial and temporal scales of hierarchic structure of ISO (taken from Nakazawa 1988). He defined a super cluster as an ensemble of cloud clusters with a horizontal scale of several thousand kilometers. Each envelope of ISO disturbance consists of several super clusters. Super clusters generally move eastward along the equator at a phase speed of  $10\text{--}15\text{ m s}^{-1}$ . Figure 2.2 is a schematic diagram for the hierarchy of intraseasonal variability (taken from Nakazawa 1988). Each individual cloud cluster, having a horizontal scale of several hundred kilometers and a time scale of 1–2 days, usually moves westward. Nakazawa (1988) found that cloud clusters within a super cluster usually exhibit different life phases, and super clusters move eastward by successive formation of new cloud clusters east of the mature-stage cloud clusters. Takayabu (1994, 1996) and Haertel and Johnson (1997) further investigated 2-day disturbances embedded within super cloud clusters. They found that the disturbance’s cloud pattern and its propagation resembled an  $n=1$  inertia-gravity wave. Hendon and Liebmann (1994) speculated that these 2-day disturbances were either long-lived squall lines or cloud clusters that were advected westward by mean tropospheric easterlies. They suggested that these disturbances did not play an active role in the evolution of the ISOs, but responded to the large-forcing of the ISOs.

Hierarchy	Horizontal Scale	Time Scale	Phase Direction
ISV	zonal wavenumber 1	30-60 days	eastward
Super cluster	several 1000 km	less than 10 days	eastward
Cloud cluster	several 100 km	1-2 days	westward

Table 2.1: Spatial and temporal scales of hierarchic structure of ISOs (taken from Nakazawa 1988).

The satellite observations of fine structure of the 30-60 day oscillation represented a significant achievement in studies on intraseasonal variabilities, and led to many modeling

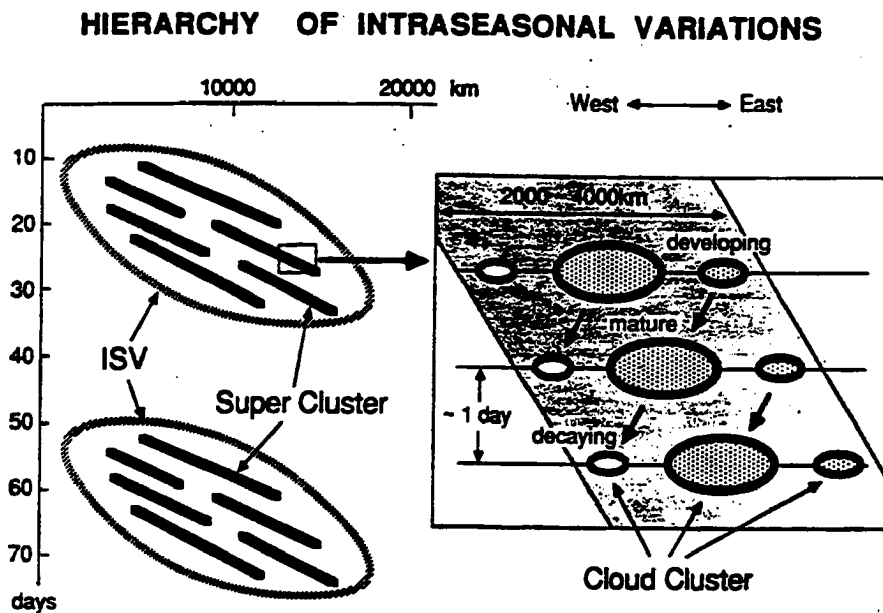


Figure 2.2: Schematic describing the details of the large-scale eastward propagating cloud complexes [slanting ellipses marks ISV (intraseasonal variability) on the left-hand side]. Slanting heavy lines represent super cloud clusters (SCC) within the larger complexes or ISV. The right-hand side illustrates the fine structure of the SCC with smaller westward-moving cloud cluster that develop, grow to maturity, and decay in a few days (from Nakazawa 1988).

studies to simulate and explain the eastward moving super cloud clusters and westward moving cloud clusters (e.g., Lau et al. 1989; Chao and Lin 1994).

Multiscale variabilities of the atmosphere and the ocean associated with the intraseasonal oscillation have not been well documented over the tropical western Pacific, especially with regard to the phase relationship among the ISO-related deep convection, surface fluxes, SST, and maximum westerlies. Chu and Frederick (1990) examined relationship between westerly wind bursts and surface heat fluxes in a case study. They found that the major axis of the surface divergence was located on the west of maximum westerlies throughout the burst period, while the region of maximum surface convergence was on the eastern terminus of the burst. The transfer of latent heat fluxes was noticed to increase markedly from the pre-burst to the burst period. Sui and Lau (1992) studied the multiscale nature in connection with the ISOs over the tropical western Pacific. They found that the ISOs and westerly wind bursts not only strongly modulated the onset of Australian summer monsoon, as found by Murakami et al. (1986) and Hendon and Liebmann (1990a), but also exerted a strong control of high-frequency disturbances and diurnal cycle. An inverse relationship between diurnal cycle and intraseasonal disturbances was found over the maritime continent: the diurnal cycle is most active during the periods when the ISOs are absent and is much suppressed during the passage of the ISOs.

Zhang (1996), using data from TOGA TAO buoys, satellite, and ECMWF wind analysis, studied surface intraseasonal fluctuations and their relationships to the ISOs in the troposphere above the boundary layer. He found that positive anomalies of atmospheric deep convection associated with the ISO tended to occur in regimes of surface westerly perturbations, and the intraseasonal variations at the surface may play active roles in the ISO above the boundary layer. A near-quadrature relation was noted to exist between SST and atmospheric deep convection with maximum convection coinciding with the most rapid decrease in SST. Positive anomalies of surface turbulent heat fluxes and surface wind convergence slightly lead the positive anomalies of convection and wind speed.

Chen et al. (1996), mainly based on satellite data and operational model analyses, investigated multiscale variability of deep convection in relation to large-scale circulation in

TOGA COARE. They found that the SST had an intraseasonal signal in lagged quadrature with the cold cloudiness and rainfall in COARE, and the strongest westerlies tended to be located between synoptic-scale cyclonic gyres on both sides of the equator.

### *2.1.2 Overview of theoretical and simple modeling studies*

The observational and diagnostic studies provided much insight into the general features of the ISO. However, many questions remain unanswered, e.g. why and how does the ISO originate over the Indian Ocean? By what mechanism does it propagate eastward? What is its relationship to other tropical phenomena? Many theories have been proposed to explain the origin and characteristics of the 30-60 day oscillation (see the review by Hayashi and Golder 1993). Three categories of theories can be classified, which we will briefly elaborate in the following sections.

#### **Kelvin waves and wave-CISK theories**

Observations (Madden and Julian 1971; Parker 1973) show that the waves associated with the 30-60 day oscillation have some similar features as the equatorial trapped Kelvin waves: (1) signals of the 30-60 day oscillation are confined to the tropics with maximum amplitude along the equator; (2) the 30-60 day waves generally propagate eastward and upper-level features tend to circulate around the globe; (3) the role of the meridional component is negligible.

On the other hand, there has been a primary difficulty to reconcile the observed slow phase speed and large vertical wavelength of the ISOs based on the traditional Kelvin-wave theory. Observed 30-60 day waves usually have a Doppler-shifted phase speed of 10-15 m s<sup>-1</sup> or even less. With such slow phase speeds, the classical  $\beta$ -plane wave theory (Matsuno, 1966) and the wave-CISK (Conditional Instability of the Second Kind) theory (Hayashi 1970; Lindzen 1974) would predict a vertical wavelength of 8 ~ 9 km. This is in contrast to the observed vertical wavelength of the ISOs (15 - 30 km) which can influence

the entire troposphere, and middle and low stratosphere. In other words, the observed vertical wavelength suggests a phase speed twice as fast as the observed phase speed.

As an early attempt to solve this discrepancy, Chang (1977) included a simple damping term to take into account the effect of strong viscosity due to cumulus momentum transport in the previous inviscid equatorial wave theory. He found that two types of dispersive relationships could result for the forced Kelvin waves: the one with the viscous damping time scale has slower zonal phase speed, and can be used to explain slow eastward propagation of the 30-60 day oscillation.

The basic idea of the wave-CISK theories (e.g., Chang 1977, Lau and Peng 1987, Chao 1987, Chang and Lim 1988, Wang 1988a) is that the 30-60 day oscillation maintains itself and propagates eastward by interaction and feedback between the waves and the cumulus heating. However, the eastward phase speed predicted by the wave-CISK theory (Hayashi 1970, Lindzen 1974) is much faster than observed, even when the mean background flow and dissipation are taken into account (Chang 1977, Lim and Chang 1983). In order to have similar speed to observations, the wave-CISK theories have been modified to allow only positive heating due to condensation (e.g., Lau and Peng 1987; Hendon 1988), and the height of the heating peak has to be lowered to the low troposphere (Takahashi 1987, Lau et al. 1989), which is in conflict with the observations. Many observational studies over tropical western Pacific (e.g., Reed and Recker 1971; Yanai et al. 1973; Lin and Johnson 1996a) have indicated that climatological mean height of the convective heating peak is located between 500 and 350 hPa. Scale selection is another unsolved problem of the wave-CISK theory especially for linear models since the smallest scale has the greatest growth rate, contrary to those observed. Wang (1988a) and Wang and Chen (1989) investigated the role of the boundary-layer friction-induced moisture convergence in the selection of preferred wavenumber one waves and development of vertical structure. They found that the boundary layer convergence plays an important role in spatial scale selection: it not only suppresses unbounded growth of short waves, but also couples barotropic and baroclinic components in such a way that the generation of wave available potential energy is most efficient for planetary scales. However their conclusions have not been tested in a more complex dynamic framework such as GCMs or detailed observations.

In summary, the Kelvin wave-CISK theories have been struggling to explain two primary features of the intraseasonal oscillation: (1) slow phase speed and deep vertical structure; and (2) scale selection. No generalized wave-CISK theories have been satisfactorily proposed, and many existing theories are sensitive to many parameterized coefficients.

### **The forcing-response theories**

The forcing-response theories (e.g., Yamagata and Hayashi 1984, Hayashi and Miyahara 1987, Salby and Garcia 1987, Garcia and Salby 1987, Anderson and Stevens 1987, Hu and Randall 1994) represent another group of theories of the 30-60 day oscillation. Waves are forced by a localized, oscillatory tropical heating of low frequency that does not depend on feedbacks from the large-scale motions to the convection. Many of them stemmed from the general problem of waves forced by prescribed thermal forcing, as studied by Holton (1972) and Gill (1980). Yamagata and Hayashi (1984) applied a modified linear response model of Gill (1980) to examine the response of the equatorial troposphere to a localized heat source pulsating with a 40-day period. They showed the zonal wind oscillation in the model consists of a standing wave with a phase jump in the heating region, while its time phase propagates like traveling waves elsewhere. However, the eastward moving Kelvin waves and westward moving Rossby waves are of comparable magnitudes, which is in conflict with observations. Hayashi and Miyahara (1987) further investigated the atmospheric response to an eastward moving low-frequency heat source using a three dimensional linear model. The responding zonal wind oscillation was found to have significant components that propagate eastward around the earth as observed.

Then what might produce the low-frequency oscillating heat source? Webster and Chou (1980) and Webster (1983) hypothesized that feedbacks between hydrological processes and the differential heating between the interactive ocean and continental regimes result in low-frequency variability. Anderson and Stevens (1987) included the advective effects of a divergent Hadley type basic state in a linear, zonally symmetric model. They found some slow oscillating modes which have many features in common with the observed 30-60 day oscillation. Hu and Randall (1994) proposed that the observed low-frequency wave motions

are the response to forcing by an essentially stationary, self-excited oscillating heat source that is produced by nonlinear interactions among radiation, cumulus convection, and the surface fluxes of sensible heat and moisture. Feedback of the large-scale motions on the latent heating was considered as a side effect.

### The WISHE mechanism

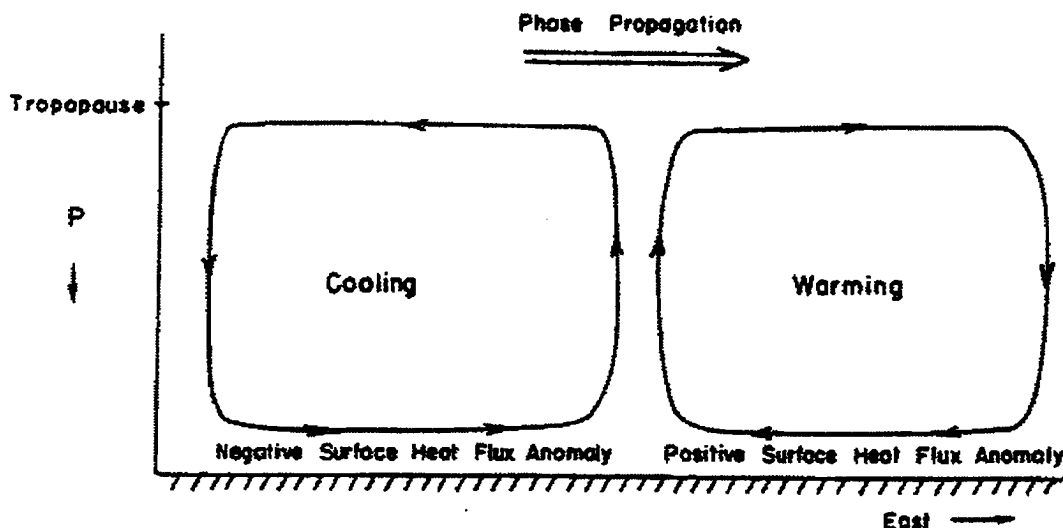


Figure 2.3: Conceptual illustration of the 30-60 day wave as an air-sea interaction instability (from Emanuel 1987). Anomalous strong easterlies at right give rise to anomalous heat fluxes from the sea surface; the moist entropy is then rapidly redistributed aloft by convection. The resulting temperature anomaly leads the surface convergence by one quarter cycle, leading to wave growth and eastward propagation.

The WISHE theory (Emanuel 1987, Neelin et al. 1987, Yano and Emanuel 1991, Numaguti and Hayashi 1991, Emanuel et al. 1994) has also been proposed as an alternative of the wave-CISK theory to explain the maintenance and eastward propagation of the 30-60 day oscillation. Figure 2.3 shows a conceptual illustration of the 30-60 day wave as an air-sea interaction instability (from Emanuel 1987). In this theory, the ISO-related disturbance will force anomalous low-level easterly (westerly) winds to the east (west) of the convective anomaly. When these anomalous winds are superimposed on the tropical mean easterly flow, there will be stronger perturbation easterlies to the east and weaker perturbation

winds to the west of the anomalous heating. Anomalous warming due to enhanced surface heat fluxes to the east and anomalous cooling due to diminishing surface heat fluxes to the west will be favorable for the disturbance to propagate eastward. The eastward propagating speeds were reasonably predicted by these models, however, scale selection still remains as a problem since the shortest waves are the most unstable waves, and it is in common to many linear theories. Yano and Emanuel (1991) were trying to solve the scale selection problem by coupling the equatorial troposphere with a passive stratosphere, but the proposed resolution has yet to be tested in global models (Chao and Lin 1994). In addition, Neelin et al. (1987) showed that the ISO can still occur when the WISHE scheme is suppressed in their model, indicating that other mechanisms may be active in maintaining the 30-60 day oscillation.

The major criticisms of the WISHE mechanism come from the observational perspective. Wang (1988b) showed that in the equatorial regions of the western Pacific and maritime continent, the monthly mean surface winds tend to be very weak. He pointed out that unless the mean equatorial easterly flow is of a significant strength, there will be negligible difference in the surface heat fluxes between easterly and westerly anomalies. Several other observational studies (Lettau 1974; Oort 1983) also suggested the existence of seasonally persistent westerly winds in the Indian and western Pacific Oceans. The absence of meaningful surface easterlies severely limits WISHE's applicability to observed tropical atmosphere (Wang 1988b). Another questionable assumption of the WISHE theory is the roles of convection and surface heat fluxes, and it has stimulated controversy. Convection is only treated as a means to rapidly redistribute heat acquired from the sea surface to the free atmosphere in the WISHE theory, rather than as a heat source. Several essential questions remain unanswered: What is the phase relationship among ISO-related deep convection, surface heat fluxes, and SSTs? and, What is the energy source for amplification and phase propagation of unstable waves?

### *2.1.3 Overview of GCM studies*

Hayashi and Sumi (1986) investigated the possibility of the generation of the ISOs as a collective motion of cumulus activity in an "aqua planet" GCM. The SST distribution

was set symmetric about the equator and uniform in the longitudinal direction. Their model integration exhibited an east-west wavenumber one circulation which resembles the observed 30-60 day oscillation in the real atmosphere. The vertical baroclinic structure and eastward propagating super clusters were well simulated, although westward-moving cloud clusters could not be resolved. Their dry experiment suggested that moist processes are essential for maintaining the 30 day oscillation. Hayashi and Golder (1986) studied ISOs appeared in a Geophysical Fluid Dynamics Laboratory (GFDL) GCM and FGGE data. Their results indicated that the intraseasonal oscillations could be simulated in a model without air-sea interactions and cloud-radiation feedbacks.

Kuma (1994) re-examined the ISO-related tropical disturbances in an aqua-planet GCM with higher resolutions. Both eastward-propagating super clusters and westward-propagating cloud clusters were simulated. They also noticed that the intraseasonal signals are much stronger for higher-resolution model integrations.

## 2.2 Studies on heat and moisture budgets

Deep convection in tropical areas constitutes the major heat source in the global general circulation. Riehl and Malkus (1958) pointed out that in order to compensate the upper troposphere heat loss due to radiation and poleward export over the equatorial trough zone, the most efficient way is to transport heat upward through undiluted ascent in the cores of large cumulonimbus clouds. To parameterize the collective effect of these subgrid-scale clouds in GCMs and numerical weather prediction models in terms of the prognostic variables of grid scale, it is essential to statistically understand how cumulus convection interacts with the large-scale environment.

Effects of cumulus convection on large-scale circulation can be inferred indirectly from heat and moisture budgets of the large-scale circulation system. Yanai et al. (1973) proposed the computational methods for  $Q_1$  (the apparent heat source) and  $Q_2$  (the apparent moisture sink), which related the unresolvable cumulus scale effect to large scale environmental variables. Based on data collected from Marshall Islands region, they found that the long-term divergence profile over the western Pacific ITCZ zone featured a deep layer

of convergence up to 350 hPa and a shallow layer of intense divergence aloft, similar to the results obtained by Reed and Recker (1971) for active cloud clusters. Mean upward motion dominated the entire troposphere and reached its maximum at 350 hPa. Figure 2.4 (from Yanai et al. 1973) shows the time-averaged vertical  $Q_1$  and  $Q_2$  profiles, along with radiative heating profile given by Dopplick (1979). The  $Q_1$  profile indicates a single peak at 475 hPa, while the  $Q_2$  profile shows a double-peak structure. The primary  $Q_2$  peak was located at low levels near 775 hPa, and the secondary peak at 525 hPa. The difference between  $Q_1$  and  $Q_2$  primary peak locations suggests the strength of eddy vertical transport of moist static energy associated with cumulus convection (Yanai et al. 1973; Yanai and Johnson 1993).

By combining the large-scale heat and moisture budgets and a bulk model of cloud ensemble, Yanai et al. (1973) concluded that *“the cloud mass flux exceeds the mean vertical mass flux required by the large-scale convergence, thus causing a compensating sinking motion between active clouds. The large-scale heating of the environmental air is primarily due to its adiabatic compression in the compensating downward motion. The cooling due to re-evaporating liquid water detrained from the clouds is also an important factor in the heat balance of the environment. Counteracting the drying due to the environmental sinking motion are the large amounts of water vapor and liquid water which are detrained from the clouds, especially from the shallow clouds in the lower troposphere, the shallower, non-precipitating cumulus clouds, by their vertical transfer of water vapor, support the growth of the deep, precipitating cumulus clouds”*. This idea was also proposed by Ooyama (1971), Arakawa (1972), Gray (1973), and Arakawa and Schubert (1974).

In the past three decades, many observational and diagnostic studies on heat and moisture budgets have been undertaken. These studies can be roughly divided into two groups: (1) Analyses of heat and moisture budgets over different parts of the world; and (2) diagnosis of cumulus effects based on cloud models.

### 2.2.1 Heat and moisture budget analyses

Since careful examination of vertical and horizontal distributions of  $Q_1$  and  $Q_2$  will yield important information on the nature of heating and moistening processes (e.g., Yanai

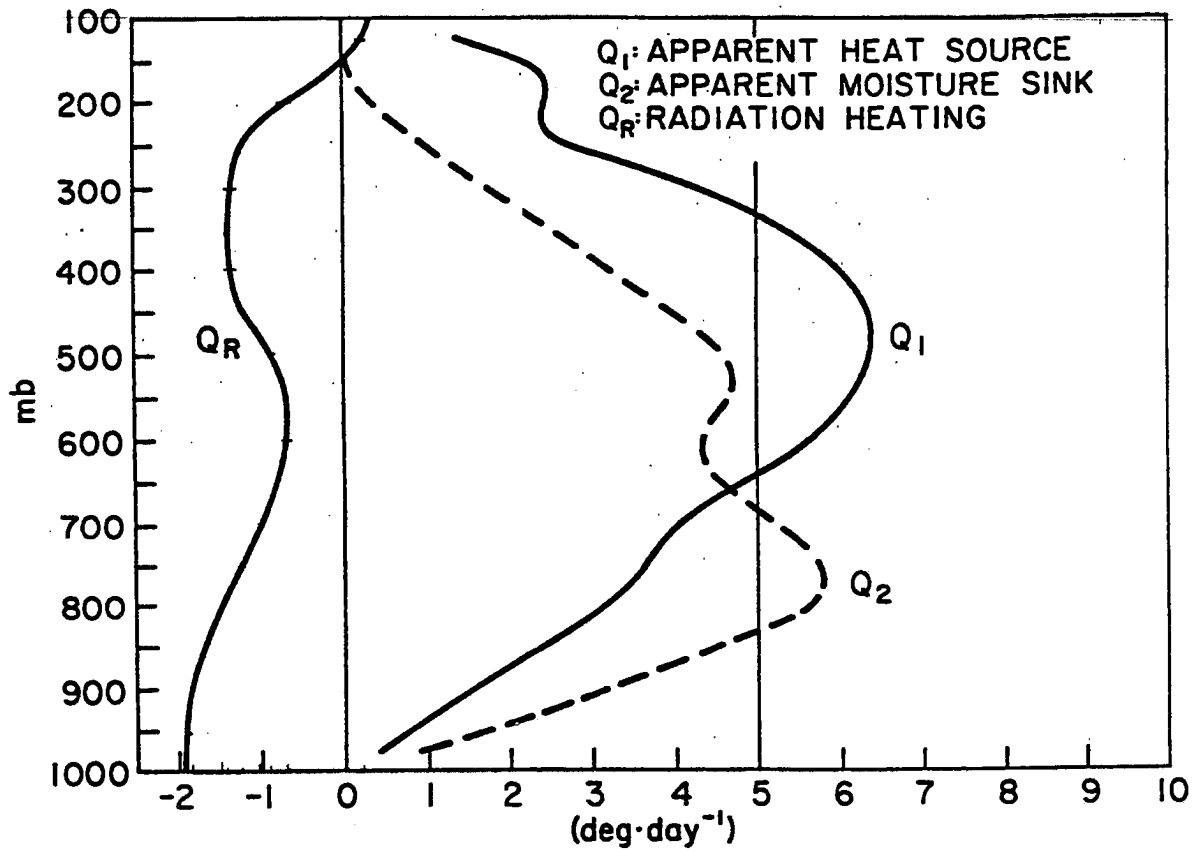


Figure 2.4: The mean apparent heat source  $Q_1$  (solid) and moisture sink  $Q_2$  (dashed) (from Yanai et al. 1973). On the left is the radiative heating profile given by Doplick (1970).

et al. 1973; Nitta and Esbensen 1974; Luo and Yanai 1984; Yanai and Johnson 1993), extensive analyses of heat and moisture budgets have been made over the world under different large-scale environment: the Atlantic trades (Nitta and Esbensen 1974); synoptic wave disturbances over the Atlantic ITCZ zone (Thompson et al. 1979); tropical mesoscale anvil clouds (Johnson 1980; Johnson and Young 1983); the tropical South Pacific (Miller and Vincent 1987; Pedigo and Vincent 1990); the Tibetan Plateau and adjacent Asian monsoon regions (Nitta 1983; Luo and Yanai 1984; Johnson et al. 1993); the Australian monsoon (Frank and McBride 1989; McBride et al. 1989); and mesoscale convective systems in central US (Lewis 1975; Ogura and Chen 1977; Kuo and Anthes 1984; Gullus and Johnson 1991).

In the earlier studies, due to temporal and spatial limitations of data, only the collective heating and moistening effects of many MCSs were evaluated (Reed and Recker 1971; Nitta 1972; Yanai et al. 1973). The time and area-averaged heating profiles showed condensational heating throughout the troposphere, representing the sum of both convective scale and mesoscale precipitation components. Later observations, especially from the 1974 GARP Atlantic Tropical Experiment (GATE), show that deep convection is usually organized into mesoscale features characterized by groups or bands of convective cloud systems, and these convective cloud systems can be properly partitioned into convective and stratiform regions (e.g., Houze 1977; Zipser 1977; Leary and Houze 1979; Johnson 1980; Leary and Houze 1980; Houze and Cheng 1981; Johnson and Young 1983; Gamache and Houze 1982 and 1983; Houze and Rappaport 1984). The degree and character of mesoscale organization appear to be strongly modulated by the environmental wind shear and stability (Yanai and Johnson 1993). How to evaluate and parameterize these mesoscale features has since remained as an interesting and important subject in heat and moisture budget studies.

Houze (1982) and Johnson (1984) found that the convective and stratiform regions have distinctly different contributions to the large-scale latent heat budget (Fig. 2.5). In the convective region, strong condensation, deposition and freezing resulting from cumulus updrafts dominate through the full depth of the troposphere and the heating peak is generally located at middle levels. In the stratiform region, condensation and deposition take place in

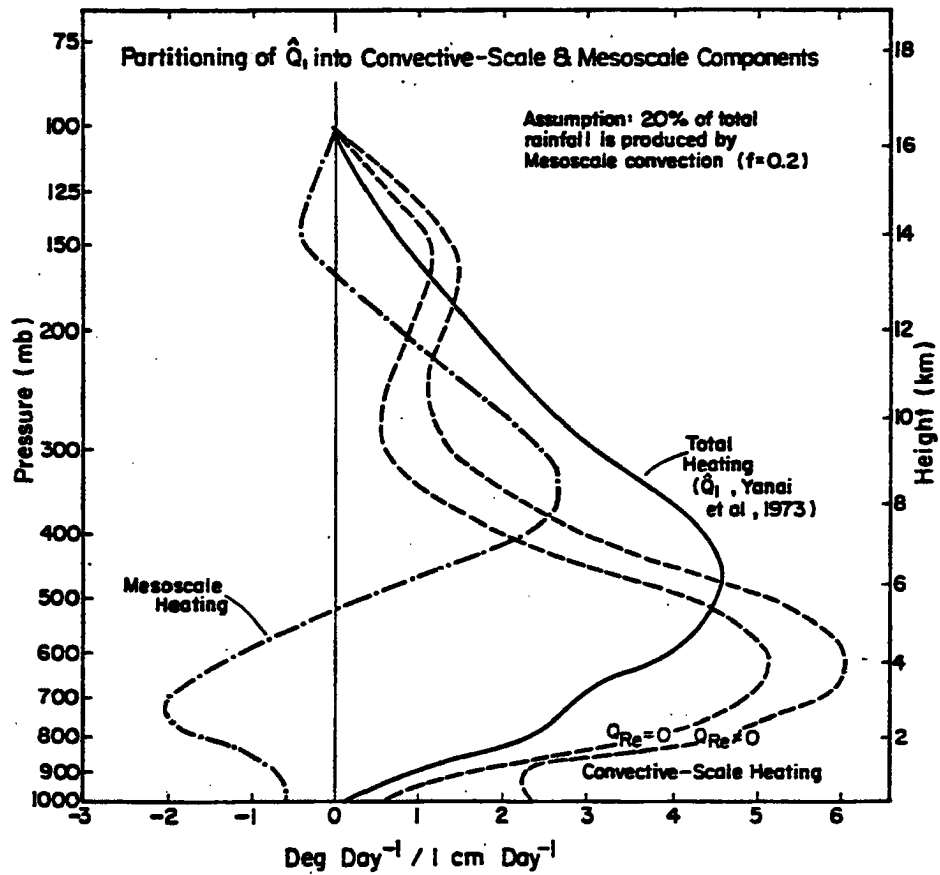


Figure 2.5: Partitioning of the normalized apparent heat source  $Q_1$  into convective-scale (cumulus) and mesoscale components for  $f=0.2$ ;  $f$  is the fraction of the total rainfall produced by mesoscale anvils (from Johnson 1984).

mesoscale updrafts at middle and high levels, evaporation occurs in mesoscale downdrafts at low levels and melting occurs near the  $0^\circ$  level. The heating profiles usually show a heating peak at high levels (about 400 hPa) and a cooling peak at low levels (near 700 hPa). Since rainfall from the stratiform region can make up a significant portion of total rainfall (Cheng and Houze 1979; Gallus and Johnson 1991; Lin and Johnson 1994), the important role of the stratiform region must be considered. The total heating depends on contributions from the convective and stratiform components during the life cycle of mesoscale convective systems.

Although the relationship between the separation of the  $Q_1$  and lower  $Q_2$  peaks and deep convection has been clarified by a number of budget studies, the cause for the mid-tropospheric drying peak is still under investigation. Johnson (1984) proposed that the double-peak  $Q_2$  structure is a result of the combination of two distinctly different drying processes. He suggested that the lower peak is a result of cumulus updrafts in the convective region while the higher one comes from the mesoscale updrafts within anvil clouds. This hypothesis is supported by the results of Esbensen et al. (1988), Gallus and Johnson (1991), and Lin and Johnson (1994). Recently, the importance of vertical eddy transport of water vapor in the  $Q_2$  profile has been investigated (Tao and Soong 1986; Dudhia and Moncrieff 1987; Lafore et al. 1988; Chong and Hauser 1990). Dudhia and Moncrieff (1987) and Lafore et al. (1988) suggested a different interpretation of the double-peak  $Q_2$  structure. Their results showed that the vertical convective eddy transport of water vapor can play an important role on  $Q_2$  profiles and may cause the higher drying peak in the double-peak structure. Although the exact nature of the mid-tropospheric drying peak of  $Q_2$  profiles is still unclear, it is assumed that the coexistence of the convective and stratiform precipitation or strong eddy transport of water vapor by deep convection or a combination of both may result in the structure (Johnson 1992).

### *2.2.2 Diagnosis of cloud effects*

Two simple cloud models have been used to diagnose cumulus effects on the large-scale environment: (1) the bulk method (Yanai et al. 1973); and (2) the spectral method (Ogura

and Cho 1973; Cho and Ogura 1974; Nitta 1975). Here, instead of showing all the equations, we only briefly summarize some features of these two models.

In Yanai et al.'s (1973) bulk model, cumulus clouds are classified according to the height of their tops and all clouds are assumed to have a common cloud-base height. By assuming that cumulus cloud detrains only at the levels where they lose buoyancy, cloud mass flux and other cloud ensemble variables can be obtained by iterating a systems of equations using input from heat and moisture budgets. It was shown that cloud mass flux exceeded large-scale mass flux, and the residual mass flux was downward. Very large detrainment can be observed at low levels and it was thought to be due to large population of shallow clouds (Yanai et al. 1973). The limitation of the bulk method is that it does not give explicit information of the mass spectrum of various cloud types (Yanai and Johnson 1993), and it is difficult to implement contributions of convective downdraft and mesoscale features. This omission lead to the overestimation of cumulus mass flux in the lower troposphere (Johnson 1976; Nitta 1977; Cheng 1989).

The spectral diagnostic model (Ogura and Cho 1973; Nitta 1975) classifies clouds into subensembles according to their levels of detrainment. Explicit assumptions on the subensemble mass and moist static energy budget equations based on a plume-type cloud model are used to uniquely relate the height reached by the clouds to their constant fractional rate of entrainment  $\lambda$ . In this cloud model, the mass flux increases exponentially with height and all the mass detrains at the top of clouds. The fractional rate of entrainment at each level  $\lambda_D(p)$  is first solved by iteration method from large-scale data, and then a Volterra integral equation of the second kind is inverted to obtain  $m_B(\lambda)$ . Ogura and Cho (1973) investigated cumulus effect using data collected from Marshall Islands. Their spectral model results also showed bimodel distribution of the cloud spectrum as did Yanai et al. (1973). Nitta (1975) applied the spectral method to investigate the cloud properties and the manner of interaction between large-scale fields and cumulus convection under strong trade inversion and disturbed situations.

Yanai et al. (1976) applied the spectral method to the same data they used for the bulk model (Yanai et al. 1973). Comparison of the results from these two methods indicates

remarkable agreement. However, the spectral method has many advantages over the bulk method. As Yanai and Johnson (1993) pointed out, it provides not only the bulk properties of the total cloud ensemble, but also the spectrum of cloud-base mass flux  $m_B(\lambda)$ . This feature makes it easy to implement convective downdrafts (e.g., Johnson 1976; Nitta 1977; Cheng 1989) and mesoscale features (e.g., Cheng and Yanai 1989).

### 2.3 Summary

Since the discovery of the intraseasonal oscillation, the ISO has been identified as an important tropical phenomenon which can not only interact upscale with seasonal and annual variabilities, but also heavily modulate smaller-scale phenomena in both tropics and extratropics. As more observational data from different platforms become available, the focus on the studies of the ISO has gradually evolved, and can be generally grouped into five stages based on the data and analysis methods:

(1) The existence of the ISO (e.g., horizontal and vertical structure in the western Pacific, frequency) based on spectral analyses of sparse soundings (Madden and Julian 1971, 1972; Parker 1973);

(2) Global extent and relevance to other tropical and extratropical phenomena (e.g., Yasunari 1979, 1980; Lorenc 1984; Weickmann et al. 1985) based on short-term satellite cloud data and operational model assimilated analyses;

(3) Propagating features and life cycles of the ISOs based on composite studies of long-term satellite data and operational model assimilated analyses (e.g., Knutson and Weickmann 1987; Rui and Wang 1990; Hendon and Liebmann 1994);

(4) Fine structure of the ISO based on high-resolution satellite IR data (e.g., Nakazawa 1986 1988);

(5) Multiscale interactions (e.g., diurnal variations modulated by the ISOs, phase relationships of different kinematic and thermodynamic features before, during and after the passage of an ISO).

In recent years, multiscale variabilities of the atmosphere and the ocean embedded within the ISOs have received much attention. However, most studies on this subject (including many other subjects) mainly based on satellite observations and operational model

analyses to investigate phase relationships among different kinematic and thermodynamic features. Although satellite cold cloud data have been widely used as an index of deep convection in the Tropics, extensive non-precipitating cirrus in the upper troposphere can severely limit the applicability of satellite data. Operational model assimilated analyses are sensitive to different physical parameterization schemes and assimilation constraints, and subject to careful comparison with observed atmospheric and oceanic data. There appears to exist a big gap of information on ISO-modulated convection and air-sea interaction if only satellite data and model assimilated analyses are relied on.

It is our motivation in this study to heavily rely on TOGA COARE atmospheric sounding and surface data to investigate multiscale variabilities in connection with the ISOs. Heat and moisture budget analyses and the cloud spectral models are two important tools to be used in this study. We hope the current study will not only help to test some existing ISO theories and stimulate more thoughts on tropical atmosphere, but also provide detailed information on modulation of deep convection by vertical wind shear, horizontal and vertical distributions of convective heating and moistening, evolution of oceanic surface along with the passages of westerly wind bursts. This information is essential to cloud-resolving and single column modeling studies which aim at improving physical parameterization schemes in ocean-coupled general circulation models. Satellite data and operational model assimilated analyses will be used only as supplemental datasets.

Furthermore, this research shares many common goals and interests with NASA's Tropical Rainfall Measuring Mission (TRMM). NASA is going to launch the TRMM radar (the first quantitative precipitation radar) into space in the near future. The radar data will provide the first opportunity to estimate the four-dimensional structure of latent heating in the tropical atmosphere, and examine the relative contributions of convective and stratiform precipitation in different parts of the Tropics and in different seasons. To fulfill TRMM's objective using remote sensing devices, comparison with ground truth validation by surface and budget-type rain determinations is needed.

Since the topics in this study are quite diverse, we try to present our results in a relatively independent way. Chapter 3 describes data and analysis methods used in this

study. Chapter 4 presents the basic kinematic and thermodynamic features and horizontal variability over the western Pacific warm pool. Chapter 5 discusses heating, moistening, and rainfall distributions over the western Pacific warm pool. Chapter 6 talks about diurnal variation in convection under the clear-sky, light-wind and cloudy-sky strong-wind conditions. Chapter 7 determines shallow cloud populations and other cloud properties using a cloud spectral model. Chapter 8 presents a summary of the findings, and addresses some future work.

## Chapter 3

### DATA AND ANALYSIS METHODS

#### 3.1 The TOGA COARE field experiment

The Tropical Ocean Global Atmosphere (TOGA) program represented a 10-year effort (1985 – 1995) to establish the physical basis for the variability of climate on intraseasonal time scales and forecast the variability (Webster and Lukas 1992). In order to better understand the ENSO event and the intraseasonal variability of the coupled atmosphere-ocean system, the TOGA Coupled Ocean-Atmosphere Response Experiment (TOGA COARE) was designed to better specify the coupling of the ocean and the atmosphere. As discussed in Webster and Lukas (1992), the scientific goals of COARE were to describe and understand:

- the principal processes responsible for the coupling of the ocean and the atmosphere in the western Pacific warm pool system;
- the principal atmospheric processes that organize convection in the warm-pool region;
- the oceanic response to combined buoyancy and wind-stress forcing in the western Pacific warm-pool region;
- the multiple-scale interactions that extend the oceanic and atmospheric influence of the western Pacific warm-pool system to other regions and vice versa.

The TOGA COARE experiment consisted of three major components:

- an interface component, in which the major emphasis are the measurement and modeling of the interfacial fluxes between the atmosphere and the ocean over a wide variety of atmospheric and oceanic conditions;

- an atmospheric component, where the emphasis is on the measurement and modeling of those processes that determine the state of the atmospheric boundary layer, and, thus, influence the interfacial fluxes of heat, water, and momentum;
- an oceanographic component, where the emphasis is on the measurement and modeling of the response of the upper ocean in order to assess the response to the varying fluxes at the interface that occur over the range of weather events and types encountered in the warm pools of the tropical oceans.

Through these components, long-term atmospheric and oceanic data could be collected to characterize and quantify the processes of air-sea interaction over the western Pacific and the relationship of the warm-pool structures to the larger-scale context. The data will not only be very useful for the initialization and validation of coupled models, but also allow the calibration of satellite retrieval algorithms and provide ground truth for rainfall estimations.

## 3.2 Data and analysis methods

### 3.2.1 Rawinsonde data

Figure 3.1 shows the TOGA/COARE sounding network which was established over the equatorial western Pacific to determine the mesoscale to synoptic-scale structure of atmospheric circulation systems over the warm pool. It consisted of nested arrays, ranging from the synoptic scale (the Large Scale Array or LSA, 140°E to 180°E, 10°S to 10°N, with twice-per-day soundings), to the subsynoptic and mesoscale (the Outer Sounding Array or OSA and the Intensive Flux Array or IFA, both with four-per-day soundings). The IFA was centered at 2°S, 156°E bounded by a polygon consisting of two land stations, Kapingamarangi (1°N, 154°E), Kavieng (3°S, 151°E), and two research vessels, the *Kexue* #1 (4°S, 156°E), and the *Shiyan* #3 (2°S, 158°E). The majority of the high-density meteorological and oceanographic observations in COARE were taken within the IFA. Integrated sounding systems (ISS, Parsons et al. 1994), consisting of Omegasondes, 915 MHz wind profilers, acoustic sounders, and surface meteorology stations, were employed at these four sites.

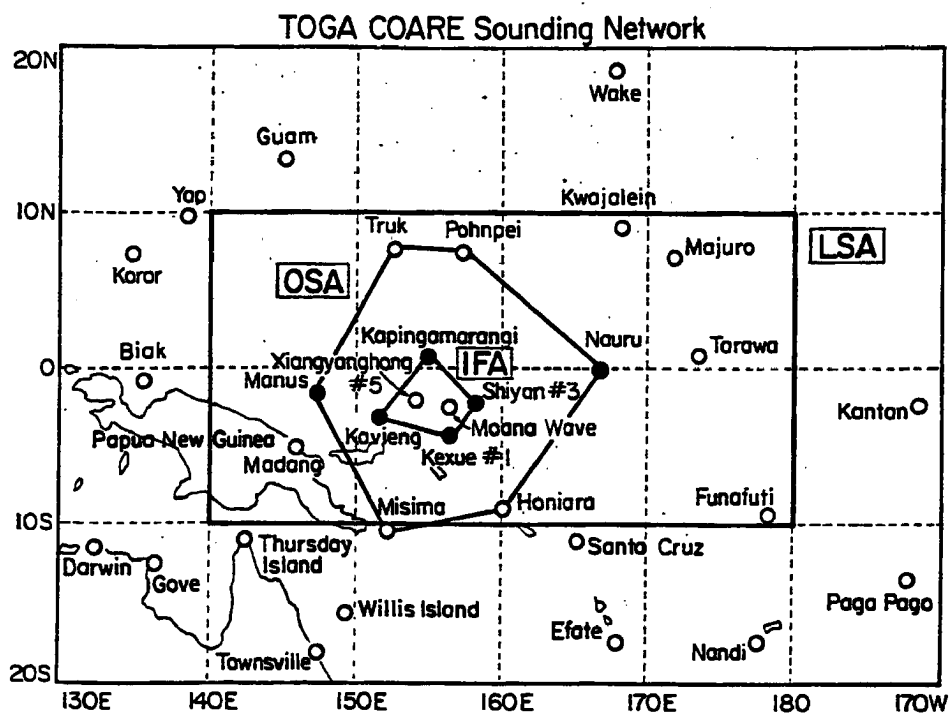


Figure 3.1: The TOGA COARE sounding network. The solid circles indicate ISS stations and the open circles represent other sounding stations.

Soundings were also released from research vessels including *Xiangyanghong #5*, *Vickers*, and *Moana Wave* within the IFA.

All available sounding data from the stations in Fig. 3.1 were combined to perform computations at 6-hour intervals throughout the four-month IOP from November 1, 1992 to February 28, 1993. Table 3.1 shows the number of released soundings and instrument type for stations within the OSA that were used in this study during the COARE IOP.

Station Name	# of soundings	Instrument Type	Station Type
Truk	477	OMEGA	Island
Honiara	414	ISS	Island
Kapingamarangi	475	ISS	Atoll
Kavieng	468	ISS	Island
Kexue 1	356	ISS	Ship
Manus	448	ISS	Island
Moana Wave	257	OMEGA	Ship
Nauru	471	ISS	Island
Pohnpei	480	OMEGA	Island
Shiyan 3	330	ISS	Ship
Vickers	111	OMEGA	Ship
Xiangyanghong 5	263	OMEGA	Ship

Table 3.1: Some characteristics of sounding stations within Large Scale Array during COARE IOP.

During the TOGA COARE IOP, the Vaisala humidity sensor mounted on the Omega Sonde was used to detect the water vapor over the OSA and IFA. It provides accurate and high resolution humidity data in the lower and middle troposphere. Unfortunately, measurements from the field showed the sensor to regularly “ice up” at temperatures below about  $-44^{\circ}\text{C}$  (about 250 hPa) so that the upper-level humidity could not be sampled. However, this problem does not affect the main results of our study.

ISS Omegasondes provided high quality information on pressure, temperature, dew point temperature, zonal and meridional wind components, and latitude and longitude of the measurement at approximately 50-m vertical resolution. Quality control parameters for pressure, temperature, relative humidity, and zonal and meridional wind components were

utilized to exclude bad data from the analyses. Additional hydrostatic, horizontal, and statistical checks were performed to eliminate erroneous sounding data.

The rawinsonde data (temperature, specific humidity, zonal and meridional wind components, and height) were first vertically interpolated from 1000 to 25 hPa at intervals of 25 hPa. A 1-2-1 smoothing scheme was used to filter out small-scale fluctuations in the vertical. Then they were objectively interpolated onto a  $1.0^\circ$  by  $1.0^\circ$  grid over a region larger than the LSA ( $130^\circ\text{E}$  to  $170^\circ\text{W}$ ,  $20^\circ\text{S}$  to  $20^\circ\text{N}$ ) using several different approaches described below. In previous studies involving tropical field experiments over the western Pacific and the eastern Atlantic, several different analysis techniques have been used to determine horizontal divergence, e.g., the Bellamy (1949) or line-integral method, least-squares fitting, and optimal statistical interpolation (Ooyama 1987). The line-integral method is usually used over small areas surrounded by three or more stations. The area-averaged properties can be coarsely estimated, although problems can occur with poor distribution of the stations and nonlinear variations of fields between vertices (Davies-Jones 1993). The least-squares fitting method usually utilizes a linear or quadratic surface to approximately represent the horizontal fields. It is suitable for an analysis over a small area where the curvature of the surface is small. However, for the areas considered and the uneven distribution of COARE stations, including the existence of several sounding sites within the IFA, it is found that neither a linear surface nor a quadratic surface is accurate enough to represent the variations of basic fields over the IFA and OSA, especially for moisture and wind fields. The Barnes analysis scheme (Barnes 1964, 1973) has been used in our study. The percentage of the resolved wavelengths can be easily estimated by varying the influence radius. Large-scale and mesoscale features can be recovered while smaller scale disturbances are suppressed. A cubic-spline analysis package (courtesy of Dr. Steve Lord, National Centers for Environmental Prediction (NCEP)), which is based on the mechanical interpolation method described by Ooyama (1987), was also tested. The results were very similar to those from the Barnes analysis.

Since the average distances between sounding stations within the COARE domain varied considerably from about 300 km in the IFA to 700 km in the OSA, values at each grid

point were interpolated from the 6 closest stations. A filter response of about fifty percent at the mean distance among the grid point and the six stations was selected. Soundings were generally released twice per day outside of the OSA. In this study, unless otherwise specified, the IFA-averaged profiles are based on data at 6-hour intervals, while horizontal and vertical cross sections over larger areas are based on data at 00 and 12 UTC. Spatial derivatives were calculated using a finite centered-difference method. Vertical velocities were calculated by integrating the mass continuity equation in  $p$  coordinates from the surface to the tropopause. A constant correction has been applied at each grid point to the divergence at all levels to satisfy mass continuity for the whole volume. Vertical velocity at 75 hPa was set to zero since the tropopause was usually between 100 and 85 hPa in the tropical western Pacific. Vertical velocity at the surface was computed from surface wind and pressure data.

The apparent heat source  $Q_1$ , and the apparent moisture sink  $Q_2$  (Yanai et al. 1973) are computed by

$$Q_1 \equiv c_p \left[ \frac{\partial \bar{T}}{\partial t} + \bar{\mathbf{v}} \cdot \nabla \bar{T} + \left( \frac{p}{p_0} \right)^\kappa \bar{\omega} \frac{\partial \bar{\theta}}{\partial p} \right] \quad (3.1)$$

$$Q_2 \equiv -L \left( \frac{\partial \bar{q}}{\partial t} + \bar{\mathbf{v}} \cdot \nabla \bar{q} + \bar{\omega} \frac{\partial \bar{q}}{\partial p} \right) \quad (3.2)$$

where  $T$  is temperature,  $\theta$  potential temperature,  $q$  mixing ratio of water vapor,  $\kappa = R/c_p$ ,  $R$  and  $c_p$  gas constant and the specific heat at constant pressure of dry air, respectively,  $L$  latent heat of condensation,  $p_0 = 1000$  hPa,  $\omega$  vertical  $p$ -velocity, and the overbar refers to a horizontal average. Here,  $Q_1$  is a measure of radiative heating, latent heating from net condensation and ice phase changes, and the convergences of the vertical and horizontal eddy transports of sensible heat. Here,  $Q_2$  is a measure of the net condensation and the horizontal and vertical convergences of the eddy moisture transports.

Once the distributions of surface sensible and latent heat fluxes and radiative heating are known, rainfall rates can be estimated from heat and moisture budgets by integrating (Eq. 3.1) and (Eq. 3.2) from  $p_T$  (the pressure at cloud top) to  $p_s$  (surface pressure) (Yanai et al. 1973):

$$P_0 = \frac{1}{gL} \int_{p_T}^{p_s} (Q_1 - Q_R) dp - \frac{S_0}{L} \quad (3.3)$$

$$P_0 = \frac{1}{gL} \int_{p_T}^{p_s} Q_2 dp + E_0 \quad (3.4)$$

where  $P_0$  is precipitation,  $S_0$  and  $E_0$  the surface sensible heat flux and evaporation, respectively, and  $Q_R$  radiative heating.

In this study, surface sensible and latent heat fluxes are calculated from surface data. Since information on the radiative heating profile is currently not available, rainfall rate is diagnosed from the moisture budget (Eq. 3.4).

### 3.2.2 Satellite data

Japanese Geostationary Meteorological Satellite (GMS) brightness temperature data (courtesy of Dr. Tetsuo Nakazawa) were used to facilitate the analysis. The data, collected every hour, have a spatial resolution of approximately 11 km. Data at each pixel were first averaged to get values in a  $1^\circ$  grid box, and then the box values were averaged to generate mean brightness temperatures over the LSA and the IFA-mean time series.

Two remote sensing rainfall estimations from satellite data were used to compare with budget-derived rainfall results: GOES Precipitation Index (GPI) and the rainfall retrievals from the DMSF Special Sensor Microwave/Imager (SSM/I). GPI estimates the area-averaged rainfall by multiplying the fractional coverage of an area by infrared radiation (IR) temperature lower than 235 K by a coefficient of  $3.0 \text{ mm h}^{-1}$  (Arkin and Meisner 1987). Gridded data of GMS brightness temperature were used to calculate GPI over the LSA, and daily GPI was averaged over the IFA. SSM/I measurements (courtesy of Drs. Judy Curry and Guosheng Liu) detected liquid and ice hydrometers in the atmosphere based on an algorithm that combines the emission and scatter regimes of microwave radiation (Liu and Curry 1992) and then integrated them from the surface to the tropopause. The SSM/I data have a spatial resolution of 40–50 km. Since the microwave sensor is on a polar orbiting satellite, the data points are not regularly gridded, nor the sampling time regular.

For a specific area over the COARE domain, the sampling frequency was approximately twice per day. Considering this non-regularity, all available pixels located within the IFA during a day were used to estimate the daily averaged rainfall rate (Dr. Guosheng Liu, 1995, personal communication).

### 3.2.3 *Surface data*

Figure 3.2 shows locations of moorings in COARE domain. Calculation of the surface latent and sensible heat fluxes requires SST, surface air temperature, relative humidity, wind speed, pressure, and measurement height. Several surface data sources were used in this study, including (1) surface ISS data on *Kerue #1* ( $2^{\circ}15'S$ ,  $158^{\circ}E$ ) and *Shiyan #3* ( $4^{\circ}S$ ,  $156^{\circ}E$ ), and SST measurements from these two ships; (2) data from the Improved Meteorological surface mooring (IMET) (courtesy of Drs. Robert Weller and Steve Anderson), which was located at the center of the IFA ( $1^{\circ}45'S$ ,  $156^{\circ}E$ ) (Weller and Anderson 1996); (3) data from three TOGA TAO ATLAS (Automated Temperature Line Acquisition System, McPhaden 1993) moorings: mt163a ( $5^{\circ}S$ ,  $156^{\circ}E$ ), mt165a ( $2^{\circ}S$ ,  $156^{\circ}E$ ), and mt166a ( $0^{\circ}S$ ,  $157^{\circ}E$ ) (courtesy of Dr. Michael McPhaden; names of these buoys are based on their file names); (4) ECMWF TOGA COARE surface heat fluxes (courtesy of Drs. Tony Hollingsworth and Ernst Klinker). Surface sensible and latent heat fluxes from ships and buoys were calculated according to bulk aerodynamic formulation developed by Liu et al. (1979) and subsequently revised for COARE by Fairall et al. (1996). Although there is no surface pressure in TOGA TAO buoy data, we use surface pressure data from the IMET buoy to approximately represent it since surface pressure is only used to calculate air density near the surface in the bulk flux formula and surface air density varies little over the warm pool. Other important parameters that were not available at buoys (e.g., downward IR flux) were also taken from IMET. Since the fluxes principally depend on variables that are measured at the buoys, the results are not very sensitive to this assumption.

### 3.2.4 *Operational model analyses*

A special ECMWF TOGA COARE data set for 15 November 1992 – 15 February 1993 (courtesy of Drs. Tony Hollingsworth and Ernst Klinker, ECMWF) was used in this

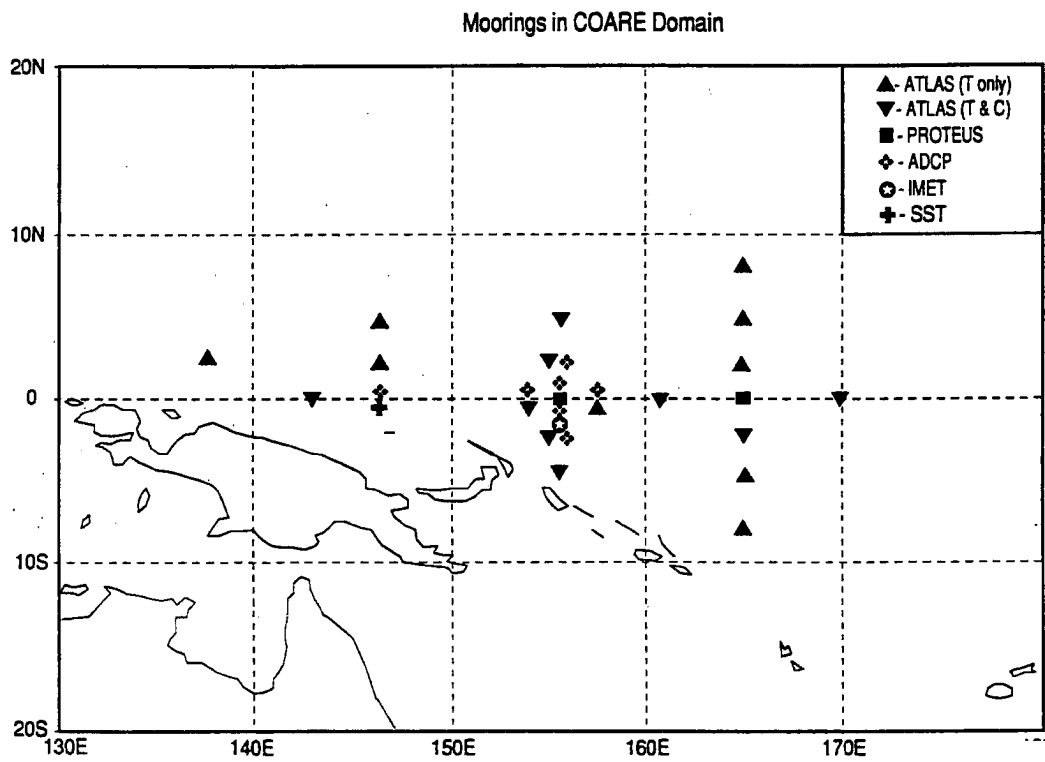


Figure 3.2: Locations of moorings in COARE domain.

study. The fields consist of operational initialized analyses, truncated to T106, and of forecast fields (for 3 and 6 hours) from special model runs with the same model version as the current operational model. Six-hour forecast fields of evaporation, surface sensible heat flux, and precipitation were used to compare with observations and diagnosed results.

## Chapter 4

### BASIC KINEMATIC AND THERMODYNAMIC FEATURES

#### 4.1 Observations from OLR and IR data

##### *4.1.1 Mean distributions*

To define the mean location of deep convection over the warm pool and study its seasonal transition, the IOP-mean brightness temperature over the LSA, and monthly-averaged distributions are shown in Fig. 4.1. The IOP-mean brightness temperature (Fig. 4.1a) indicates that the maximum deep convection was east of the IFA. The IFA was in a transition zone with a minimum in deep convection to the west. A double-ITCZ structure can be observed: the northern one was located between 2°N and 5°N, while the Southern Pacific Convergence Zone (SPCZ) was close to the equator around 170°E and extended southeastward across the Date Line. Cold clouds were usually found over large islands such as New Guinea.

In November (Fig. 4.1b), two cold cloud bands can be observed in the eastern part of the LSA with their lowest values located at 7°N and 7°S, respectively. Over the IFA region, there was a large zonal gradient along the equator with convection being generally suppressed over the western part of the LSA. A large single cold cloud band can be observed in the December mean plot (Fig. 4.1c) south of the equator, extending from 140°E to the Date Line. This convection was associated with the December westerly wind burst. In January (Fig. 4.1d), there was a cold cloud band (between 2° and 7°N) in the Northern Hemisphere extending across the LSA with the strongest convection in the east. Convection in the Southern Hemisphere and SPCZ was notably weak in January. The February mean plot (Fig. 4.1e) indicates a quite different pattern from previous months. The area covered

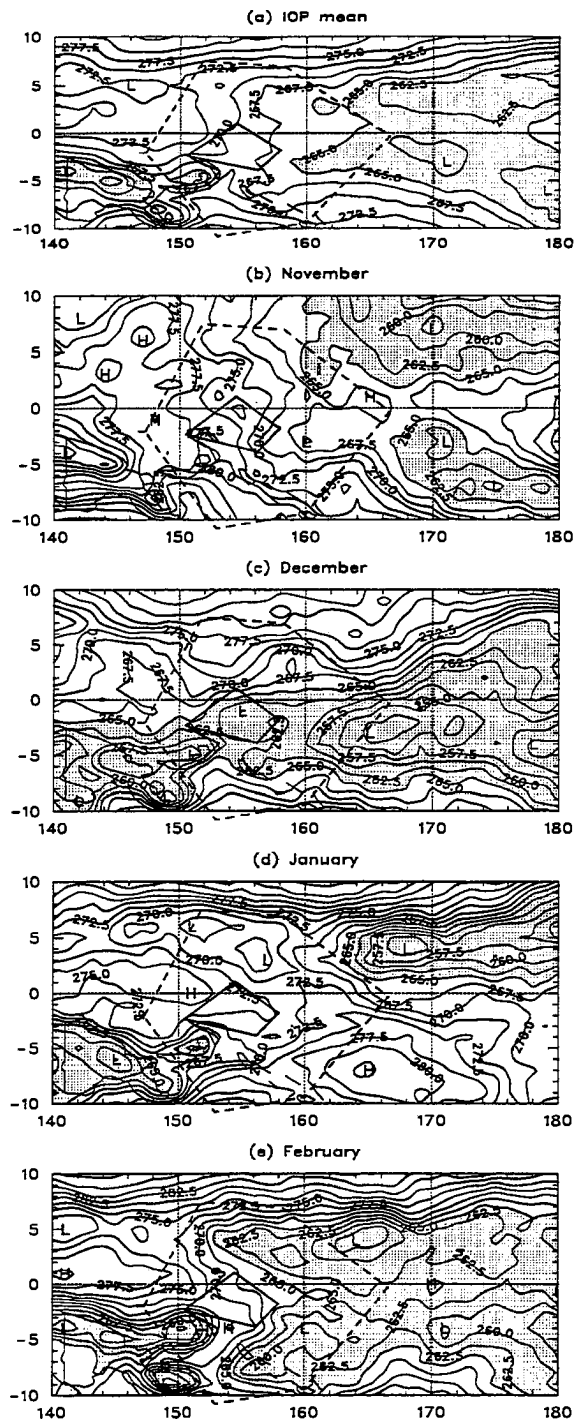


Figure 4.1: IOP-mean and monthly mean brightness temperatures over the Large Scale Array. Contour intervals 2.5 K and areas with temperature less than 265 K are shaded. (a) IOP mean, (b) November, (c) December, (d) January, (e) February.

by cold clouds increased dramatically and most cold clouds were over the central and eastern LSA. The double-ITCZ structure became quite clear across the LSA.

Gutzler et al. (1994) summarized the seasonal-scale variability leading up to and following the COARE IOP. The COARE IOP was found to occur during a period when an exceptional long-lasting warm ENSO episode in the tropical Pacific increased in amplitude. By overlapping 3-month averages of OLR and SST across the tropical western Pacific, they showed that both the warmest SST region and cold cloud region gradually migrated southeastward, consistent with the climatological seasonal cycle. The climatological mean center of deep convection during COARE IOP was located near and just west of  $180^\circ$ .

To summarize, although there was a general north-to-south shift in convection during the IOP, marked variability in the patterns occurred on a month-to-month basis.

#### *4.1.2 Intraseasonal variabilities*

Many researchers have investigated the large-scale intraseasonal variabilities during the TOGA COARE IOP using satellite data (Kiladis et al. 1994; Gutzler et al. 1994; McBride et al. 1995; Nakazawa 1995; Chen et al. 1996). To avoid redundancy, we summarize some of the results in this subsection to provide a large-scale context.

Figure 4.2a is a Hovmöller diagram of pentad OLR values averaged between  $5^\circ\text{S}$  and  $5^\circ\text{N}$  for September 1992 – March 1993 (from Gutzler et al. 1994). Their analyses show that a large-scale envelope of deep convection typically developed over the Indian Ocean, then propagated eastward into the tropical western Pacific, weakened somewhat over Indonesian maritime continent, then intensified again over the warm pool, and finally dissipated after passing the date line, probably due to the cooler sea surface. Three intraseasonal convection anomalies can be observed during the COARE IOP. The first one crossed the western Pacific in mid-to late October, and progressing eastward at about  $1 \text{ m s}^{-1}$ ; The second and third ones occurred between late November 1992 and early February 1993, traversing the region from  $70^\circ\text{E}$  to the date line at approximately  $6 \text{ m s}^{-1}$  (Gutzler et al. 1994; Nakazawa 1995; Chen et al. 1996).

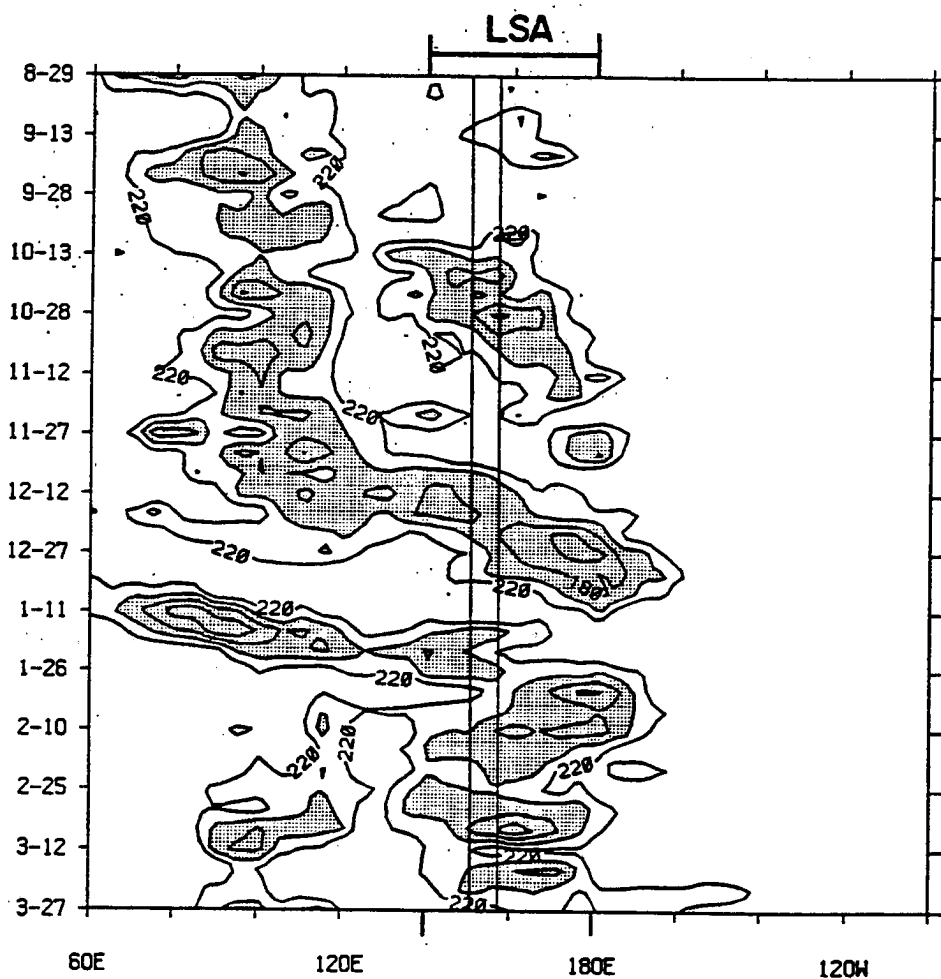


Figure 4.2: (a) Hovmöller diagram of pentad OLR values averaged between 5°S and 5°N for September 1992 - March 1993 (from Gutzler et al. 1994). Vertical axis labels indicated initial month-day of each pentad average. The longitude of the LSA are bracketed at the top of the figure and the approximate longitudinal extent of the IFA is delineated by vertical lines running down the plot. Contour intervals 20  $W m^{-2}$ . Shading denotes OLR greater than 200  $W m^{-2}$ .

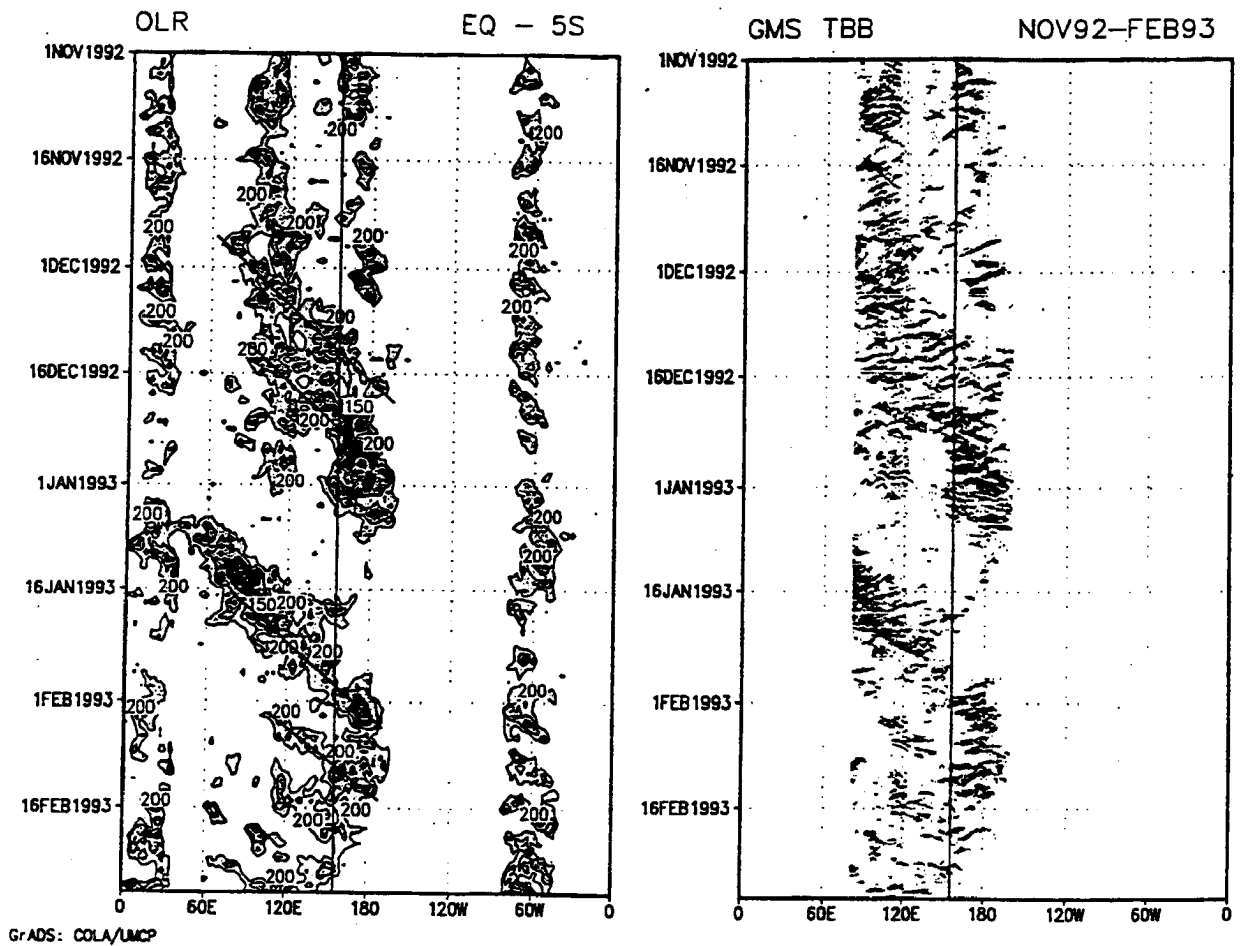


Figure 4.2: Continued. (b) Time-longitude section of OLR (left) and GMS IR (right) averaged between the equator and  $5^{\circ}$  during the TOGA COARE IOP from November 1, 1992 to February 28, 1993 (from Nakazawa 1995).

Nakazawa (1995) showed time-longitude sections of OLR and high-resolution GMS IR averaged between the equator and 5°S (Figure 4.2b). Each eastward-moving ISOs can be seen to consist of several eastward-moving super cloud clusters, and each super cluster consisted of several westward-moving cloud clusters with a life cycle of about 2 days or so. Kiladis et al (1994), Velden and Young (1994), and Chen et al. (1996) all noticed a marked increase in higher-frequency cloudiness/convection over the warm pool during the active phase of the ISO.

## 4.2 Basic kinematic features

### 4.2.1 Zonal wind

Climatological studies show that weak easterly winds generally dominate the low levels along the equator in the tropical western Pacific with speeds on the order of 1–5 m s<sup>-1</sup> (Lau 1985; Peixoto and Oort 1992). The easterlies are often interrupted by westerly wind bursts on intraseasonal time scales in association with the Madden-Julian Oscillation (Madden and Julian 1971, 1972) or extratropical interactions, e.g., via cold surges (Love 1985; Chu 1988; Kiladis et al. 1994). Fig. 4.3a shows the time series of the zonal wind component averaged over the IFA at 0000 UTC throughout the IOP (5-day running mean). Three prominent westerly wind burst periods can be clearly identified during the four-month IOP: (1) early to mid-November, (2) middle December to early January, and (3) late January to the end of February. The Dec.–Jan. case was a major event (Gutzler et al. 1994; Velden and Young 1994): the westerly winds first developed near the surface from Dec. 10 to 15 and gradually increased in depth and magnitude. Maximum westerly winds occurred around Jan. 1 between 850 and 600 hPa at speeds exceeding 12 m s<sup>-1</sup>, while maximum easterlies in excess of 32 m s<sup>-1</sup> were found at about 100 hPa. Unfiltered zonal wind shows maximum easterlies of 37 m s<sup>-1</sup> in the upper troposphere and maximum westerlies of 17 m s<sup>-1</sup> at low levels. The westerly winds at this stage dominated most of the troposphere and extended from the surface up to 200 hPa. The great vertical extent of the westerlies in this case may have been influenced by tropical cyclones Kina and Nina to the south of the IFA. The strong vertical wind shear and out-of-phase relationship between upper- and lower-level

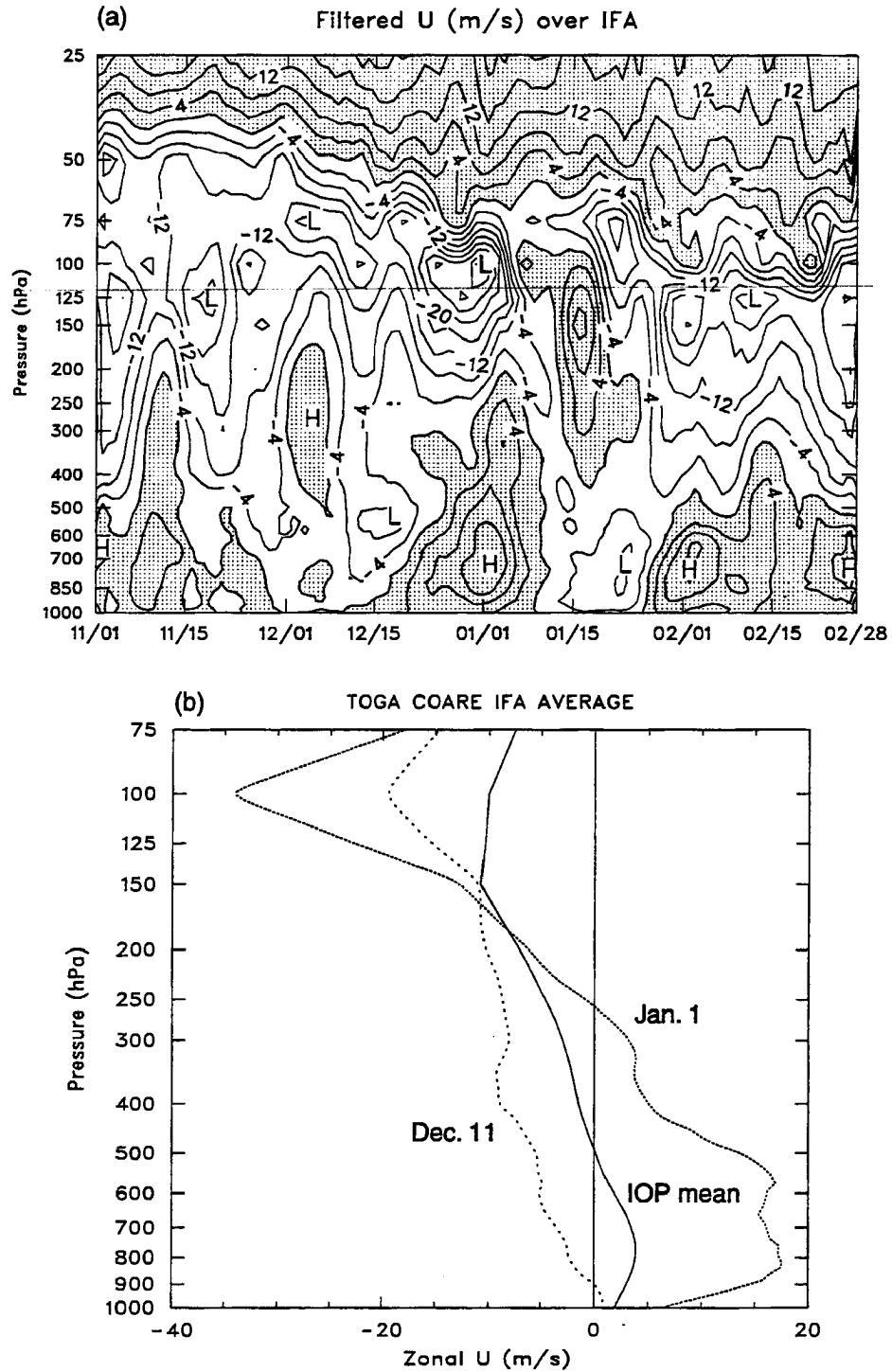


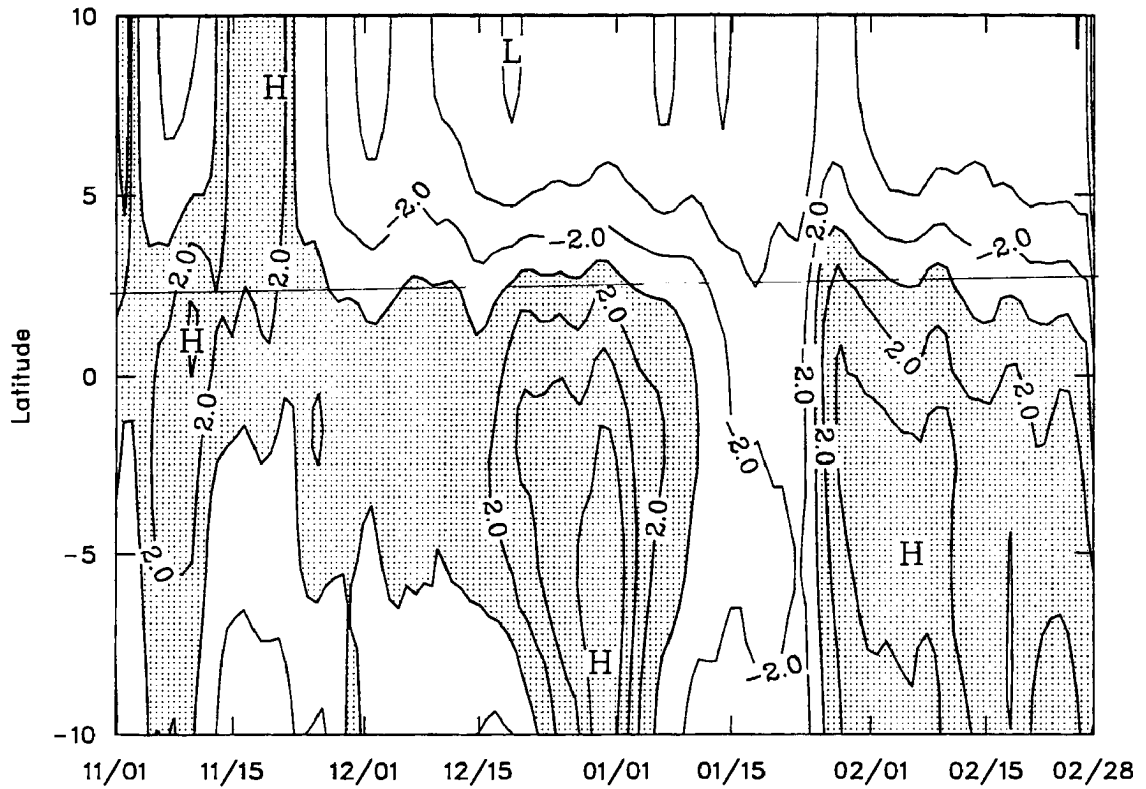
Figure 4.3: (a) Time series of zonal U component ( $\text{m s}^{-1}$ ) at 0000 UTC averaged over the Intensive Flux Array (5-day running mean). Contour intervals  $4 \text{ m s}^{-1}$  and westerlies are shaded. (b) The IOP-mean vertical profile of zonal U component over the IFA (solid curve), and daily-averaged U profiles on December 11 and January 1. Positive values indicate westerlies.

winds are consistent with previous findings (Madden and Julian 1971, 1972; Knutson and Weickmann 1987). The westerlies stopped abruptly and reversed to easterlies in the middle and lower troposphere toward mid-January, while strong westerlies appeared in the upper troposphere. Between 50 and 150 hPa, there appears to be some evidence of downward-propagating equatorial Kelvin waves (Wallace and Kousky 1968; Gutzler et al. 1994) from Dec. 1 through the end of February. Above 50 hPa in the stratosphere, the zonal wind field was in general dominated by westerlies since the IOP was during the westerly phase of the quasi-biennial oscillation (QBO). The gradual downward propagation of the QBO westerly regime is also readily apparent in Fig. 4.3a.

Figure 4.3b shows the IOP mean zonal wind profile over the IFA based on 6-hourly data. To illustrate the dramatic change in the vertical wind shear during the westerly wind burst, daily-averaged vertical profiles for Dec. 11 and Jan. 1 are shown. In the mean, there were westerlies at low levels and easterlies aloft. The Dec. 11 profile was at a time of strong upward motion (Fig. 4.9, later) and deep convection as westerlies converged with easterlies at low levels near the IFA. Weak westerlies existed from the surface to 900 hPa and easterlies above. Vertical wind shear in the mid-troposphere was relatively weak. On Jan. 1, when the convection was suppressed over the IFA (Fig. 4.9, later), westerly winds in the lower troposphere reached a maximum (about  $17 \text{ m s}^{-1}$ ) with easterlies at nearly  $35 \text{ m s}^{-1}$  at 100 hPa. This vertical wind shear of over  $50 \text{ m s}^{-1}$  through the depth of the troposphere was probably too strong to support deep convection, as found in some midlatitude studies (e.g., Weisman et al. 1988). The vertical wind shear and the vertical extent of westerlies during the peak westerly wind bursts were far greater than previously recognized.

In order to examine the evolution of the meridional structure of the westerly wind bursts near the surface, a time-latitude cross section of zonal component of the wind at 1000 hPa was constructed using gridded data between  $150^\circ\text{E}$  and  $160^\circ\text{E}$ , where there were dense sounding stations during the IOP. Again, three westerly wind bursts can be identified during the four-month period (Fig. 4.4a). In the November case, the westerlies first developed between  $4^\circ\text{N}$  and  $10^\circ\text{S}$ , with a peak at  $2^\circ\text{N}$ . Then they migrated northward between Nov. 10

a. U (m/s) at 1000 hPa averaged between 150E and 160E



b. IR temperature (K) averaged between 150E and 160E

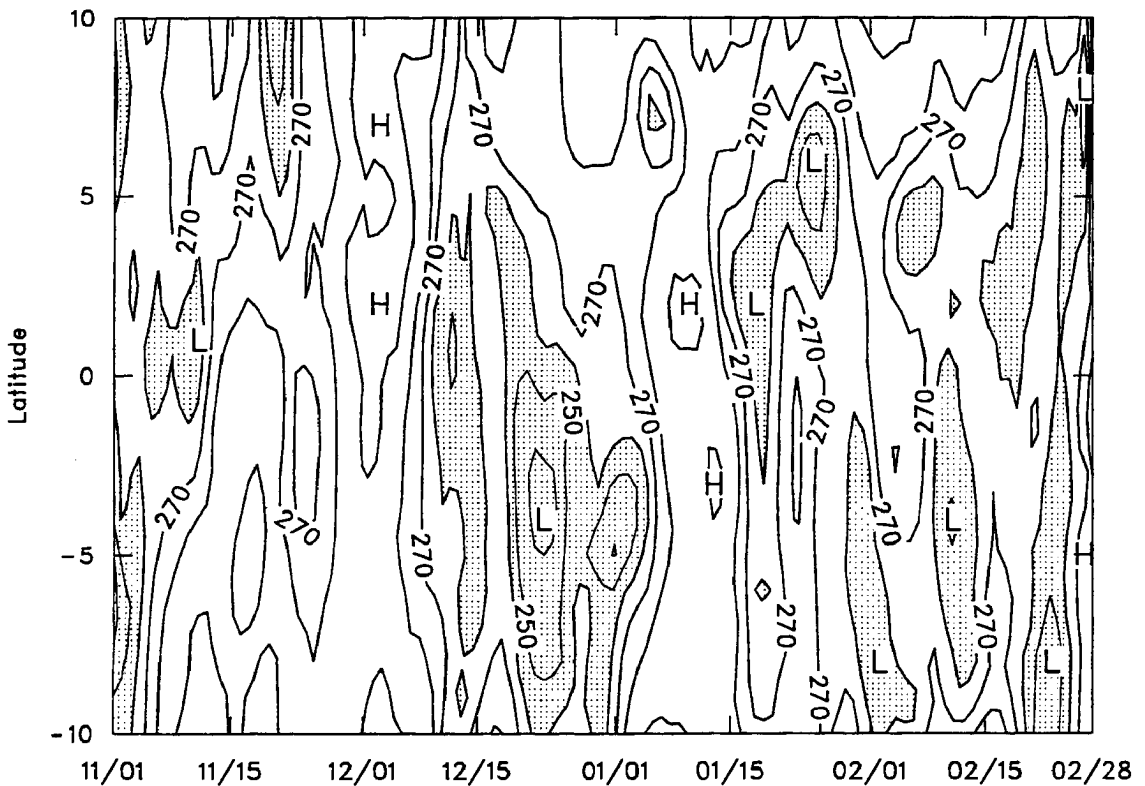


Figure 4.4: (a) Time-latitude cross section of zonal component of the wind at 1000 hPa. Westerlies are shaded. The intervals are  $2 \text{ m s}^{-1}$ . (b) Time-latitude cross section of GMS brightness temperature (in unit of K). The regions with T less than 260 K are shaded.

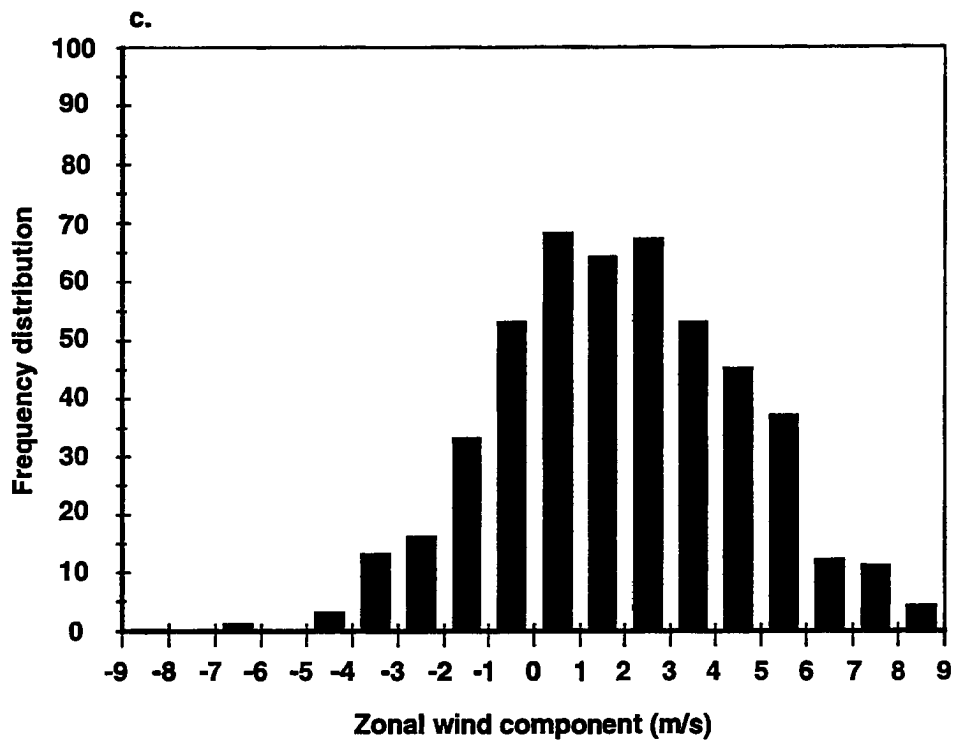


Figure 4.4: Continued. (c) Frequency distribution of zonal wind component at 1000 hPa over the IFA during COARE IOP. Ordinate values are numbers of 1000 hPa zonal wind component during the COARE IOP at 6-hour intervals. Positive values indicate westerlies.

and Nov. 25, with the maximum located between 3°N and 10°N around the time of the development of typhoons Gay and Hunt in the northwest Pacific. Both the December-January and the February cases occurred south of 3°N, with their westerly maxima originating near the equator and then shifting to around 5°S over a ~1-week period. This southward shift is related to the development of tropical cyclones in the Southern Hemisphere following the westerly wind bursts (e.g., Keen 1982; Nitta 1989; Lander 1990; McBride et al. 1995). In the December case, tropical cyclones Kina and Nina formed in the southwest Pacific, whereas in February it was tropical cyclone Oliver. Easterly trade winds dominated to the north of 3°N from December to February.

During the TOGA COARE IOP, deep convection and maximum precipitation associated with the ISOs usually occurred 1-3 weeks prior to the peak westerly wind bursts. The behavior can be seen particularly well for the December burst by comparing IR data (Fig. 4.4b) with 1000 hPa zonal winds (Fig. 4.4a). It is interesting to note that low level westerly winds following the IR minimum were always stronger than the winds preceding it, similar to the flow pattern derived from an analytic model for heat-induced tropical circulation (Gill 1980). The absence of significant easterly flow can be seen alternatively (to avoid the possible bias of very strong surface westerly winds in a few cases) in a frequency distribution of the 1000 hPa zonal wind component in  $1 \text{ m s}^{-1}$  bins over the IFA at 6-hour intervals during COARE IOP (Fig. 4.4c). It is evident that there was a general absence of strong equatorial easterlies over the IFA and the mean zonal flow was westerly during the three ISO events (although the easterlies were slightly undersampled because the easterly phase of the first ISO occurred before 1 November). This evidence does not appear to support the WISHE mechanism (Emanuel 1987; Neelin et al. 1987), which requires a pre-existing tropical mean easterly flow, and stronger perturbation winds to the east of the disturbance to explain the maintenance and eastward propagation of the 30-60 day oscillation. An easterly acceleration of the flow did occur north of 5°N around December 1 (about two weeks prior to the heaviest rainfall); however, it was weak, and analyses similar to Fig. 4.4a between 160°E and 170°E and between 170°E and 180°E (not shown) indicate no concurrent easterly acceleration east or northeast of the IFA.

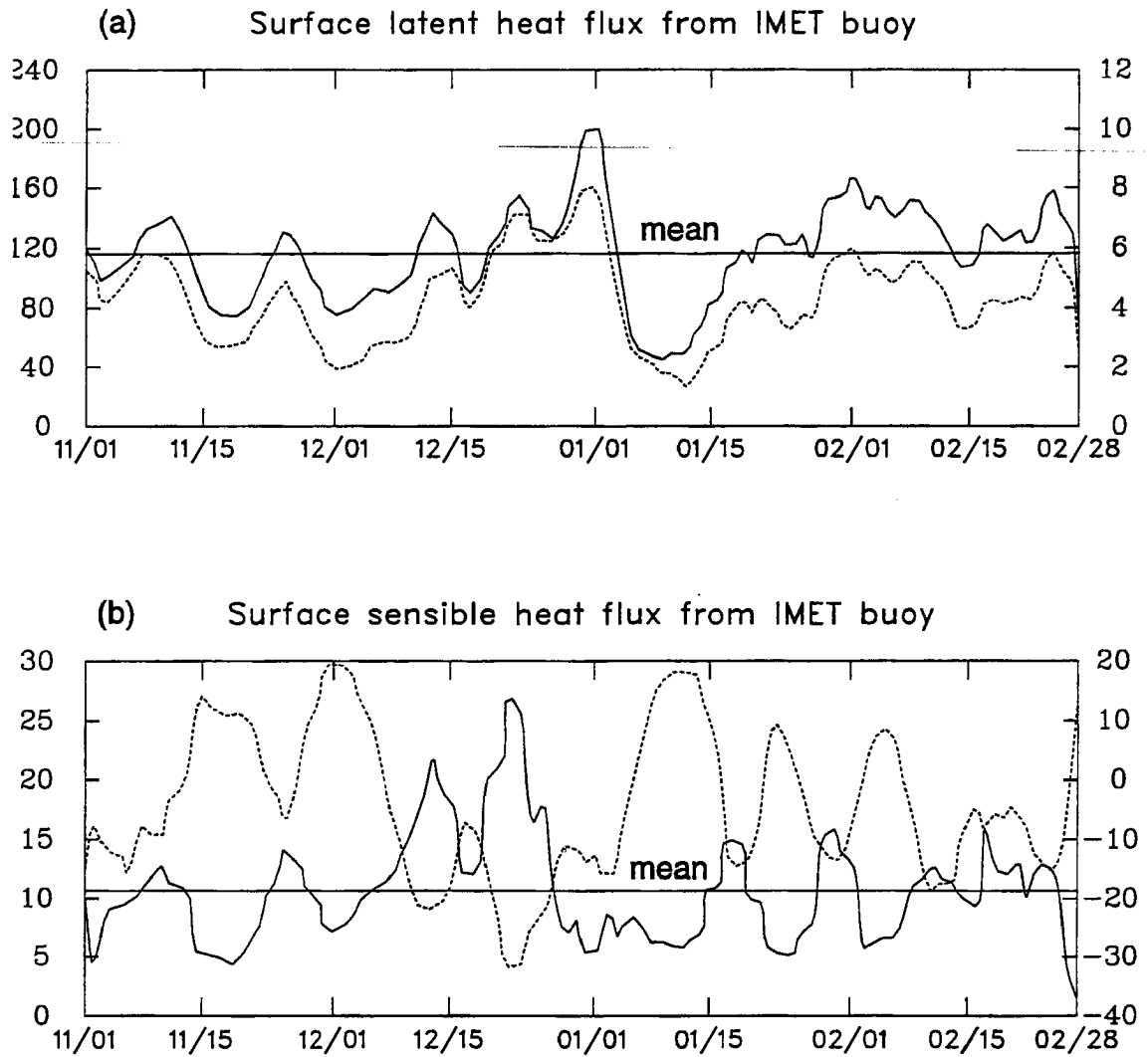


Figure 4.4: Continued. (d) Time series of the surface latent heat flux (solid line) from WHOI IMET buoy ( $\text{W m}^{-2}$ ). Superimposed is surface wind speed (dashed line) from the IMET buoy ( $\text{m s}^{-1}$ ). Mean latent heat flux of  $117 \text{ W m}^{-2}$  is indicated. (e) Time series of the surface sensible heat flux (solid line) from WHOI IMET buoy ( $\text{W m}^{-2}$ ). Superimposed is GMS brightness temperature (dashed line) over the IFA. Mean sensible heat flux is indicated. (The IMET buoy data courtesy of Drs. Robert Weller and Steve Anderson, WHOI).

Further evidence that enhanced evaporation follows rather than leads ISO convection can be seen in time series of surface latent and sensible heat fluxes from the IMET buoy (Figs. 4.4d and 4.4e). The surface latent heat flux (Fig. 4.4d) exhibited a good correlation with surface wind speed. During the late-December and late-January westerly wind bursts, evaporation began increasing 3 to 4 weeks prior to the peak westerlies. Pronounced increase of the latent heat flux also occurred when disturbances passed, probably induced by gust winds and convective and mesoscale downdrafts. Evaporation reached its maximum during the peak westerly wind bursts when maximum deep convection had moved to the east of the IFA (not shown). The surface sensible heat flux (Fig. 4.4e) shows a different pattern from that of the latent heat flux. It correlates better (in a negative sense) with the brightness temperature than the surface wind speed, presumably as a result of strong winds and cool downdrafts associated with deep convection and heavy precipitation. In summary, time series of evaporation and sensible heat flux at the IMET buoy indicates that maximum surface energy transfer usually occurred during and after the arrival of the convectively active phase of the 30-60 day oscillation, not before.

The IOP-averaged zonal wind components at 850 and 150 hPa over the LSA are illustrated in Fig. 4.5. During the IOP, the wind pattern at 850 hPa was very similar to that at 1000 hPa, although both westerlies and easterlies were stronger at 850 hPa. Westerly winds generally dominated the warm pool between 3°N and 10°S, with maxima located at about 3°S. The westerlies were stronger west of 165°E and decreased toward the Date Line, consistent with the observations of an IR minimum in the eastern part of the LSA (Fig. 4.1). There was a strong horizontal shear near 4°N, which separated the northeast trades from the equatorial westerlies. At 150 hPa (Fig. 4.5b), the mean zonal wind was everywhere easterly. The maximum easterlies were located at the equator in the western part of LSA, again consistent with maximum convection toward the east.

#### 4.2.2 *Meridional wind*

In their review paper, Madden and Julian (1994) summarized some results of the 30-60 day oscillation in the tropics and found little evidence that the meridional wind played a

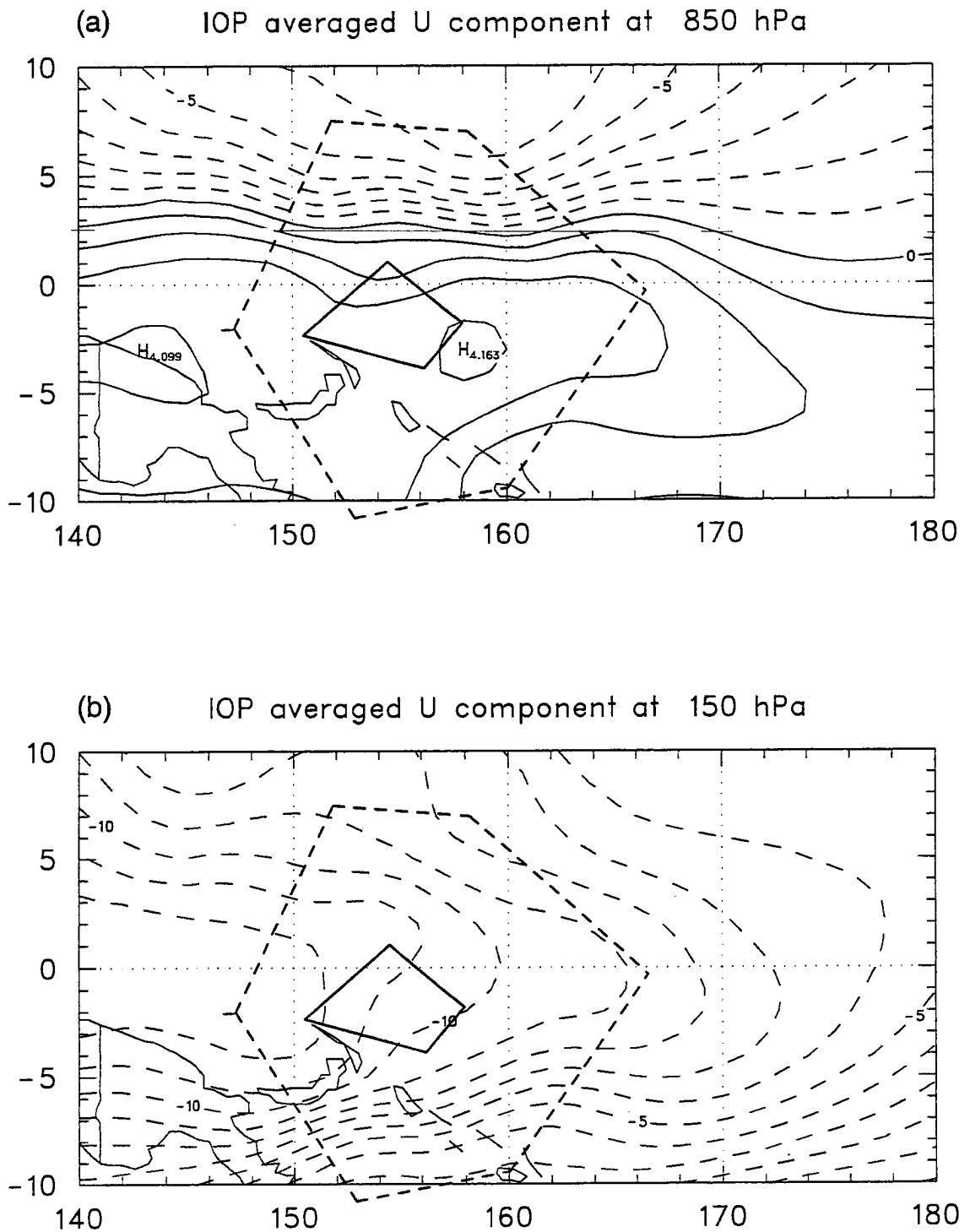


Figure 4.5: The IOP-mean zonal wind component at (a) 850 hPa, (b) 150 hPa over the Large Scale Array. Solid lines indicate westerlies, while dashed lines represent easterlies. The intervals are  $1 \text{ m s}^{-1}$ .

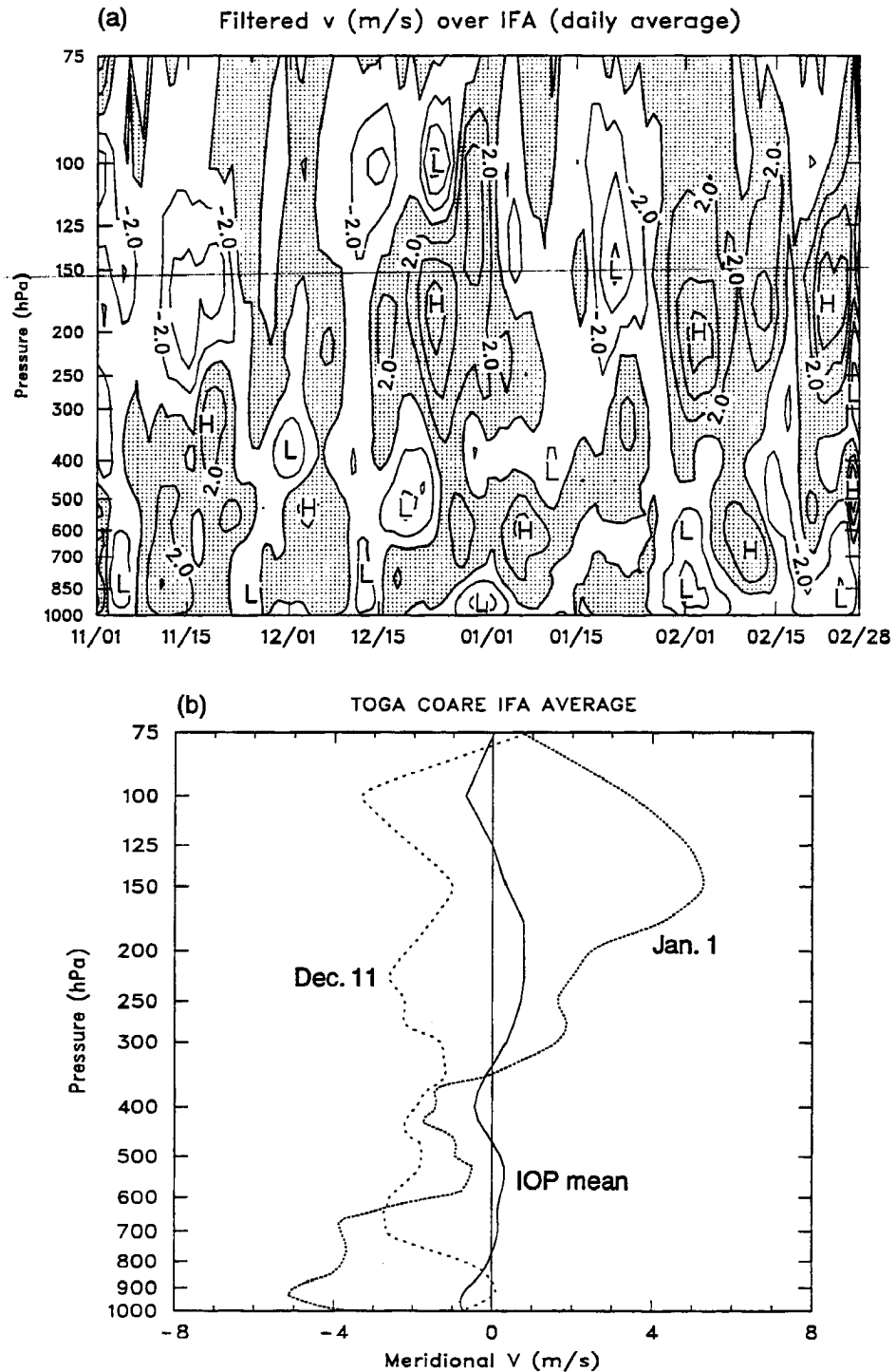


Figure 4.6: (a) Time series of daily-mean meridional  $V$  component ( $\text{m s}^{-1}$ ) averaged over the Intensive Flux Array (5-day running mean). Contour intervals  $2 \text{ m s}^{-1}$  and southerlies are shaded. (b) Vertical profiles of meridional wind (in  $\text{m s}^{-1}$ ) averaged over the IFA. The solid line represents the IOP-mean, and dashed lines are for Dec. 11 and Jan. 1 cases.

role in the variations within individual seasons (Madden and Julian 1971; Parker 1973). Fig. 4.6a shows the time series of the IFA-mean vertical profiles of the meridional wind component. Although the signal was much weaker than that in the zonal wind profiles, northerly winds usually occurred and strengthened at low levels when the westerly wind bursts developed (e.g., January 1 and February 1 cases). The westerly wind burst was actually a west-north westerly flow over the IFA. Southerly flows can be observed at upper levels during these periods.

Fig. 4.6b contains the IOP-averaged meridional wind component over the IFA, as well as vertical profiles for Dec. 11 and Jan. 1. Since the IFA was at times located between double-ITCZ bands and other times not (Fig. 4.1), the IOP-mean meridional wind component was very small and fluctuated with height. On Dec. 11, when convection was enhanced over the IFA, northerly winds generally dominated the entire troposphere with weak vertical wind shear, except at levels below 700 hPa. On Jan. 1, when the low-level westerly wind burst reached its peak, there were relatively strong northerlies over the IFA below 600 hPa with southerlies above with a peak of about  $5 \text{ m s}^{-1}$  near 150 hPa. This vertical profile of  $v$  is consistent with the existence of inflow at low levels and outflow aloft from deep convection and tropical cyclones Kina and Nina to the south of the IFA (Fig. 4.4b).

#### 4.2.3 Divergence

Figure 4.7 illustrates a north-south cross section of IOP-mean divergence averaged between  $150^{\circ}\text{E}$  and  $160^{\circ}\text{E}$ . Two convergence maxima are located at low levels between  $5\text{-}8^{\circ}\text{S}$ ,  $2\text{-}5^{\circ}\text{N}$ , with corresponding divergence maxima at upper levels. This pattern is consistent with the double-ITCZ structure shown in Fig. 4.1a at the longitudes of the IFA.

The IFA was located between the double-ITCZ bands, at least in an IOP-mean sense. The divergence pattern over the IFA was quite different from that within the ITCZ bands to the north and south (Fig. 4.8). Over the IFA, weak convergence occurred at middle and low levels with divergence in the upper troposphere. Maximum convergence was located between 700 and 800 hPa with very weak divergence near the surface. On the other hand,

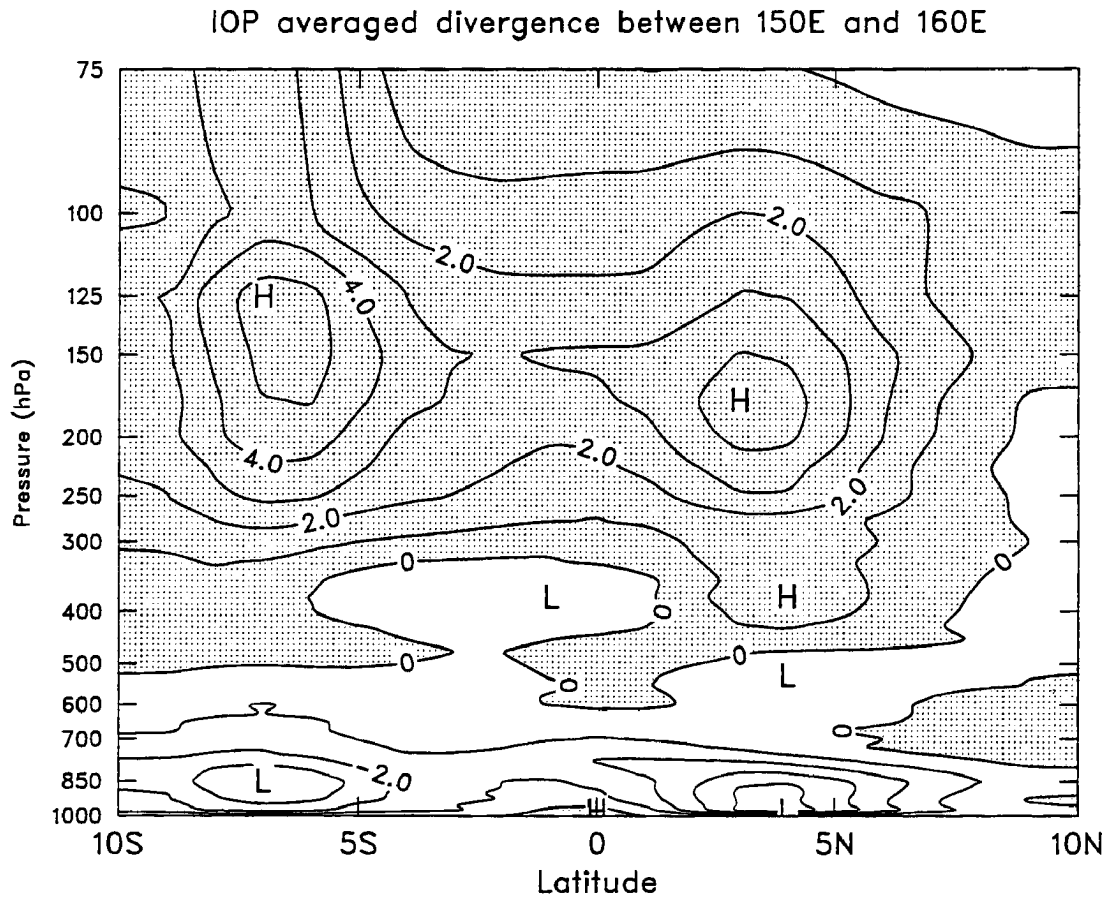


Figure 4.7: The north-south cross section of horizontal divergence averaged between 150°E and 160°E ( $10^{-6} \text{ s}^{-1}$ ). Positive regions, indicative of divergence, are shaded.

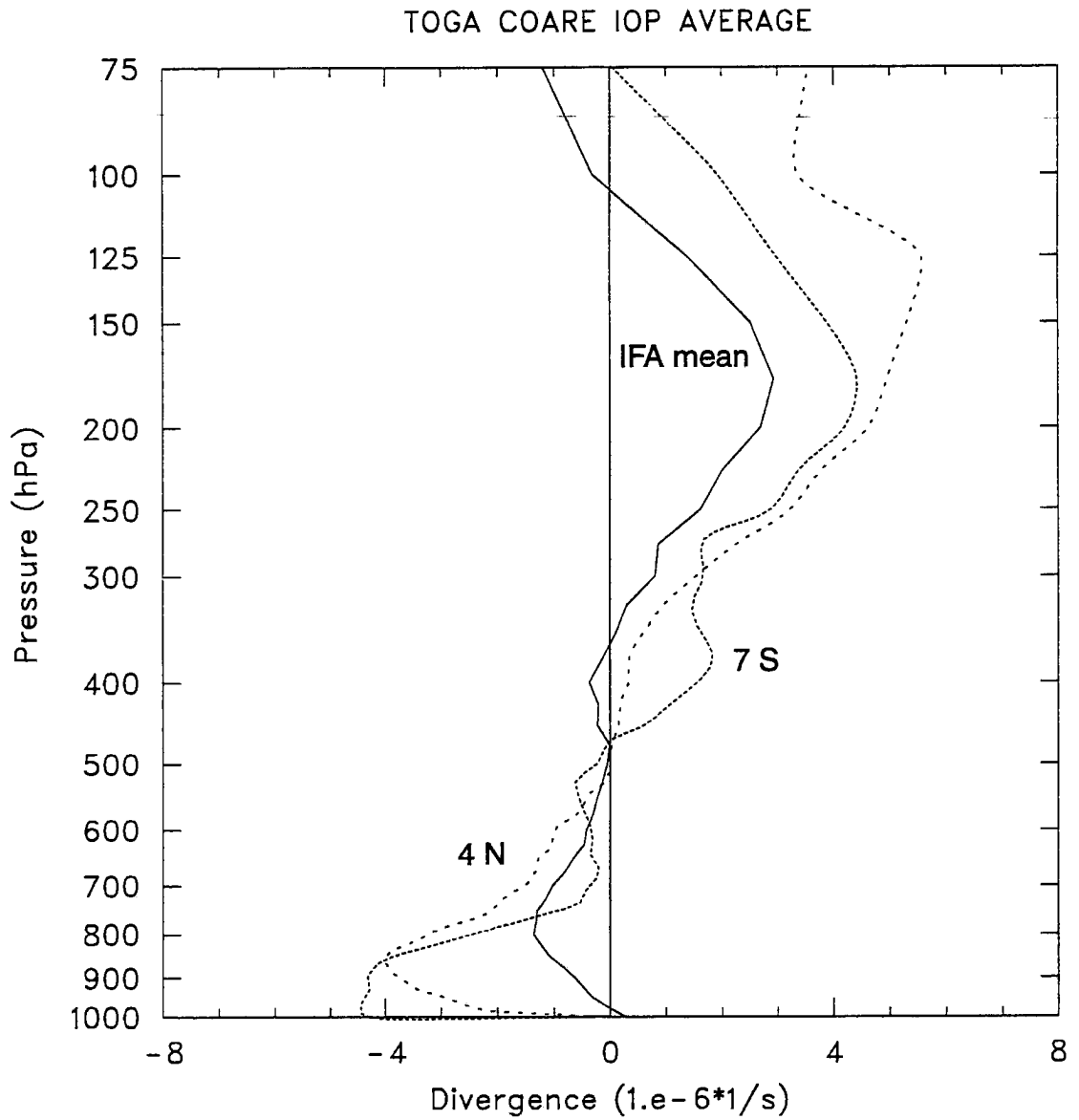


Figure 4.8: The IOP averaged vertical profiles of horizontal divergence over the Intensive Flux Array and the double-ITCZ bands (4°N and 7°S) ( $10^{-6} \text{ s}^{-1}$ ).

the profiles in the ITCZ bands show strong low-level convergence from the surface to about 700 hPa with strong divergence aloft. These profiles are more consistent with those from previous studies of the tropical western Pacific (Reed and Recker 1971; Yanai et al. 1973). Yanai et al. (1973) investigated the basic kinematic features within the ITCZ using sounding data from the Marshall Island region (centered near 8°N). Their divergence profile shows a deep layer of convergence from the surface to 350 hPa with a peak located at 950 hPa and divergence aloft peaking near 200 hPa. Their findings are very similar to the profiles at 4°N and 7°S during COARE IOP, where the mean double-ITCZ bands were located, although the convergence in our case only extended to 475 hPa. During periods of deep convection over the IFA, the divergence profile (not shown) looks like those at 4°N and 7°S, suggesting similar convective characteristics whenever and wherever convection is strong. However, the striking difference between the IOP-mean IFA and ITCZ band divergence profiles, particularly at low levels, over short north-south distances suggests that great care should be exercised in generalizing divergence and vertical motion profiles from one region to another over the western Pacific warm pool.

#### 4.2.4 *Vertical motion*

Time series of brightness temperature from Japanese GMS satellite data, vertical motion over the IFA, and wind speed at 1000 hPa from the COARE analyses are shown in Fig. 4.9. The sounding-derived vertical motion pattern is in general consistent with satellite data: strong upward motion usually corresponds to increased high clouds (lower brightness temperatures), whereas downward motion or weak upward motion usually corresponds to decreased high clouds (higher brightness temperatures). Maximum upward motion implying heavy precipitation usually occurred one or three weeks prior to the peak westerly wind bursts when the surface winds were strongest (e.g., December and January cases), consistent with previous satellite observations of Knutson and Weickmann (1987). The upward motion maxima were usually located at upper levels between 500 and 350 hPa. Low-level subsidence or weak upward motion was observed when strong westerly winds prevailed (also corresponding to times of strong vertical wind shear between 850 hPa and the tropopause, Fig. 4.3).

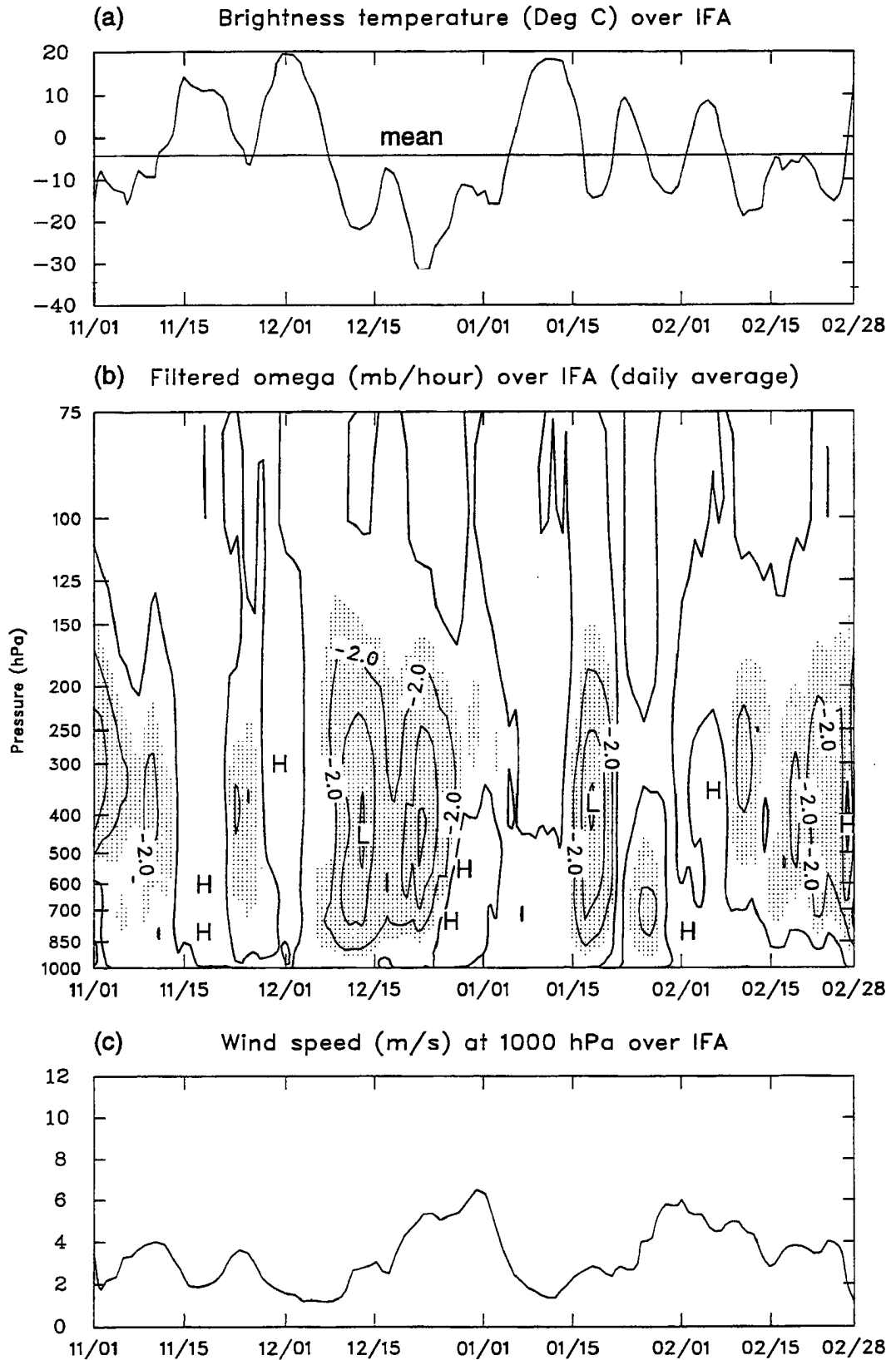


Figure 4.9: (a) Time series of the IFA-averaged GMS brightness temperature (Deg C). (b) Time series of the IFA-averaged vertical motion ( $\text{mb h}^{-1}$ ) throughout the COARE IOP. Areas with  $\omega \leq -1.0 \text{ mb h}^{-1}$  are shaded. (c) Time series of 1000 hPa wind speed over the IFA. (5-day running mean).

Toward January 1 when the westerly wind burst reached its peak, subsidence generally dominated the middle and low levels over the IFA, but the brightness temperatures remained quite low. Rainfall analyses by Lin and Johnson (1994) based on rawinsonde-derived results and satellite data suggest that the relatively low brightness temperatures over the IFA during this period were a result of the frequent occurrence of non-precipitating high cirrus. The cirrus advected across the IFA from convection to the east by strong easterly flow (Fig. 4.3a).

Methods using satellite data have been developed to estimate rainfall rate according to the relationship between cold clouds and deep convection (e.g., Arkin and Meisner 1987). However, it is not clear how well cold clouds correlate with vertical motion at all levels of the atmosphere. Figure 4.10 shows scatter plots of brightness temperature vs.  $\omega$  at 300 and 700 hPa, respectively, over the IFA using 6-hour data. Omega at 300 hPa (Fig. 4.10a) shows a nearly linear correlation with brightness temperature, suggesting that cold clouds are a good indicator of upper-level vertical motion. For brightness temperatures less than  $-20^{\circ}\text{C}$  (253 K, the IFA-averaged temperature at 375 hPa), all but 3 cases show upward motion at 300 hPa. However, such is not the case for vertical velocity at 700 hPa (Fig. 4.10b). For the IFA-averaged cloud tops above 375 hPa, about one third of the cases indicate downward motion at 700 hPa. Extensive optically-thick anvil cloud and non-precipitating high cirrus dominated the IFA during these periods. Many of these cases occurred in high wind shear regimes, when strong easterlies advected cirrus westward from convection to the east of the IFA. A number of the cases are also probably associated with extensive stratiform precipitation anvils, which characteristically have downward motion in the lower troposphere (Houze 1982). Rutledge (personal communication 1996) also noted that Doppler radar data often indicated little precipitation under extensive cold clouds during COARE IOP, and there was a large phase lag between observed surface rainfall and very cold cloud cover. For brightness temperatures above  $-20^{\circ}\text{C}$  (cloud top below about 375 hPa), roughly half the cases indicate upward motion and half indicate downward motion. In this situation, vertical motion at 700 hPa is essentially independent of cloud top temperature.

Figure 4.11 shows the IOP-mean and monthly-mean north-south cross sections of  $\omega$  averaged between  $150^{\circ}\text{E}$  and  $160^{\circ}\text{E}$ . Although there were large monthly variations across

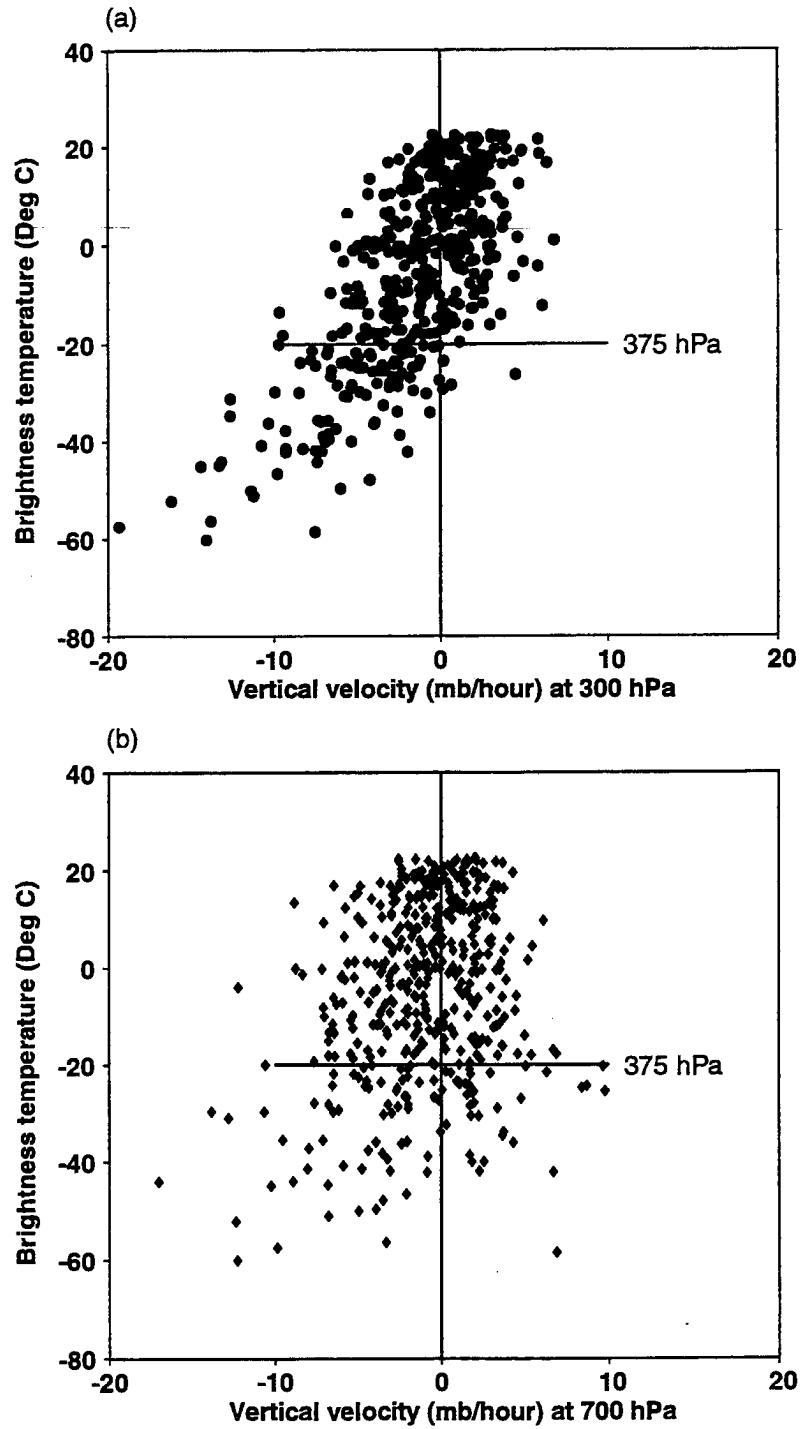


Figure 4.10: Scatter plots of brightness temperature and vertical motion over the IFA. (a)  $\omega$  at 300 hPa, (b)  $\omega$  at 700 hPa.

the equator, a region of significant upward motion, which corresponds to the ITCZ, can be clearly observed in each hemisphere, consistent with the two convergence/divergence couplets shown in the divergence plot (Fig. 4.7). The IOP-mean plot (Fig. 4.11a) indicates that upward motion generally dominated the tropical western Pacific, although weak subsidence can be noticed north of  $8^{\circ}\text{N}$ , probably induced by the subtropical high in the Northern Hemisphere. The SPCZ was stronger than the northern ITCZ during COARE IOP, with peak upward motion around  $7^{\circ}\text{S}$  between 350 and 600 hPa, while the northern ITCZ had its peak  $\omega$  located near  $4^{\circ}\text{N}$  between 400 and 650 hPa. The order of magnitudes and altitudes of the peak upward motion within the ITCZ bands were quite similar to previous studies over the western Pacific (e.g., Nitta 1972; Yanai et al. 1973). The IFA, which was located between the two significant rising regions, had relatively constant upward motion between 700 and 250 hPa.

Consistent with the IR data (Fig. 4.1b), convection was generally suppressed in November between  $150^{\circ}\text{E}$  and  $160^{\circ}\text{E}$ , and upward motion was weak (Fig. 4.11b). The peak of the SPCZ was located between  $4^{\circ}\text{S}$  and  $1^{\circ}\text{S}$ , which is closer to the equator than the IOP mean. The northern ITCZ had its peak located between  $4^{\circ}\text{N}$  and  $5^{\circ}\text{N}$  and extended farther north than in the later months, consistent with a gradual transition of the convergence zone from boreal autumn to boreal winter. Downward motion occurred south of  $7^{\circ}\text{S}$  presumably due to the control of the Southern Hemisphere subtropical high. Deep convection intensified in December to the south of the equator, and upward motion predominated the tropical southwestern Pacific with the peak upward motion shifting to  $7^{\circ}\text{S}$  (Fig. 4.11b). The northern ITCZ also intensified, migrating  $1^{\circ}$  south with its peak located at low levels near 600 hPa. Due to the influence of the strong westerly wind burst in early January, convection was suppressed to the south of the equator during the first few days of the month. The January mean upward motion weakened within the SPCZ (Fig. 4.11d), with a peak located at low levels between 550 and 750 hPa. On the other hand, the northern ITCZ strengthened and had its peak at higher levels, consistent with satellite data (Fig. 4.1d). Although the large-scale circulation patterns changed, the position of the double-ITCZ was almost the same as it was in December. In February, vigorous convection started again in both hemispheres

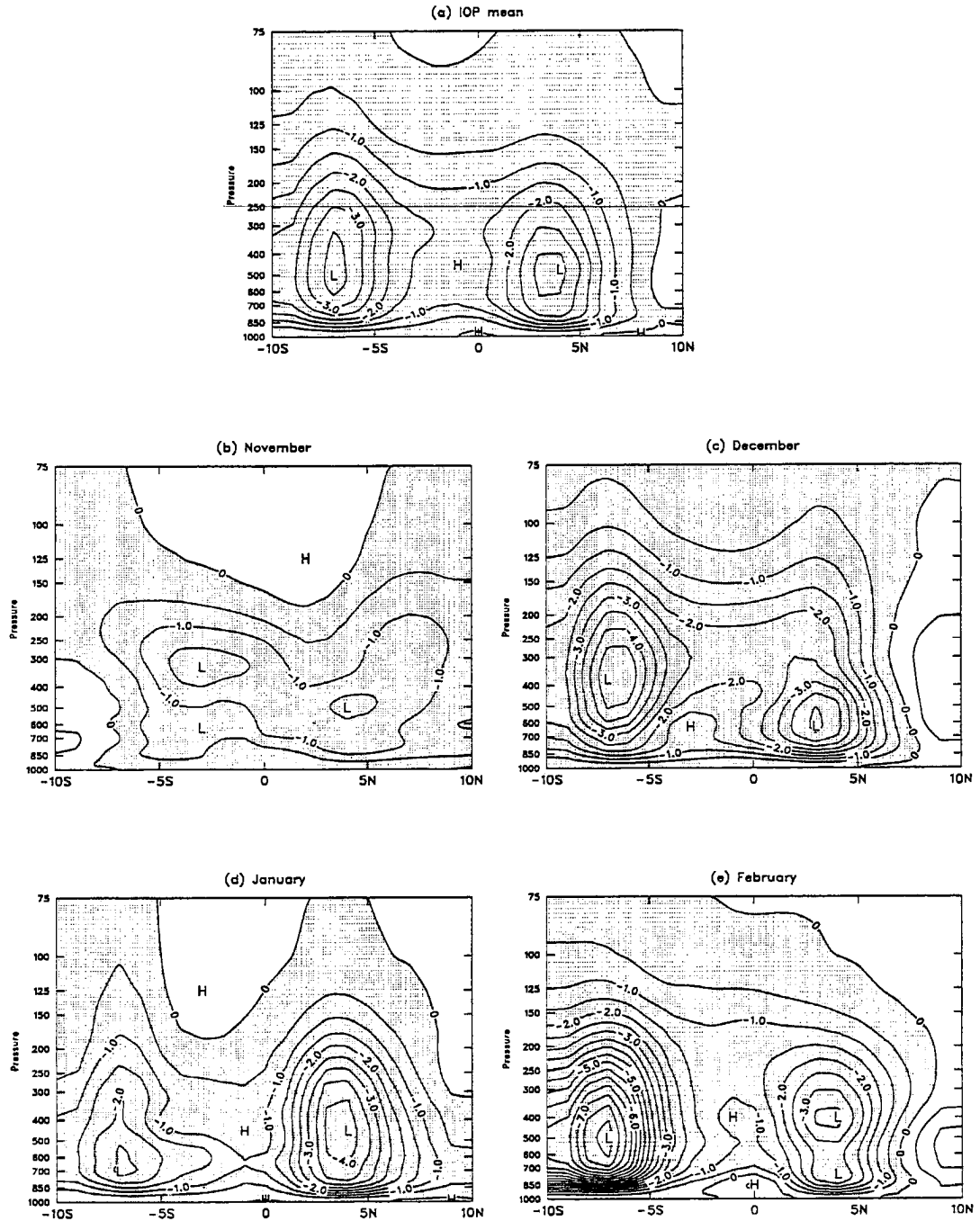


Figure 4.11: North-south cross section of  $\omega$  ( $\text{mb h}^{-1}$ ) between  $150^\circ\text{E}$  and  $160^\circ\text{E}$ . Regions of upward motion are shaded. (a) IOP mean, (b) November, (c) December, (d) January, (e) February. Contour interval is  $0.5 \text{ mb h}^{-1}$ .

(Figs. 4.1e and 11e), and the SPCZ reached its maximum at about 7°S. Downward motion can be observed near the equator from the surface to 800 hPa, probably induced by strong convergent flows into the double-ITCZ.

In order to examine the zonal variations of vertical motion in the tropical western Pacific, an east-west cross section of IOP mean  $\omega$  (Fig. 4.12a) was constructed from 140°E to 180°E using gridded data at 00Z and 12Z between 5°N and 5°S. Mean upward motion generally increased toward the east, the strongest values being located around 170°E (acknowledging that caution should be exercised since data east of 170°E are sparse), consistent with the findings in Fig. 4.1 which showed the lowest IOP-mean brightness temperature over this region. The Gutzler et al. (1994) DJF averages of OLR across the LSA also indicate the center of deep convection near the Date Line. The upward motion was quite weak in the western part of the LSA and downward motion can be observed around 144°E between 850 and 300 hPa. Although the IOP-mean plot (Fig. 4.1a) shows that there were considerable cold clouds at 5°S over the land between 140°E and 150°E, the highest brightness temperatures along the equator, indicative of frequent clear skies, were usually found over the open ocean to the north of the land. The level of peak upward motion also ascended from near 700 hPa around 150°E to 350 hPa around 170°E, indicating convective intensification over the warm pool.

Fig. 4.12b shows the east-west variation of IOP-mean SSTs between 5°N and 5°S. The data, based on the global SST analyses from the Coupled Model Project at NCEP, were produced weekly on a one degree grid (Reynolds and Smith 1994). Higher SSTs (above 29.3 °C) can be observed between 170°E and 180°E, decreasing toward the west to 28.8 °C around 140°E. Comparisons of the vertical heating profiles over the GATE (GARP Atlantic Tropical Experiment, 1974) area and the western Pacific suggest that a higher altitude of heating maximum is usually correlated with higher SSTs (Webster 1991; Webster and Lukas 1992). The zonal variation of SSTs and vertical motion from 140°E to 170°E appears to support these findings. A number of studies have suggested that deep convection usually occurs more frequently and more intensively over the areas with higher SSTs up to some threshold, approximately 27.5-28°C (e.g., Gadgil et al. 1984; Graham and Barnett 1987).

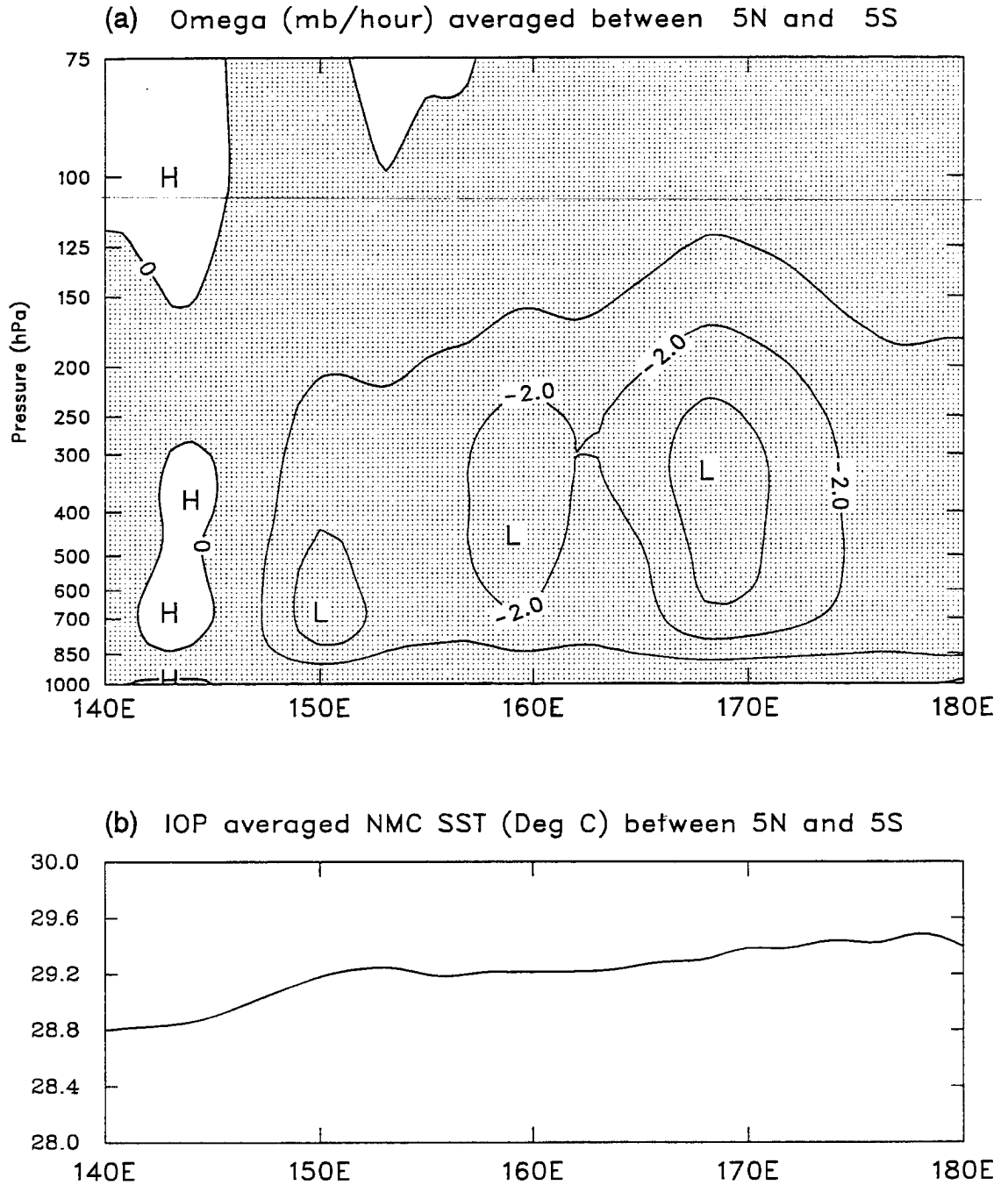


Figure 4.12: (a) East-west cross section of IOP-mean  $\omega$  averaged between 5°N and 5°S. Shaded regions indicate upward motion. (b) East-west variation of NCEP SST averaged between 5°N and 5°S (Deg C).

However, SST over the COARE LSA always exceeded this threshold, yet a relationship between SST, OLR and vertical motion continued to exist. From Fig. 4.11. the intensity of upward motion decreased from 170°E to the Date Line, although SSTs kept increasing to 29.5 °C at 178°E. Waliser et al. (1993) and Waliser and Graham (1993), using satellite data, found that the amount/intensity of convection tends to decrease with increasing SST at temperatures above about 29.5 °C. It is possible that the COARE data support this idea; however, the relationship between convection and SST over the warm pool cannot be described in simple terms, rather it is a complex function of evaporation, cloud cover, precipitation and ocean mixing – all of which are strongly modulated on the time scale of the 30-60 day oscillation (Webster 1994).

### **4.3 Basic thermodynamic features**

#### *4.3.1 Humidity*

Figure 4.13 shows the time series of the IFA-mean relative humidity profiles and 700 hPa wind speed through the COARE IOP. RH was calculated with respect to ice above the -10°C level (about 450 hPa) and with respect to liquid water below. Consistent with the vertical motion profiles (Fig. 4.9b), high RH, suggesting strong upward motion, was observed extending from low to upper levels several weeks prior to the late-December westerly wind burst. Dry conditions dominated above about 800 hPa when the peak westerly winds prevailed. At this time, peak RH was usually located at low levels between 900 and 950 hPa or near the top of the mixed layer, however a secondary peak in late December was observed at middle to upper levels where there was strong upward motion (Fig. 4.9b). Strong advection of dry air in the middle and low levels can often be observed during the COARE IOP (e.g., Numaguti et al. 1995; Mapes and Zuidema 1996). These dry intrusions emanated from the subtropics of both hemispheres and may account for some of the dry episodes in Fig. 4.12.

Figure 4.14 shows the IOP-mean relative humidity profiles over the IFA. Two solid curves were generated from COARE data, one with respect to liquid water and the other

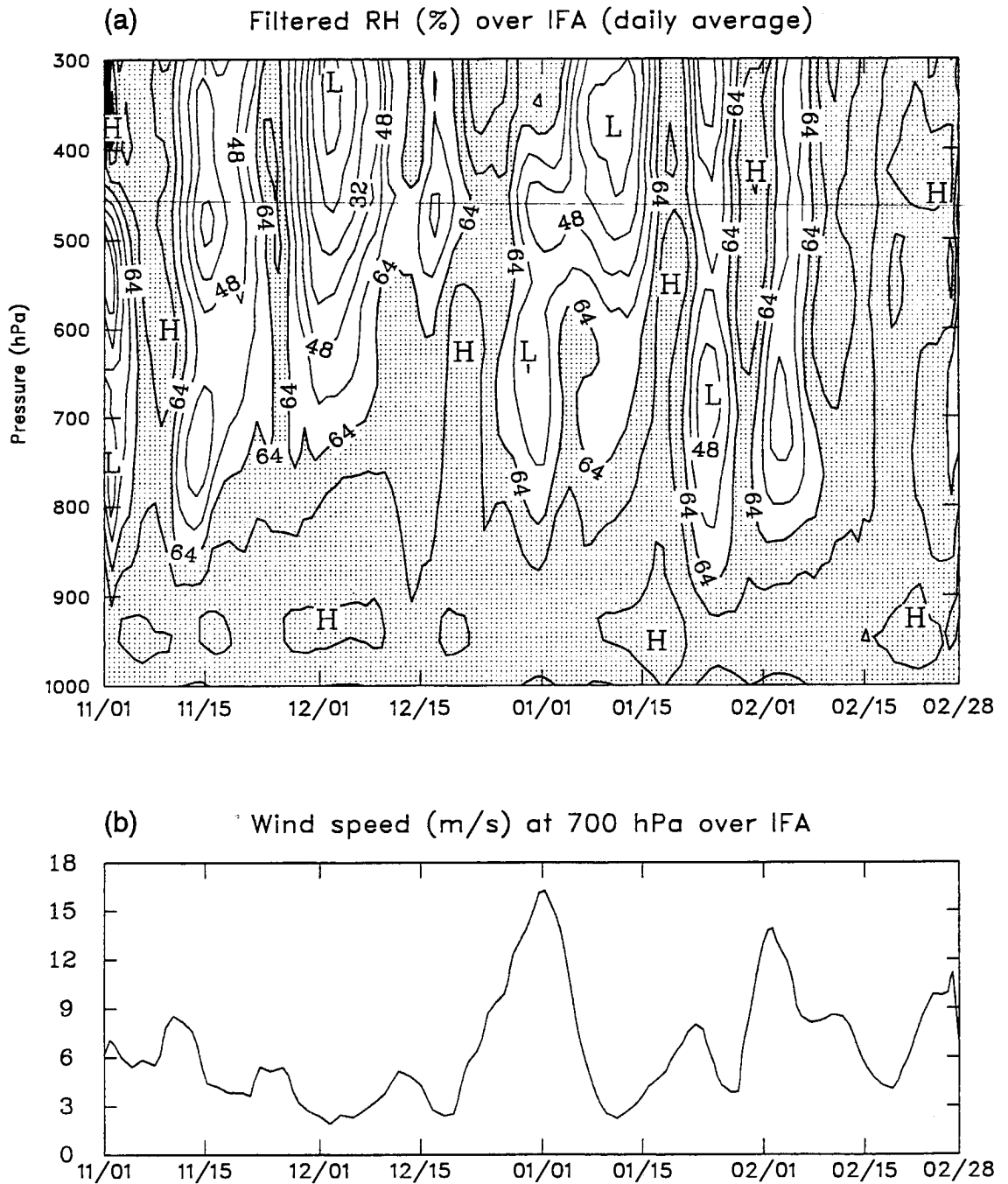


Figure 4.13: (a) Time series of the daily-mean relative humidity (%) over the Intensive Flux Array. Shaded area indicates RH > 64%. (b) Time series of the IFA-mean wind speed ( $\text{m s}^{-1}$ ) at 700 hPa. (5-day running mean).

with respect to ice above the 0°C level. ECMWF and NCEP operational analyses are used to compare with the COARE sounding data. ECMWF data are at 12 vertical levels while NCEP data are at 11 (standard mandatory) levels. The horizontal resolution of both model analyses is 2.5 degrees, which is converted to 1.0 degree in order to match the sounding analysis.

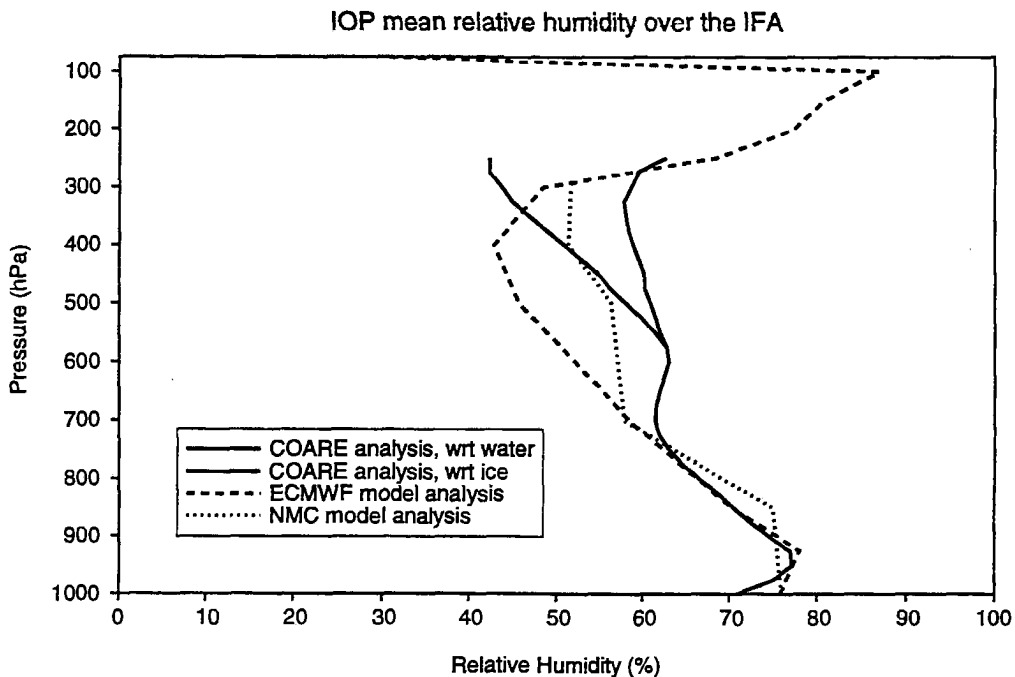


Figure 4.14: IOP-mean profiles of relative humidity over the IFA. Solid lines are from the COARE analysis, with respect to liquid water and ice. Dashed lines are from ECMWF and NCEP model assimilated analyses.

Both ECMWF model-assimilated and rawinsonde results show a primary peak at low levels at the top of the mixed layer ( $\sim 950$  hPa), consistent with previous studies of tropical humidity profiles (Liu et al. 1991; Gutzler 1993). They agree very well between 750 and 925 hPa, with a linear relationship between pressure and RH. The NCEP model-assimilated profile, however, shows the maximum RH near the surface, decreasing gradually from 1000 to 850 hPa, probably due to coarser vertical resolution (ECMWF data have an extra level at 925 hPa). The primary peak at the top of the mixed layer is not captured.

The largest discrepancy among the COARE data and model analyses occurs at middle levels. The COARE mean RH gradually increases above 700 hPa and shows an apparent

secondary peak near 550 hPa (near the 0°C level). This feature has not received much attention, although it can be noticed in the climatological studies of Oort (1983), Liu et al. (1991), and Gutzler (1993). Johnson et al. (1996) have recently investigated this feature and related it to stable layers near the 0 °C level associated with melting in precipitating systems. They argued that deep convection penetrating or congestus impinging upon the stable layers could lead to enhanced detrainment and moistening near that level. Another possibility is that a significant number of mesoscale convective systems with attendant saturated upper-tropospheric stratiform regions could perturb the mean RH profile in the manner shown in Fig. 4.13. The secondary peak, however, is not present in either ECMWF or NCEP operational analyses (although it is more closely matched by NCEP). The midtroposphere is much dryer in the two model analyses, particularly in the ECMWF model as also noted by Schmetz and Van den Berg (1994). In the upper troposphere, the ECMWF RH increases rapidly and shows a peak at about 100 hPa, presumably due to cirrus clouds associated with deep convection. Although RH sampling is questionable above 250 hPa, the COARE analysis with respect to ice also shows an increasing tendency above 300 hPa.

#### *4.3.2 Temperature perturbations*

Time series of daily averaged temperature perturbations and brightness temperature (repeated from Fig. 4.9a) over the IFA are illustrated in Figure 4.15. Two warm anomalies, possibly associated with latent heat release (Reed and Recker 1971), longwave radiative warming (Webster and Stephens 1980) or shortwave absorption (Randall et al. 1991), can be clearly seen in the middle and upper troposphere (Fig. 4.15a) during the active phases of the 30-60 day oscillation (e.g., Dec. 5–25, Jan. 13–22), when upward motion was the strongest (Fig. 4.9) and high-cloud coverage was a maximum (Fig. 4.15b). This feature is consistent with the easterly wave composite findings in Reed and Recker (1971) and Thompson et al. (1979), although their composited temperature anomalies were smaller. Anomalous cooling can be seen at low levels during these active phases, possibly due to melting and evaporation in downdrafts (Zipser 1969; Reed and Recker 1971) or as a large-scale response to upper-level heating (e.g., Mapes and Houze 1995). Strong anomalous

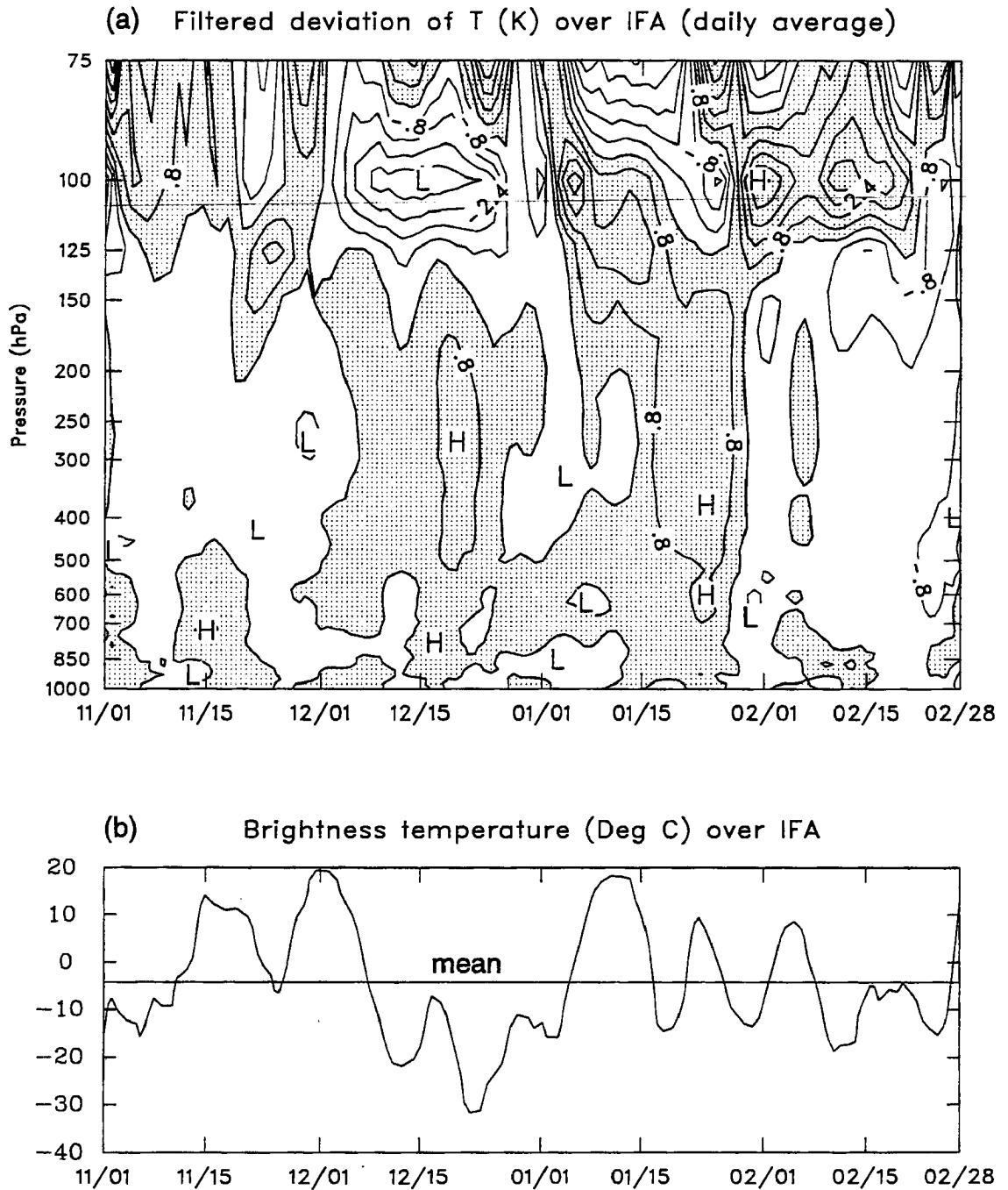


Figure 4.15: (a) Time series of temperature perturbation (deviation from the COARE mean) over the IFA. Contour interval 0.8 K and anomalous warming is shaded. (b) Time series of the IFA-averaged GSM brightness temperature (Deg C).

cooling, (Webster and Stephens 1980), existed near and above the tropopause around 100 hPa (between Dec. 5 and Dec. 24, Jan. 16 and Jan. 20), very similar to those shown in Reed and Recker (1971) and Thompson et al. (1979). Johnson and Kriete (1982) observed similar strong cooling above mesoscale convective systems just north of Borneo during December 1979. Hendon and Liebmann (1990b) showed a temperature perturbation plot (their Fig. 5d) for a composited 30-60 day oscillation. The rainfall region in their study also coincided well with a warm middle and upper troposphere and a cool pool below 850 hPa. However, the anomalous cooling feature near 100 hPa is not present in their analysis. During the period when the low-level westerlies were strong, cool anomalies generally dominated the middle and upper troposphere (Fig. 4.15a).

#### 4.4 Synthesis of observations

Madden and Julian (1972), in a broad-scale sense, schematically depicted the 30-60 day oscillation as a large-scale disturbance originating over the Indian Ocean and propagating into the tropical Pacific. Lau et al. (1989), mainly based on satellite observations and numerical model results, schematically showed the mutual connection among super cloud cluster (Nakazawa 1988), westerly wind bursts, and the 30-60 day oscillations in the western Pacific (see their Fig. 11). In this paper, the observed characteristics of the December-early-January westerly wind burst, the most prominent in COARE, are synthesized (Fig. 4.16) based on the kinematic and thermodynamic features over the IFA from rawinsonde analyses and ISS surface and buoy data. The data are presented with time increasing to the left so that the section can also be thought of as an east-west section (west on left); however, the extent to which a time-to-space transformation can be made is limited since analysis of preliminary data from over Indonesia suggest that much of the intensification of the low-level westerlies and upper-level easterlies occurs in situ and cannot be completely explained by propagation from the west. In this composite, Day 0 corresponds to January 1.

About 4 ~ 6 weeks prior to the peak westerly wind burst (day -37.5), convection was generally suppressed over the western Pacific warm pool. Weak winds dominated through the entire troposphere and the vertical wind shear was very weak. The SST was at its

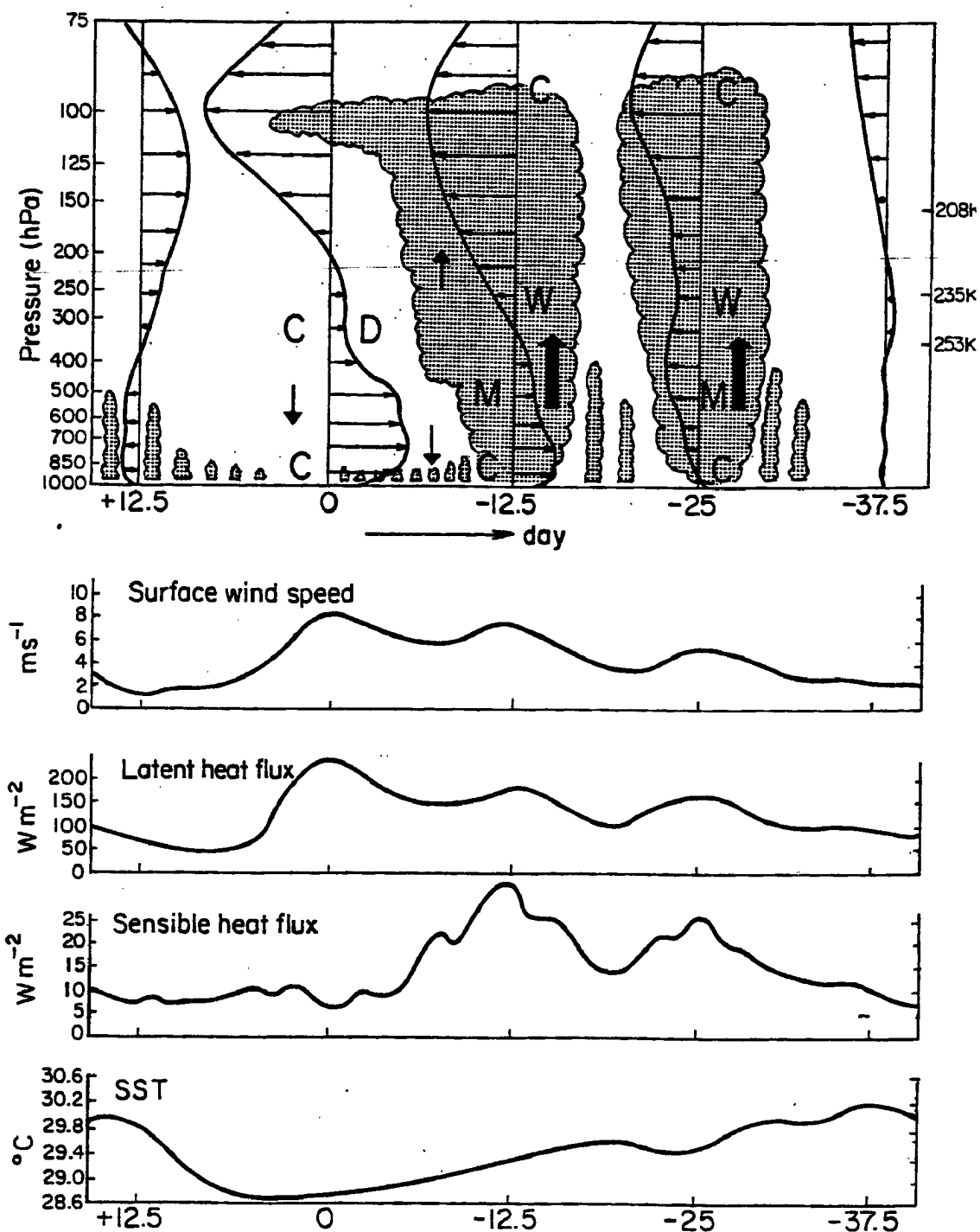


Figure 4.16: A descriptive model of the kinematic, thermodynamic and surface properties of the December-early-January westerly wind burst as it passed the IFA. Day 0 is time of maximum low-level westerlies, with earlier times indicated by negative days (placed to the right so that the left portion of the diagram is to the west: see caution in text, however, about fully interpreting diagram as west-east section). Letters in figure refer to anomalies: W = warm, C = cool, M = moist and D = dry. Heavy arrows indicate strong vertical motion, light arrows weak vertical motion. Clouds are schematic, horizontal scales exaggerated. Temperatures corresponding to pressure levels are indicated on right.

maximum during this suppressed phase and both surface sensible and latent heat fluxes were relatively small.

About 10 days after the suppressed period (day -25), convection gradually intensified over the warm pool. Westward-propagating convective systems, usually with 2-day life cycle (Sui and Lau 1992; Hendon and Liebmann 1994; Takayabu 1994; Chen et al. 1996), were observed near the equator. The zonal winds were dominated by easterlies above about 900 hPa with a peak near 100 hPa. Weak westerlies appeared near the surface and the convective intensity was likely enhanced by the convergence between westerlies and weak easterlies at low levels. Moistening occurred through most of the troposphere and warm anomalies can be observed at middle and upper troposphere. Cool anomalies usually occurred near the surface and the tropopause.

One to two weeks prior to the peak westerly wind burst (day -12.5), vigorous convection continued to occur over the warm pool, although it was episodic with frequent westward propagating systems. However, the large-scale envelope of convection propagated eastward. The most prominent feature during this stage was the rapid increase of the midtropospheric vertical wind shear within the convective systems: strengthening westerlies can be observed at middle and low levels (with a peak around 800 hPa) and strong easterlies aloft. The thermodynamic features within the convective systems are similar to those at day -25. In addition, the areal coverage of anvil clouds and high cirrus increased during the latter part of this stage. In an average sense, the surface wind speed gradually increased with time and SSTs continued to drop, in association with increased evaporative cooling, cloud cover and ocean mixing (Chu and Frederick 1990; Webster 1994). Superimposed on the large-scale evolution are short-period features induced by the convective systems. Stronger surface wind speeds along with peaks in the surface latent and sensible heat fluxes can be observed with the passage of the major convective systems (see Fig. 4.9b). Similar features have also been observed by Saxen (1996) when analyzing relationship between surface fluxes and radar derived rainfall.

At the time of the peak westerly wind burst (day 0), downward motion generally dominated the middle and low levels and convection was typically suppressed. Tropospheric

vertical wind shear was strongest during this stage with deep westerlies underlying strong upper-level easterlies. Cool anomalies occurred in the upper troposphere and at low levels. Surface wind speeds reached their maxima while SSTs continued to decrease until several days after the passage of the peak westerly wind burst. It is interesting to note that while surface latent heat fluxes followed the surface wind speed and showed a primary peak at this stage, sensible heat fluxes peaked at an earlier time. The absence of a peak in the sensible heat flux at Time 0 is related to the strong cooling of the ocean surface at the time of maximum mixing.

About 1 to 2 weeks after the passage of the peak westerly wind burst (day +12.5), surface wind speeds fell to 2 to 3 m s<sup>-1</sup> and the SST gradually recovered. Weak easterlies appeared at middle and low levels and numerous shallow clouds were observed over the warm pool. Vertical wind shears became much weaker and both surface latent and sensible heat fluxes returned to near their mean values (116 W m<sup>-2</sup> and 11 W m<sup>-2</sup> respectively).

#### 4.5 Summary and discussions

Rawinsonde and satellite data have been used to document the mean and transient behavior and horizontal convective variability of the atmosphere over the warm pool throughout the four-month TOGA COARE IOP. IOP-mean brightness temperatures indicate that the maximum deep convection was located in the eastern part of the LSA between 170°E and 180°E, similar to the findings of Gutzler et al. (1994). The IFA was in a transition zone with a minimum in deep convection to the west. Cold clouds were usually found over large islands such as Papua New Guinea and a double-ITCZ structure was usually observed along the equator north and south of the IFA. Although there was a general north-to-south shift in convection during the IOP, marked variability in the patterns occurred on a month-to-month basis.

Three prominent westerly wind burst episodes passed the COARE domain during the IOP: early to middle November, middle December to early January, and late January to the end of February. In the major event between December and January, maximum easterlies of 37 m s<sup>-1</sup> in the upper troposphere and maximum westerlies of 17 m s<sup>-1</sup> at low levels

averaged over the IFA occurred at the time of the peak wind burst. During this event, westerly winds dominated most of the troposphere and extended from the surface to 200 hPa, possibly influenced by tropical cyclones Kina and Nina. The out-of-phase relationship between upper- and low-level winds is consistent with previous findings (Madden and Julian 1971, 1972; Knutson and Weickmann 1987), although the vertical wind shear measured during COARE was far greater than previously recognized.

Infrared and 1000 hPa zonal wind data indicate that both the Dec.-Jan. and the February westerly wind bursts occurred south of  $3^{\circ}\text{N}$ , with their westerly maxima centered near  $5^{\circ}\text{S}$ . There was a general absence of mean equatorial easterlies south of  $3^{\circ}\text{N}$  during the COARE IOP when these westerly wind bursts occurred. Low-level westerly winds following the disturbance associated with the 30-60 day oscillation were always stronger than the winds preceding it. This evidence does not appear to support the WISHE mechanism (Emanuel 1987; Neelin et al. 1987), which requires a pre-existing tropical mean easterly, and stronger perturbation winds to the east of the disturbance to explain the maintenance and eastward propagation of the 30-60 day oscillation. Further evidence from the IMET buoy and ISS surface data indicates that the maximum surface energy transfer usually occurred during and after the arrival of the disturbance associated with the 30-60 day oscillation.

The IOP-mean divergence profiles within the double-ITCZ show strong low-level convergence from the surface to about 700 hPa with strong divergence above 300 hPa, consistent with previous studies in the tropical western Pacific (Reed and Recker 1971; Yanai et al. 1973). The IFA was located between the double-ITCZ bands with weak convergence at middle and low levels and divergence aloft. Averaged over the entire IOP, maximum convergence in the IFA was located between 700 and 800 hPa with very weak divergence near the surface; however, IFA profiles at times of deep convection closely resembled those in the ITCZ bands to the north and south. Therefore, although the divergence and vertical motion profiles tend to look alike whenever and wherever the convection is strong, caution should be exercised in generalizing long-period mean divergence and vertical motion profiles from one region to another over the western Pacific warm pool.

A double-ITCZ structure can be clearly observed in both vertical motion and divergence cross sections across the equator. While there was upward motion in the mean over

the warm pool during the COARE IOP, the strong upward motion over the IFA, indicative of enhanced convection, usually occurred 1 to 3 weeks prior to the peak westerly wind burst, with peak upward motion located at upper levels between 500 and 350 hPa. Subsidence or weak upward motion was observed when the peak westerly winds prevailed. The IOP-averaged vertical motion shows apparent zonal variations along the equator in the LSA, with the climatological mean center of deep convection around 170 °E, consistent with brightness temperature data. The magnitudes of upward motion gradually increased with SST from the west to the east, and the altitude of the peak also increased from low levels in the western part of LSA to upper levels around 170°E.

Very cold clouds were found to be *a good indicator of vertical motion only at upper levels*. At low levels (IFA-mean brightness temperatures above -20 °C or cloud tops below 375 hPa), vertical motion at 700 hPa was essentially independent of cloud top temperature. For IFA-mean brightness temperatures below -20°C, about one third of the cases show downward motion at 700 hPa, suggesting a significant number of cases in which deep convection was absent under very cold cloud tops or mesoscale downdrafts below stratiform precipitation anvils were occurring (Houze 1982). Extensive optically-thick anvil cloud and non-precipitating high cirrus are believed to dominate the IFA in these cases.

The IOP-averaged relative humidity profile over the IFA shows a primary peak at low levels at the top of the mixed layer (~ 950 hPa). A secondary peak can be clearly seen around 550 hPa (near the 0°C level), which has been related to stable layers near the 0°C level associated with melting in precipitating systems (Johnson et al. 1996). The secondary peak at middle levels is not present in either ECMWF or NCEP operational model-assimilated analyses, possibly due in part to coarser resolution in the models.

Based on the kinematic and thermodynamic features in the atmosphere, and surface and buoy data, a descriptive model is constructed to illustrate the life cycle of the December-January COARE westerly wind burst. This model is not intended to apply to all westerly wind bursts in the equatorial Pacific. The vertical wind shear gradually increases as the peak westerly wind bursts approaches and SST continues to drop with strengthening surface wind speed. Surface sensible heat flux peaks prior to the strongest westerlies, while the latent heat flux peaks at the time of the peak westerly winds.

## Chapter 5

### HEATING, MOISTENING, AND RAINFALL

#### 5.1 Surface heat fluxes

Accurate determination of surface heat fluxes over the tropical open oceans is crucial to better understanding of the coupling between the ocean and the atmosphere (Weare et al. 1981; Zhang and McPhaden 1995). Several researchers have computed heat fluxes in the Pacific using data ranging from conventional marine weather reports to satellite measurements (Wyrтки 1965; Weare et al. 1981; Reed 1985; Liu 1988; Liu and Gautier 1990). However, the calculation has long been uncertain over the western Pacific warm pool due to the sparse measurements. For the COARE IOP, we use information from different platforms to estimate surface heat fluxes, which will subsequently be used in rainfall computations. In order to obtain representative area-mean values, careful examination and comparison of these estimations are important.

Figure 5.1 compares daily-mean surface latent heat flux (5-day running mean) from the IMET and three TOGA TAO buoys (Fig. 5.1a), two ships, and the ECMWF IFA mean (Fig. 5.1b). These buoys were selected since they were close to or within the IFA, and their data cover almost the entire IOP. The IMET buoy ( $1^{\circ}45'S$ ,  $156^{\circ}E$ ) and one TOGA TAO buoy (mt165a,  $2^{\circ}S$ ,  $156^{\circ}E$ ) were located at the center of the IFA, while the other two buoys, mt163a ( $5^{\circ}S$ ,  $156^{\circ}E$ ) and mt166a ( $0^{\circ}S$ ,  $157^{\circ}E$ ) were located to the north and south of the IFA, respectively. Although surface latent heat flux varied with geographical location and convective scales, the results derived separately from different buoys and ships around the IFA appear to be very similar, suggesting fluxes are coherent over a relatively large area, at least on long time scales. The surface latent heat flux varied between 50 and 100  $W m^{-2}$  during light winds. It increased dramatically and the maximum reached more than 200  $W$

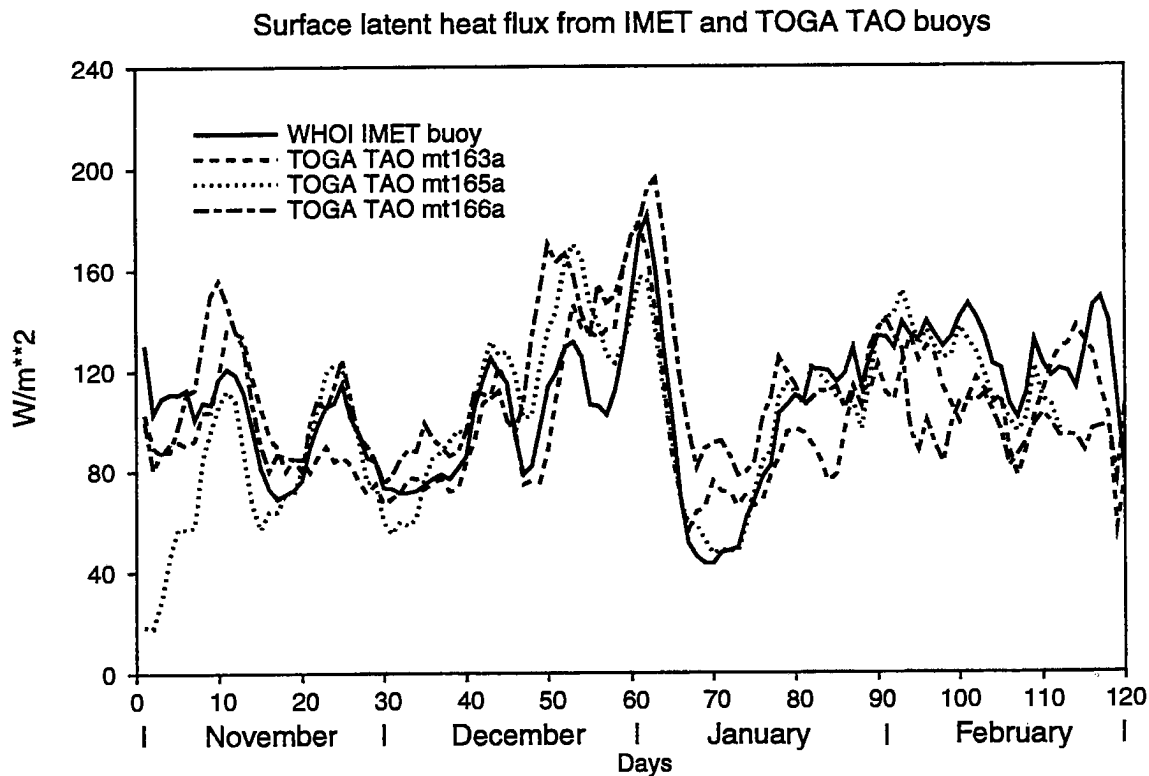


Figure 5.1: Comparisons of surface latent heat flux ( $\text{W m}^{-2}$ , 5-day running mean) (a) from IMET buoy ( $1^{\circ}45'S$ ,  $156^{\circ}E$ ) and three TOGA TAO buoys (mt163a:  $5^{\circ}S$ ,  $156^{\circ}E$ ; mt165a:  $2^{\circ}S$ ,  $156^{\circ}E$ ; mt166a:  $0^{\circ}S$ ,  $157^{\circ}E$ ). (b) from IMET buoy, R/V Shiyan #3, R/V Kexue #1, and the ECMWF IFA-mean. A time series of surface wind speed over the IFA ( $\text{m s}^{-1}$ ) is superimposed in (b) for comparison.

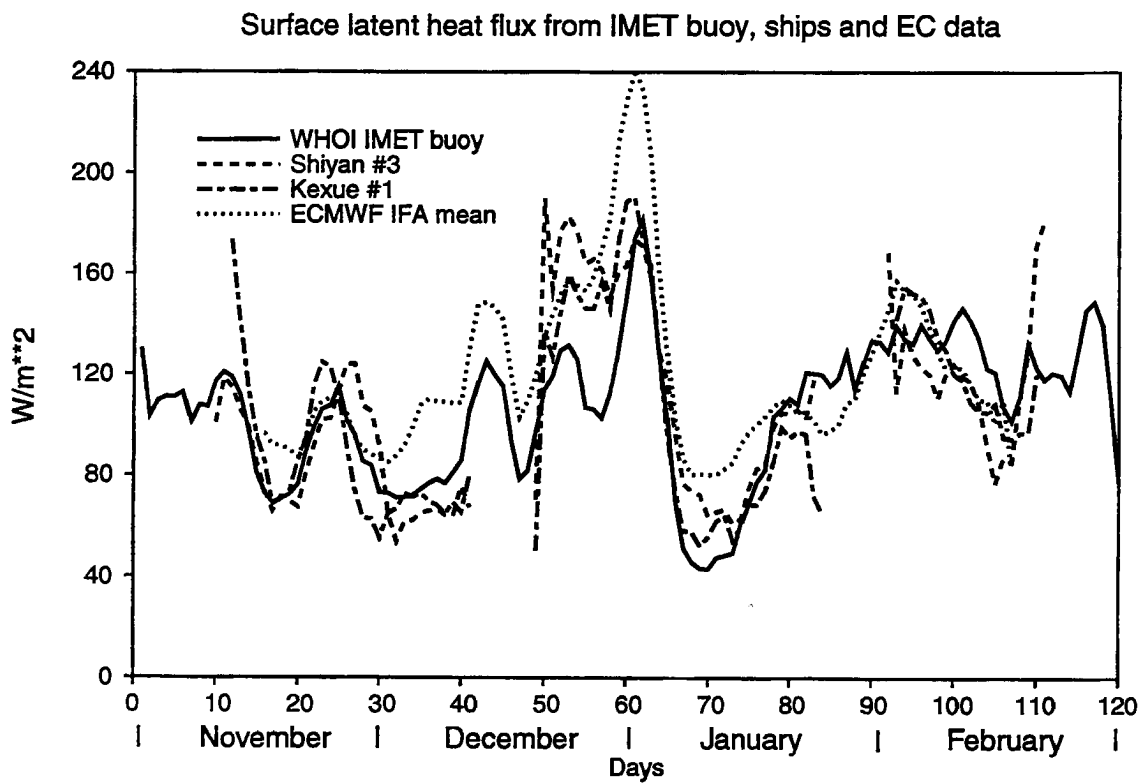


Figure 5.1: Continued.

$\text{m}^{-2}$  during the major westerly wind burst between December and January (around day 60) when the surface wind speed exceeded  $8 \text{ m s}^{-1}$  (Lin and Johnson 1996a). It also increased greatly during the November and February westerly wind events. As shown earlier, deep convection usually occurred 1 to 3 weeks prior to the peak westerly wind bursts. Large increases of surface latent heat flux due to convective and mesoscale downdrafts were often superimposed on the larger-scale increases of the surface latent heat flux associated with the ISOs (Lin and Johnson 1996a; Saxen 1996).

The ECMWF model forecast analysis agrees relatively well with the latent heat flux derived from the IMET buoy (Fig. 5.1b), although the ECMWF and ship IOP-means are higher than the buoy means (Table 5.1). The largest discrepancy of the ECMWF is during the strongest westerly wind burst between late December and early January. The ECMWF values are larger by an average of  $40 \text{ W m}^{-2}$  during this period (keep in mind ECMWF represents an IFA average and the others are point values). However, they compare quite well during the February wind burst even though it was also a windy period. The agreement between the surface latent heat fluxes is better during the light-wind periods, reflecting the improved ECMWF's inclusion of buoyancy-induced fluxes in near-calm conditions as described by Miller et al. (1992). Miller et al. (1992) examined the sensitivity of the ECMWF model to the parameterization of evaporation in light-wind conditions and noticed a dramatic impact on almost all aspects of the model's simulation of the tropics due to a moderate increase of surface latent heat flux (about  $25 \text{ W m}^{-2}$ ).

	IMET	mt163a	mt165a	mt166a	Kexue #1	Shiyan #3	ECMWF
LH flux	106	99	101	111	105	119	120
SH flux	8.6	6.0	7.6	9.4	5.8	7.4	9.9

Table 5.1: The IOP-mean surface latent and sensible heat fluxes ( $\text{W m}^{-2}$ ) from different sources.

Comparison of daily-mean surface sensible heat flux (5-day running mean) among the IMET and TOGA TAO buoys, two ships, and the ECMWF IFA-mean is shown in Figure 5.2. The buoy (Fig. 5.2a) and ship data are generally similar to one another and do not follow the pattern of low-level wind speed as the surface evaporation does. Values usually

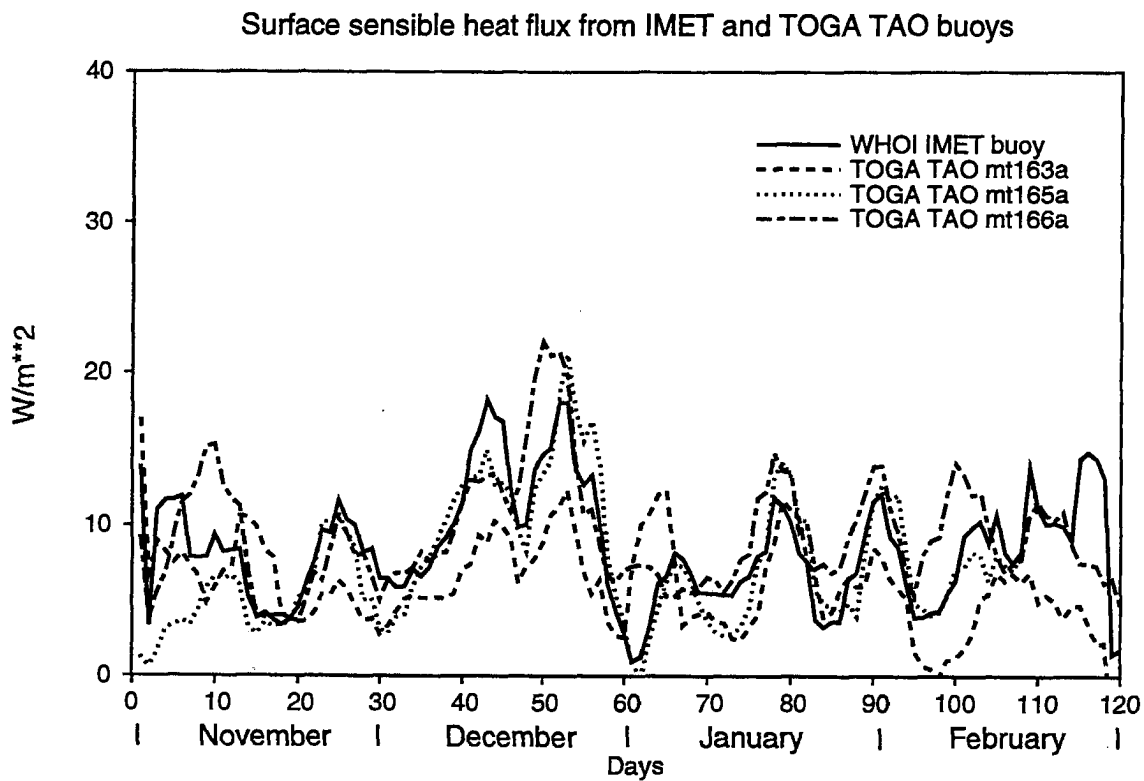


Figure 5.2: Comparisons of surface sensible heat flux ( $\text{W m}^{-2}$ , 5-day running mean) (a) from IMET buoy ( $1^{\circ}45'S$ ,  $156^{\circ}E$ ) and three TOGA TAO buoys (mt163a:  $5^{\circ}S$ ,  $156^{\circ}E$ ; mt165a:  $2^{\circ}S$ ,  $156^{\circ}E$ ; mt166a:  $0^{\circ}S$ ,  $157^{\circ}E$ ). (b) from IMET buoy, R/V Shiyan #3, R/V Kexue #1, and the ECMWF IFA-mean.

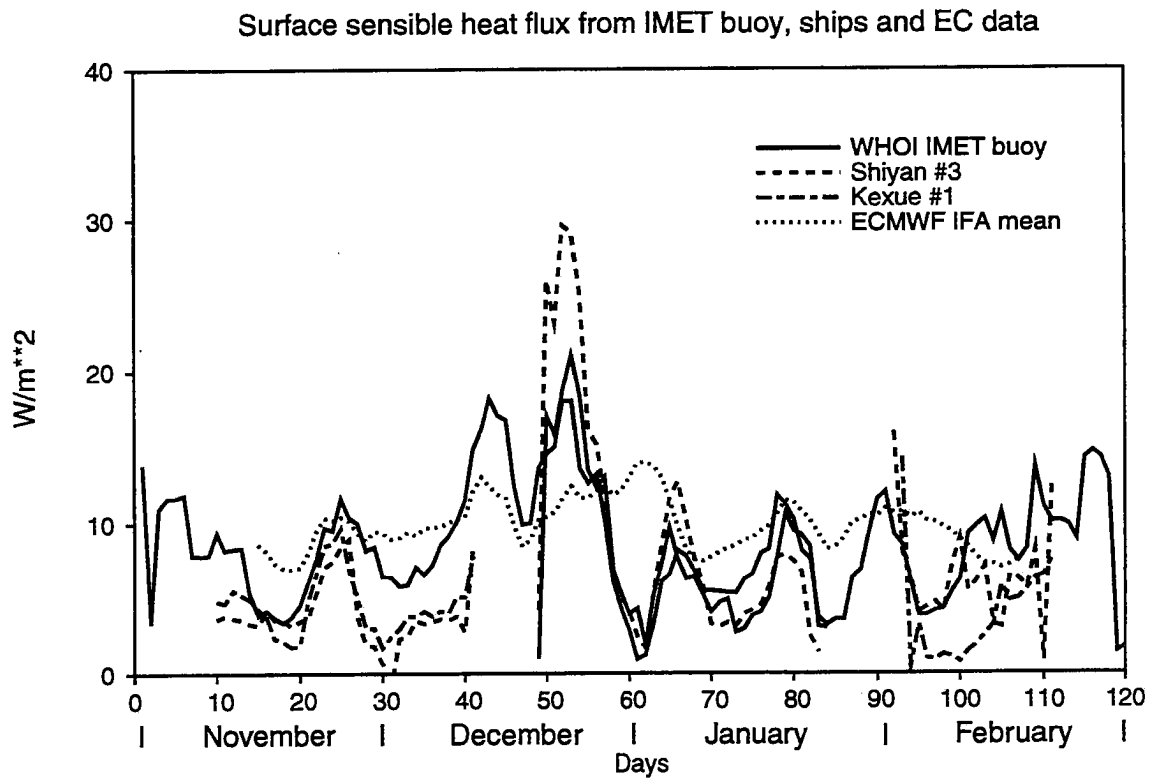


Figure 5.2: Continued.

peaked when convective systems occurred in the IFA (Fig. 5.8, later). The ECMWF data (Fig. 5.2b), however, appear to follow the low-frequency pattern of the surface wind speed and reached a maximum during the peak westerly wind burst between late December and early January. Comparisons of components in the computation of the heat fluxes indicate that although the time series of surface wind speed are very similar to those derived from ship and buoy data, surface air temperature was usually overestimated in the ECMWF data, especially during deep convective periods. Weller and Anderson (1996) meticulously compared the IMET buoy data with the ECMWF forecast results. They found that buoy mean air temperature and specific humidity were consistently lower than the ECMWF data, and also noticed that the model did not produce the decreases in air temperature observed in late December deep convection. Therefore, ECMWF does not capture the enhanced sensible heat fluxes during days 40–60, perhaps suggesting the need for a parameterization of downdraft and mesoscale enhancement of fluxes (Esbensen and McPhaden 1996).

Surface heat flux data covering the entire LSA were unavailable directly from observations during the COARE IOP. In order to approximate surface evaporation and sensible heat flux over the LSA, all ECMWF fluxes outside the IFA were adjusted separately for each time based on differences between ECMWF and mean buoy values around the IFA. (Caution should be exercised when interpreting results far from the IFA.) The resultant ECMWF-adjusted IOP-mean surface latent and sensible heat fluxes over the LSA are shown in Figure 5.3. Along the equator from 140°E to the date line, a band with minimum evaporation (between 100 and 120  $\text{W m}^{-2}$ ) appeared between 4°N and 1°S (Figure 5.3a), approximately coincident with a light-wind band along the equator (not shown). The IFA was within this low-evaporation region. Evaporation gradually increased to the north and south, associated with enhanced southeast and northeast trades. The pattern and magnitudes are similar to the long term annual mean derived from marine weather reports based on aerodynamic formulas (Weare et al. 1981). A minimum band in sensible heat flux (Figure 5.3b) also existed along the equator from 150 °E to 170°E. Two bands of higher heat flux were to the north and south of the equator, approximately coincident with the double ITCZ. The very high values of evaporation and sensible heat flux over New Guinea (southwest corner of LSA) are not reliable.

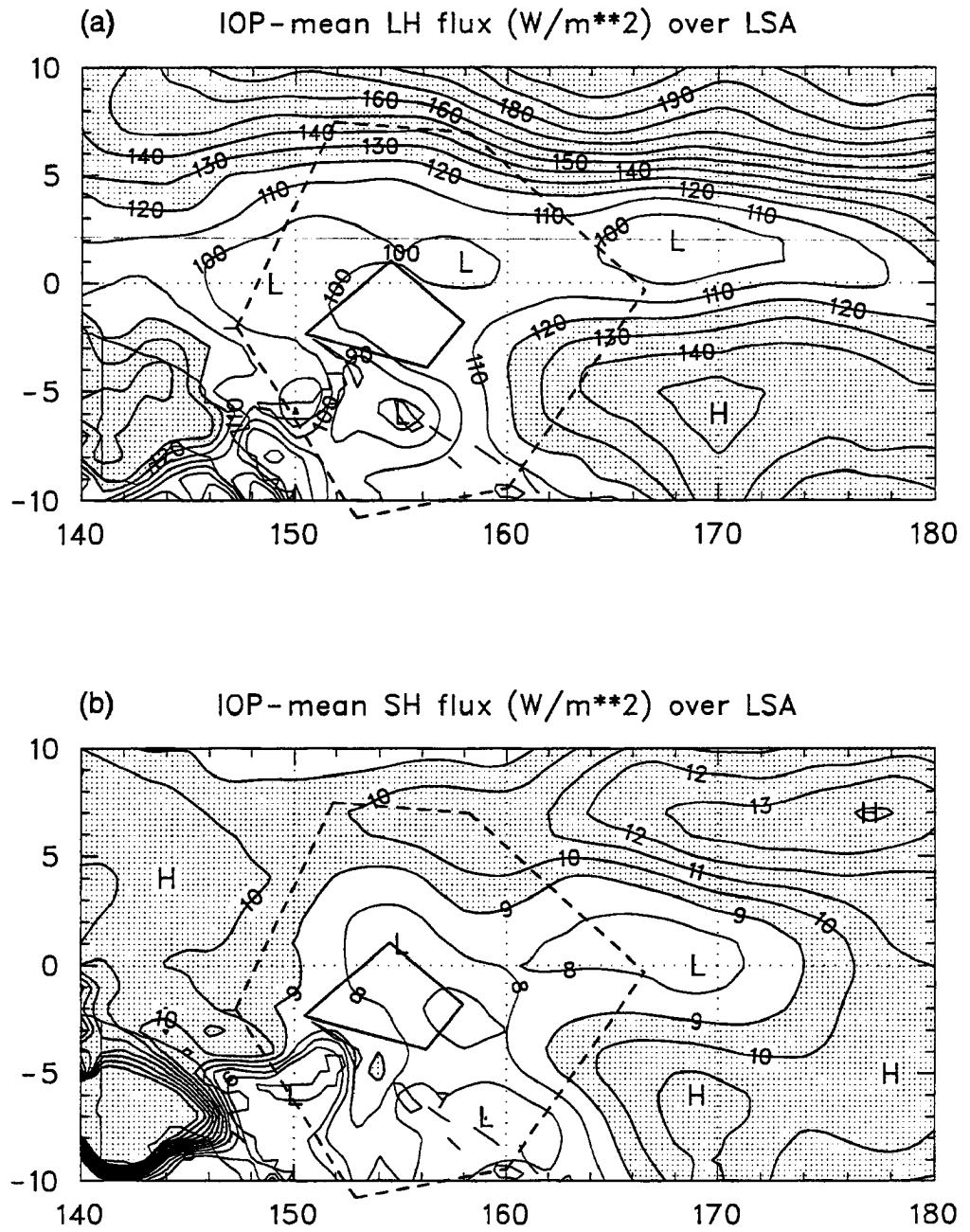


Figure 5.3: (a) The IOP-mean surface latent heat flux ( $\text{W m}^{-2}$ ) over the Large Scale Array. Contour intervals  $10 \text{ W m}^{-2}$  and areas with values  $> 120 \text{ W m}^{-2}$  are shaded. (b) The IOP-mean surface sensible latent heat flux ( $\text{W m}^{-2}$ ) over the Large Scale Array. Contour intervals  $1.0 \text{ W m}^{-2}$  and areas with values  $> 9 \text{ W m}^{-2}$  are shaded.

For budget computations over the IFA, the four-buoy data are used to approximate the IFA-mean surface latent heat flux due to their better temporal and spatial coverage, as well as the good comparisons among them. Over the LSA, adjusted ECMWF evaporation rates are used to estimate surface rainfall rate for the moisture budget (section 5.3).

## 5.2 Broad scale considerations

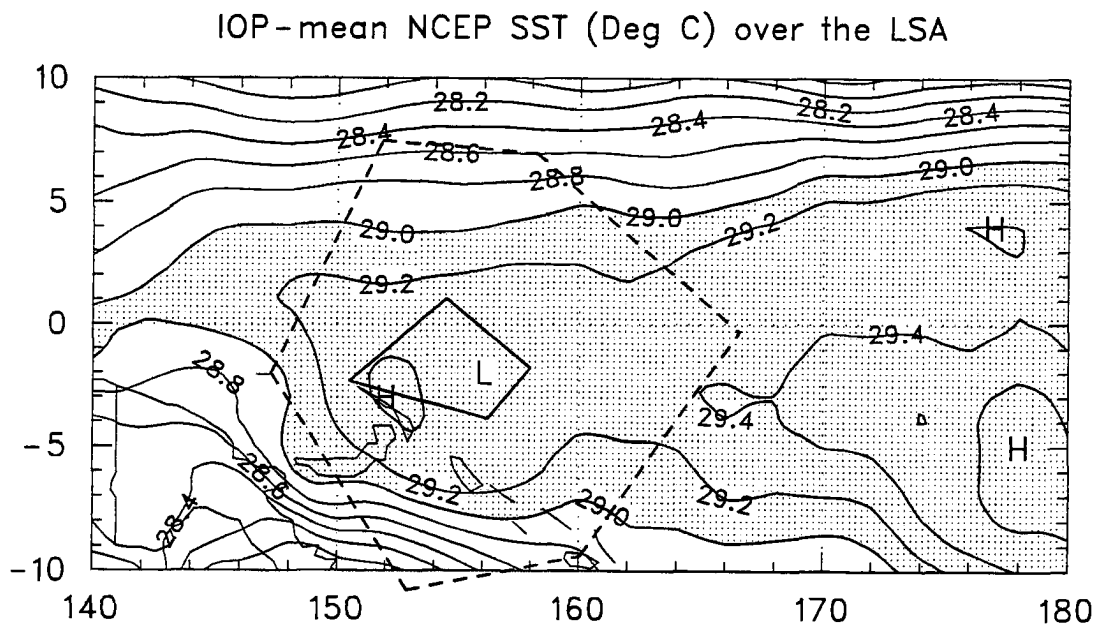


Figure 5.4: The IOP-mean NCEP SST (Deg C) over the LSA. Contour intervals  $0.2^\circ$  and areas with SST  $> 29.0^\circ$  are shaded.

Figure 5.4 shows the IOP-mean NCEP SSTs over the LSA (courtesy of Dr. Richard Reynolds). The COARE IOP occurred during a period when a weak El Niño/Southern Oscillation (ENSO) gradually increased in amplitude (McPhaden 1993; Gutzler et al. 1994). The region with the warmest sea surface was generally located south of the equator at the southeast corner of the LSA, coincident with the area of lowest IOP-mean brightness temperature (Figure 2, Lin and Johnson 1996a). SSTs gradually decreased along the equator from the date line to the west. The mean SST over the IFA was above  $29.2^\circ\text{C}$ . Gutzler et al. (1994) investigated the seasonal variability leading up to the COARE IOP: warmest waters

migrated southeastward as the seasons progressed. Monthly-mean cloud-top temperatures shown in McBride et al. (1995) clearly indicate a southeastward progression of the tropical convective heat source as the Southern Hemisphere monsoon developed and matured.

During the TOGA-COARE IOP, the ISOs strongly modulated clouds, precipitation, and evaporation over the warm pool on a 30 to 60 day time scale. Figure 5.5 shows a time series of the zonal component of the flow (Lin and Johnson 1996a), of the precipitation ( $P$ ), and of the evaporation ( $E$ ) over the IFA during the IOP. The precipitation was estimated from the moisture budget (Eq. 3.4) using evaporation derived from buoy data. Three low-level westerly wind bursts can be seen, with the most prominent one peaking around 1 January. Strong vertical wind shear occurred during peak westerly wind bursts. Heavy precipitation usually fell 1 to 3 weeks prior to the peak westerly wind bursts while convection was generally suppressed during the peak bursts.

Averaged over the entire IOP, evaporation estimated from buoy data was about  $3.7 \text{ mm day}^{-1}$  ( $1 \text{ mm day}^{-1} \approx 28.9 \text{ W m}^{-2}$ ) and budget-derived precipitation over the IFA was about  $5.6 \text{ mm day}^{-1}$ . In other words,  $P$  was about 50% greater than  $E$  over the IFA. However, regionally,  $P$  was locally minimal over the IFA (Figure 7). Considerably greater precipitation rates ( $P > E$ ) were embedded in east-west ITCZ bands north and south of the IFA (near  $4^\circ\text{N}$  and  $7^\circ\text{S}$ ), and east of the IFA. During the heavy rain,  $P$  exceeded  $E$  by 3 to 5 times (Figure 5.5), the excess arising from large-scale moisture convergence (water vapor storage was small). Convection at this time was characterized by numerous squall systems with attendant stratiform precipitation (Rickenbach and Rutledge 1996a). During other times, including both light- and strong-wind periods,  $P$  closely matched  $E$ .  $P$  was even occasionally less than  $E$  during high winds, meaning that water vapor was being transported out of the IFA and/or the shallow cloud field moistened the lower troposphere.

### 5.3 Rainfall analysis

#### 5.3.1 Mean distribution of rainfall

Figure 5.6 shows the IOP-mean rainfall distributions over the LSA for the  $Q_2$  budget based on the buoy-adjusted ECMWF values of  $E_0$  in Fig. 5.3a, the ECMWF model forecast

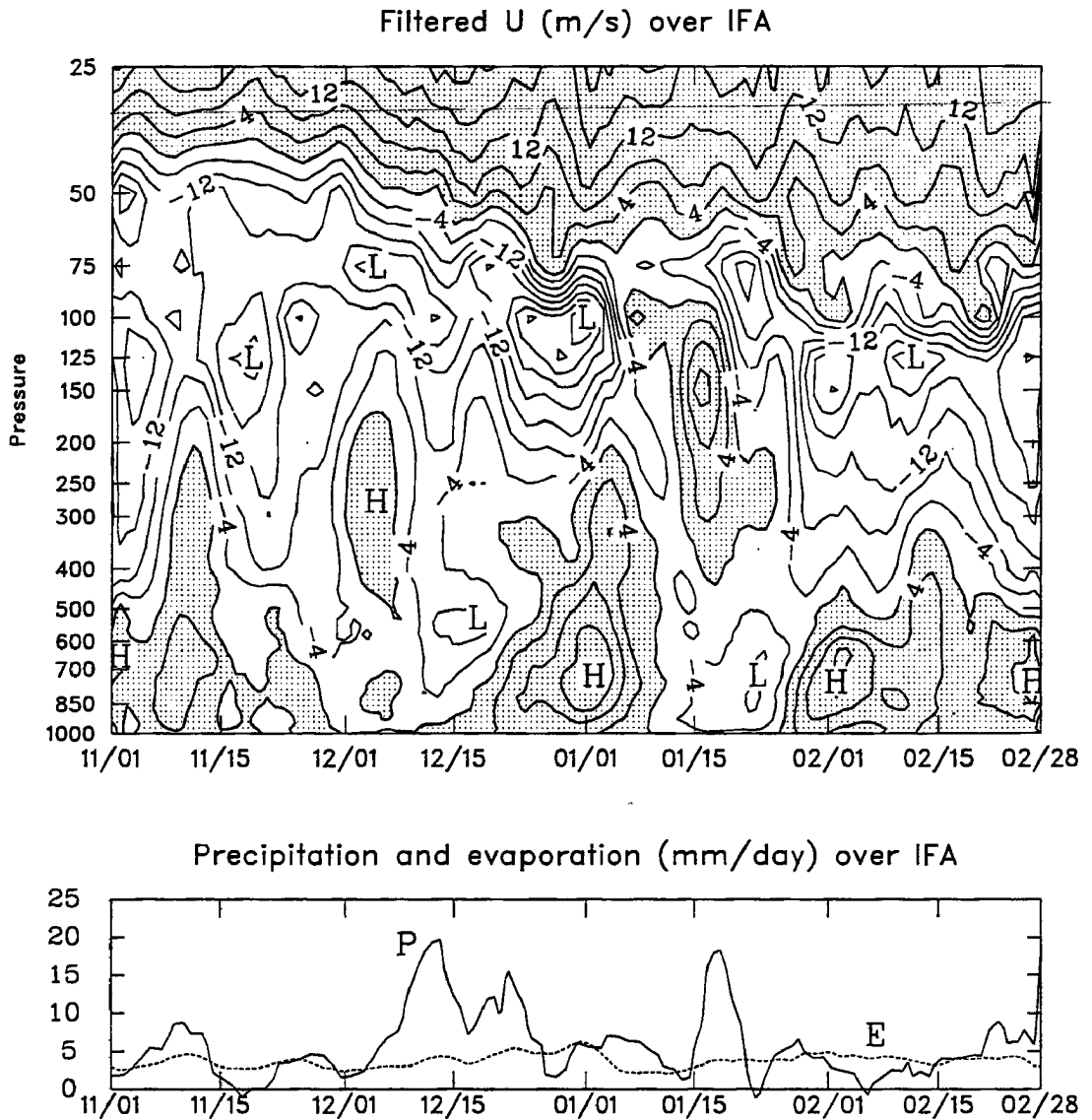


Figure 5.5: Time series of daily-mean zonal U component ( $\text{m s}^{-1}$ ), precipitation and evaporation ( $\text{mm day}^{-1}$ ) averaged over the Intensive Flux Array (5-day running mean). Contour intervals  $4 \text{ m s}^{-1}$  and westerlies are shaded.

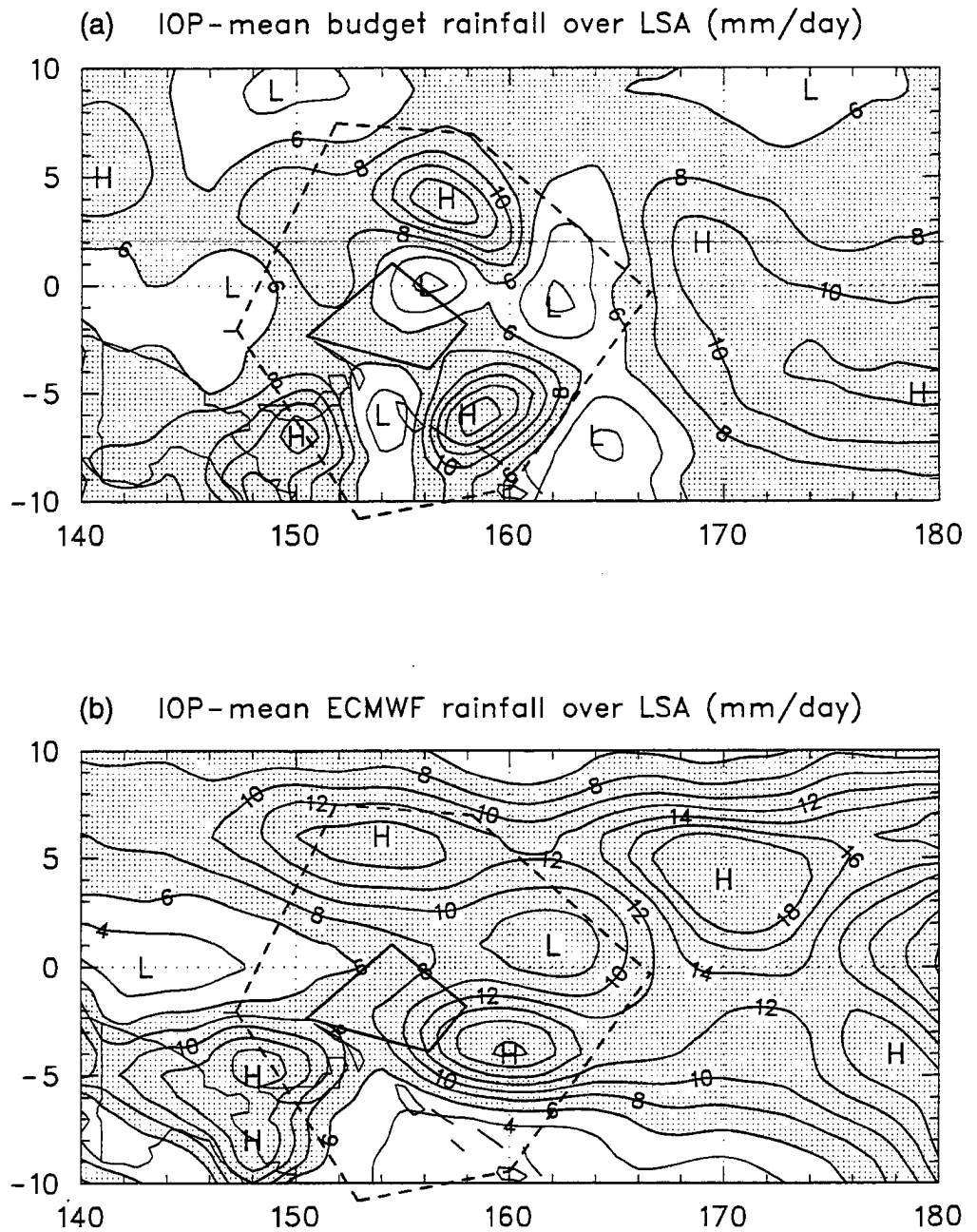


Figure 5.6: Comparison of the IOP-mean rainfall distributions over the LSA ( $\text{mm day}^{-1}$ ): (a) Budget determination, (b) ECMWF forecast result, (c) SSM/I measurements, (d) GPI estimation. Contour intervals  $2 \text{ mm day}^{-1}$  and areas with rainfall rate  $> 6 \text{ mm day}^{-1}$  are shaded.

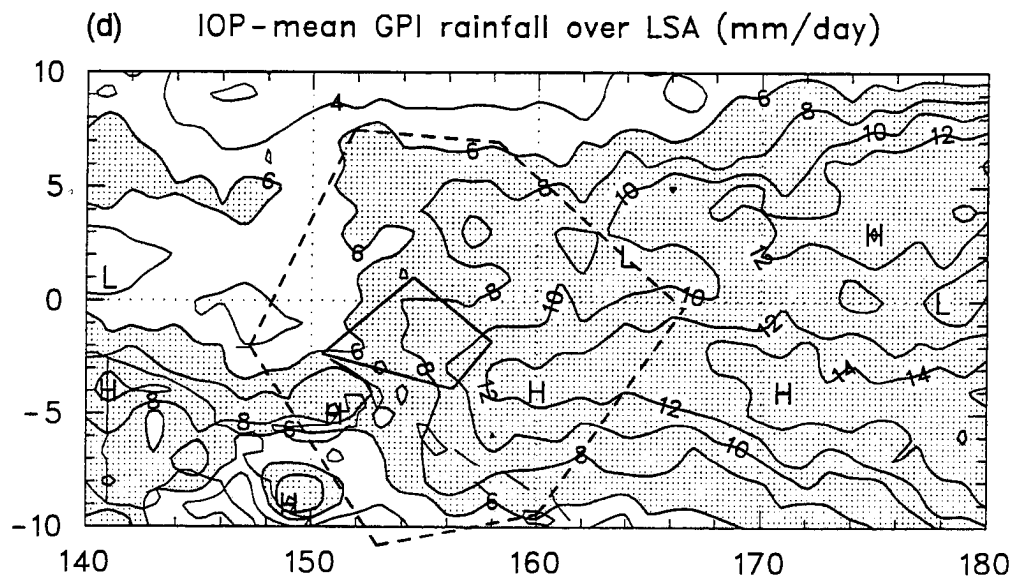
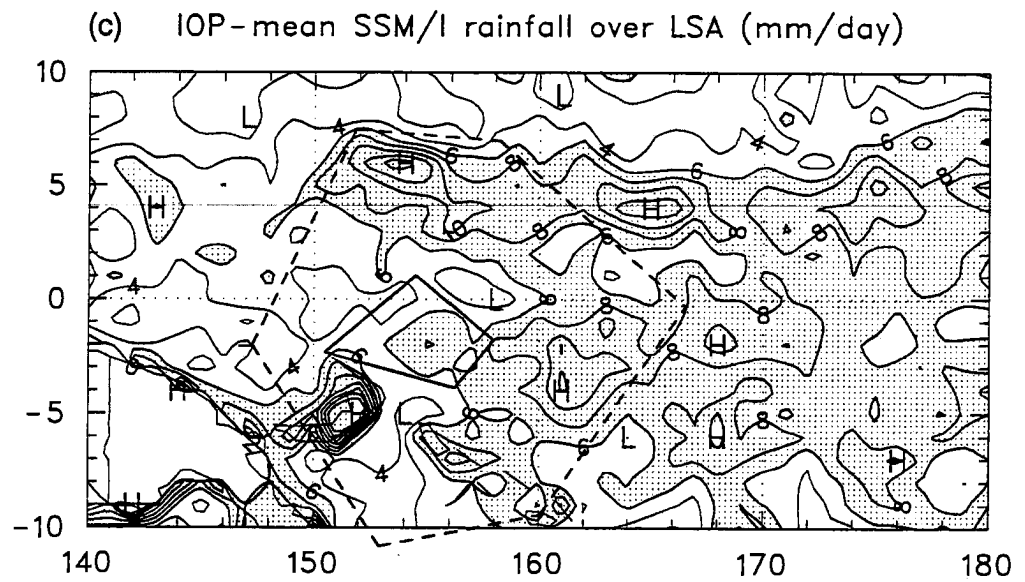


Figure 5.6: Continued.

result, the SSM/I measurements, and the GPI estimation (The budget-derived and ECMWF rainfalls are actually 3-month averages from 15 November 1992 – 15 February 1993). The four rainfall maps generally compare well with one another over the IFA: two heavy rainfall bands were located to the north and south of the IFA, consistent with the double ITCZ shown in the IOP-mean brightness temperature plot (Lin and Johnson 1996a). There was an east-west zone with minimal rainfall along the equator from 140°E to 165°E. The IFA was approximately within this band. Extensive heavy rain, coincident with the region of the warmest sea surface, fell to the east of the IFA from 165°E to the date line. Previous rainfall studies based on surface and satellite observations (Taylor 1973; Janowiak and Arkin 1991; Janowiak 1992) also clearly indicated a minimum rainfall band along the equator between two ITCZ bands, similar to the IOP-mean distributions. However, the minimum from the budget determination and SSM/I measurements during the COARE IOP was lower than expected, with values at some equatorial locations as low as the mean evaporation rate (3–4 mm day<sup>-1</sup>). Climatological studies usually show an eastward decrease of rainfall along the equator over the warm pool. During the COARE IOP, however, heavy precipitation, high clouds, as well as the positive SST anomalies appear to have been located near the date line, and to have decreased toward the west (see also Gutzler et al. 1994).

Within the OSA, all four estimations consistently indicate two local maxima to the southeast and southwest of the IFA, and one local maximum to the north of the IFA. The diagnosed rainfall from the  $Q_2$  budget indicates less precipitation over the northern and northeastern IFA, mainly because of the rainfall minimum band along the equator. However, the analyses from SSM/I retrievals, GPI, and ECMWF data all show less precipitation over the western IFA and more precipitation over the east. The IOP-mean rainfall rates over the IFA for the  $Q_2$  budget, ECMWF, SSM/I retrievals, and GPI are 5.6, 9.1, 5.6, and 10.9 mm day<sup>-1</sup>, respectively. Both the ECMWF and GPI rainfall rates are about 3 to 6 mm day<sup>-1</sup> higher than those from the  $Q_2$  budget and SSM/I retrievals over the IFA and the minimum rainfall band along the equator. (One possible reason for higher GPI rainfall will be discussed in the next subsection.) The higher IFA-mean values from the ECMWF forecast and GPI may also have been influenced by the local maximum southeast of the

IFA. Ding and Sumi (1995) presented the IOP-mean horizontal cross sections of vertically integrated  $Q_1$  and  $Q_2$  over the COARE domain based on the global objective analysis of the Japan Meteorological Agency. Although the major heating and condensation occurred near the date line, the double ITCZ and the minimum rainfall band along the equator, especially for the features within the OSA, were not resolved in their analyses.

To the west of the OSA, the ITCZ maintained its double structure, with the southern rainfall band mainly located over New Guinea. The rainfall rates over the northern rainband vary greatly among the four estimations, with the ECMWF data the highest (greater than  $8 \text{ mm day}^{-1}$ ) and the SSM/I measurement the lowest (around  $4 \text{ mm day}^{-1}$ ). The  $Q_2$  budget and GPI rainfall rates are between  $5$  and  $6 \text{ mm day}^{-1}$ . All four rainfall analyses clearly indicate that major heating and drying occurred from the east of the OSA to the date line during the COARE IOP. However, caution should be exercised while interpreting the budget rainfall due to the sparsity of sounding stations over this region.

### 5.3.2 Comparison of rainfall rates

Figure 5.7 compares the IFA-averaged rainfall rates (5-day running mean) from the moisture budget with the rates from two remote sensing results: GPI and SSM/I retrievals. The agreement of the pattern of temporal variability among the sounding- and remote-sensing-derived results is generally quite good. Heavy rainfall occurred in mid-December over the IFA, about 1 to 3 weeks prior to peak westerlies (Figure 5.5). The IOP-mean rainfall rates over the IFA from the moisture budget and SSM/I retrievals are both  $5.6 \text{ mm day}^{-1}$  (SSM/I value; Drs. Judy Curry and Guosheng Liu, 1995, personal communication). The R/V Kexue #1 and the R/V Shiyan #3 were occasionally absent during the COARE IOP. For the three cruises when both ships were within the IFA, the period-mean rainfall rates are  $4.2 \text{ mm day}^{-1}$  (11 November–11 December),  $7.1 \text{ mm day}^{-1}$  (18 December–23 January), and  $3.0 \text{ mm day}^{-1}$  (31 January–18 February), respectively. GPI values are generally much higher due to the frequent occurrence of non-precipitating cirrus over the western Pacific warm pool. For example, toward the end of December and early January, rainfall from GPI was about two times the SSM/I values and budget estimations. GMS

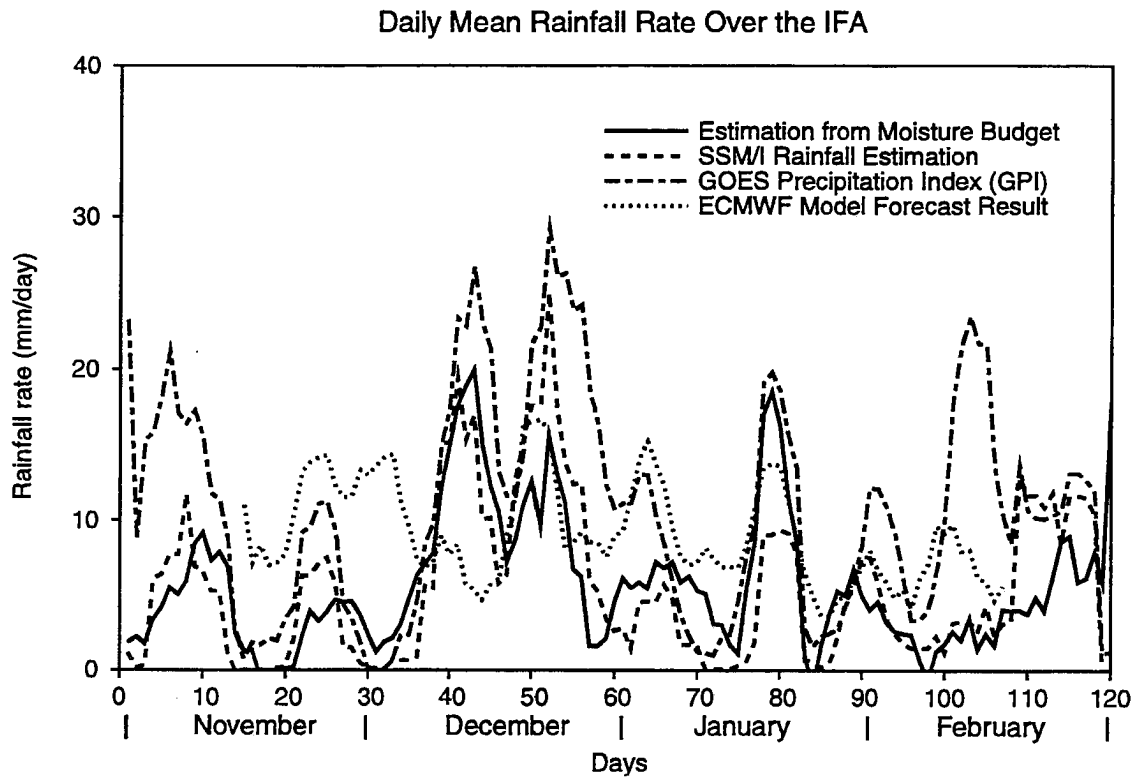


Figure 5.7: Comparison of daily-mean rainfall rates ( $\text{mm day}^{-1}$ ) over the IFA from moisture budget, SSM/I retrievals, GPI and ECMWF model forecast result (5-day running mean).

satellite images during this period indicate that large and deep convection were confined to east of 170°E while non-precipitating cirrus was advected westward across the IFA by strong easterly flow (Velden and Young 1994). The flow field surrounding severe tropical cyclones Kina and Nina also contributed to the advection. Low surface rainfall rates were further supported by rainfall analyses derived from MIT radar data (Rickenbach and Rutledge 1996a). Analysis of vertical velocity in Lin and Johnson (1996a) also suggests that although weak upward motion existed at upper levels during this period, downward motion generally dominated the middle and lower levels, and deep convection was suppressed over the IFA. The ECMWF time series (Figure 5.7) does not match the other rainfall estimations, largely because many of the COARE soundings were not transmitted on the GTS (Global Telecommunication System) and therefore were excluded from the assimilation scheme. This result emphasizes the importance of detailed in situ observations to accurate forecasts over the warm pool. Other factors, such as deficiencies in the 6-hour forecast, cumulus and other model parameterizations, may also affect the accuracy of the forecast fields.

### *5.3.3 Components of the moisture budget*

Figure 5.8 shows as a byproduct of the moisture budget, the time series of precipitation, evaporation, moisture convergence, and storage terms (Eq. 3.4) over the IFA during the IOP. The water vapor storage was generally small and contributed little to precipitation. Evaporation generally varied with surface wind speeds associated with the low-frequency ISOs. Evaporation did not follow the pattern of rainfall, although it increased slightly during heavy precipitation, probably induced by gusty winds generated by the convective systems. The large-scale moisture convergence closely matched the precipitation curve during heavy rain, and surface evaporation appeared to be only a passive player in the precipitation cycle.

## **5.4 Heat and moisture budgets**

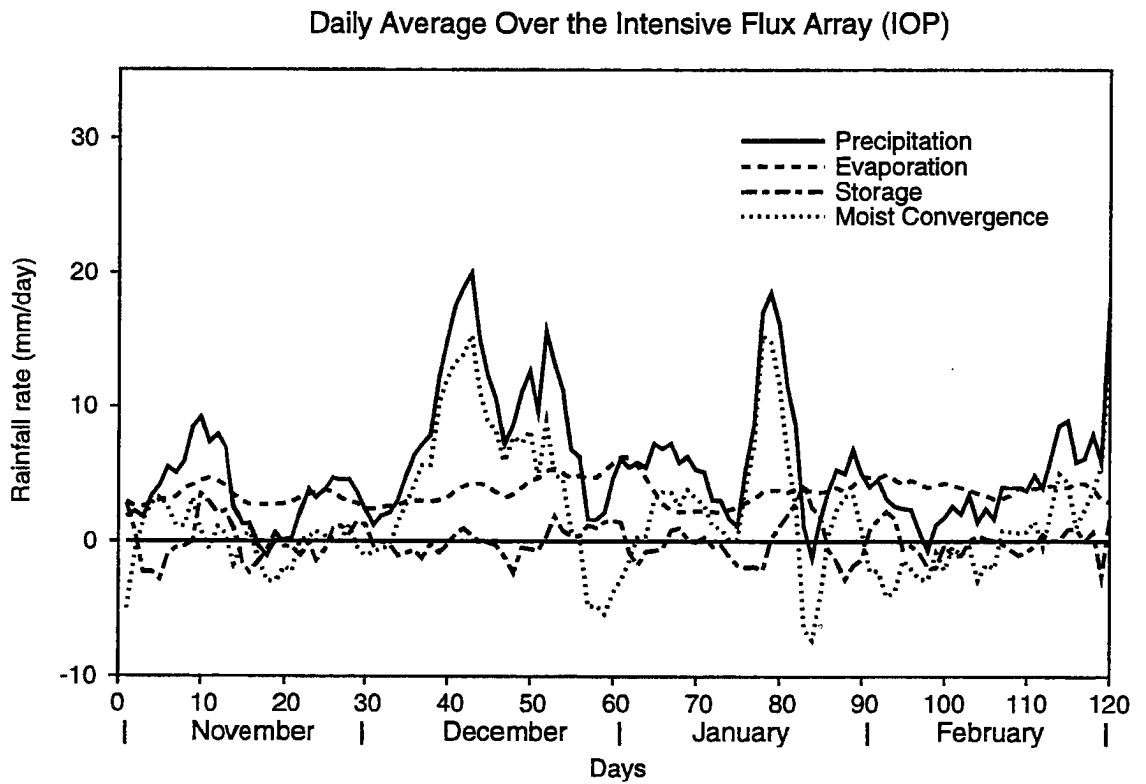


Figure 5.8: Comparison of components of the moisture budget: precipitation, evaporation, storage and moisture convergence over the IFA ( $\text{mm day}^{-1}$ , 5-day running mean).

### 5.4.1 Monthly time series

Time series of the apparent heat source  $Q_1$  and the apparent moisture sink  $Q_2$  over the IFA are illustrated month by month in Figure 5.9, along with time series of the IFA-mean SST, 1000-hPa wind speed, GMS brightness temperature, surface latent and net longwave radiative heat fluxes. A 1–2–1 filter was applied. Such detailed information of long-term surface and upper-air data is unique for studying the interaction between the ocean and the atmosphere and was generally unavailable in previous field experiments.

In November (Figure 5.9a), the IFA-mean surface wind speed generally remained below  $3 \text{ m s}^{-1}$ , except for a moderate westerly wind burst in early and middle November and a few convective cases. Moderate heating/drying occurred above 500 hPa between 1 November and 4 November with peaks located between 350 and 400 hPa, while some weak cooling and moistening existed at middle and lower levels, similar to the features found within anvil clouds (Houze 1982; Johnson and Young 1983). Although most research vessels were not on site during this period, GMS satellite maps (not shown) indicate frequent cirrus around the IFA from dissipating convective systems.

Associated with a moderate westerly wind burst, low-level winds started to intensify on 5 November and reached a maximum at about 700 hPa on 13 November (Figure 5.5). Heating and drying occurred a few days prior to the peak westerly wind burst. Surface latent heat flux positively correlated with the surface wind speed and gradually increased from about  $80 \text{ W m}^{-2}$  on 5 November to  $150 \text{ W m}^{-2}$  on 12 November. SSTs slowly decreased with increasing wind speed due to heat loss from the ocean and vertical mixing in the near-surface ocean. Surface net longwave radiative flux varied little with time (around  $60 \text{ W m}^{-2}$ ), although some small increases can be observed during sunny days. Between 10 and 11 November, a cloud system induced by broad convergence between low-level westerlies and easterlies drifted from the east and passed through the IFA. Heating/drying generally dominated throughout most of the troposphere. Here,  $Q_1$  peaked between 400 and 500 hPa while  $Q_2$  peaked at low levels. Strong moistening can be observed near the surface and gradually extended upward, the latter presumably due to precipitation evaporation.

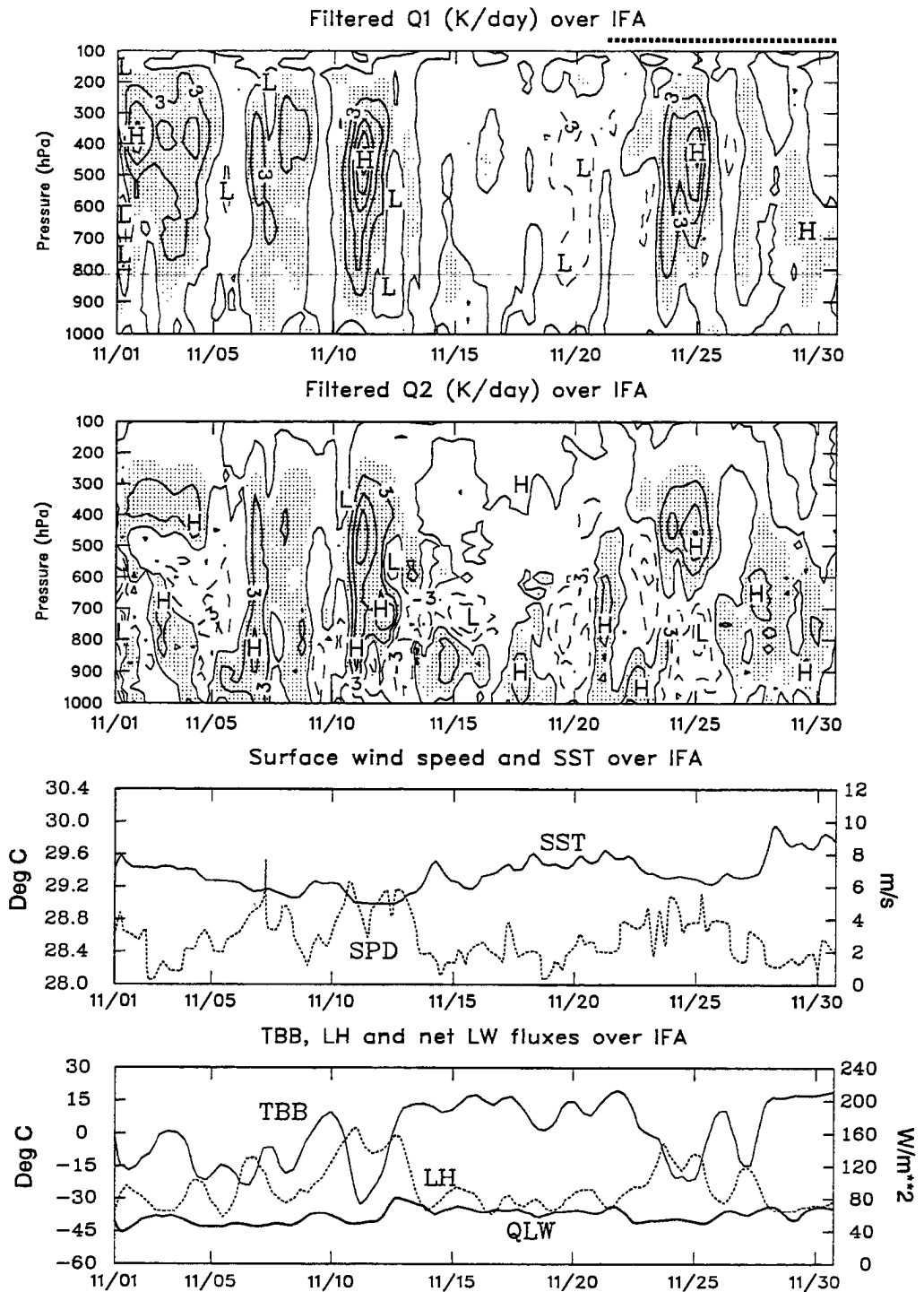


Figure 5.9: Monthly time series of the IFA-mean apparent heat source  $Q_1$  ( $K day^{-1}$ ), the apparent moisture source  $Q_2$  ( $K day^{-1}$ ), SST (Deg C), surface wind speed ( $m s^{-1}$ ), GMS brightness temperature (Deg C), surface latent and net longwave radiative heat fluxes ( $W m^{-2}$ ). November, December, January, and February. The contour intervals for  $Q_1$  and  $Q_2$  are  $3 K day^{-1}$  and areas  $> 1.0 K day^{-1}$  are shaded. Dotted lines above the  $Q_1$  figures indicate periods during the COARE IOP when both ships Kexue #1 and Shiyang #3 were out of the IFA.

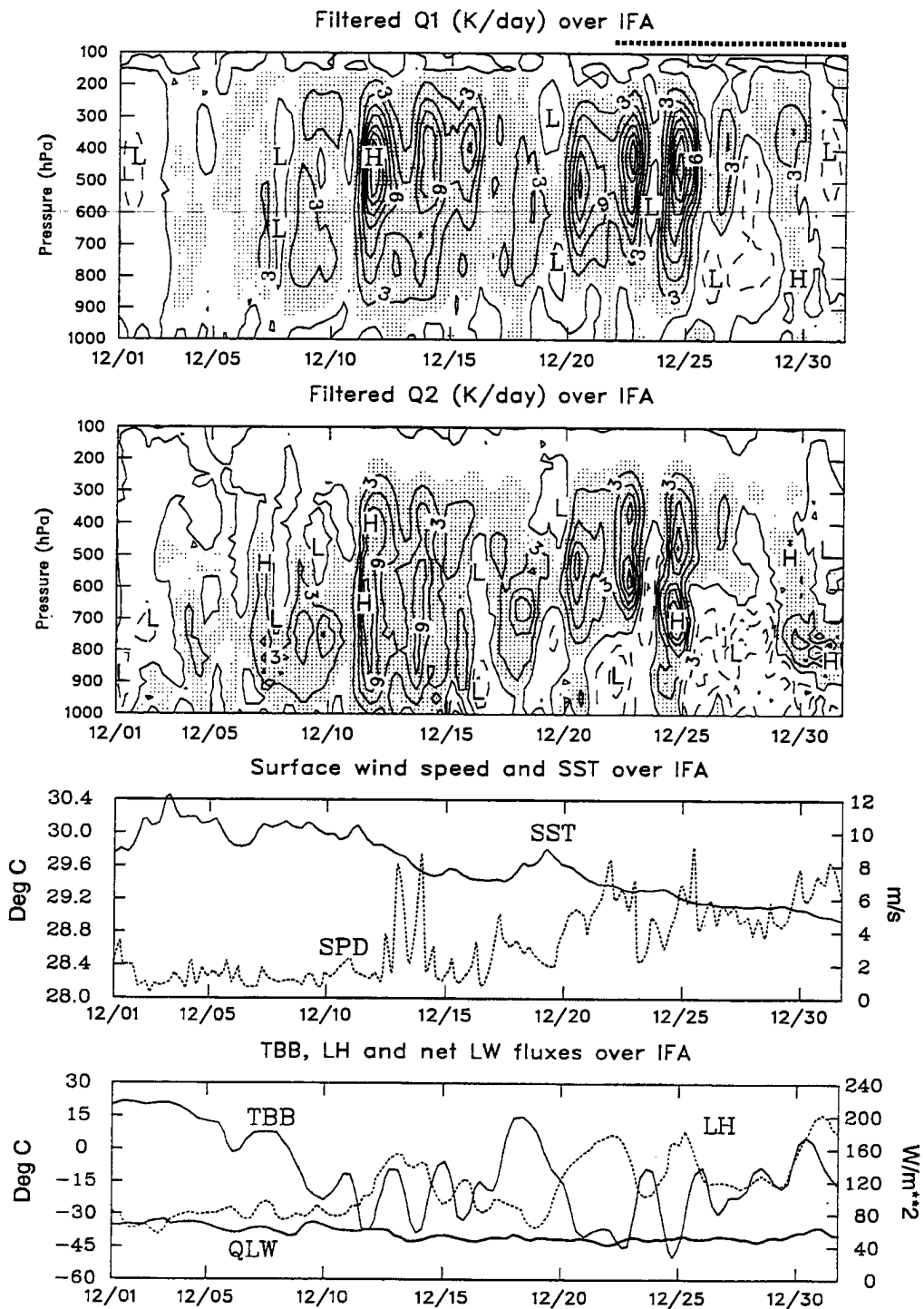


Figure 5.9: Continued.

Between 13 November and 5 December (except for two individual convective cases around 24 and 27 November), the GMS brightness temperature over the IFA was relatively high and remained nearly constant around 15°C. This period was characterized by very weak surface winds, and surface latent heat flux remained around 80 W m<sup>-2</sup>, slightly larger than net longwave radiative flux. Due to the light winds and absent deep convection, this period can be defined as the undisturbed phase of the ISO. The atmosphere warmed and dried at low levels and cooled and moistened above (500 to 700 hPa), suggesting frequent shallow cumulus clouds (Nitta and Esbensen 1974) and cumulus congestus, consistent with MIT radar scans which show only isolated cumulonimbus during this undisturbed period (TCIPO TOGA COARE Operations Summary 1993). Rainrate analyses derived from MIT radar (Rickenbach and Rutledge 1996a) also indicated rainfall was light during this undisturbed period, and most rainfall was from sub-MCS (mesoscale convective system) non-linear convective systems. Weak cooling, probably due to radiation, dominated throughout most of the middle and upper troposphere. Since the heat transfer from the ocean to the atmosphere was weak and the absorbed solar radiation by the ocean surface was high due to less cloud cover (Weller and Anderson 1996), SSTs gradually increased with time (except for the period with individual deep convection) during the undisturbed period and reached a maximum in early December, providing a favorable environment for deep convection to develop later.

The period between 5 and 12 December was still characterized by light surface winds (Figure 5.9b). However, heating and drying over the IFA was stronger. Values of  $Q_1$  peaked between 500 and 800 hPa, while  $Q_2$  peaked between 700 and 850 hPa, generally higher than those during the undisturbed phase, but lower than those during deep convective systems, suggesting the gradual development of midlevel cumuli. The vertical shear during this period was very weak (Figure 5.5). Having reached a maximum of 30.4°C on 3 December, SSTs started to slightly decrease under increasing cloud cover (decreasing brightness temperature). In the meantime, the surface latent heat flux remained nearly constant between 80 and 100 W m<sup>-2</sup>.

The most intense convection over the IFA occurred in middle and late December, prior to the peak westerly wind burst around 1 January. Westerlies started to appear

near the surface over the IFA in early December and gradually developed and intensified, although the middle and upper troposphere was still dominated by easterlies (Figure 5.5). Tropical cyclones Kina and Nina in the southwest Pacific reinforced low-level westerlies (McBride et al. 1995). The moderate vertical wind shear favored organized deep convection. There were several major convective events around 11-15 December and 21-25 December, mainly due to low-level large-scale convergence of easterlies and westerlies. Time series of GMS brightness temperature show several distinct troughs during these events. Both the surface wind speeds and surface latent heat fluxes increased dramatically when the convection occurred within the IFA, although net longwave radiative flux remained nearly the same. SSTs gradually decreased as latent and sensible heat fluxes from the ocean to the atmosphere, vertical mixing in the upper ocean, and cloud cover increased. Strong heating dominated throughout the troposphere but the surface cooled weakly. All of these cases show a similar order of magnitude of peak heating (more than  $10 \text{ K day}^{-1}$ ) between 350 and 500 hPa. However, the apparent moisture sink  $Q_2$  shows distinctly different patterns in these cases. The first convective period (11–15 December) shows separated peaks of  $Q_1$  and  $Q_2$ , suggestive of vigorous deep convection (Luo and Yanai 1984). However, during the 21-24 December period, the  $Q_2$  peaks shifted upward becoming more coincident with the  $Q_1$  peaks, suggesting a greater contribution from stratiform precipitation as the wind shear increased (e.g., Johnson and Young 1983). Strong evaporative moistening began at low levels, then gradually deepened. Rickenbach and Rutledge (1996a), based on MIT Doppler radar data, estimated total and non-convective rainrates (their Figure 6) within the radar sample area (about one fourth of the IFA). Contribution from non-convective rainfall was quite small (less than 15 %) during early December, gradually increased with strengthening vertical wind shear, and then almost dominated the total rainfall during the 21-25 December period (more than 60 %). Here, rawinsonde and radar data yield very consistent information on organization of vertical wind shear on convective and stratiform cloud elements and their contribution to surface rainfall.

From 27 December to 2 January, a few days after the convective phase, surface wind speed continued to increase, partly due to the influence of tropical cyclones Kina and

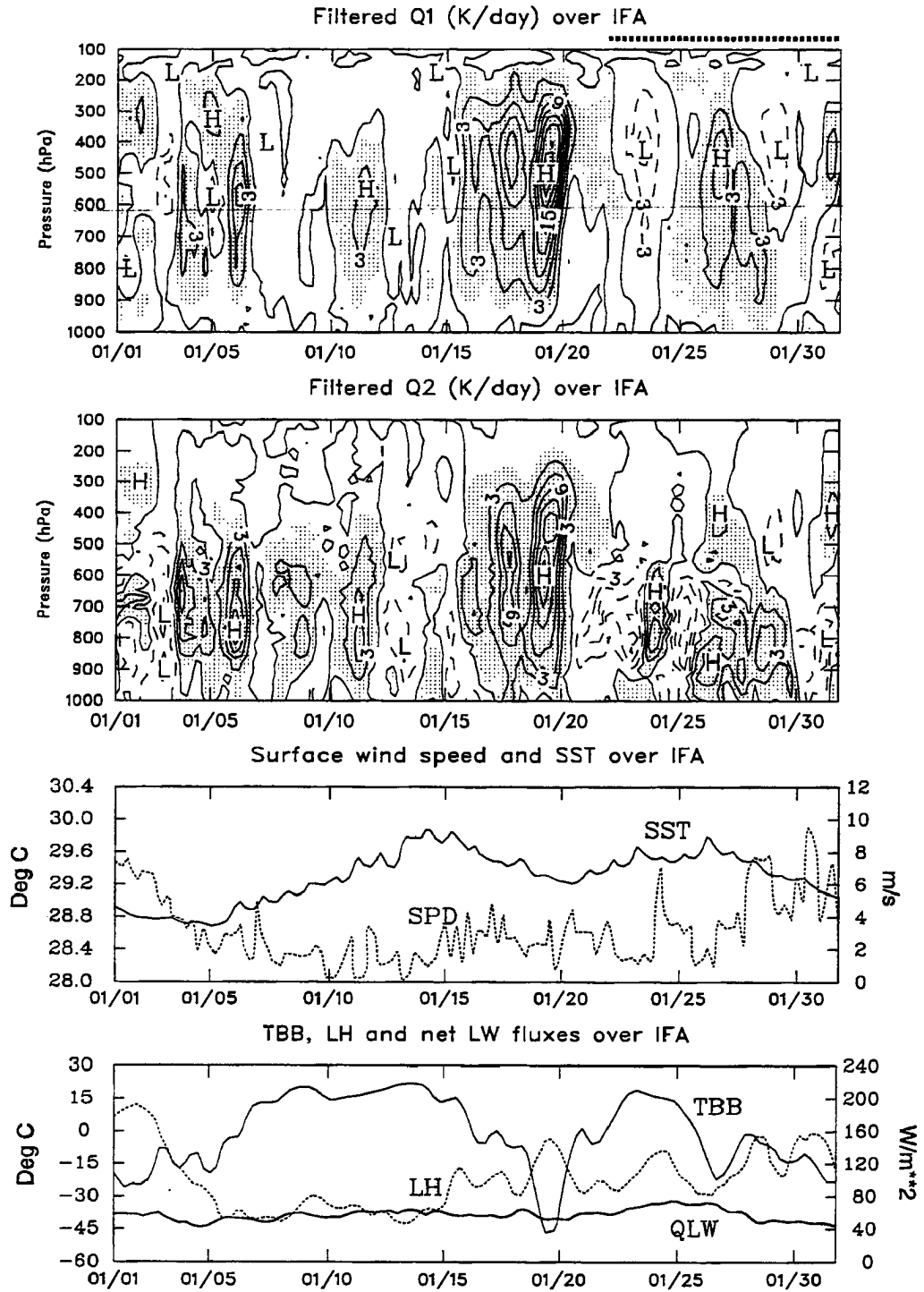


Figure 5.9: Continued.

Nina. SSTs continued to drop with increasing loss of heat by evaporation and strong ocean mixing. The troposphere cooled between 400 and 850 hPa, presumably due to radiative cooling and/or evaporative cooling from stratiform clouds. Weak warming existed between 200 and 350 hPa, consistent with satellite maps that show thin cirrus advecting from the convective systems east of the IFA (Velden and Young 1994). Weak warming below 850 hPa was probably induced by enhanced heat fluxes from the ocean surface in the strong winds. These features are consistent with the  $Q_2$  profiles, which show moistening at middle and lower levels.

From 4 January to 15 January, low-level westerlies weakened and reversed to weak easterlies (Figure 5.5). Although scattered convection persisted at the south end of the IFA between 4 and 6 January, intense deep convection was generally absent over the IFA, and the GMS brightness temperature was relatively high (Figure 5.9c). Both the surface wind speed and latent heat flux dramatically decreased to their values of the undisturbed phase. SSTs, after reaching a minimum (about 28.8°C) around 5 January, started to recover. Some disorganized isolated cumuli (about 5–15 km in horizontal) again appeared on MIT radar scans (TCIPO TOGA COARE Summary 1993). Moderate heating/drying occasionally occurred with cooling and moistening dominating at other times. The 19 January case was another strong convective event. However, the synoptic situation was quite different from the 21–25 December event. Easterly flow prevailed at low levels from near the date line westward to the IFA, and convection over the IFA arrived from the east with the easterly surge. Heating and drying dominated the entire troposphere with peaks at the middle and upper levels. Within a few days after the deep convective case, cooling/moistening dominated middle and lower levels, presumably due to evaporation of stratiform precipitation. SSTs decreased as the convection intensified, then recovered later. Toward late January, the surface wind gradually strengthened as another westerly wind burst approached. Surface latent heat flux increased while SSTs gradually decreased.

February was a month with much chaotic convection over the IFA (Figure 5.9d). The convection was suppressed between 1 and 8 February, when lower levels were again dominated by strong westerly flow. In middle and late February, westerly flows, although weaker

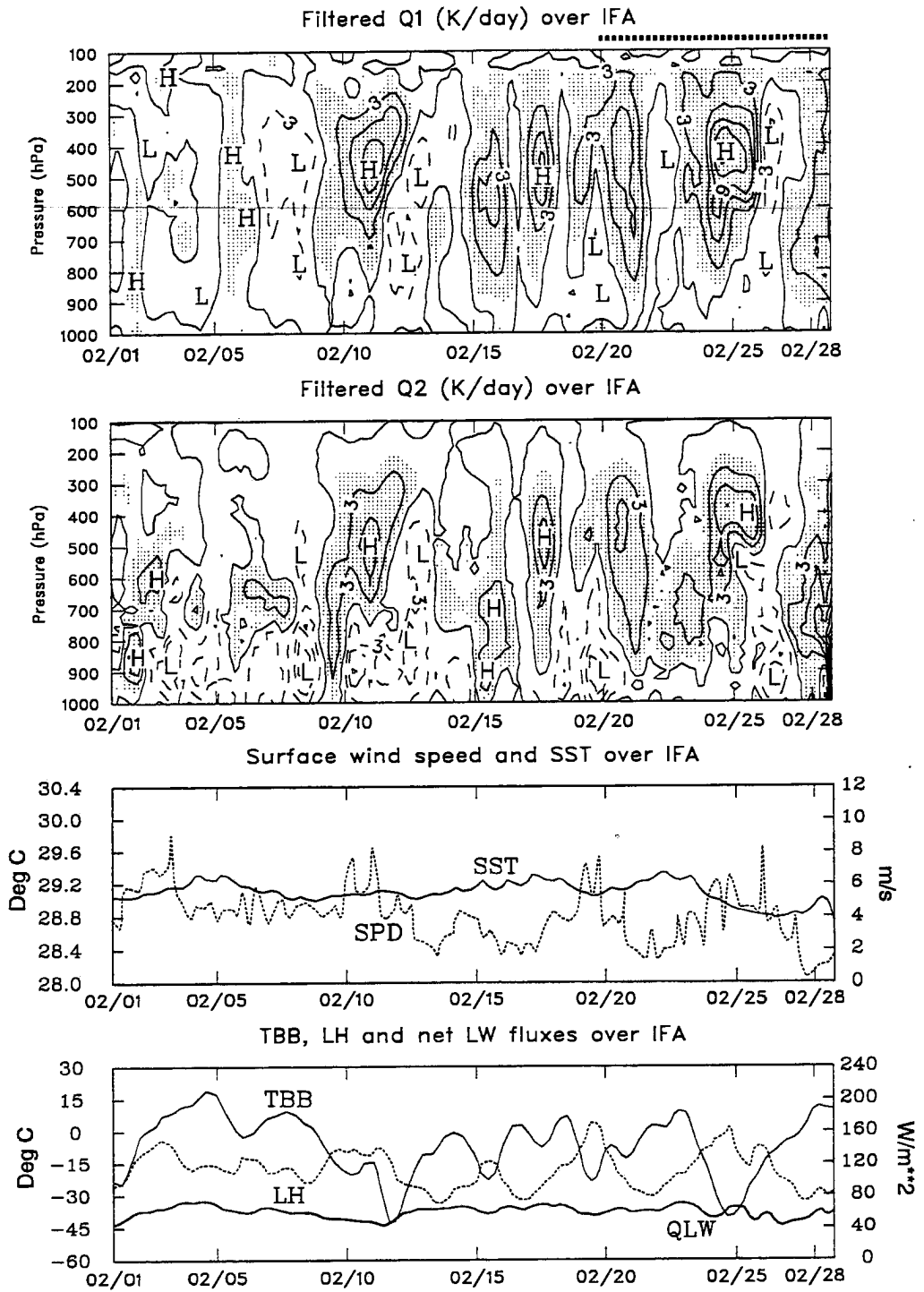


Figure 5.9: Continued.

than those in early February, still dominated levels below 500 hPa (Figure 5.5). Quite a few large  $Q_1$  peaks were located in the middle and upper troposphere with weak cooling at lower levels, probably induced by mesoscale downdrafts. Large  $Q_2$  peaks were also located at middle and upper levels, similar to the altitudes of  $Q_1$  peaks, indicating that stratiform clouds dominated the IFA during this period. The most interesting feature is at lower levels where  $Q_2$  shows strong moistening below about 700 hPa throughout almost the entire month. This moistening could be a consequence of precipitation evaporation and/or evaporation by shallow cumuli (Nitta and Esbensen 1974). SSTs varied little in February due to convection intermittency.

#### 5.4.2 Mean profiles

In order to examine the representative heating profiles over the western Pacific warm pool, Figure 5.10 compares the normalized  $Q_1$  over the IFA, the OSA, the Marshall Islands (Yanai et al. 1973), and the GATE region (Thompson et al. 1979). All profiles represent composites of many tropical convective systems. The IFA was mainly located in the minimum rainfall band along the equator while the OSA included the minimum rainfall band along the equator and the double ITCZ to the north and south of the equator. The other two profiles are from the ITCZ bands over the western Pacific and eastern Atlantic, respectively. The heating profiles over the western Pacific, although from regions with distinctly different characteristics, are surprisingly similar to one another. Their peaks are located between 400 and 450 hPa. The curve from the eastern Atlantic ITCZ has a lower heating peak located at about 600 hPa, which Thompson et al. (1979) attribute to the different cloud population and lower SSTs in the GATE region.

Houze (1982) assessed atmospheric net heating produced by a mature tropical cloud cluster. In total, the convective and stratiform clouds enhance heating of the middle and upper troposphere by latent heating within convective and mesoscale updrafts; weak warming or cooling at low levels results from the balance between latent heating in the convective region and evaporative cooling within mesoscale downdrafts. The heating profile is distinctly different from the one produced by convective clouds alone, in which latent heating

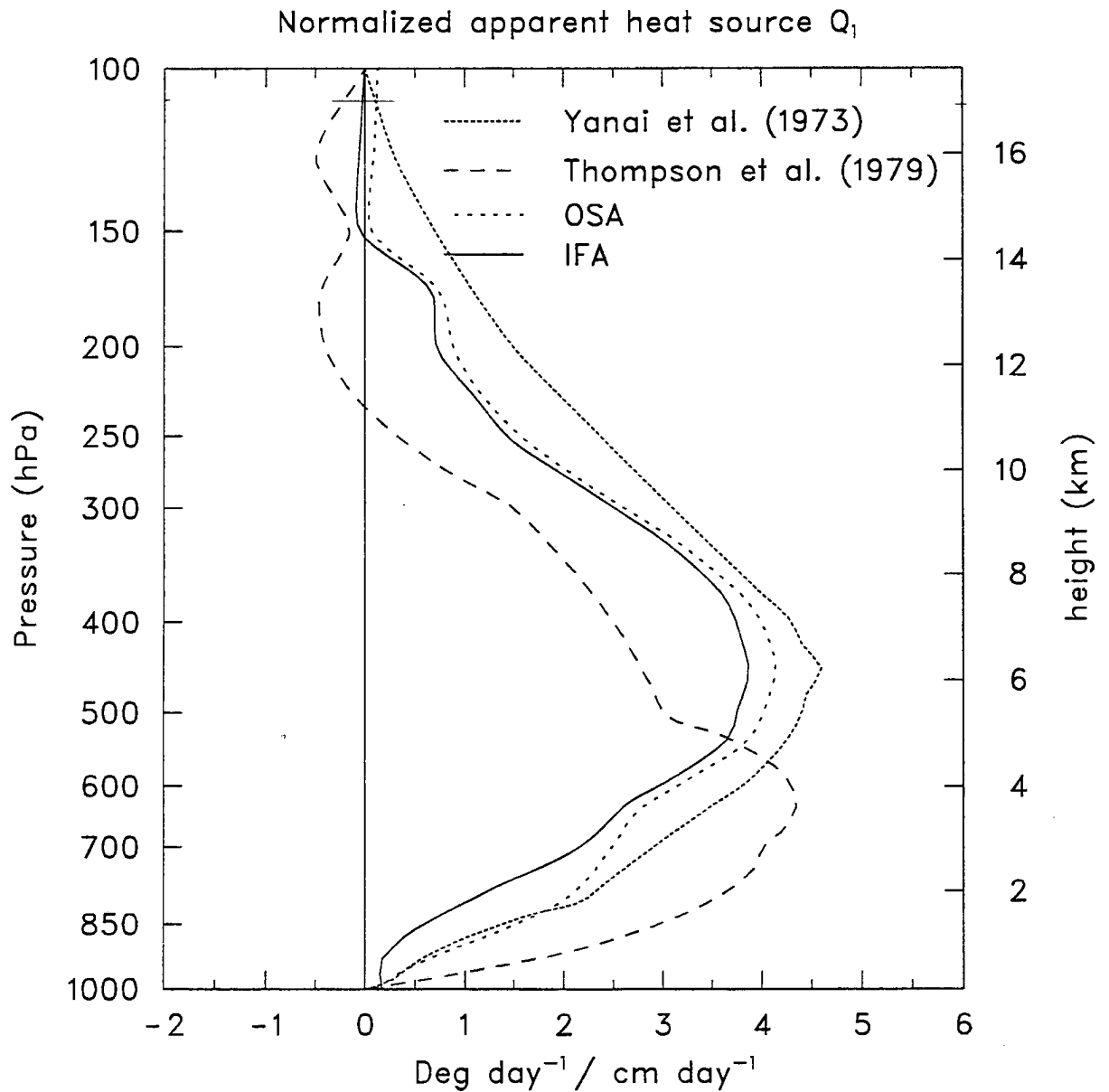


Figure 5.10: Comparison of rainfall-normalized apparent heat source  $Q_1$  (in units of  $\text{K day}^{-1}/1 \text{ cm day}^{-1}$ ) from the IFA, the OSA, the Marshall Islands region (Yanai et al. 1973) and the GATE region (Thompson et al. 1979).

dominates throughout the troposphere. Hartmann et al. (1984) investigated the sensitivity of simulated tropical east-west circulations using a conventional profile for the convective region and one from a mature cloud cluster (given by Houze 1982). They suggest that the mature cloud cluster heating profile may provide the appropriate vertical distribution of tropical diabatic heating in many cases. Although this might be the case for individual large mesoscale convective systems (MCSs) that may last at most a few days, the results here suggest that *the long-term mean heating profiles over the western Pacific warm pool have large positive contributions at all levels of the troposphere, implying that contributions from shallow cumuli are important.* The frequent presence of shallow cumulus clouds over the warm pool warms the low levels by condensational heating, which appears to offset the cooling contribution of the stratiform region at low levels.

Although the heating profiles over different regions of the western Pacific warm pool are similar to one another, the drying/moistening profiles are significantly different. Figure 5.11 shows the rainfall-normalized IOP-mean  $Q_2$  over the IFA and the OSA with the ITCZ profiles from Yanai et al. (1973) and Thompson et al. (1979). The curve from Yanai et al. (1973) indicates a double-peak structure with a drying minimum near 600 hPa. The lower peak is at about 700 hPa while the higher peak is about 500 hPa. Johnson (1984) proposed that the double-peak structure is a result of the combination of two distinctly different drying processes. He suggested that the lower peak is a result of cumulus updrafts in the convective region, while the higher one comes from the mesoscale updrafts within anvil clouds. The profile over the OSA also indicates a double-peak structure. However, the magnitude is about half of that from Yanai et al. (1973), and the lower drying peak is between 800 and 850 hPa. The most striking difference is in the curve for the IFA, which indicates strong moistening below 850 hPa with a peak near 950 hPa. This moistening is probably due to strong evaporation and upward transport of moisture by shallow cumuli during high winds, as was observed in the trade wind zones (Nitta and Esbensen 1974).

Figure 5.12 illustrates the IOP-mean pressure-latitude cross sections of  $Q_1$  and  $Q_2$  averaged between 150°E and 160°E, where sounding stations were dense during the COARE IOP. The double ITCZ can be clearly identified, as has been found in Lin and Johnson

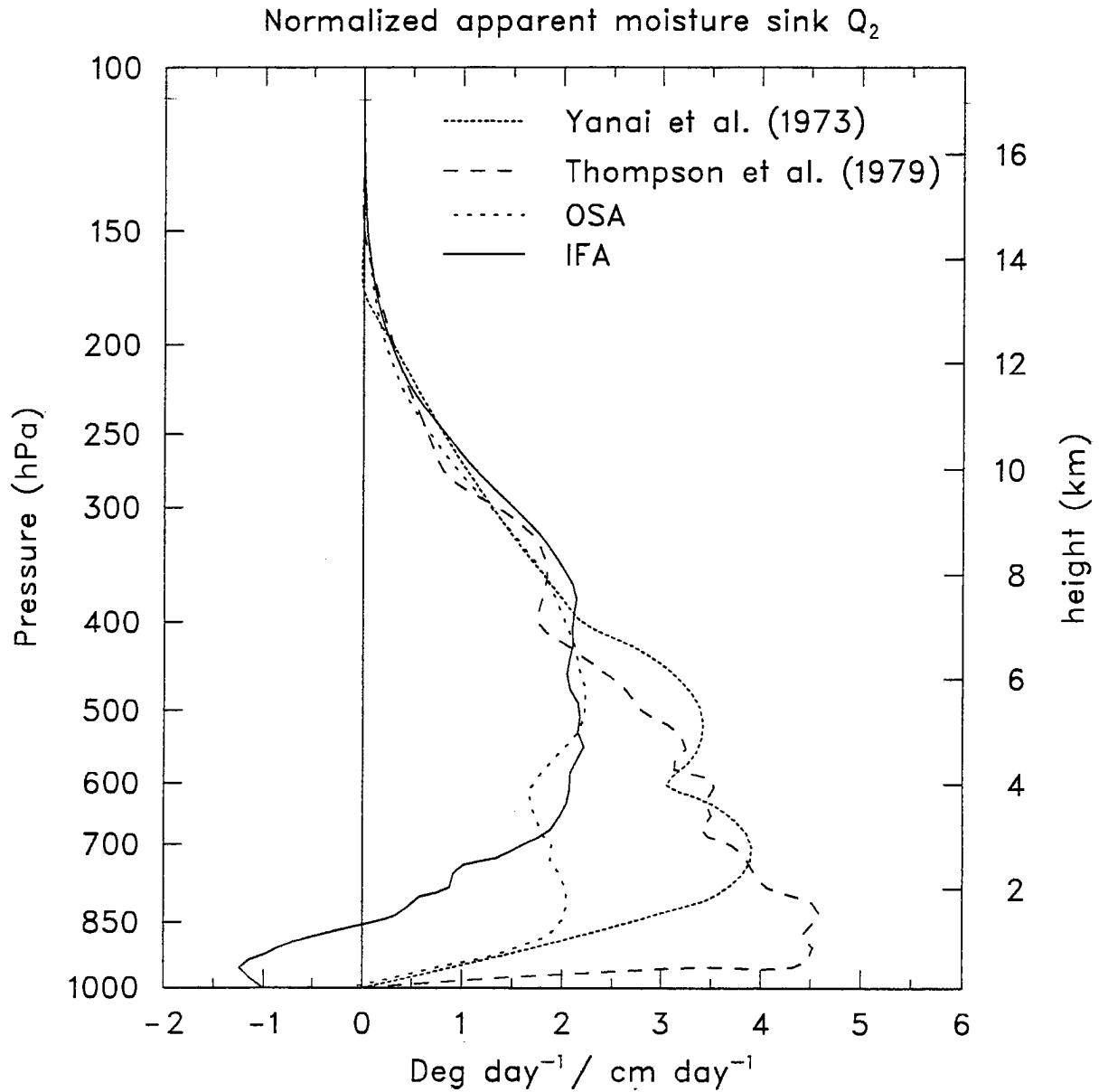


Figure 5.11: Comparison of rainfall-normalized apparent heat source  $Q_2$  (in units of  $\text{K day}^{-1} / 1 \text{ cm day}^{-1}$ ) from the IFA, the OSA, the Marshall Islands region (Yanai et al. 1973) and the GATE region (Thompson et al. 1979).

(1996a). The convergence zone over the Northern Hemisphere was located between  $2^{\circ}\text{N}$  and  $5^{\circ}\text{N}$ ; the heating peaked (more than  $4\text{ K day}^{-1}$ ) between 350 and 600 hPa (Fig. 5.12a). A secondary heating maximum was located around 700 and 850 hPa, suggesting a different cloud population. The  $Q_2$  peak (Figure 5.12b) was generally located around 850 hPa, much lower than the primary  $Q_1$  peak, indicating the dominance of the convective component north of the equator. The convergence zone over the Southern Hemisphere was located between  $8^{\circ}\text{S}$  and  $5^{\circ}\text{S}$  and produced a different pattern of  $Q_2$  profiles. Both the heating and drying peaks were located between 400 and 500 hPa, suggesting more stratiform precipitation over the Southern Hemisphere convergence zone. The IFA was located between the two convergence zones and the heating rate was much weaker, with the heating maximum located around 350 and 450 hPa. In contrast, the IOP-mean profile of  $Q_2$  between the ITCZ bands near the equator, while exhibiting drying aloft, shows moistening below 850 hPa between  $1^{\circ}\text{N}$  and  $4^{\circ}\text{S}$ . Time series of  $Q_2$  (Figure 5.9) show that this moistening occurred primarily during the westerly wind bursts, presumably as a result of strong evaporation and upward transport of moisture by shallow cumuli.

## 5.5 Summary and discussions

In this chapter, rawinsonde, surface and satellite data collected from the 4-month TOGA COARE IOP have been used to investigate the distributions of heating, moistening, rainfall, and evaporation over the western Pacific warm pool. Three westerly wind bursts were observed during the COARE IOP, with the most prominent one peaking around 1 January. Convective heating and moistening were strongly modulated by the tropospheric vertical wind shear associated with tropical low-frequency oscillations. Heavy precipitation usually fell 1 to 3 weeks prior to the peak westerly wind bursts. Deep convection was generally suppressed over the IFA during peak westerly winds.

Comparison of surface latent heat fluxes suggests coherence over a relatively large area on time scales of a day or longer. Surface latent heat flux was positively correlated with surface wind speed and varied between  $50$  and  $100\text{ W m}^{-2}$  during light winds to more than  $200\text{ W m}^{-2}$  during strong westerly wind bursts. In order to obtain evaporation

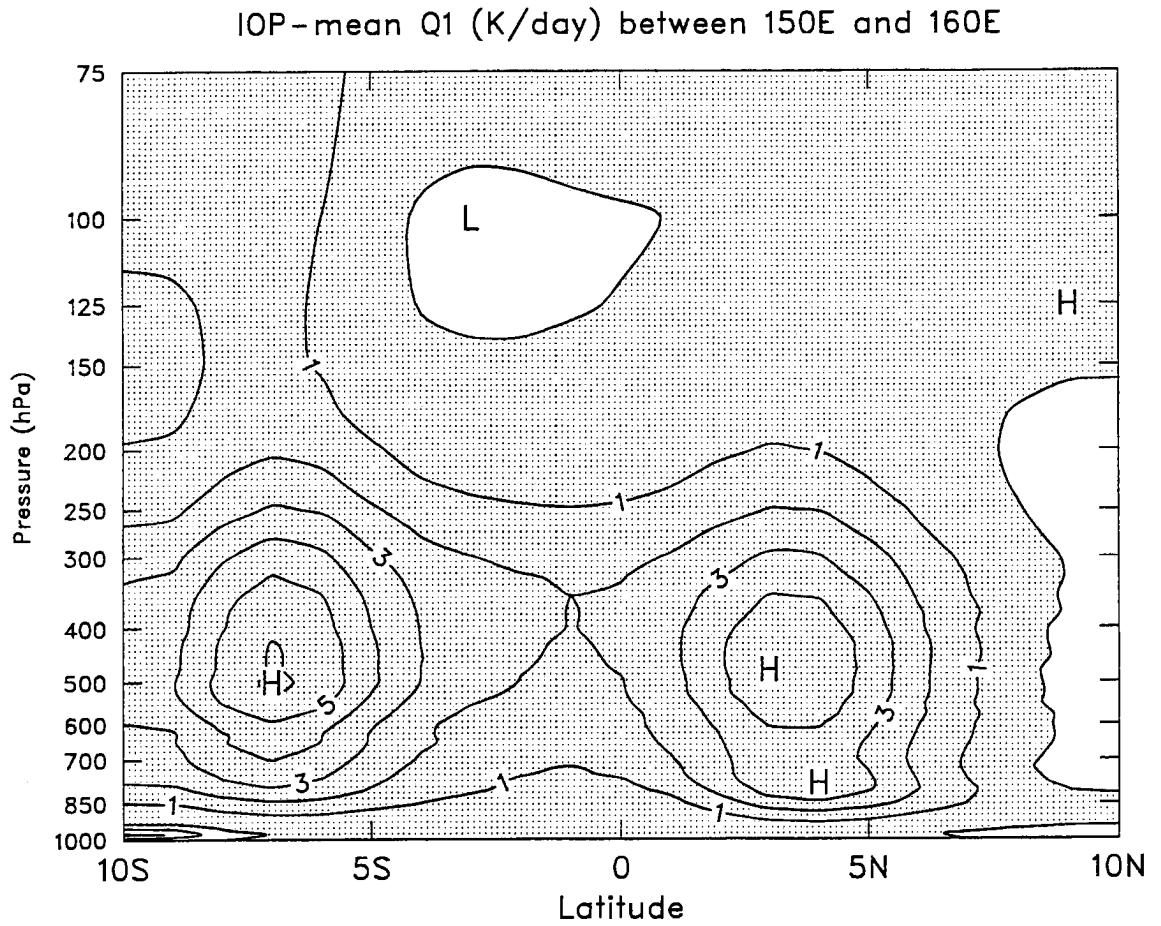


Figure 5.12: North-south cross sections of (a)  $Q_1$  and (b)  $Q_2$  (K day<sup>-1</sup>) between 150°E and 160°E. Contour intervals are 1 K day<sup>-1</sup> and areas with positive values are shaded.

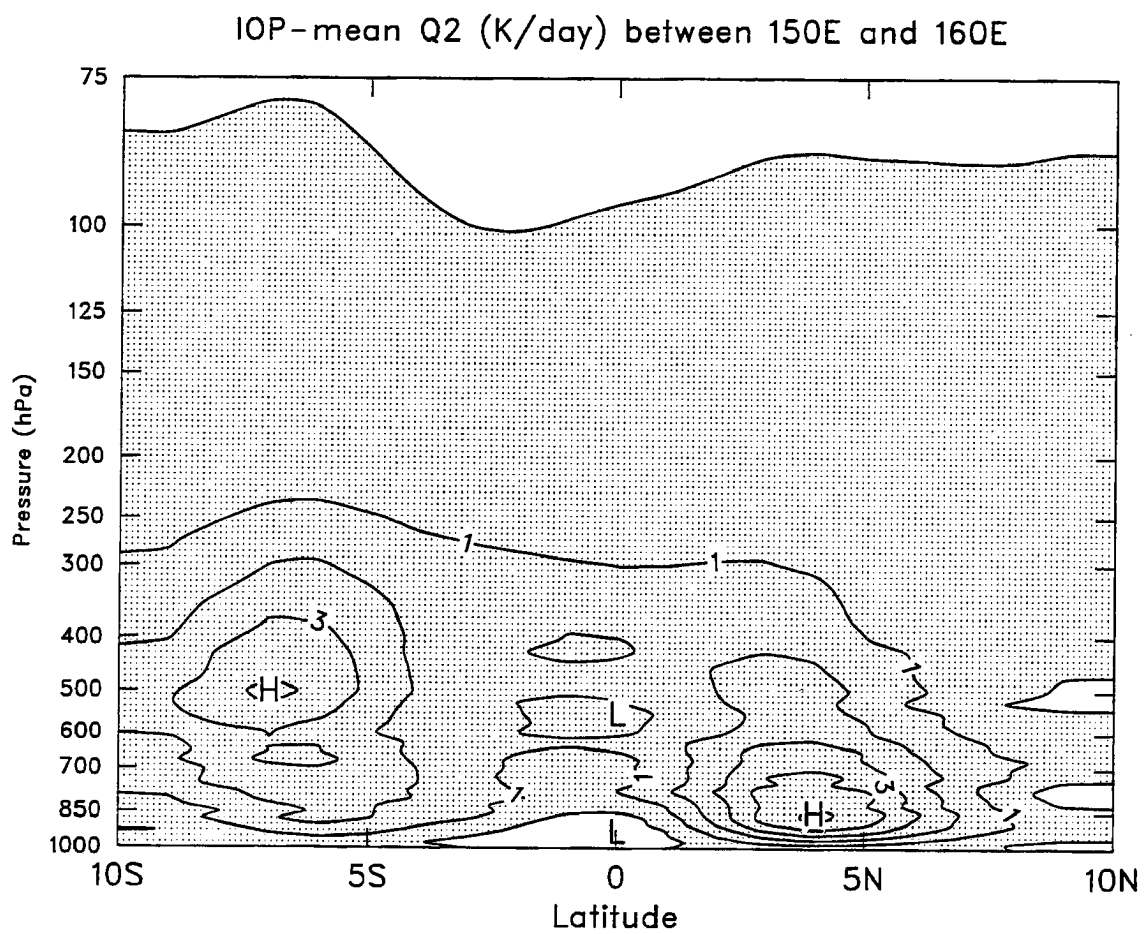


Figure 5.12: Continued.

estimates over the LSA to use in moisture-budget computations of precipitation, we adjusted ECMWF evaporation fields for the LSA based on intercomparisons between buoy estimates and ECMWF values over the IFA. The ECMWF-adjusted IOP-mean latent heat fluxes over the LSA show a minimum evaporation band along the equator in association with weak equatorial surface winds. Evaporation gradually increased to the north and south, associated with enhanced northeast and southeast trades.

Surface sensible heat fluxes estimated from buoys and ships does not follow the pattern of surface wind speed, whereas ECMWF fluxes do. Peak values from buoys and ships were normally observed when deep convective systems were present occurring over the IFA, suggesting convective and mesoscale downdrafts are the main factors in enhancing the change of surface sensible heat flux (also see Saxen 1996). The ECMWF-adjusted IOP-mean sensible heat flux exhibits two maximum bands to the north and south of the equator, appropriately coinciding with a double ITCZ in the western Pacific.

The  $Q_2$  budget-determined IOP-mean rainfall distribution over the LSA is compared with two satellite remote sensing results SSM/I retrievals and GPI, and with the ECMWF model forecasts. All four methods indicate an east-west zone with minimum rainfall along the equator. Two heavy rainfall bands, coinciding with the double ITCZ, were located to the north and south of the equator. The IFA was mainly located within the minimum rainfall band near the equator. During the COARE IOP, heavy precipitation, high clouds, and the positive SST anomalies were all located near the date line, and decreased toward the west. Although the four methods produced similar large-scale rainfall patterns over the tropical western Pacific, the ECMWF and GPI rainfalls in general are about 3 to 6  $\text{mm day}^{-1}$  higher than those from the  $Q_2$  budget estimation and SSM/I measurements. Comparison of time series of the IFA-mean rainfall rate indicates that the budget-derived rainfall rate and SSM/I retrievals are in close agreement—the IOP-mean values both being  $5.6 \text{ mm day}^{-1}$ . GPI usually overestimated the rainfall rate due to the frequent occurrence of non-precipitating cirri over the western Pacific warm pool. The ECMWF time series does not match the other rainfall estimates owing to the incomplete ingestion of COARE sounding data into the operational analyses.

Large-scale westerly wind bursts associated with the ISOs significantly modulated convection, surface fluxes, and SSTs. The December-January event was well captured by the COARE sounding network and may serve as a typical example to study the air-sea interaction over the warm pool. About 25 to 45 days prior to the peak westerly wind burst around 1 January, deep convection was generally suppressed and shallow cumuli were frequently present over the IFA. SSTs gradually increased due to strong absorption of solar radiation and less evaporation and ocean mixing in association with light surface winds, providing a favorable environment for deep convection to occur later. Middle-level clouds, as inferred from the heat and moisture budgets, gradually developed after the undisturbed period, as weak westerly winds appeared near the surface. The dynamical control of organized convection by tropospheric vertical wind shear (Ludlam 1980; Moncrieff and Klinker 1996) can be clearly observed. Low-level westerlies eventually strengthened and deep convection occurred over the IFA about 15 days prior to the peak westerly wind burst. A large separation of  $Q_1$  and  $Q_2$  peaks at this time suggests a dominance of deep convection (e.g., Luo and Yanai 1984). As the low-level westerlies intensified and the vertical wind shear increased, budget results indicate that convective systems with a greater stratiform component occurred over the IFA as evidenced by the juxtaposition of  $Q_1$  and  $Q_2$  maxima. Rainrate analyses from MIT Doppler radar (Rickenbach and Rutledge 1996a) also support our budget findings. The  $Q_2$  profiles exhibit a double-peak structure, as has been found elsewhere in the western Pacific (e.g., Yanai et al. 1973). Both the surface wind speed and latent heat flux dramatically increased after the heaviest rainfall. SSTs continued to drop due to large loss of heat by evaporation and ocean mixing. During this period of strong vertical wind shear, lower levels cooled and moistened with warming and drying in middle and upper troposphere, similar to what happens in the presence of stratiform clouds (Houze 1982; Johnson and Young 1983). During the peak westerlies, deep convection was generally suppressed and strong moistening occurred at middle and lower levels.

During the COARE IOP, locations east of the ISO-related deep convection were usually characterized by higher SSTs, weaker surface winds, and lower surface heat fluxes than those to the west (Lin and Johnson 1996b). Observations from the Central Equatorial

Pacific Experiment (CEPEX) indicate similar results (Flatau et al. 1996). This evidence is in contrast with the wind induced surface heat exchange (WISHE) mechanism (Emanuel 1987; Neelin et al. 1987; Yano and Emanuel 1991) which is used to explain the maintenance and eastward propagation of the ISOs.

The IFA was mainly located within a minimum rainfall band along the equator while the OSA included the minimum rainfall band and two ITCZ heavy-rainfall bands. The magnitudes and altitudes of heating peaks of the rainfall-normalized  $Q_1$  profiles over the IFA and OSA are very similar to the one derived over a tropical western Pacific ITCZ band (Yanai et al. 1973), suggesting these profiles are representative of long-term mean heating rates over the western Pacific warm pool. In contrast, the  $Q_2$  profiles are distinctly different over these compared regions. The profile over the ITCZ band (Yanai et al. 1973) exhibits drying throughout the entire troposphere with a double-peak structure. Near the equator, however, low-level moistening (below 1.5 km) is evident in the profile averaged over the IFA, probably due to strong evaporational moistening and upward transport of moisture by shallow cumuli during high winds.

Mesoscale convection and the organizing effect of wind shear on cloud elements are not properly resolved or parameterized in general circulation models (Moncrieff and Klinker 1995). Convective organization and oceanic response associated with the ISOs are still not well understood. The cloud resolving model (CRM) is valuable in estimating the statistical properties of cumuli (e.g. Soong and Ogura 1980; Soong and Tao 1980; Krueger 1988; Xu et al. 1992) and evaluating the interaction between mesoscale convection and surface fluxes (Jabouille et al. 1996; Trier et al. 1996). The observed and diagnosed surface and upper air data not only provide the time-evolving large-scale forcings (i.e., the large-scale advective tendencies of temperature and moisture, and varying SSTs), but also serve as the verification for the CRM (Grabowski et al. 1996; Xu and Randall 1996). The TOGA COARE data, with much more detailed long-term information of surface fluxes and SSTs at various scales, and of different large-scale environmental conditions in connection with the ISOs, are expected to yield more fruitful results.

## Chapter 6

### DIURNAL VARIATION IN CONVECTION

#### 6.1 Introduction

Numerous observations have indicated that the strongest convection over summer continents occurs in the late afternoon or early evening due to dominant daytime boundary layer heating except in regions where land-sea contrast and/or orographic forcings are strong (Wallace 1975). Over tropical oceans far from continents, although the diurnal variations are ultimately induced by daily-varying solar warming/longwave cooling of the ocean and the atmosphere, they are further complicated by large-scale forcings, radiation-cloud interactions, and air-sea interactions.

Gray and Jacobson (1977) noticed a large diurnal cycle of oceanic, tropical, deep cumulus convection: The more intense the deep convection and the more it is associated with organized weather disturbances, the more likely a morning maximum appears in the diurnal cycle. Many later observations over tropical oceans based on rawinsonde and satellite data support their findings (Foltz and Gray 1979; McBride and Gray 1980; Murakami 1983; Mapes and Houze 1993; Chen and Houze 1996). Gray and Jacobson (1977) hypothesized that this diurnal cycle likely resulted from day-versus-night variations in tropospheric radiational cooling between the weather system and its surrounding cloud-free region (referred to as radiation-dynamics-convection interactions by Randall et al. 1991). The atmosphere has to compensate longwave radiative cooling by large-scale subsidence warming. The cloudy, convectively active region would experience less radiative cooling (thus less downward motion) during the night than the surrounding cloud-free region. Therefore deep convection is more likely to be enhanced during the night where there is pre-existing convection, and

suppressed over the cloud-free region. The difference of the net heating profiles between weather disturbances and their surrounding cloud-free region becomes smaller during the day due to shortwave heating so that the strongest deep convection usually occurs in early morning. The horizontal gradient of radiative cooling between cloudy and cloud-free regions is considered to be the dominant mechanism for driving the diurnal cycle.

Randall et al. (1991) investigated diurnal variability of the hydrologic cycle in a general circulation model (GCM). Their results indicated that an oceanic diurnal cycle of precipitation occurred in the absence of neighboring continents and tended to have a morning maximum. When the radiative effects of clouds were omitted, the simulated diurnal cycle of precipitation was much weaker. Their GCM simulations showed that the stabilization due to absorption of solar radiation by clouds would tend to suppress convection during the afternoon, relative to the period before sunrise, to such an extent that the direct radiation-convection interactions alone can account qualitatively for the observed diurnal cycle of precipitation over oceans. The vertical gradient of radiative heating/cooling is considered as the dominant mechanism for driving the diurnal cycle.

The above two mechanisms on atmospheric diurnal variability assume a pre-existence of large-scale weather disturbances, so that the cloud radiative forcings can take effect. Over the western Pacific warm pool, we could observe not only frequent large-scale weather disturbances, but also many clear-sky situations with only scattered shallow cumulus clouds, especially outside of the ITCZ bands. However, the diurnal variability of the ocean and the atmosphere associated with these clear-sky scattered-cloud situations has rarely been documented in previous studies due to sparse observations and weak signals. Regional and periodic diurnal cycle in convection can be distinctly different due to the roles played by different interaction mechanisms and large-scale forcings (Albright et al. 1985).

Figure 6.1 shows time series of a few surface variables measured at the IMET buoy during COARE IOP (taken from Weller and Anderson 1996). Strong diurnal variability in SST, apparently due to clear sky and light wind conditions, can be observed about 1-3 weeks before the ISO-related heavy precipitation. Frequent shallow cumulus clouds and cumulus congestus could be observed in the afternoon during the undisturbed period

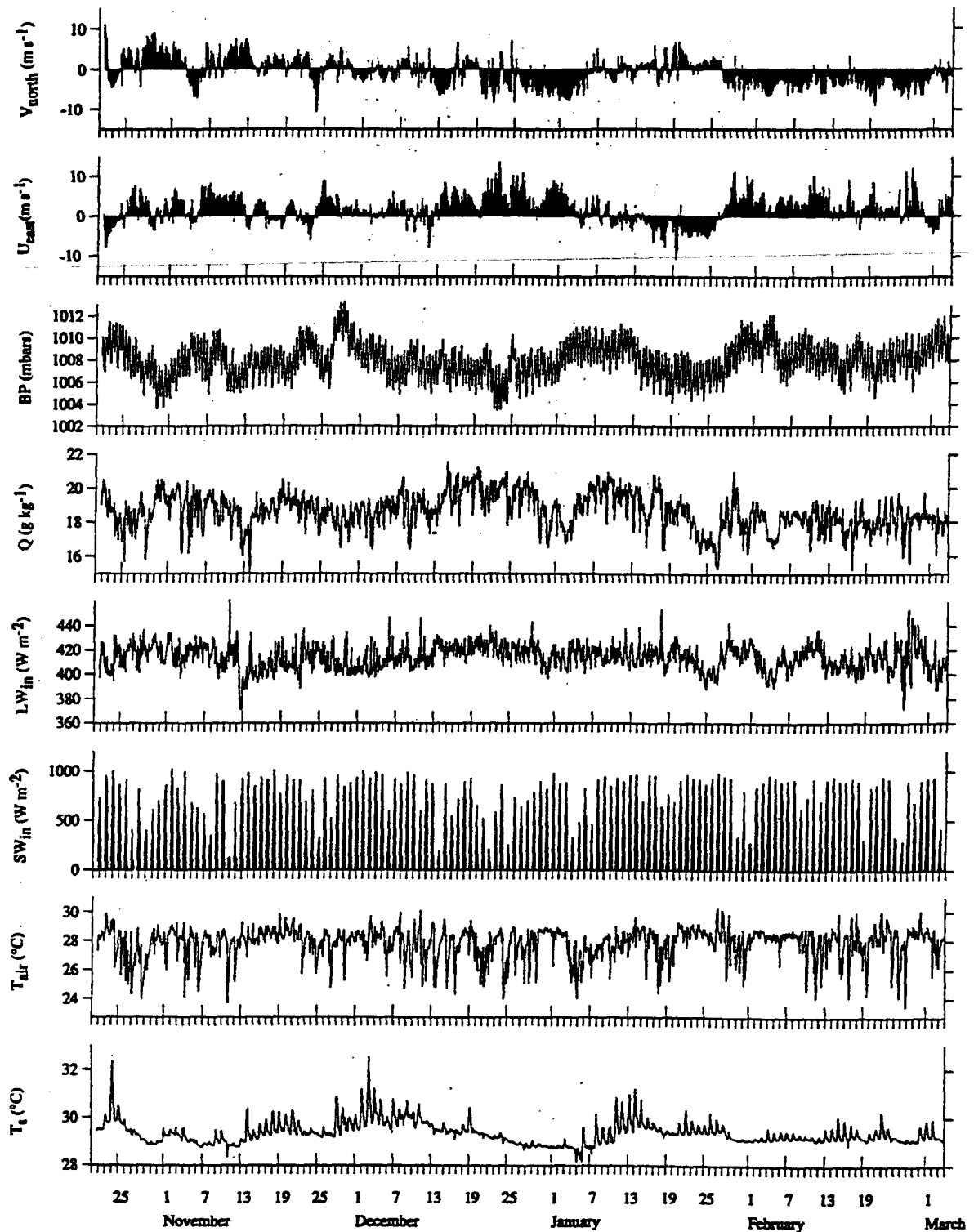


Figure 6.1: Time series of near-surface meteorological observables measured at the WHOI buoy (taken from Weller and Anderson 1996). Two-hour averages of, from top to bottom, the wind component toward the north, the wind component toward the east, barometric pressure, specific humidity, incoming longwave radiation, incoming shortwave radiation, air temperature, and sea surface temperature (0.45 m depth).

(TCIPO TOGA COARE Operations Summary 1993). The diurnal signals were greatly diminished during the periods of high winds and/or heavy precipitation. From the viewpoint of an oceanographer, a diurnal cycle at the sea surface occurs when solar heating warms and stabilizes the upper ocean, thus limiting the downward penetration of turbulent wind mixing (Price et al. 1986). This stability competes with surface winds which tend to increase downward turbulent mixing and surface evaporation. If surface winds are light under clear sky, a thin layer of warm water usually forms near the surface, and skin SSTs tend to closely follow the diurnal cycle of the sun (Lukas and Webster 1992). Warmer ocean surface in the afternoon increases the atmospheric convective instability, providing a favorable environment for cumulus clouds to develop. During the disturbed periods, downdrafts and gust fronts from organized convection usually cool the ocean surface by strong mixing and upward heat transfer, thus surface diurnal variability is suppressed. Table 6.1 shows some characteristics of the ocean and the atmosphere during undisturbed and disturbed periods.

	the undisturbed period	the disturbed period
weather conditions	clear sky, light winds	cloudy sky, strong winds
vertical wind shear	weak	moderate to strong
large-scale forcing (advection)	weak	moderate to strong
cloud radiative forcing	weak	moderate to strong
diurnal variabilities at the surface	large	small
downward turbulent mixing	small	large
surface evaporation	moderate	large

Table 6.1: Some characteristics of the ocean and the atmosphere during undisturbed and disturbed periods.

Although some efforts have been made to investigate possible roles of SSTs and surface heat fluxes on diurnal variabilities of convection (e.g., Ostapoff and Worthem 1974; Greenhut 1978; Price et al. 1986), there are few systematic studies to quantitatively document the interactive diurnal nature of the ocean surface and overlying atmosphere for both disturbed and undisturbed conditions. Some recent cloud modeling studies have been trying to understand roles of vertical wind shear, large-scale forcings, cloud-radiative effect, and

microphysics on diurnal convective variability (e.g., Sui et al. 1997; Liu and Moncrieff 1997). It is important to compare modeling results in some way with observations.

The objective of this chapter is to separate the entire COARE IOP into several different phases of the ISOs, and quantitatively document the diurnal variability of the ocean surface and the atmosphere during (1) clear-sky, light-wind, (2) cloudy-sky, strong-wind conditions. Observational data were available in GATE; however, diurnal variability in the eastern Atlantic is significantly affected by the African continent. Therefore the COARE data represent a first real chance to get at the diurnal cycle over the open ocean, presumably far enough away from land masses to avoid contamination by them.

In this study, gridded dataset computed from corrected rawinsonde data released by NCAR were used (see Lin and Johnson 1996a for detailed information). In order to better resolve low-level features, wind measurements from ISS wind profilers were also merged into the COARE rawinsonde data (Ciesielski et al. 1996). GMS brightness temperature data, IMET buoy data, and MIT Doppler radar data were used to supplement the analysis.

## 6.2 Clear-sky, light-wind conditions

Figure 6.2 shows the unfiltered time series (at 6-h intervals) of  $Q_1$ ,  $Q_2$ , 1000 hPa wind speed, and  $T_{BB}$  over the IFA, along with SST and latent heat flux measured at the IMET buoy between 11 November and 10 December. This period is also coincident with the first cruise of R/V Vickers when MIT radar rainrate estimation is available. The most significant feature is the prominent diurnal variability in SST between 14 and 22 November, and between 28 November and 5 December (indicated by dotted lines). As shown in Chapters 4 and 5, these two periods were generally characterized by very weak surface winds (less than  $2 \text{ m s}^{-1}$ ), and surface latent heat fluxes remained around  $80 \text{ W m}^{-2}$ . Except for two individual convective cases around 24 and 27 November, the GMS brightness temperatures over the IFA were relatively high and remained nearly constant around  $15 \text{ }^\circ\text{C}$ , suggesting frequent clear skies.  $Q_1$  and  $Q_2$  profiles generally showed weak heating/cooling and drying/moistening throughout the troposphere. Due to the light winds and absent deep convection, we also define this period as the undisturbed phase of the

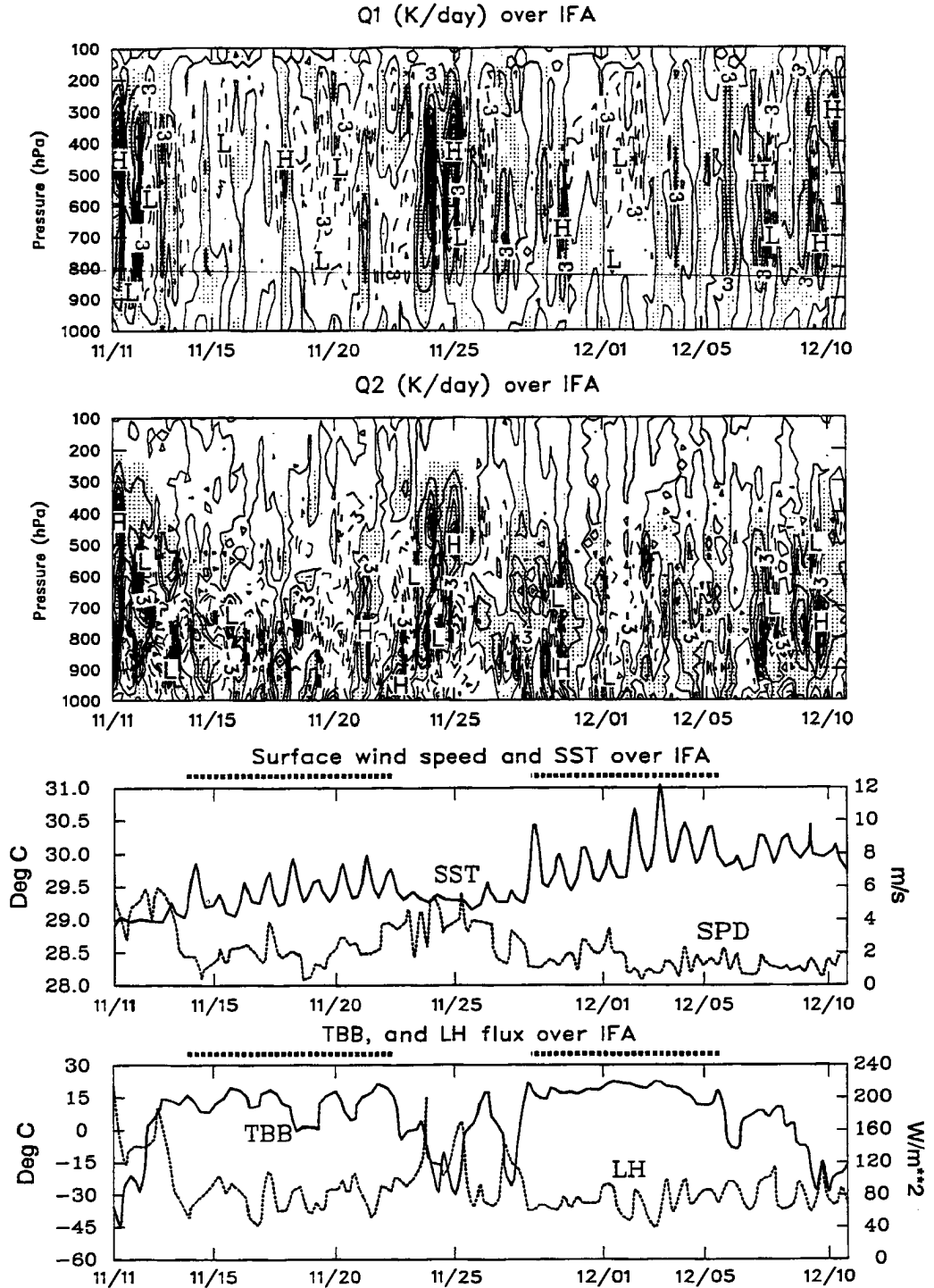


Figure 6.2: Time series of unfiltered apparent heat source  $Q_1$  ( $\text{K day}^{-1}$ ), the apparent moisture source  $Q_2$  ( $\text{K day}^{-1}$ ), 1000 hPa wind speed ( $\text{m s}^{-1}$ ), GMS brightness temperature (Deg C) over the IFA, along with SST (Deg C) and surface latent heat fluxes ( $\text{W m}^{-2}$ ) from the IMET buoy between 11 November and 10 December, 1992. The contour intervals for  $Q_1$  and  $Q_2$  are  $3 \text{ K day}^{-1}$  and areas  $> 1.0 \text{ K day}^{-1}$  are shaded. Dotted lines above the SST figure indicate periods during the COARE IOP when the clear-sky, light-wind condition prevailed.

ISO, and locally it would have minimum contributions from the cloud-radiative effect and large-scale advection.

Rickenbach and Rutledge (1996a) categorized observed precipitating events during the COARE IOP into four groups based on MIT radar data: (1) sub-MCS non-linear; (2) sub-MCS linear; (3) MCS linear; (4) MCS non-linear. They found that although most of the rainfall was associated with MCS scale systems, sub-MCS scale convection was the most common and produced a significant portion of the total rainfall. Figure 6.3a shows time series of total and non-convective rainrates (in  $\text{mm day}^{-1}$ ) for cruise 1 (Figure 6a in Rickenbach and Rutledge 1996a). The time intervals when events of each type were present are also shown. Time series of radar-derived total rainrates coincides very well with time series of  $Q_1$  and  $Q_2$  profiles from large-scale sounding data, indicating consistency of the data between two different observing platforms. During the two periods when SSTs showed a pronounced diurnal variability, rainrates were generally very low. Precipitating events were dominated by sub-MCS non-linear systems, and most of the rainfall was convective.

Fig. 6.3b illustrates an example of the sub-MCS non-linear system (from TCIP TOGA COARE Operations Summary 1993). It is typically with an MLO (maximum level of organization) spatial scale  $\leq 100$  km, and does not display linear organization (Rickenbach and Rutledge 1996a). During COARE IOP, it was usually characterized by a field of popcorn-type isolated convective cells or small groups of cells. Rickenbach and Rutledge (1996a) found that these sub-MCS non-linear systems were present over the IFA for more than 50% of the time and contributed to more than 10% of the total rain volume.

Diurnal variations (at 1-h intervals) in surface latent and sensible heat fluxes, SST, and surface air temperature under the clear-sky, light-wind condition (for periods between 14 and 22 November, and between 28 November and 5 December) are shown in Figure 6.4. The averaged SST usually reached its peak at 14 LST, and was about  $1.0^\circ\text{C}$  higher during the noon hours than the minimum at 06 LST. On individual days, the SST difference between the day and night could be more than  $2^\circ\text{C}$ . Surface latent heat flux was often about 20 to  $30 \text{ W m}^{-2}$  higher in the early afternoon than that during the night. Both surface air temperature and surface sensible heat flux appeared to follow a similar solar heating

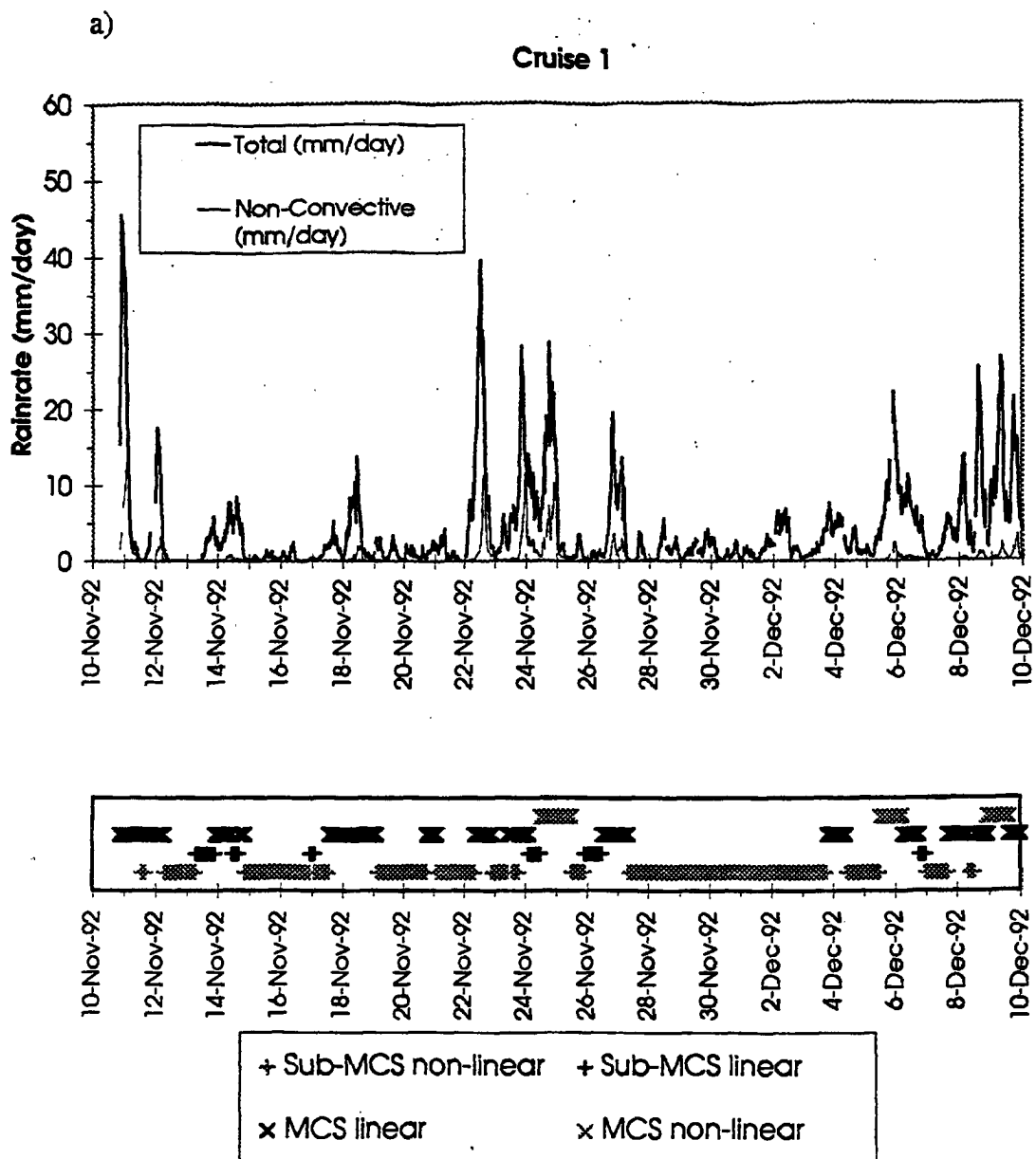


Figure 6.3: (a) Time series of total rainrate (think solid line) and non-convective rainrate (thin solid line) in  $\text{mm day}^{-1}$  for Cruise 1 (taken from Rickenbach and Rutledge 1996a). The time intervals when events of each types were present are also shown.

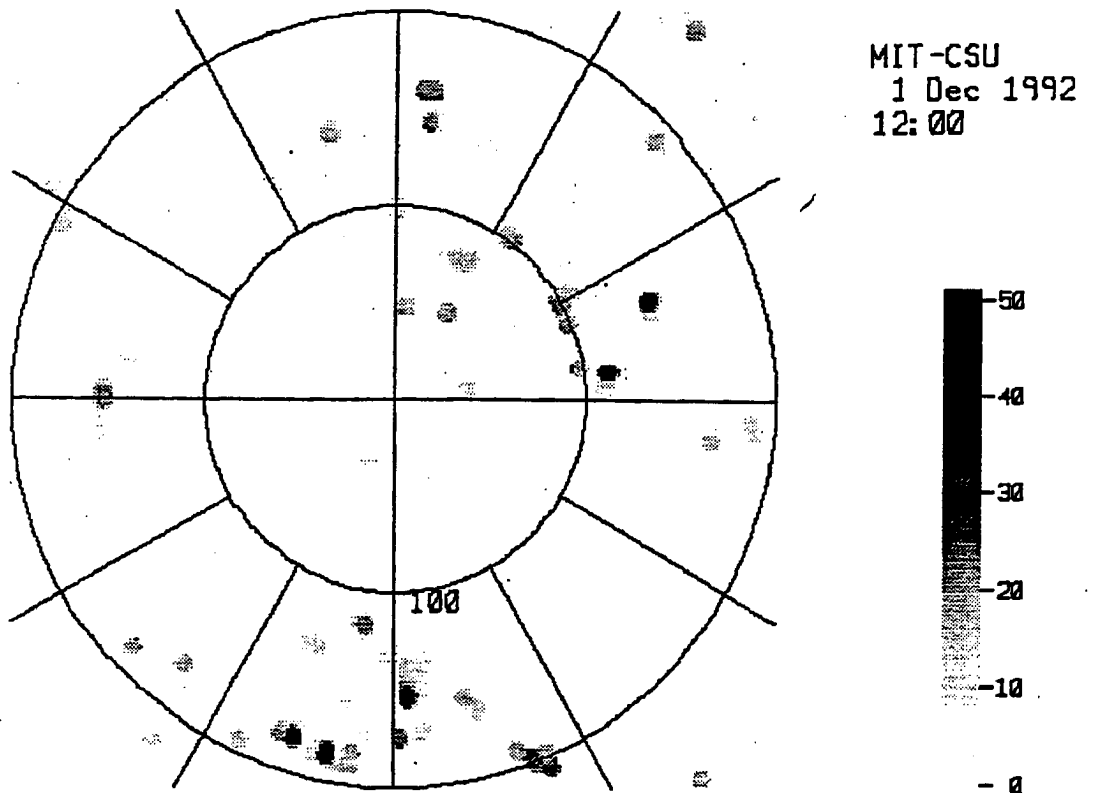


Figure 6.3: Continued. (b) A radar reflectivity map at a height of 2 km for a sub-MCS scale non-linear event on 1 December 1992 (from TCIPO TOGA COARE Operations Summary).

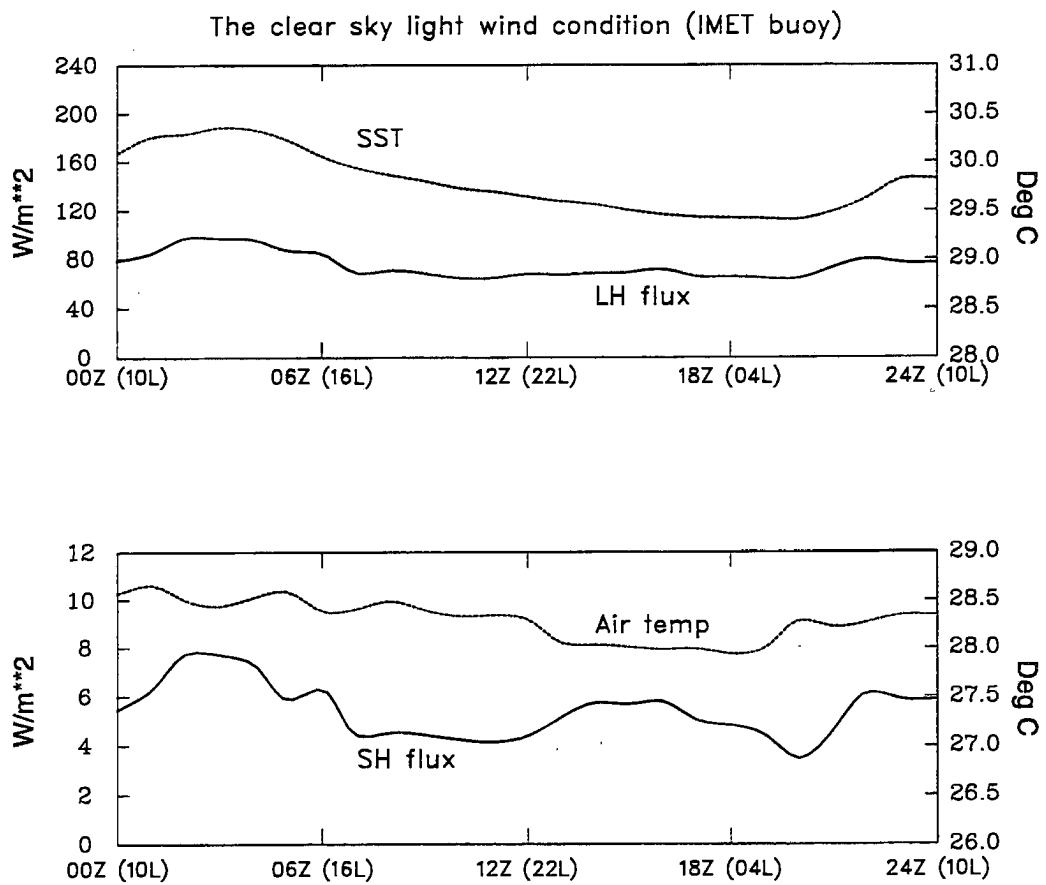


Figure 6.4: Diurnal variations (1-h intervals) in surface latent and sensible heat fluxes ( $W m^{-2}$ , SST (Deg C), and near surface air temperature (Deg C) under the clear-sky, light-wind condition. (IMET buoy data courtesy of Drs. Weller and Anderson, WHOI).

cycle, although the magnitude of the diurnal cycle in air temperature is small. Combining both oceanic observations and mixed-layer model results, Webster et al. (1996) showed that under clear and calm weather, there was a significant increase of skin SST due to solar insolation during the day. However, this increase of surface temperature hardly penetrated the mixed layer 5 m below the surface, and the peak heating at 4.5 m depth occurred about 7 hours after the maximum value of skin SST. In summary, weak downward mixing and high insolation made the ocean surface during the clear-sky, light-wind condition behave similarly to the continental land surface in summer.

Figure 6.5 shows the diurnal variabilities in divergence, vertical motion, temperature deviation, and  $Q_2$  over the IFA under the clear-sky, light-wind condition. Weak convergence can be observed below 670 hPa in the afternoon (16L) with a maximum near the surface. Divergence generally dominated the middle levels with a peak around 300 hPa. Toward late evening, low-level convergence gradually weakened and the largest convergence occurred between 670 and 750 hPa. Strong divergence dominated the low levels from late night to early morning, similar to those results obtained by Nitta and Esbensen (1974) for the disturbed period over the tropical Atlantic Ocean.

There is a clear diurnal variation in vertical motion profiles. In the afternoon, weak upward motion extended from the surface to about 300 hPa with a peak at about 630 hPa, probably an indication of the dominance of shallow cumulus and cumulus congestus. Some deep precipitating cells may also develop in the afternoon and coexist with populations of shallow clouds (confirmed by radar rainrate analysis). Near early morning (04 LST), downward motion generally dominated the entire troposphere with a peak at about 700 hPa. Since there were no large-scale convective systems during this undisturbed period, the afternoon-to-evening upward motion was likely induced by higher skin SSTs in the afternoon.

Temperature deviation from the daily mean  $T'$  clearly indicates that the atmospheric temperatures during the day are warmer than those during the night. Two afternoon-maximum/morning-minimum couplets can be noticed at 1000 hPa and between 400 and 500 hPa. The near-surface one is apparently induced by diurnal SST variations, and the

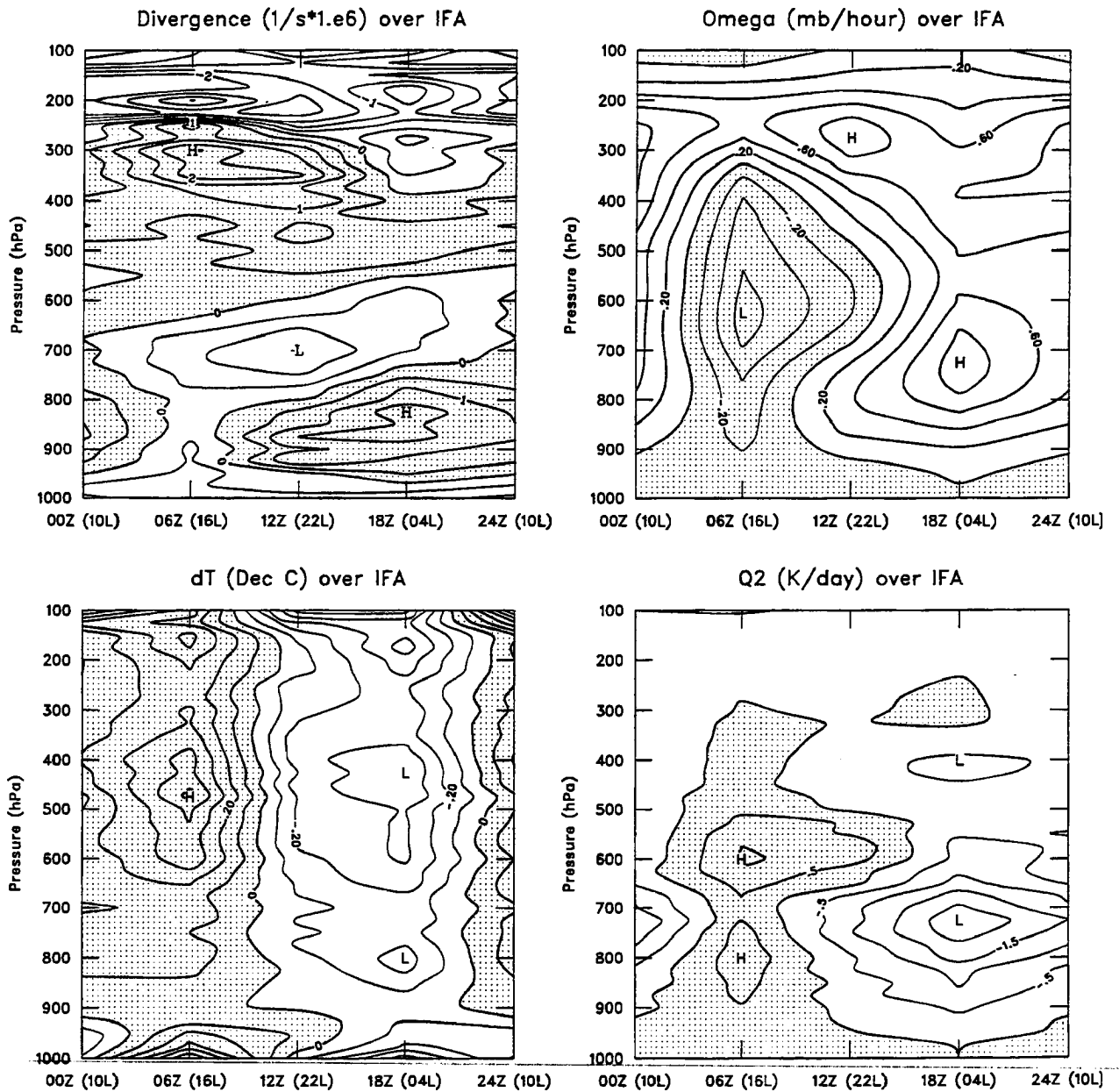


Figure 6.5: Diurnal variations in divergence ( $10^{-6} s^{-1}$ ), vertical motion ( $mb h^{-1}$ ),  $T'$  (Deg C), and  $Q_2$  ( $K day^{-1}$ ) over the IFA under the clear-sky, light-wind condition. Shaded regions indicate divergence, upward motion, positive T deviation, and drying, respectively.

difference is about  $1.0^{\circ}\text{C}$ , consistent with the buoy data. The midlevel one could possibly be related to (1) shortwave absorption (Randall et al. 1991) and/or (2) latent heat release associated with the popcorn-type precipitating cells. The temperature difference is about  $0.7^{\circ}\text{C}$ . Between 600 and 900 hPa, the afternoon-vs-morning temperature difference is generally quite small (about  $0.2 - 0.3^{\circ}\text{C}$ ).  $Q_2$  profiles indicate drying throughout the middle and low troposphere from the afternoon to early evening, also suggesting existence of precipitating cells associated with the higher SSTs in the afternoon. Moistening can be observed at middle and low levels from late night to early morning with a peak located at 750 hPa, probably indicating detrainment from shallow cumulus clouds near a weak tradewind inversion layer.

Based on the above observations, we hypothesize that there are always some populations of shallow cumulus clouds over the western Pacific warm pool during the undisturbed period. In the afternoon, due to higher skin SSTs and weaker radiative cooling, some deep precipitating cells can also develop and coexist with those shallow clouds. These precipitating cells contribute to drying the middle and lower atmosphere, competing with the moistening effect of non-precipitating shallow clouds. From late night to early morning, lower skin SSTs and stronger radiative cooling will favor compensating downward motion. A weak tradewind inversion layer is formed, while precipitating cells are suppressed. Moistening by detrainment from shallow cumuli is dominant. It is necessary to point out that although evidence of tradewind inversion can be noticed, it is usually very weak over the warm pool, and detrainment from shallow cumuli can extend to middle levels.

Further evidence of the moistening effect from the late-night-to-early-morning shallow cumuli can also be seen in Figure 6.6. After the passage of a deep convective system in 11 November, relative humidity at middle and low levels dropped dramatically (e.g., between 400 and 850 hPa, the 48% contour). During the following undisturbed phase (e.g., between 14 and 22 November), middle- and low-level relative humidity gradually recovered. Precipitable water between middle levels and the surface gradually increased. Since moistenings occurred above mixed layer, it can only be explained by vertical transport/detrainment by clouds or by horizontal advection. Since horizontal advection was weak under the clear-sky,

light-wind condition, the most probable mechanism for moistening middle and low levels is through detrainment of those shallow cumuli from late night to early morning.

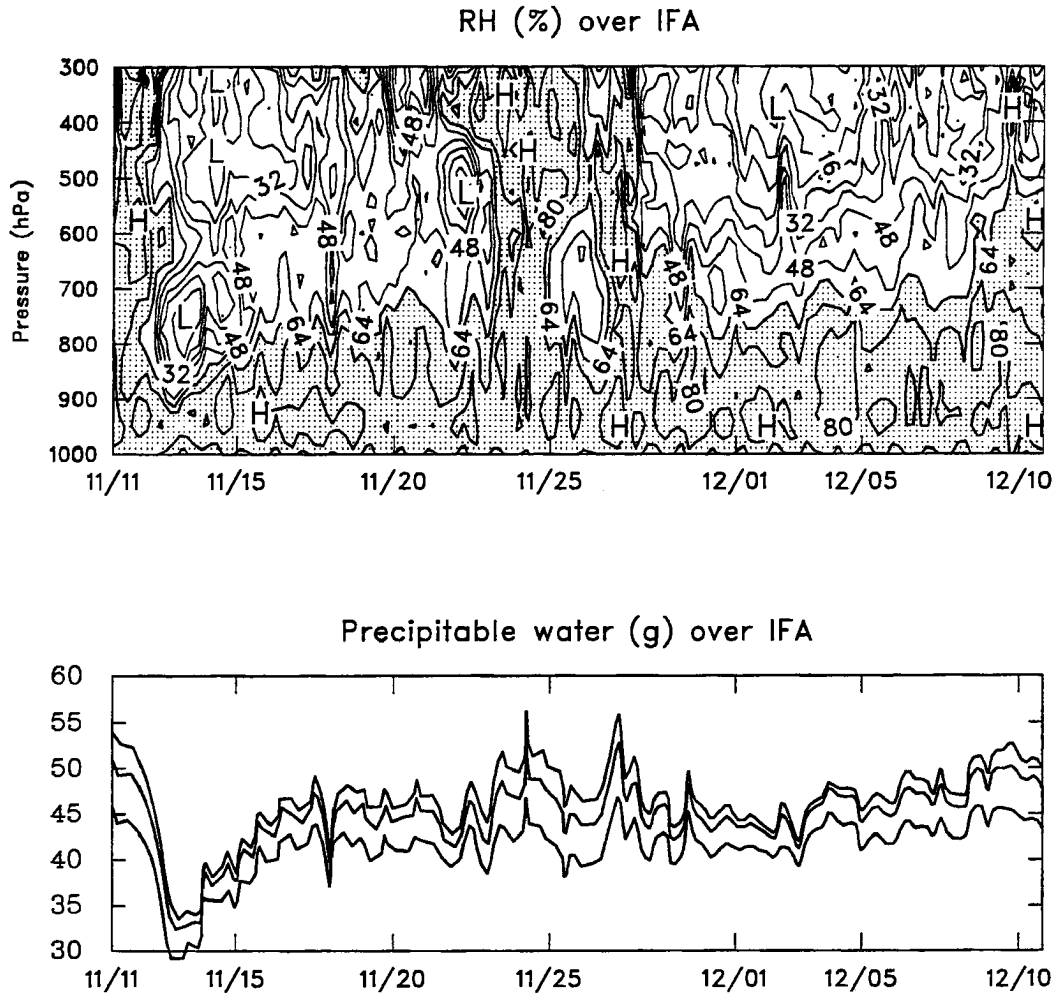


Figure 6.6: Time series of (a) relative humidity (%) profiles; (b) precipitable water (in g, 400-1000 hPa; 500-1000 hPa; 600-1000 hPa) over the IFA between 11 November and 10 December, 1992.

The results derived from large scale observations require support from information of local cloud populations. Figure 6.7 shows the diurnal variation in rainfall for sub-MCS non-linear events under the clear-sky, light-wind condition (courtesy of Drs. Rickenbach and Rutledge). There is a clear afternoon maximum in rainfall for those popcorn-type precipitating cells, consistent with what we hypothesized from  $\omega$  and  $Q_2$  plots. Indeed, most of the rainfall was from convective component. There is almost no indication of

diurnal variation in non-convective rain. Figure 6.8 further illustrates that under the clear-sky, light-wind condition, tops of most precipitating cumuli were located between 5 and 7 km.

It is necessary to add that the diurnal variabilities we described and hypothesized above are only a plausible scenario supported in some way by rawinsonde and radar observations. Information about populations of non-precipitating shallow clouds would provide a test for it. It is unfortunate that neither radar nor satellite data can provide such information. In the near future, we will probably have to rely on cloud photos from ship-based full-sky camera to further examine the diurnal variabilities during the clear-sky, light-wind condition.

### 6.3 Cloudy-sky, strong-wind conditions

Figure 6.9 shows the unfiltered time series (at 6-h intervals) of  $Q_1$ ,  $Q_2$ , 1000 hPa wind speed, and  $T_{BB}$  averaged over the IFA, and SST and latent heat flux measured at the IMET buoy between 11 December and 10 January. Deep convection associated with the December ISO occurred vigorously over the IFA between 11 and 25 December (indicated by a dashed line), about 1 to 3 weeks prior to peak westerly wind burst around 1 January. Strong heating dominated throughout the troposphere with peaks located between 350 and 500 hPa. As tropospheric vertical wind shear increased, drying peaks gradually shifted from low levels upward becoming more coincident with the  $Q_1$  peaks, suggesting a greater contribution from stratiform precipitation (Luo and Yanai 1984; Johnson and Young 1983). Strong evaporative moistening began at low levels, then gradually deepened. Time series of GMS  $T_{BB}$  show several distinct troughs. Both the surface wind speeds and surface latent heat fluxes increased dramatically when the convection occurred within the IFA. SSTs gradually decreased as heat fluxes from the ocean to the atmosphere, vertical turbulent mixing in the upper ocean, and cloud cover increased. Because of frequent occurrence of organized deep convection, and strong surface winds, we also define this period as the disturbed phase of the ISO.

The second cruise of R/V Vickers started in 21 December, 1992, and MIT radar unfortunately was not able to capture the whole sequence of deep convection in connection with

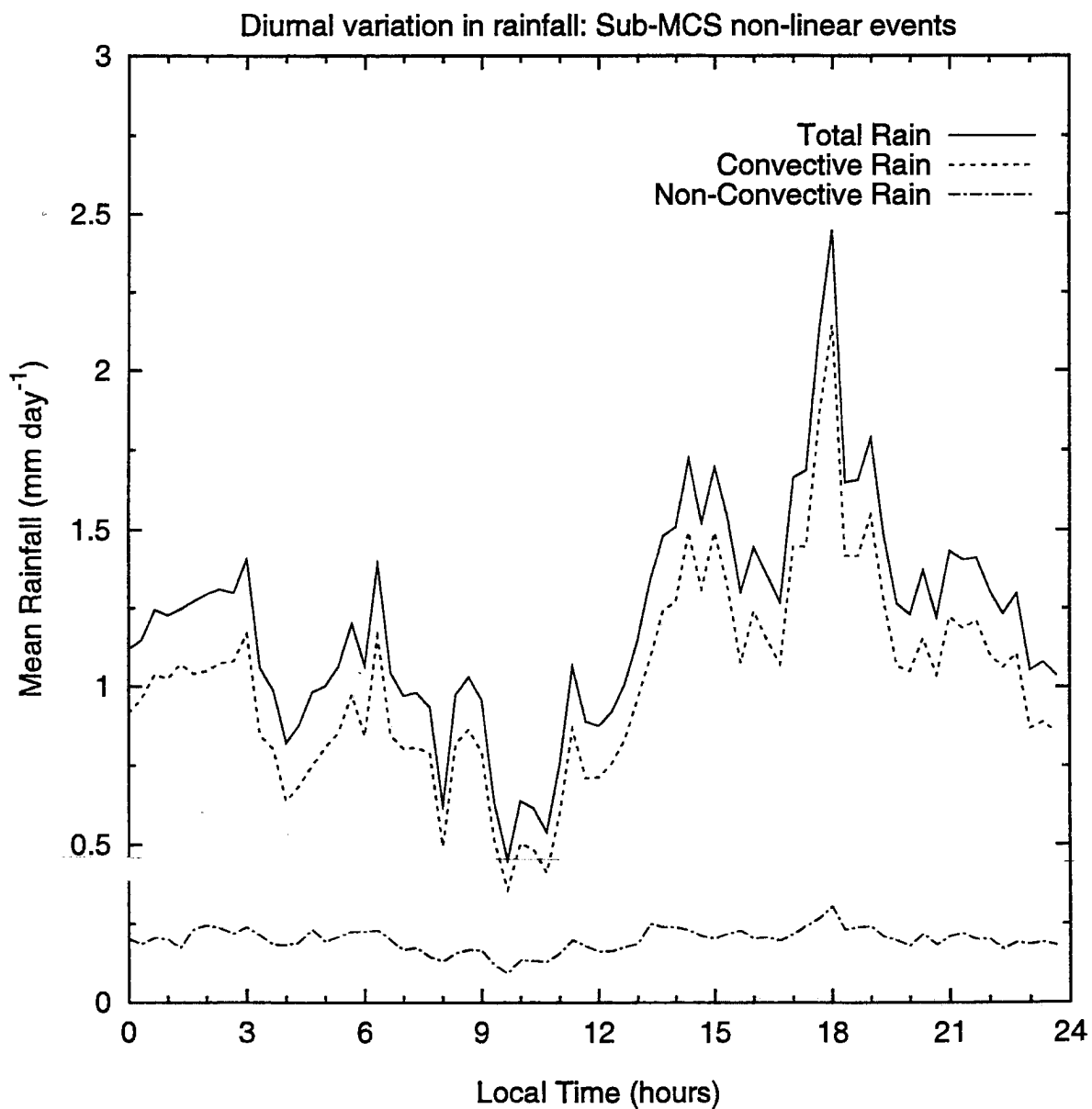


Figure 6.7: Diurnal variation in MIT Doppler radar rainfall for sub-MCS non-linear events under the clear-sky, light-wind condition (courtesy of Drs. Tom Rickenbach and Steve Rutledge, CSU).

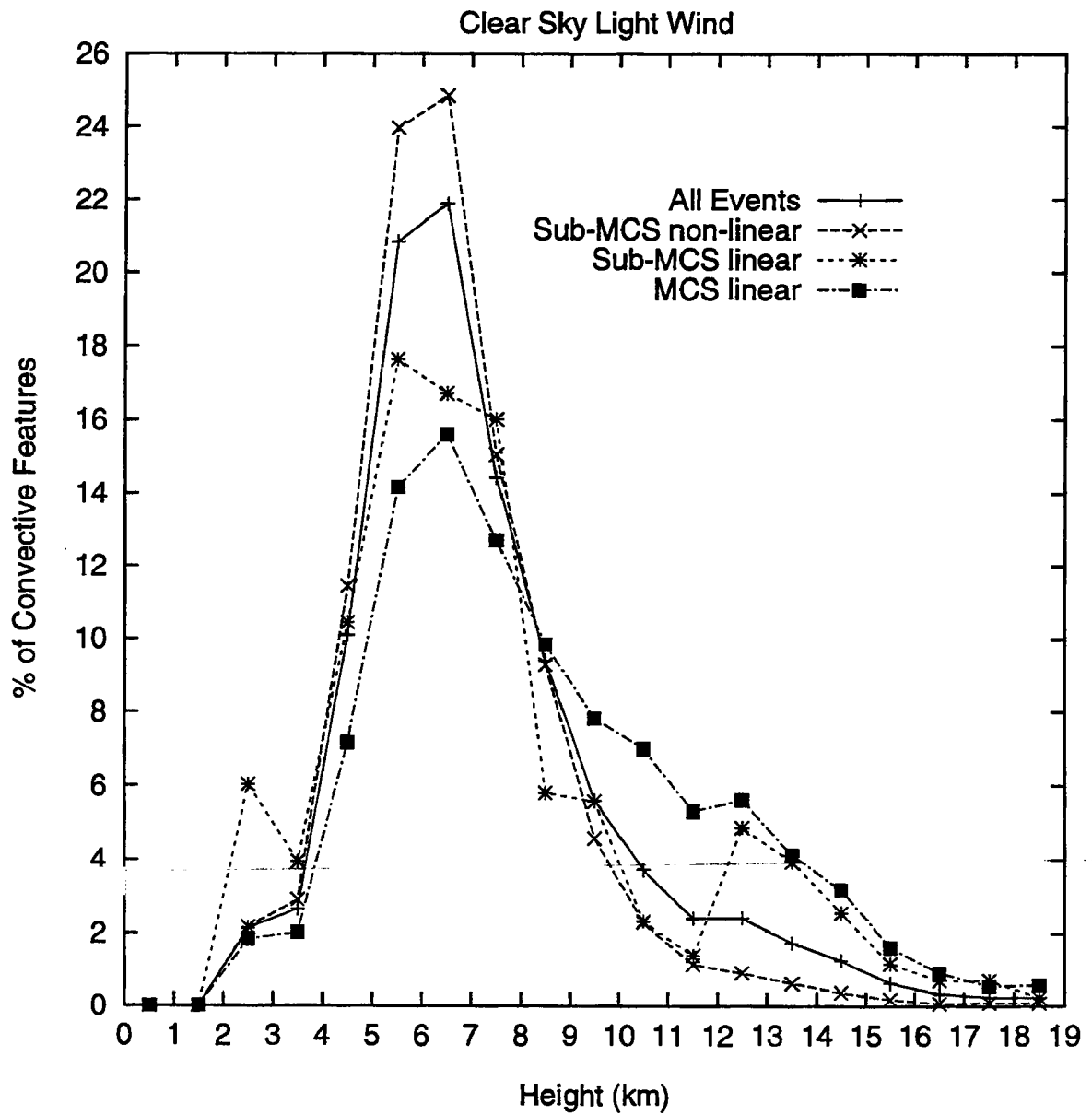


Figure 6.8: Histograms of the fraction of convective features occurring in 1 km convective feature height bins, for each event type and for all events combined under the clear-sky, light-wind condition (courtesy of Drs. Tom Rickenbach and Steve Rutledge, CSU).

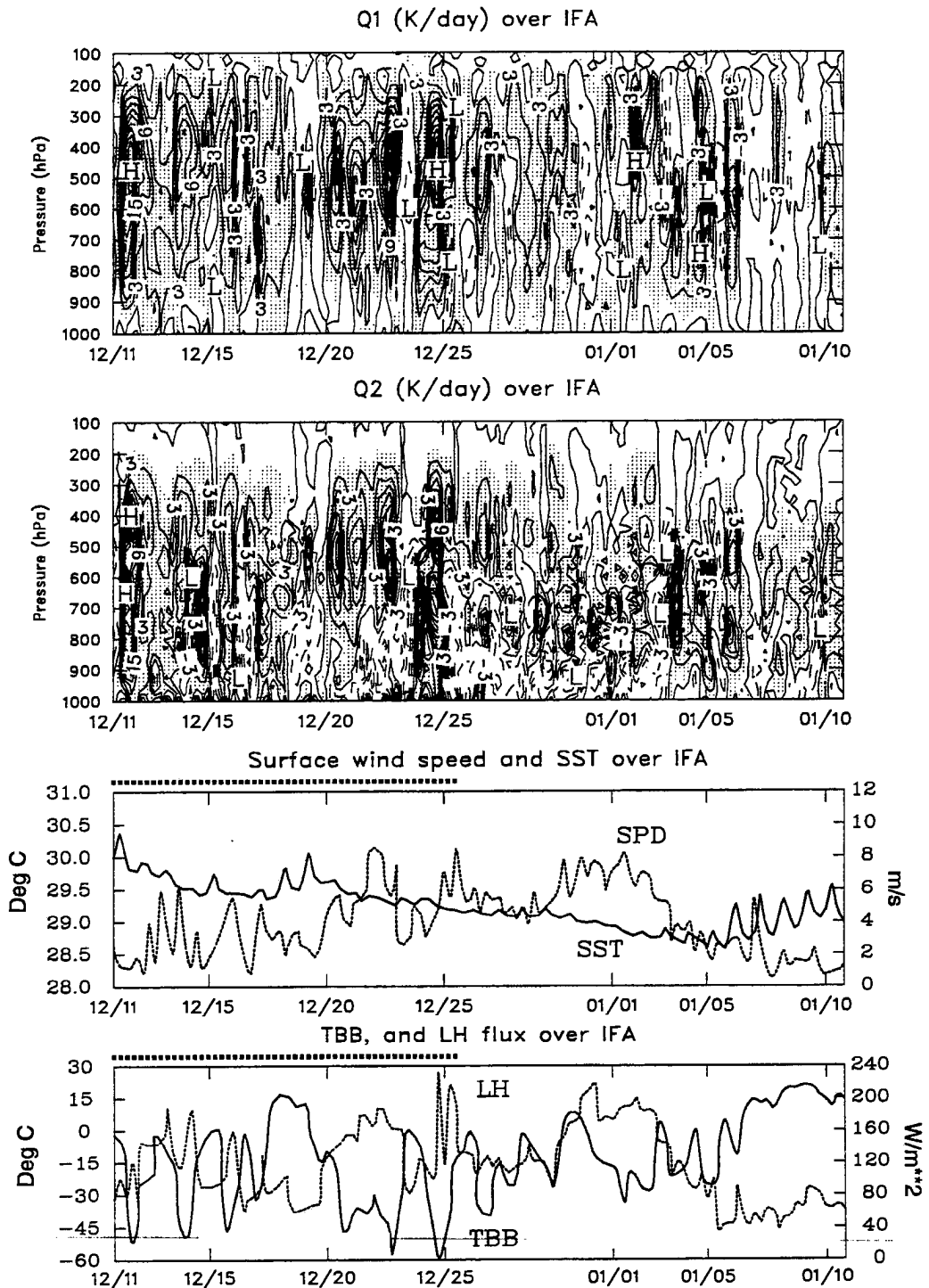


Figure 6.9: Time series of unfiltered apparent heat source  $Q_1$  ( $\text{K day}^{-1}$ ), the apparent moisture source  $Q_2$  ( $\text{K day}^{-1}$ ), 1000 hPa wind speed ( $\text{m s}^{-1}$ ), GMS brightness temperature (Deg C) over the IFA, along with SST (Deg C) and surface latent heat fluxes ( $\text{W m}^{-2}$ ) from the IMET buoy between 11 December and 10 January, 1992. The contour intervals for  $Q_1$  and  $Q_2$  are  $3 \text{ K day}^{-1}$  and areas  $> 1.0 \text{ K day}^{-1}$  are shaded. Dotted lines above the SST figure indicate periods during the COARE IOP when the cloudy sky strong wind condition prevailed.

Cruise 2

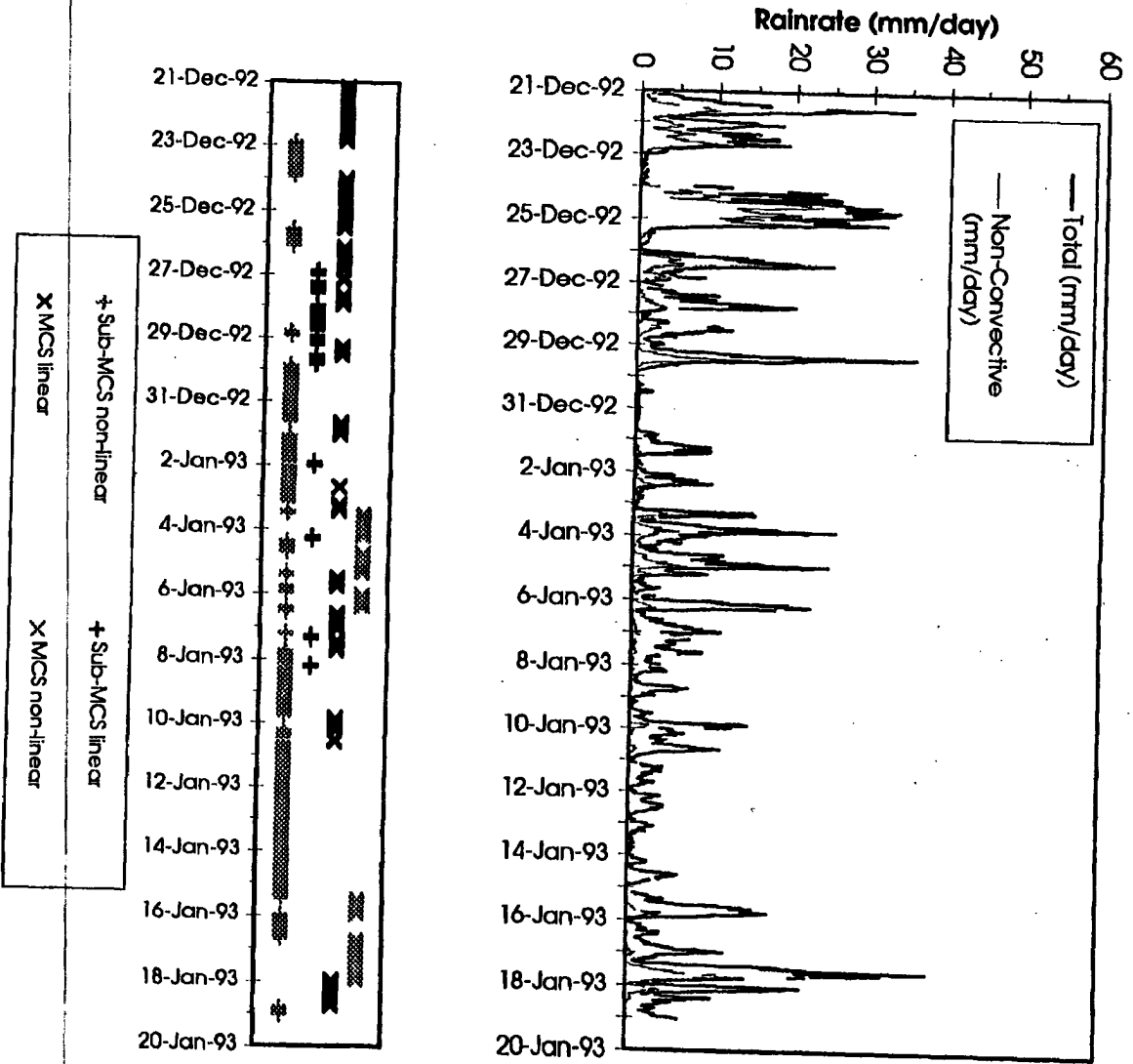


Figure 6.10: (a) Time series of total rainrate (think solid line) and non-convective rainrate

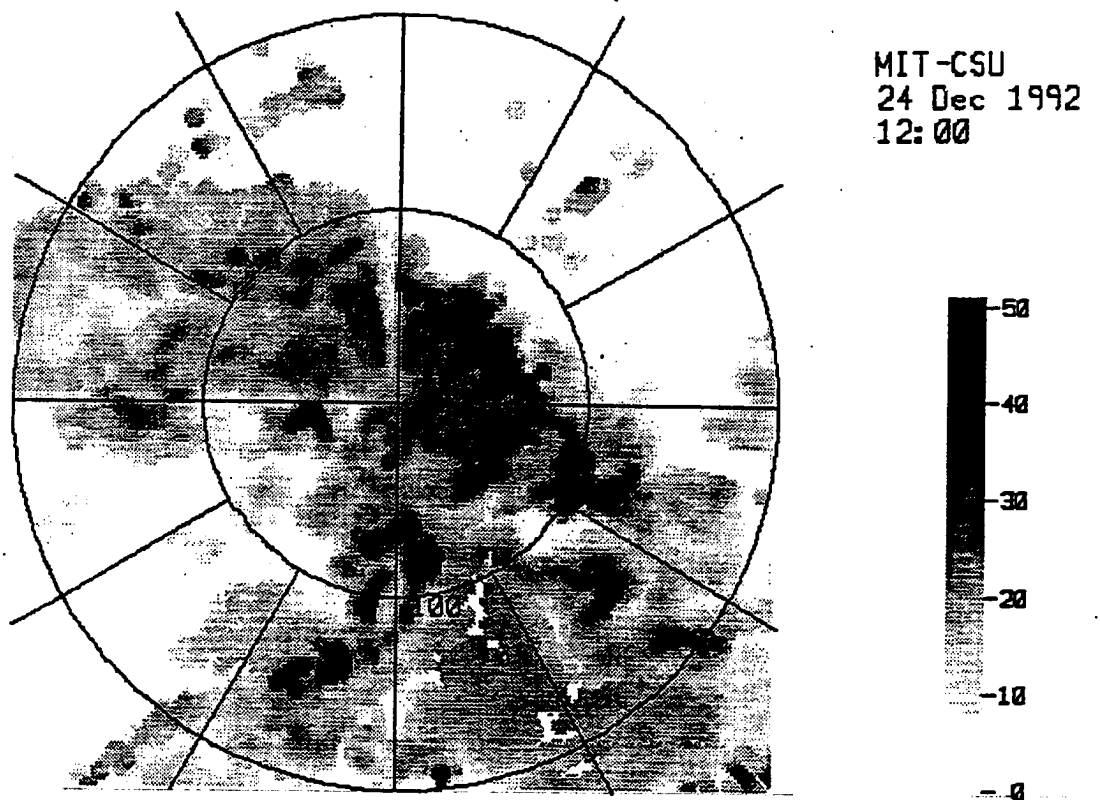


Figure 6.10: Continued. (b) A radar reflectivity map at a height of 2 km for a MCS scale linear event on 24 December 1992.

the December ISO. Rickenbach and Rutledge (1996a) found that MCS-scale linear systems dominated the precipitating events between 21 and 27 December (Fig. 6.10a, from Rickenbach and Rutledge 1996a). Fig. 6.10b shows an example of the MCS-scale linear system (from TCIP TOGA COARE Operations Summary, 1993). As noted by Rickenbach and Rutledge (1996a), these systems commenced as a line of convective cells forming within or being advected into the radar sample area. Often, stratiform precipitation formed rearward of the convective line. The convective line had to remain coherent and greater than 100 km in length for at least twenty minutes for the event to be characterized as a MCS scale linear event (Rickenbach and Rutledge 1996). From Fig. 6.10a, it can be seen that most of the rainrate was from non-convective component, consistent with findings inferred from heat and moisture budgets (Lin and Johnson 1996b).

Chen et al. (1996) subdivided area covered by  $\leq 208\text{K}$  IR cloudiness by cloud cluster size (4 being the largest and 1 the smallest) throughout the COARE IOP. They found that the largest clusters had the greatest diurnal variation, with a maximum in the early morning. The smallest clusters were found to have only a minor diurnal variation. Based on shipboard radar measurement, Rickenbach and Rutledge (1996b) also noticed there was a nighttime maximum in rainfall from large convective systems.

IMET buoy data (Fig. 6.11) indicated that diurnal variation of SST became very small during the disturbed phase (for period between 11 and 25 December) as a result of strong mixing in the upper ocean, diminished incoming solar insolation, and strong evaporation. Therefore, surface forcing induced by daytime solar heating can not explain the diurnal cycle in convection at this stage. Near surface air temperature showed a minimum between 22 and 04 LST, and both sensible and latent heat fluxes showed weak maxima between night and early morning and minima at 10 LST. Convective and mesoscale downdrafts induced by deep convection are believed to be responsible for the enhancement of the surface fluxes during the night.

During the disturbed phase, the divergence profiles (Fig. 6.12) generally showed convergence at low levels, and divergence in the upper troposphere. The maximum low-level convergence occurred at 22 LST, while the maximum divergence was located around 200 hPa

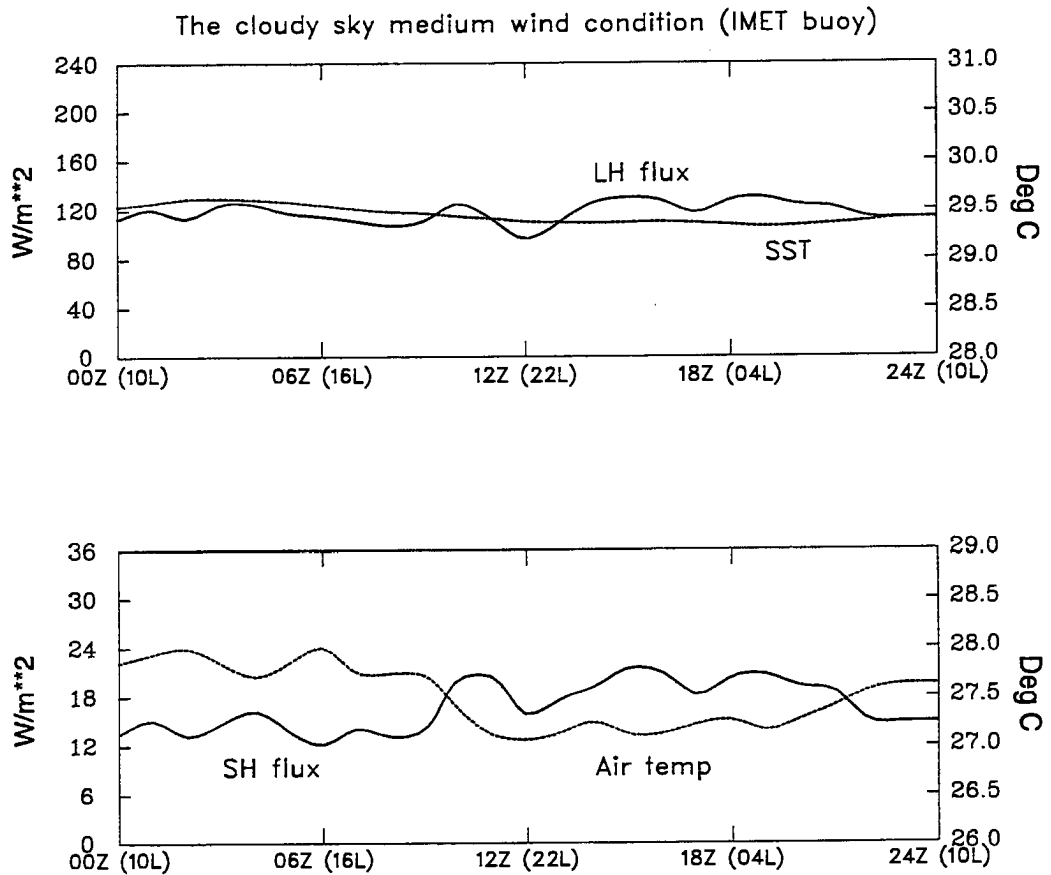


Figure 6.11: Diurnal variations (1-h intervals) in surface latent and sensible heat fluxes ( $\text{W m}^{-2}$ , SST (Deg C), and near surface air temperature (Deg C) under the cloudy sky strong wind condition. (IMET buoy data courtesy of Drs. Weller and Anderson, WHOI).

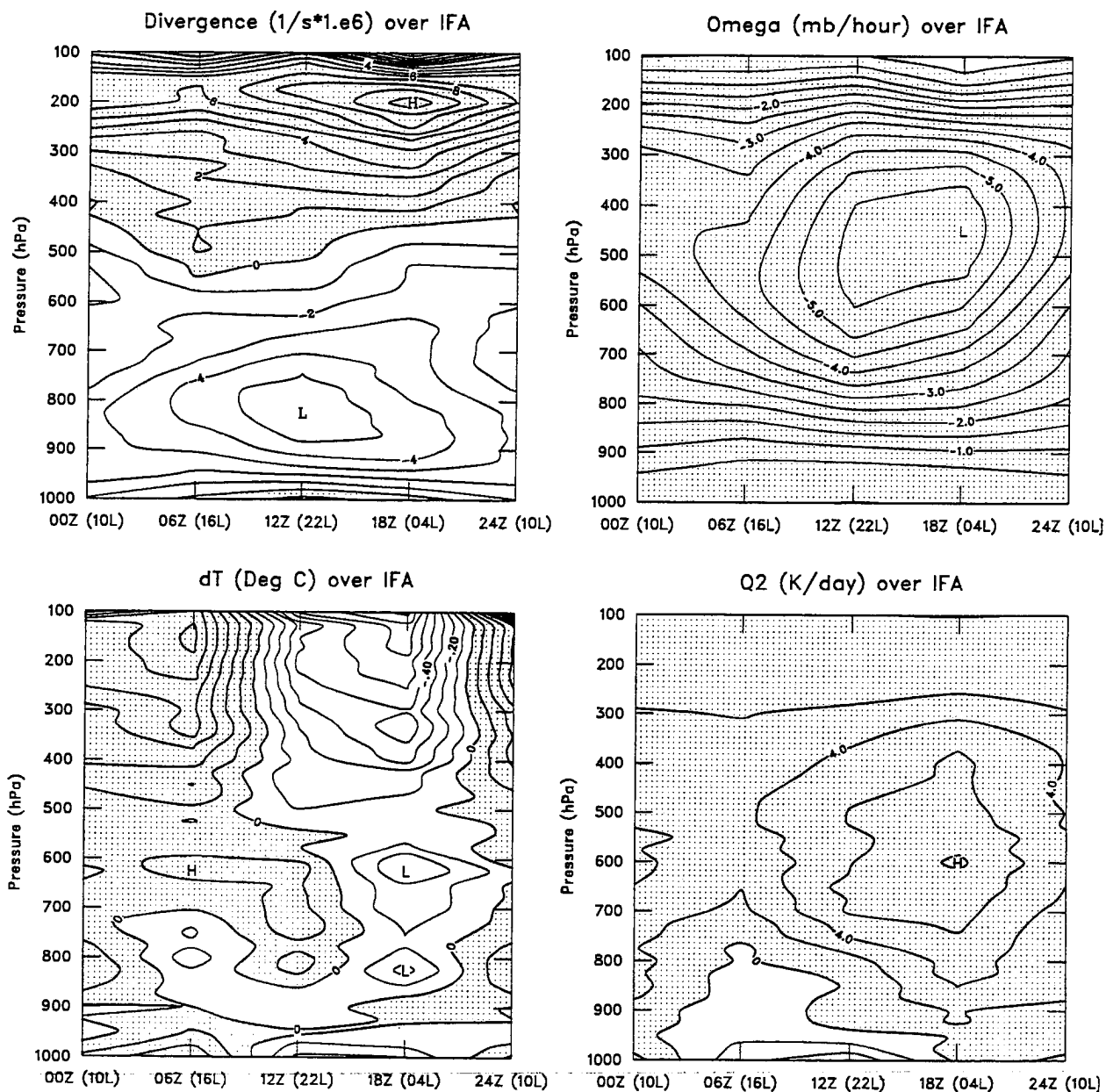


Figure 6.12: Diurnal variations in divergence ( $10^{-6} s^{-1}$ ), vertical motion ( $mb h^{-1}$ ),  $T'$  (Deg C), and  $Q_2$  ( $K day^{-1}$ ) over the IFA under the cloudy sky strong wind condition. Shaded regions indicate divergence, upward motion, positive T deviation, and drying, respectively.

in the early morning (04 LST). Both omega and  $Q_2$  profiles indicated that the strongest convection occurred between late evening and early morning with a maximum at 04 LST, consistent with many previous observational studies on diurnal variations in oceanic deep convection (e.g., Gray and Jacobson 1977). Diurnal variations of surface heat fluxes and surface air temperature (decrease in SST, increases in fluxes) appeared to be responses of diurnal variations in deep convection.  $T'$  profiles show primarily one afternoon-maximum/morning-minimum couplet near tropopause, a clear indication of strong upper-level cloud-radiation interactions (Randall et al. 1991). The largest afternoon-vs-morning temperature difference is about 1.2°C. The temperature differences at middle and low levels are generally small.

Since considerable deep convection occurred over the night during the disturbed phase, radiation-dynamics-convection interaction (Gray and Jacobson 1977) and/or direct radiation-convection interaction (Randall et al 1991) might explain the diurnal variations in convection during this disturbed stage. Xu and Randall (1995) examined the impact of cloud-radiations using a 2-D cloud ensemble model. Their simulations confirmed the dominant role of the direct radiation-convection interaction mechanism, as proposed by Randall et al. (1991). The radiation-dynamics-convection mechanism of Gray and Jacobson (1977) was found to play a secondary role in the diurnal cycle of precipitation. In this study, with only observational data, it is very hard to distinguish which mechanism is more important in the western Pacific during the disturbed phase of the ISO.

#### 6.4 Conclusions and discussion

In this chapter, diurnal variabilities of the atmosphere and ocean surface under two distinctly different situations: the clear-sky, light-wind, and the cloudy-sky, strong-wind conditions, are investigated. The undisturbed phase of the ISO was characterized by clear sky and calm winds. Ocean surface usually warmed up quickly in the afternoon as a result of high solar insolation, and weak turbulent mixing and evaporation. The diurnal variation in convection is similar to the summer diurnal cycle over continents. In the afternoon, some popcorn-type precipitating cells were usually enhanced over the warm pool in response to strong surface heating. They tended to dry the atmosphere, competing with the moistening

effect from coexisting shallow cumuli and cumulus congestus. From late night to early morning, these precipitating cells were suppressed. Detrainment from the large populations of shallow cumuli is hypothesized to be a dominant mechanism in moistening the middle and low levels of the tropical atmosphere. This moistening would eventually provide a favorable environment for ISO-related deep convection to occur later.

The disturbed phase of the ISO was characterized by frequent occurrence of organized deep convection. The strong surface winds were induced by both ISO-related westerly wind burst and convection-induced gust fronts. Diurnal variability in SST was greatly diminished due to strong turbulent mixing in the upper ocean, strong evaporation, and decreasing solar insolation. Organized deep convection tended to occur more frequently during the night and usually had a maximum in early morning. The radiation-dynamics-convection mechanism (Gray and Jacobson 1977) and/or direct radiation-convection mechanism (Randall et al 1991) may explain the early morning convection maximum during this period. The diurnal variabilities in surface heat fluxes and surface air temperature appeared to be responses to diurnal variation in deep convection.

In this study, based on our experience in analyzing various dataset over open oceans, we would like to emphasize that there are large diurnal variabilities in convection over the western Pacific warm pool. They can be distinctly different due to the role played by different interaction mechanisms and large-scale forcings. It is more reasonable to pick apart what is actually causing the variance in the diurnal variations of those atmospheric and surface features, and then perform composite analyses. Otherwise, the composited results would be messy and inconsistent. For example, besides the two conditions studied in this chapter, there were situations when the clear-sky, strong-wind condition prevailed over the IFA (between 27 December and 3 January, 1992). A few studies have tried to use satellite IR thresholds to separate COARE IOP into disturbed and suppressed phases, and to investigate diurnal variation in precipitation (e.g., Sui et al. 1997; Chen and Houze 1996). These simple classifications are too arbitrary and not to be based on possible mechanisms of the diurnal cycle, and therefore we do not recommend them.

## Chapter 7

### DIAGNOSIS OF SHALLOW CUMULUS EFFECTS

In Chapter 5, we have found that the IFA-averaged  $Q_2$  profiles show strong low-level moistening below about 700 hPa during the December and February westerly wind bursts. This feature is prominent enough to impact the seasonal distribution of boundary-layer moistening since the IOP-mean  $Q_2$  profile over the IFA also exhibits large negative values at low levels. Considering the western Pacific warm pool experiences the greatest rainfall of any oceanic region on earth, what then, is the cause of the negative  $Q_2$  at low levels within the IFA? In Chapter 5, we have hypothesized that this low-level moistening is a consequence of precipitation evaporation and/or evaporation by shallow cumuli, as found by Nitta and Esbensen (1974) in Atlantic tradewind regimes. In this Chapter, we will examine the heating and moistening distributions in more detail. A cloud spectral model is utilized to identify which processes contribute to the low-level moistening.

The cloud spectral diagnostic method was developed by Ogura and Cho (1973), Cho and Ogura (1974) and Nitta (1975) according to Arakawa's (1969) spectral representation of cumulus clouds. Cho and Ogura (1974) adopted this approach to diagnose deep cumulus effects over the tropical western Pacific. Nitta (1975) has applied this method to study shallow cumulus regimes in the western Atlantic. Johnson (1976) implemented convective downdrafts into the cloud spectral model. In this chapter, we repeat the derivation of this diagnostic model based on Johnson (1976), and then describe how the computation based on TOGA COARE data are performed. The aim of this study is two-fold: (1) to discuss heating and moistening variabilities over the western Pacific warm pool for the westerly wind burst and undisturbed periods; (2) to demonstrate how cumulus clouds respond to different synoptic conditions associated with the ISOs during the COARE IOP. Two periods in which

shallow cumulus clouds dominated are selected: (1) the period during the peak westerly wind burst when strong surface wind prevailed and deep convection was suppressed due to strong vertical wind shear, and (2) a few weeks before the ISO-related heavy precipitation when clear sky light wind condition prevailed. The latter is selected in order to assess the role of surface winds and compare the similarities and differences between these two ISO phases with shallow cumulus clouds. Although shallow cumulus may have downdrafts driven by evaporation of cloud water, the contribution from downdrafts are expected to be small (e.g., as found by Nitta and So 1980), therefore we neglect their effects in the spectral model.

### 7.1 The cloud spectral diagnostic model

As shown in Chapter 3, the apparent heat source  $Q_1$  and the apparent moisture sink  $Q_2$  (Yanai et al. 1973) equations can be written as:

$$Q_1 \equiv \frac{\partial \bar{s}}{\partial t} + \bar{\mathbf{v}} \cdot \nabla \bar{s} + \bar{\omega} \frac{\partial \bar{s}}{\partial p} = Q_R + L(\bar{c} - \bar{e}) - \frac{\partial}{\partial p} \overline{s' \omega'} \quad (7.1)$$

$$Q_2 \equiv -L \left( \frac{\partial \bar{q}}{\partial t} + \bar{\mathbf{v}} \cdot \nabla \bar{q} + \bar{\omega} \frac{\partial \bar{q}}{\partial p} \right) = L(\bar{c} - \bar{e}) + L \frac{\partial}{\partial p} \overline{q' \omega'} \quad (7.2)$$

Combing (7.1) and (7.2) we can get

$$Q_1 - Q_2 - Q_R = -\frac{\partial}{\partial p} \overline{h' \omega'}, \quad (7.3)$$

where  $h = s + Lq$  is the moist static energy.

The large-scale mean mass flux  $\bar{M}$  consists of two components:  $M_u$  the mass flux in cumulus updrafts, and  $\tilde{M}$  the environmental or between-cloud mass flux (here convective downdrafts and mesoscale features are neglected). Thus

$$\bar{M} = M_u + \tilde{M} \quad (7.4)$$

In this steady-entraining plume model, each cumulus updraft has a characteristic entrainment rate  $\lambda$  which uniquely determines the cloud depth (Ogura and Cho 1973; Arakawa and Schubert 1974). It is assumed that the fractional mass entrainment rate is constant for each cloud, i.e.,

$$\frac{1}{m_u(\lambda, z)} \frac{\partial}{\partial z} m_u(\lambda, z) = \lambda, \quad (7.5)$$

where  $m_u(\lambda, z) d\lambda$  is the mass flux contribution from cloud updrafts with entrainment rates between  $\lambda - d\lambda/2$  and  $\lambda + d\lambda/2$ . Assuming there exists a continuum of cloud sizes or entrainment rates which can completely describe the cumulus population, we can solve (7.5) and have

$$m_u(\lambda, z) = m_B(\lambda) \exp\{\lambda[z - z_B(\lambda)]\}, \quad (7.6)$$

where  $m_B$  is the cloud base mass flux distribution function and  $z_B$  is the height of the cloud base. The total upward mass flux at any level due to all cumulus updrafts which penetrate that level is

$$M_u(z) = \int_{\lambda=0}^{\lambda(z)} m_u(\lambda, z) d\lambda, \quad (7.7)$$

where  $\lambda(z)$  is the entrainment rate for clouds having tops at the height  $z$ .

Transforming (7.5) into pressure coordinates, we have:

$$\frac{1}{m_u(\lambda, p)} \frac{\partial}{\partial p} m_u(\lambda, p) = -\frac{\lambda H}{P}, \quad (7.8)$$

where  $H = \frac{R_d T_v}{g}$  is the scale height of an atmosphere with a virtual temperature  $T_v = T(1 + 0.608q)$  and  $R_d$  is the gas constant for dry air. The solution of (7.8) is

$$m_u = m_u(\lambda, p) = m_B(\lambda) \eta_u(\lambda, p) \quad (7.9)$$

where

$$\eta_u(\lambda, p) = \exp\left(\int_p^{p_B(\lambda)} \frac{\lambda H}{p} dp\right) \quad (7.10)$$

$p_B(\lambda)$  is the cloud-base pressure level.

Assuming that radiative heating plays only a minor role in the growth of individual cumulus clouds, the theory for a steady-state, entraining plume (Squires and Turner, 1962) leads to the following form of the first law:

$$\frac{\partial}{\partial p}(m_u h_u) = \tilde{h} \frac{\partial m_u}{\partial p} \quad (7.11)$$

for the updraft. As has been shown in Ogura and Cho (1973) and Arakawa and Schubert (1974), the moist static energy  $h_u(\lambda, p)$  within each cumulus updraft is given by integrating (7.11) from cloud base  $p_B(\lambda)$  to the level  $p$ :

$$h_u(\lambda, p) = \frac{1}{\eta_u(\lambda, p)} \left[ h_u(\lambda, p_B) + \int_p^{p_B(\lambda)} \eta_u(\lambda, p) \frac{\lambda H}{p} \tilde{h} dp \right] \quad (7.12)$$

We assume that each cloud entrains through its entire depth up to some level  $p_D(\lambda)$  where it loses its buoyancy and detrains. At this level the cloud virtual temperature,  $T_{vc} = T_c(1 + 0.608q_c - q_l)$ , equals the virtual temperature of the environment, where  $q_l$  is the cloud condensate mixing ratio and the subscript  $c$  refers to cloud values. This condition, when combined with the two approximations (see Arakawa and Schubert 1974)

$$T_c - \tilde{T} \approx \frac{1}{c_p} \frac{1}{1 + \gamma} (h_c - \tilde{h}^*), \quad (7.13)$$

$$q_c - \tilde{q} \approx \frac{1}{L} \frac{\gamma}{1 + \gamma} (h_c - \tilde{h}^*), \quad (7.14)$$

leads to the following expression for the cloud moist static energy at the detrainment level  $p_D$ :

$$h_u(p_D) \approx \tilde{h}^* - \frac{L\mu(1 + \gamma)}{1 + 0.608\mu\gamma} [0.608(\tilde{q}^* - \tilde{q}) - q_l], \quad (7.15)$$

where  $\tilde{q}^*$  is the saturation mixing ratio,  $\tilde{h}^*$  is the saturation moist energy,  $\gamma = L/C_p(\partial\tilde{q}^*/\partial T)_p$  and  $\mu = C_p\tilde{T}/L$ .

Using large-scale observational data, we can determine  $h_u(P_D)$  at each level from (7.15). By assuming a cloud-base value of the moist static energy,  $\lambda_D(p)$  at each level can be determined by inverting (7.12).

The next step is to write the heat and moisture budget equations, especially the vertical eddy transport terms, into spectral forms. The large-scale average of any quantity  $\alpha$  at any level  $p$  can be written as:

$$\bar{\alpha}(p) = \int_0^{\lambda_D(p)} \alpha_u(\lambda, p) \sigma_u(\lambda) d\lambda + [1 - \sigma_u(p)] \bar{\alpha}, \quad (7.16)$$

where  $\alpha_u$ ,  $\bar{\alpha}$  are the values of  $\alpha$  in the cloud updraft and environment.  $\sigma_u(p)$ ,  $1 - \sigma_u(p)$  represent the total fractional area occupied by updrafts and environment, respectively. The eddy flux of any quantity  $\alpha$  is given by (according to Yanai et al. 1973):

$$\overline{\alpha' \omega'} = \overline{\alpha \omega} - \bar{\alpha} \bar{\omega} = - \int_0^{\lambda_D(p)} \sigma_u(\lambda) \omega_u(\lambda, p) [\alpha_u(\lambda, p) - \bar{\alpha}] d\lambda, \quad (7.17)$$

Taking the derivative of (7.17) with respect to  $p$ , we can get the spectral form of vertical eddy transport term:

$$\begin{aligned} \frac{\partial}{\partial p} (\overline{\alpha' \omega'}) = & \int_0^{\lambda_D(p)} \sigma_u(\lambda) \frac{\partial}{\partial p} \{ \omega_u(\lambda, p) [\alpha_u(\lambda, p) - \bar{\alpha}] \} d\lambda + \\ & \sigma_u(\lambda_D) \omega_u(\lambda_D, p) [\alpha_u(\lambda_D, p) - \bar{\alpha}] \frac{d\lambda_D}{dp} \end{aligned} \quad (7.18)$$

Bringing (7.18) into the heat and moisture budget equations, we can write  $Q_1$  and  $Q_2$  equations in the following spectral forms (see Johnson (1975) for more detailed derivation):

$$Q_1 - Q_R = -M_u \frac{\partial \bar{s}}{\partial p} - L \bar{e}_u + \delta [s_u(\lambda_D, p) - \bar{s}] \quad (7.19)$$

$$-\frac{Q_2}{L} = -M_u \frac{\partial \bar{q}}{\partial p} + \bar{e}_u + \delta [q_u(\lambda_D, p) - \bar{q}] \quad (7.20)$$

where cloud mass flux  $m_u(\lambda, p) = -\sigma_u(\lambda) \omega_u(\lambda, p)$ ,  $\delta = m_u(\lambda_D, p)d\lambda_D/dp$  the detrainment rate,  $\bar{c}(p) = \int_0^{\lambda_D(p)} c(\lambda, p) d\lambda$  the condensation rate,  $\bar{e}_u(p) = \int_0^{\lambda_D(p)} e_u(\lambda, p)d\lambda$  the evaporation rate. Equation (7.19) indicates that  $Q_1 - Q_R$  is produced by three components: environmental subsidence warming compensating the upward cumulus mass flux, cooling results from the evaporation of detrained liquid water, and detrainment of heat from cloud tops. Equation (7.20) indicates that the apparent moisture sink  $Q_2$  is produced by environmental subsidence drying compensating the upward cumulus mass flux, moistening due to evaporation of detrained liquid water, and detrainment of water vapor.

Adding (7.19) and (7.20):

$$Q_1 - Q_2 - Q_R = m_B(\lambda)\eta_D(\lambda_D, p)\frac{d\lambda_D}{dp} [h_u(\lambda_D, p) - \bar{h}] - \frac{\partial \bar{h}}{\partial p} \int_0^{\lambda_D(p)} m_B(\lambda)\eta_u(\lambda, p) d\lambda \quad (7.21)$$

Equation (7.21) is a Volterra integration equation of the second kind with only one unknown function  $m_B(\lambda)$ . The most important step here is to numerically solve cloud base mass flux distribution function  $m_B(\lambda)$  from (7.21) using large-scale data and computed  $\lambda$ , and then all the terms on the right hand sides of the heat and moisture budget equations can be determined.

## 7.2 Data and numerical methods

Application of the cloud spectral diagnostic model requires information of net radiative heating  $Q_R$  in the vertical. However, COARE observations could not provide detailed  $Q_R$  information for the full range of atmospheric conditions. In this study, we have used National Center for Atmospheric Research Community Climate Model (CCM2) one-dimensional radiation code (Kiehl et al. 1994). By neglecting effects of cloud layers, we can compute the clear-sky shortwave and longwave radiative heating profiles at six-hourly intervals based on IFA sounding and surface data. Although there are limitations to this procedure, our

main emphasis will be on periods with scattered shallow cumulus clouds, and the deduced clear-sky  $Q_R$  profiles are believed to be reasonable.

In order to obtain reliable diagnoses of the properties of the shallow cloud fields, the COARE rawinsonde data augmented by 915 MHz wind profiler data (Ciesielski et al. 1996) are used in this study to compensate data dropout problems in the ISS Omegasonde low-level winds. The IFA-mean  $Q_1$ ,  $Q_2$ ,  $Q_R$  and other large-scale data are vertically interpolated from 1000 to 75 hPa at 5 hPa intervals. Such a fine resolution is necessary in order to adequately resolve different cloud populations.

The fractional mass entrainment rate  $\lambda_D(p)$  can be determined at each pressure level from (7.12), using successive guesses of  $\lambda$ . In this study, we assume that the level of cloud base in tropical western Pacific is 950 hPa.

In this cloud spectral model, all clouds are assumed to originate from the same cloud base, and the characteristic entrainment rate  $\lambda(p)$  uniquely determines the cloud depth. Therefore,  $\lambda(p)$  should decrease monotonically with height (e.g., the deepest cloud,  $\lambda = 0$ , the shallowest,  $\lambda = \lambda_D(p_B)$ ). However, our calculations from COARE data indicate that  $\lambda$  typically decreases rapidly from cloud base to 750 hPa, then slightly increases up to 550 hPa, and finally decreases again to upper troposphere. Similar feature has also been noticed by Nitta (1975) over tropical Atlantic. We hypothesize it is a combined modulation of cloud population by trade wind inversion at low levels and a weak stable layer (probably induced by melting effect, Johnson et al. 1996) at middle levels. The increase of  $\lambda_D(p)$  between middle and low levels suggests redevelopment of cumulus clouds after they overshooting the trade wind inversion. These features will be discussed in the following sections. Since the stable layer at middle levels is weak and  $\lambda_D(p)$  only slightly increases from low levels to middle levels, we just set  $\lambda_D(p)$  values below equal to the value of midlevel peak if they are less than it, so that we can solve the whole set of equations.

Equation (7.21) can be written in the following discretized form:

$$(Q_1 - Q_2 - Q_R)_p = m_B(\lambda_n) R(p) + \sum_{i=1}^n a m_B(\lambda_i) K(\lambda_i, p) \Delta \lambda \quad (7.22)$$

where

$$p = p_D(\lambda_n), \quad \lambda_n = (n-1) \Delta \lambda,$$

$$R(p) = \eta_u(\lambda_n, p) \frac{d\lambda_D}{dp} [h_u(\lambda_n, p) - \bar{h}],$$

$$K(\lambda_i, p) = \frac{\partial \bar{h}}{\partial p} \eta_u(\lambda_i, p),$$

$$\eta_u(\lambda_i, p) = \exp \left( \Delta p \sum_{j=1}^k b \frac{\lambda_i H_j}{p_j} \right), \quad k = \frac{p_B - p}{\Delta p},$$

$$H_j = H(p_j), \quad p_j = p_B - (j-1) \Delta p,$$

$$\Delta \lambda = |\lambda_{i+1} - \lambda_i|, \quad \Delta p = |p_{i+1} - p_i|,$$

$$a = \begin{cases} 0.5 & \text{if } i=1 \text{ or } n \\ 1 & \text{otherwise} \end{cases},$$

$$b = \begin{cases} 0.5 & \text{if } j=1 \text{ or } k \\ 1 & \text{otherwise} \end{cases}.$$

Equation (7.22) describes a system of linear algebraic equations whose coefficient form a triangular matrix. After we choose  $\Delta \lambda = 0.025 km^{-1}$ , (7.22) can be solved by back-substitution.

### 7.3 Observed heating and moistening distributions

The IOP-mean  $Q_1$  and  $Q_2$  profiles (normalized by precipitation rate following Johnson 1984) for the OSA and IFA are shown in Fig. 7.1. Values for the Marshall Islands region from Yanai et al. (1973) are shown for comparison. The OSA  $Q_1$  and  $Q_2$  profiles resemble those for the Marshall Islands, except for the smaller amplitude of  $Q_2$ . This difference can be explained by noting that the areas under the  $Q_2$  curves are proportional to  $1 - E_0/P_0$  ( $E_0$ = evaporation rate,  $P_0$ =precipitation rate; Johnson 1984), which has the values 0.79

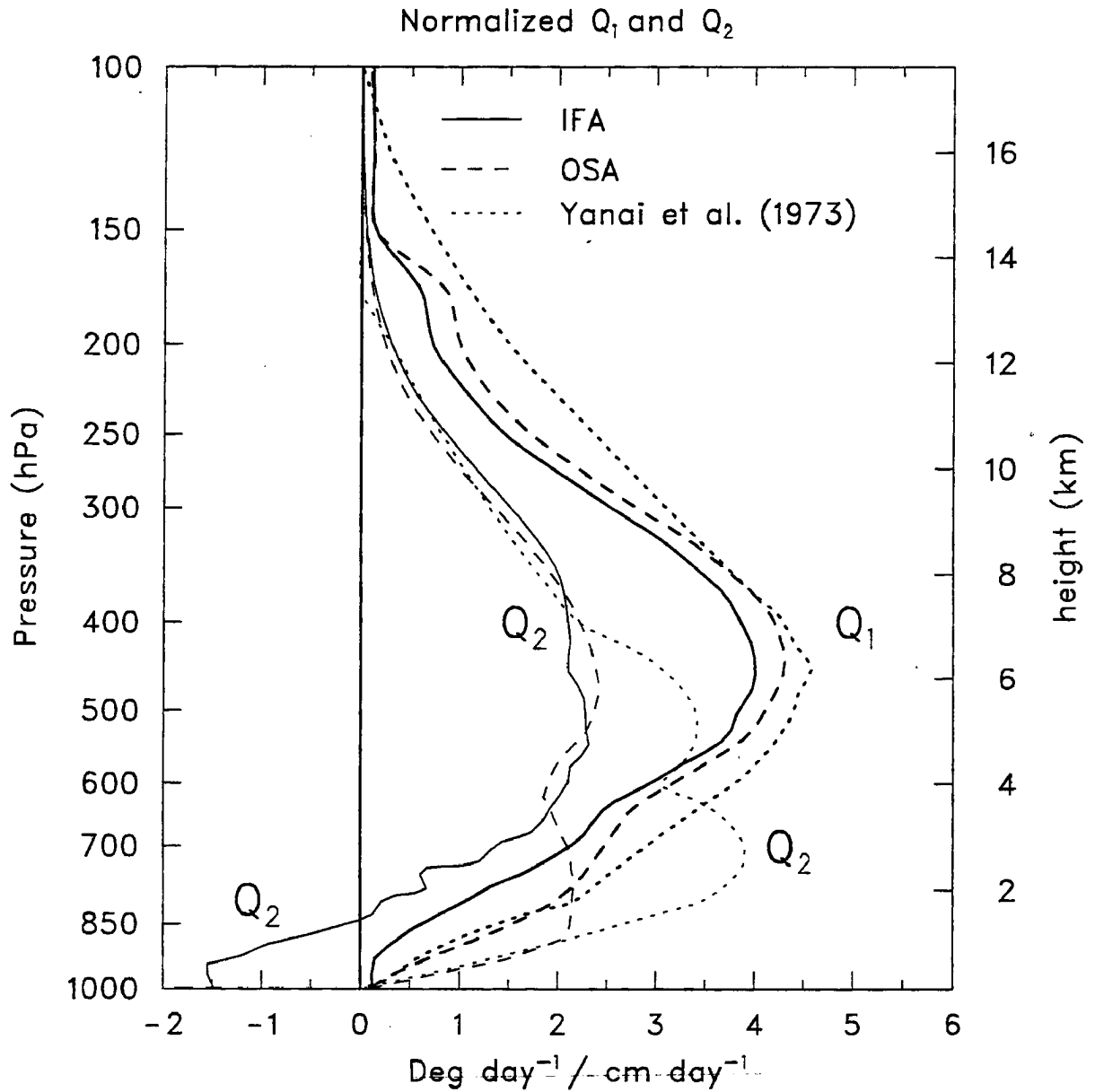


Figure 7.1: Profiles of  $Q_1$  and  $Q_2$  normalized by precipitation rate for Intensive Flux Array (IFA), Outer Sounding Array (OSA) and Marshall Islands (from Yanai et al. 1973).

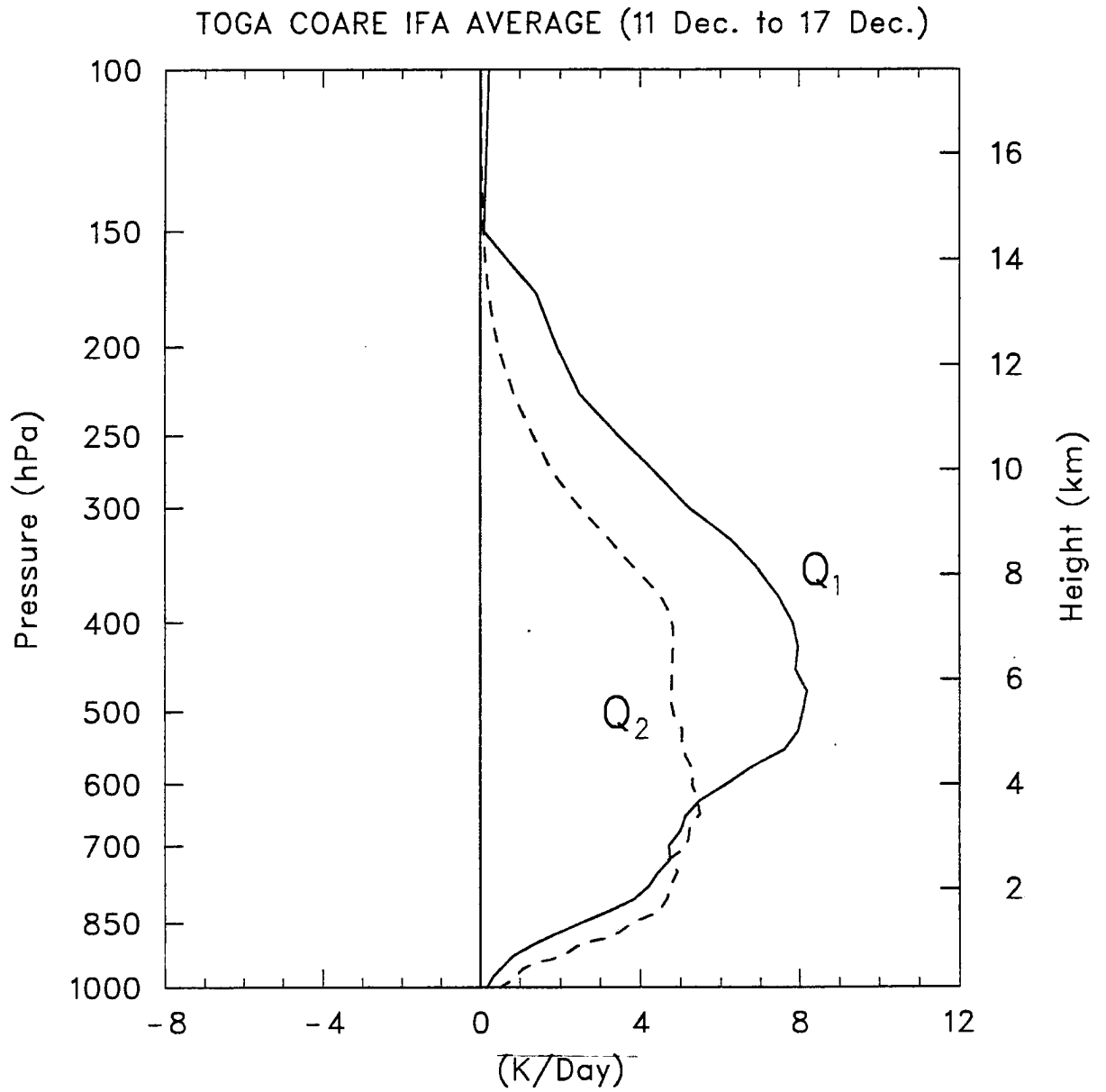


Figure 7.2:  $Q_1$  and  $Q_2$  profiles for convectively disturbed period (11-17 December 1992).

and 0.56 for the Marshall Islands and COARE OSA, respectively. In addition, both the COARE OSA and Marshall Islands  $Q_2$  profiles show a minimum near 600 hPa or 4 km, which is associated with an inflection point in the specific humidity profile likely related in some way to the effects of melting (Johnson et al. 1996).

The  $Q_2$  profile for the IFA, however, contrasts in several ways from those for the OSA and Marshall Islands. First, negative values can be seen below 850 hPa or 1.5 km. Second, the IFA  $Q_2$  profile does not exhibit a prominent double-peak structure, at least for the IOP mean. There are times, however, when the IFA  $Q_2$  profiles do resemble those for the ITCZ and Marshall Islands. An example is during a period of heavy rainfall on 11-17 December (Fig. 7.2), just prior to the strong westerly wind burst at the end of December (Gutzler et al. 1994, Kiladis et al. 1994). Averaged over this one-week period,  $Q_1$  and  $Q_2$  are positive everywhere and the peaks are displaced, indicative of deep convective activity (e.g., Yanai et al. 1973). A double peak in  $Q_2$  is also present (though not very pronounced). Note from Fig. 7.2 that both  $Q_1$  and  $Q_2$  are considerably larger than  $Q_R$  (computed assuming clear-sky conditions) during this convectively active period.

What, then, is the cause of the negative  $Q_2$  at low levels within the IFA averaged over the entire IOP? To understand this behavior, we examine time series of  $Q_2$  for the entire IOP. For the larger area, the OSA,  $Q_2$  is mostly positive throughout the troposphere, except for several short periods in November and early December (Fig. 7.3). Since

$$\frac{1}{g} \int_{P_T}^{P_s} Q_2 dp = L(P_0 - E_0), \quad (7.23)$$

where  $P_T$  is the tropopause pressure and  $P_s$  is the surface pressure, then mostly positive  $Q_2$  implies that  $P_0$  exceeds  $E_0$  most of the time. Indeed, this is true, except for brief periods in November and early December (Fig. 7.3). These results are not surprising considering that the area of the OSA is large enough to encompass significant precipitating systems for most of the IOP. In particular, the rainfall in this domain is heavy enough to produce a net positive  $Q_2$  (net removal of water vapor) most of the time, implying a net transport of water vapor into the OSA ( $P_0 > E_0$ ) on most days during the IOP.

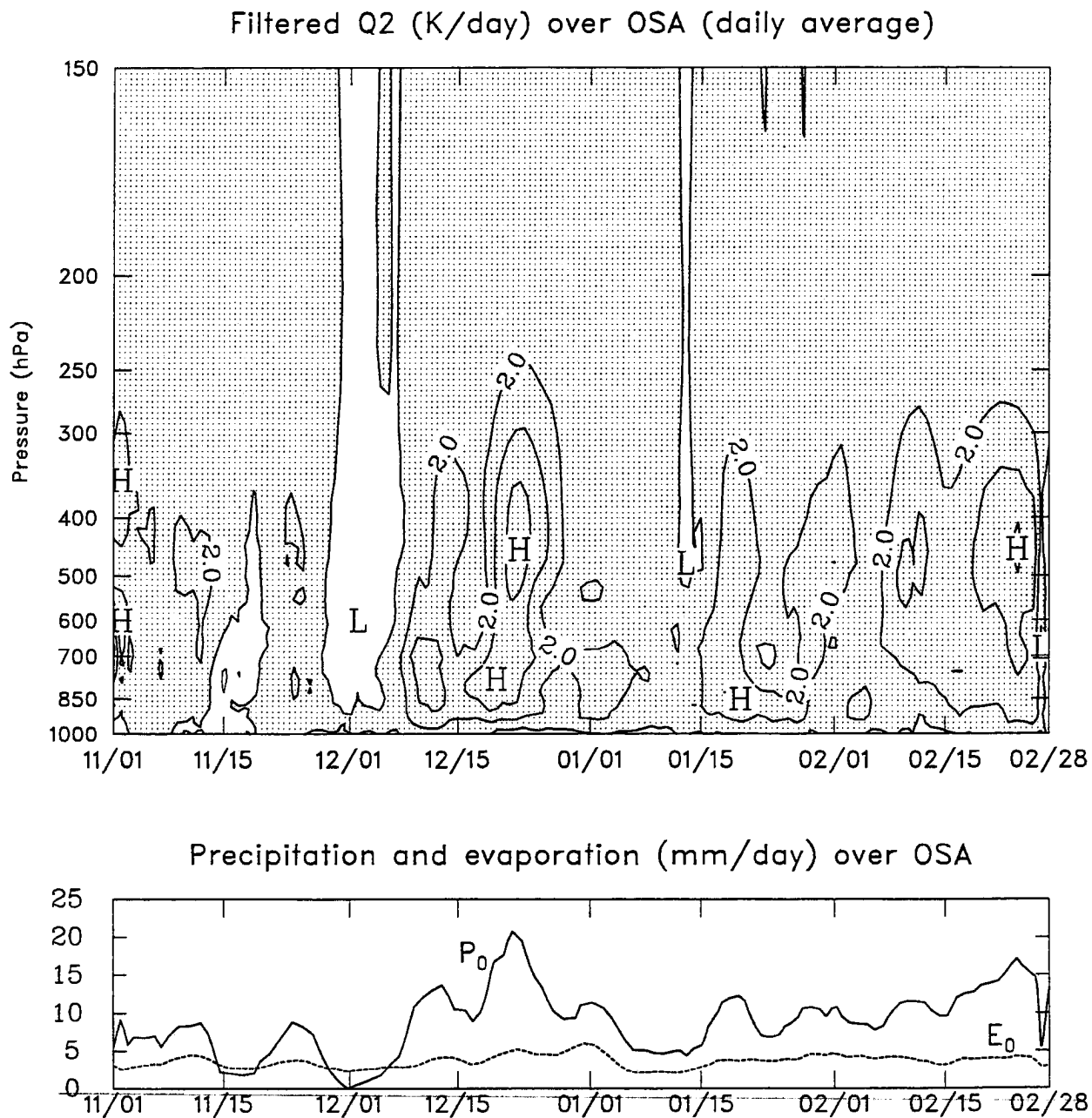


Figure 7.3: IOP time series of  $Q_2$  (top panel, positive values shaded) and precipitation rate  $P_0$  and evaporation rate  $E_0$  (bottom panel) for Outer Sounding Array.

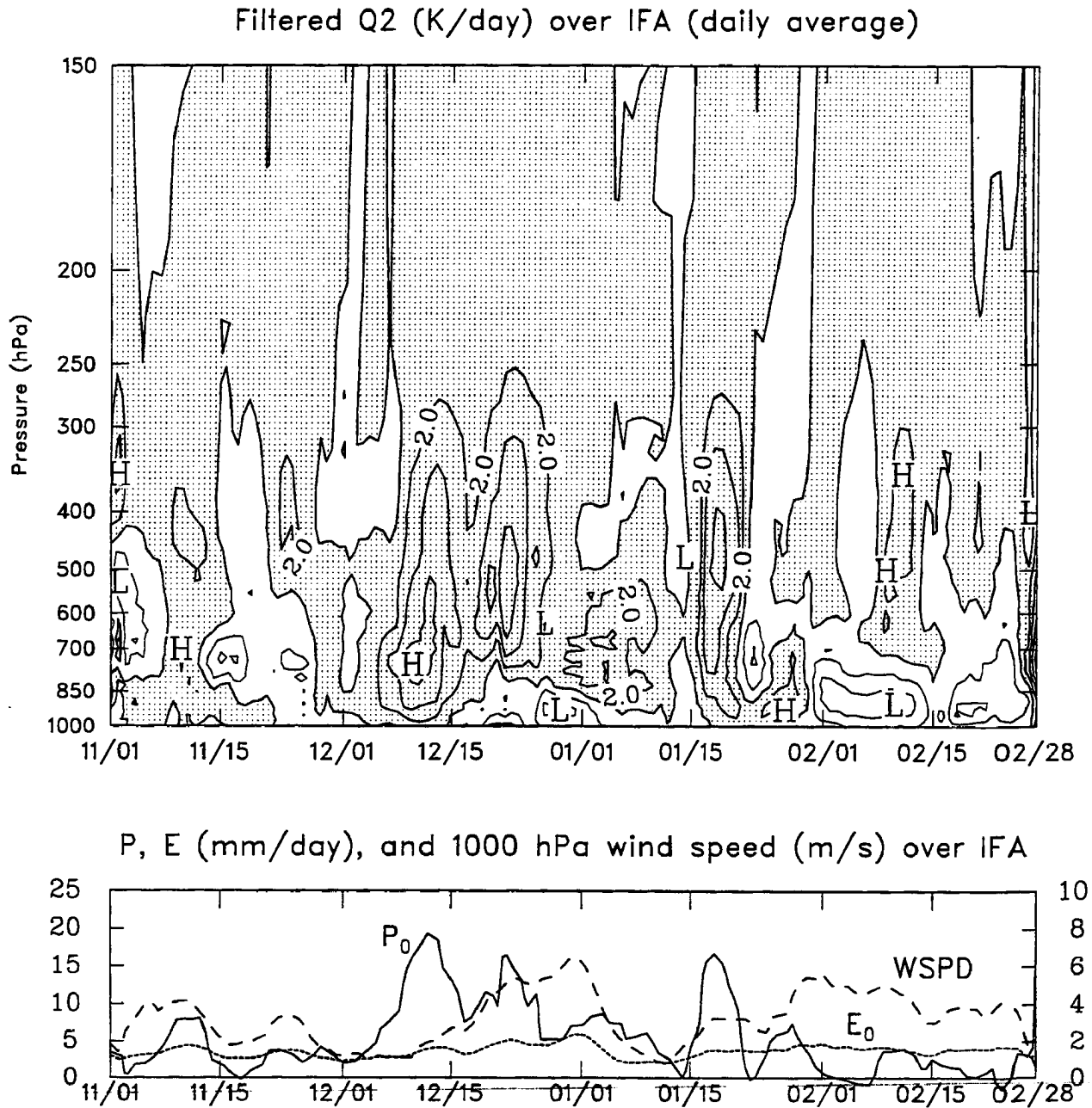


Figure 7.4: IOP time series of  $Q_2$  (top panel, positive values shaded) and precipitation rate  $P_0$  and evaporation rate  $E_0$  (bottom panel) for Intensive Flux Array. Also, surface wind speed has been added to bottom panel.

In contrast, the time series of  $Q_2$  for the IFA shows frequent periods of negative values (moistening), particularly in the lower troposphere (Fig. 7.4). Note, for example, the strong moistening below 800 hPa during the last two weeks of December and the first two weeks of February. These periods correspond to two primary westerly wind bursts during COARE, as can be seen from the time series of the surface wind speed in the lower panel. It is also evident from the lower panel that  $E_0$  is either approximately equal to or exceeds  $P_0$  during significant portions of these strong-wind periods. This behavior is consistent with the apparent moistening (negative  $Q_2$ ) in the lowest 2 km in Fig. 7.4. As will be seen, this apparent moistening is accomplished by mixed-layer turbulent transport as well as transport by shallow cumulus clouds (e.g., as in the Atlantic tradewind belt; Nitta and Esbensen 1974). However, whether or not these processes lead to an *actual* moistening depends on the balance of competing effects, namely, subsidence and advection. For example, the time series of relative humidity in Fig. 4.13a indicates drying at and just above 800 hPa during the late-December westerly wind burst whereas moistening occurs near this level during the first two weeks in February. The drying in the former case appears to be related to dry intrusions into the Tropics from the Subtropics (Numaguti et al. 1995, Yoneyama and Fujitani 1995; Mapes and Zuidema 1996), apparently associated with perturbations in the meridional wind that accompany mixed Rossby-gravity waves (Numaguti et al. 1995). In the latter case drying effects are not as prominent and there is a gradual moistening throughout the period.

The mean profiles of  $Q_1$ ,  $Q_2$ , and  $Q_R$  for the two westerly wind bursts (27 December-3 January and 2-10 February) and an undisturbed period (14 November-5 December) are presented in Fig. 7.5. The averages shown are for those times when  $P_0 < 3.5 \text{ mm day}^{-1}$  (roughly the average evaporation rate during the IOP) in an attempt to isolate periods with predominantly nonprecipitating cumulus. For this thresholding, the averages in Fig. 7.5 represent 34 %, 67 %, and 50 % of the total six-hourly soundings for the December-January, February, and November-December cases, respectively. The patterns of  $Q_1$  and  $Q_2$  are similar for all these periods: positive  $Q_1$  near the surface with negative values above and negative  $Q_2$  below 500-700 hPa.  $Q_1$  and  $Q_2$  are both generally small above 700

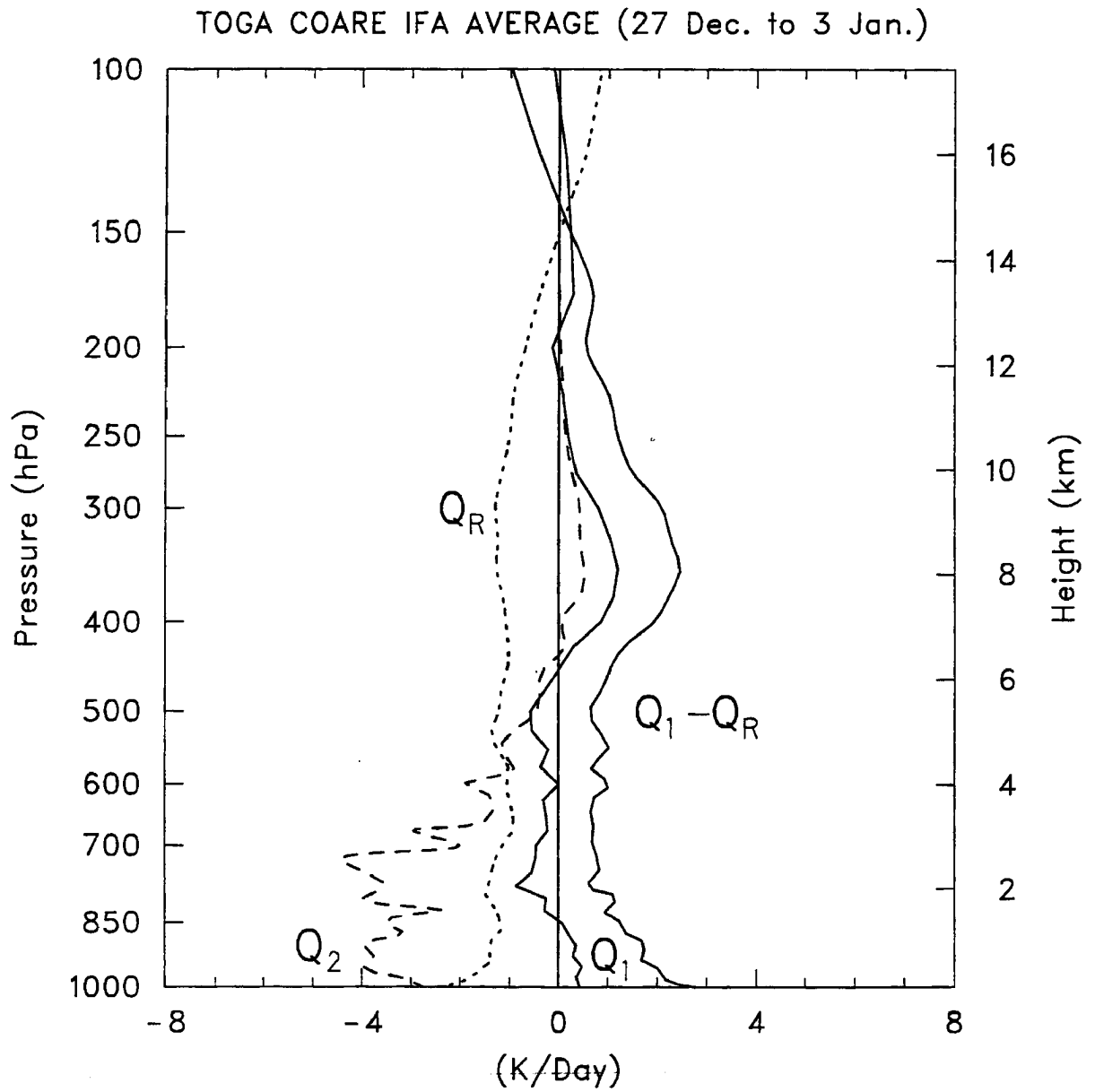


Figure 7.5:  $Q_1$ ,  $Q_2$ ,  $Q_R$ , and  $Q_1 - Q_R$  profiles for two westerly wind burst periods (27 December-3 January and 2-10 February) and an undisturbed ISO phase (14 November-5 December).

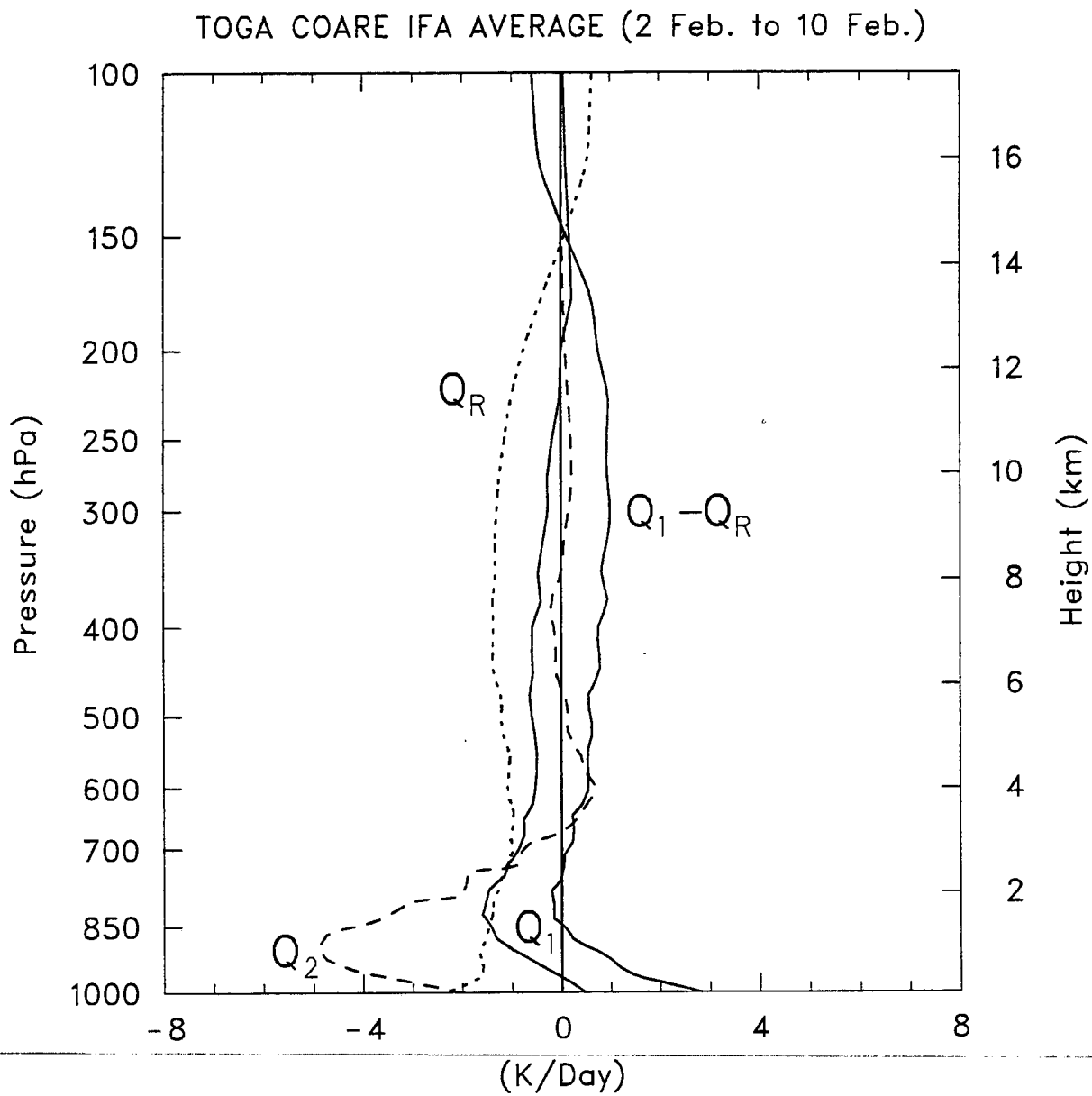


Figure 7.5: Continued.

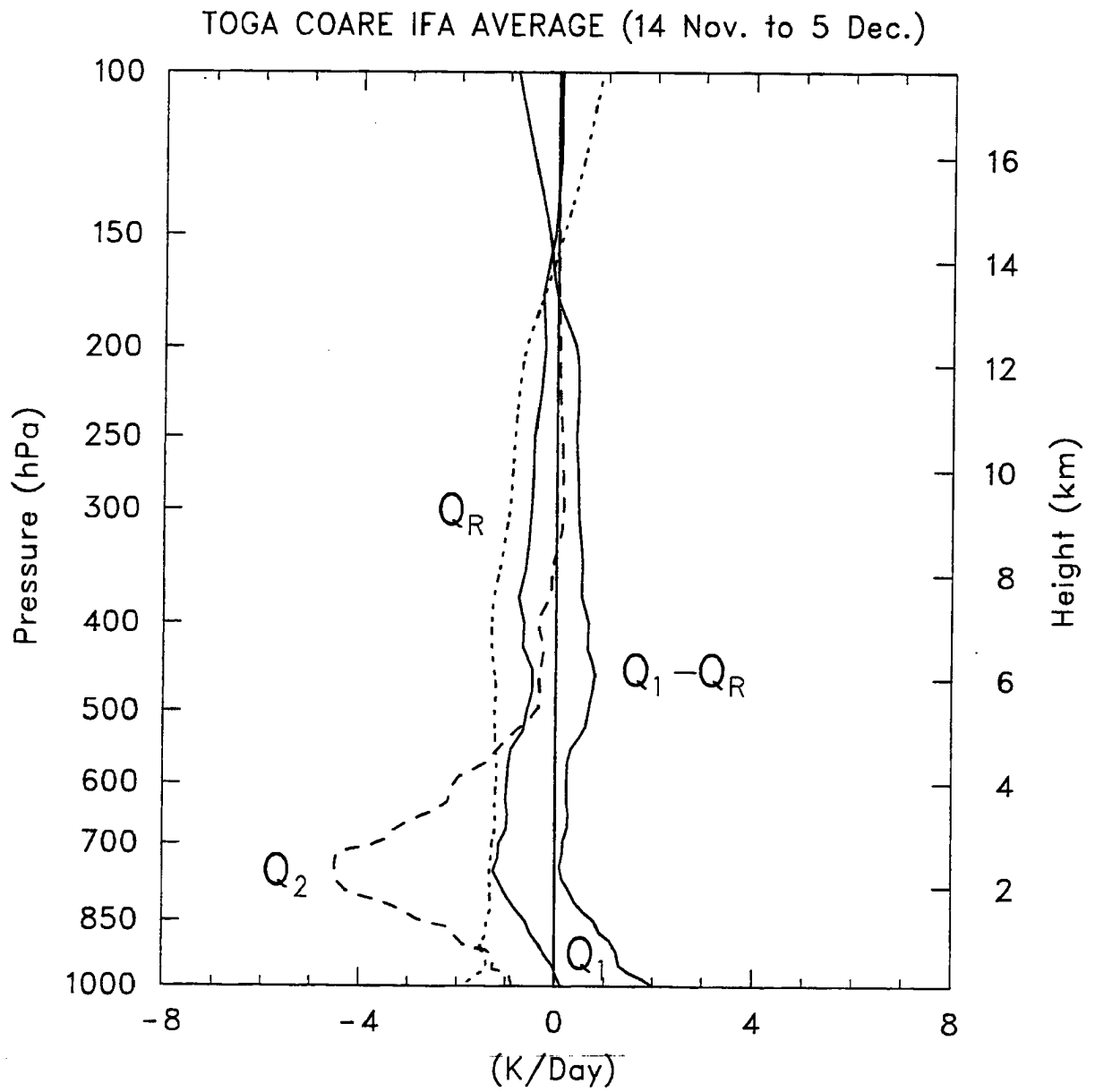


Figure 7.5: Continued.

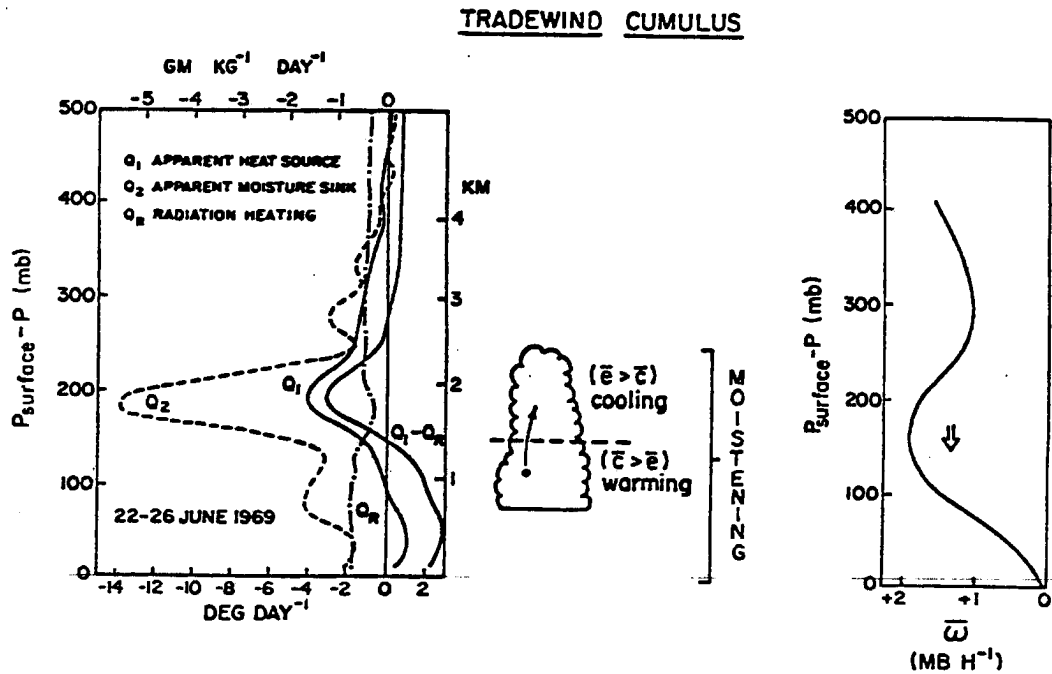


Figure 7.6: (Left) The observed  $Q_1$ ,  $Q_2$ ,  $Q_R$ , and  $Q_1 - Q_R$  for the undisturbed BOMEX period 22-26 June 1969 (From Nitta and Esbensen 1974). (Center) schematic of tradewind cumulus layer showing effects of condensation  $\bar{e}$  and evaporation  $\bar{e}$  on the heat and moisture budgets. (Right) Mean vertical  $p$ -velocity  $\bar{\omega}$  over budget area.

hPa, except in the December-January case near 300-400 hPa. These upper-level positive values reflect the abundance of high clouds present during portions of this westerly wind burst (Velden and Young 1994). The low-level profiles are qualitatively similar to those determined by Nitta and Esbensen (1974) for undisturbed tradewind conditions during the Barbados Oceanographic and Meteorological Experiment (BOMEX) (Fig. 7.6), except that the levels of the maxima and minima differ from case to case. This probably suggests that the equatorial western Pacific may act like the trade wind regime during both strong low-level winds associated with the ISOs and under undisturbed conditions. During the light wind undisturbed period (14 November-5 December), both moistening and cooling peaks are located at the same level (750 hPa), about 50 hPa higher than that for undisturbed tradewind conditions in BOMEX (Fig. 7.6). This difference may be due to more active shallow cumuli and a weaker (and slightly deeper) trade-wind inversion above a warmer sea surface in the western Pacific than in the Atlantic. During the two westerly wind burst periods, significant moistening in the lower part of the cloud layer (Figs. 7.5a and b) is an indication of the prevalence of even shallower cumulus clouds than the light-wind period. These contrasting cumulus regimes may be indicative of the two populations of tropical cumuli proposed by Esbensen (1978). One type, referred to as “sub-inversion” cumulus by Esbensen or “forced” cumulus by Stull (1985), are dynamically inactive clouds that are principally a reflection of overshooting of mixed-layer eddies. These may be the prevalent type of clouds during the high-wind periods (photographs of these clouds will be shown later). Another type, “inversion-penetrating” cumulus (Esbensen 1978) or “active” cumulus (Stull 1985), experience considerable buoyancy and growth due to latent heat release. This type may predominate during the light-wind periods.

Assuming the vertical convergence of eddy heat flux is small, the profile of  $Q_1 - Q_R$ , usually characterized in the cloud layer by a cooling aloft and a warming below, can be explained by an excess of evaporation over condensation in the upper half of the cloud layer and the reverse below. As confirmed in the diagnostic study of Nitta (1975), this behavior occurs as cloud droplets, condensed in the lower part of the cloud layer, are carried aloft, where they are detrained and evaporated (also see Betts 1975). The pronounced moistening

in the upper part of the cloud layer is consistent with this explanation. The cloud and subcloud layers are closely coupled because it is the surface evaporation which provides the source for the moistening of the entire layer. For the steady-state tradewind boundary, this convective moistening is offset by subsidence drying. In our TOGA COARE cases,  $Q_1 - Q_R$  values, although positive most of the times (except the February case), do show minima in the upper part of the cloud layer. The positive values of  $Q_1 - Q_R$  in the upper part of the cloud layer are due to two possible reasons: (1) there might be a mixture of convective regimes, especially some deep convective cells; (2) the vertical convergence of eddy heat flux might not be small in the cloud layers (LeMone, personal communication). Positive values of  $Q_1 - Q_R$  in the subcloud layer (where  $\bar{c}$  and  $\bar{e}$  are zero) are from (7.1) consistent with a heat flux in the mixed layer that decreases with height (e.g., LeMone and Pennell 1976).

## 7.4 Diagnostic model results

### 7.4.1 Late-December/early-January westerly wind burst

Profiles of saturation moist static energy  $\bar{h}^*$  and moist static energy at cloud-top level  $h_D$  for the period 27 December-3 January are shown in Fig. 7.7. Evidence of a weak trade inversion can be seen in a  $\sim 100$ -hPa layer centered near 800 hPa where  $\bar{h}^*$  increases with height. While this inversion is not nearly as strong as the trade inversion during undisturbed periods in the western Atlantic BOMEX region (Nitta and Esbenson 1974, Fig. 4 upper panel; Nitta 1975, Fig. 4), it does resemble those observed during disturbed periods of the Atlantic trades (Nitta and Esbenson 1974, Fig. 4 lower panel; Nitta 1975, Figs. 10 and 14). While the inversion in Fig. 7.7 is relatively weak, it is apparently still of sufficient strength to retard the growth of cumulus clouds and lead to a trade-like cumulus population over the warm pool (Schubert et al. 1995; Mapes and Zuidema 1996; Johnson et al. 1996). Compared to other periods of the IOP, the inversion near 800 hPa is particularly strong during the late-December westerly wind burst.

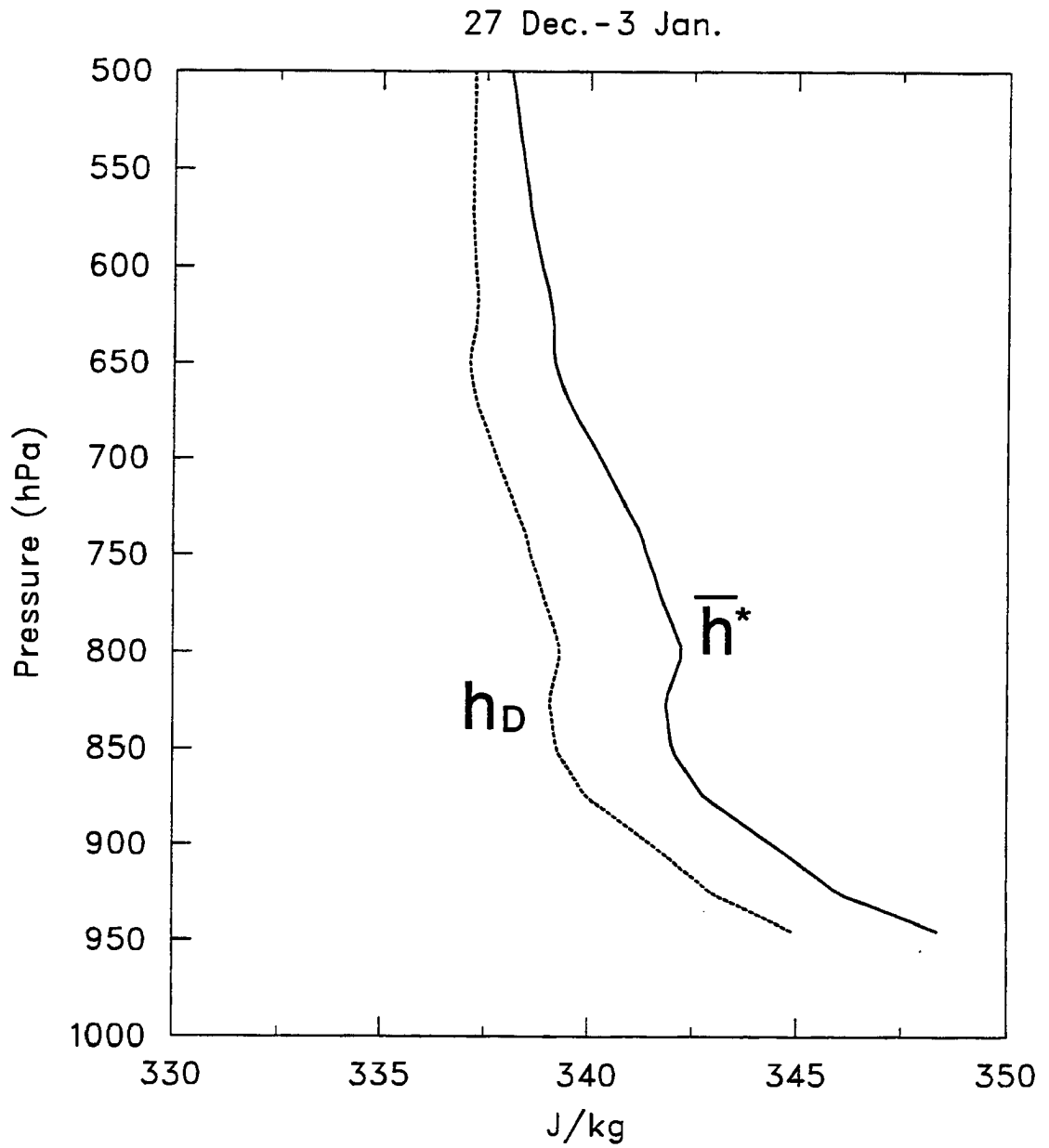


Figure 7.7: Vertical profiles of saturation moist static energy of the environment  $\bar{h}^*$  and moist static energy of the clouds at the detrainment level  $h_D$  during 27 December-3 January westerly wind burst.

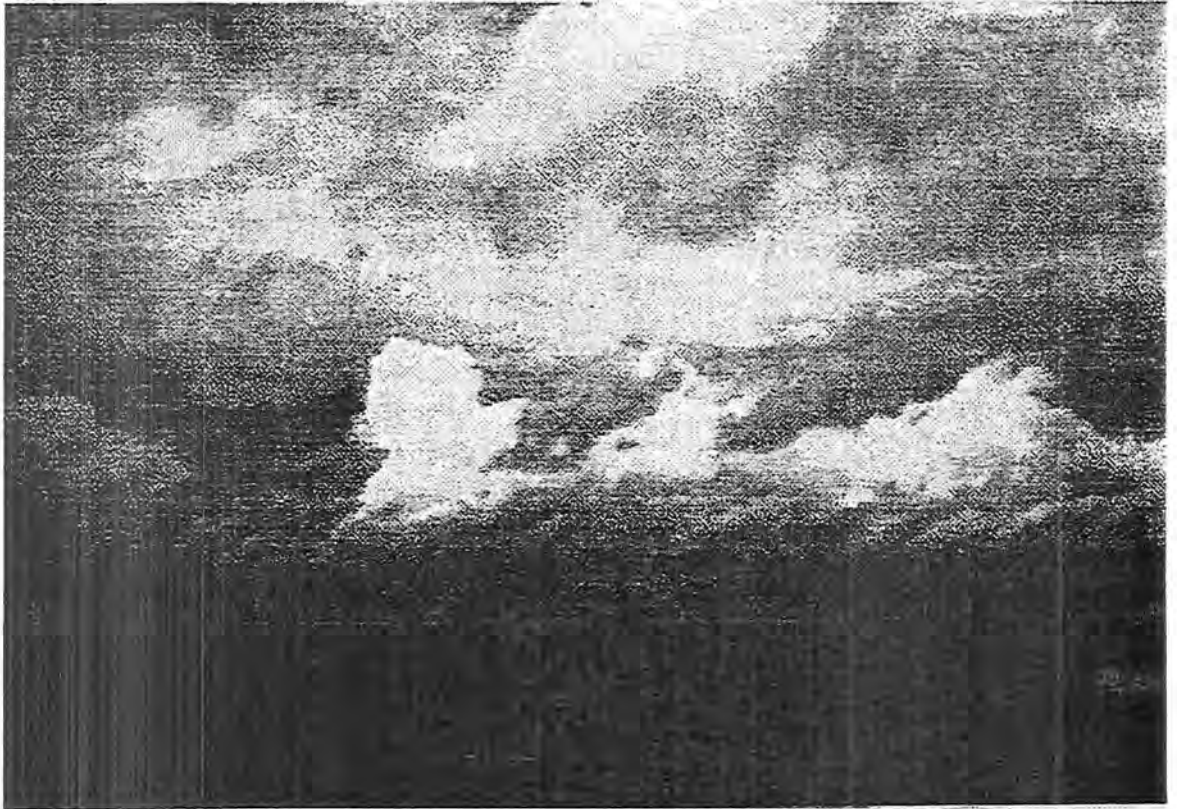


Figure 7.8: A photograph taken from the R/V *Vickers* ( $2.1^{\circ}\text{S}$   $156.3^{\circ}\text{E}$ ) around 0100 UTC on 26 December 1992 (Courtesy Tom Rickenbach). The photograph shows shallow cumulus with tops near 2-2.5 km (assuming a cloud base of  $\sim 0.5$  km) and higher clouds above.

During the 27 December-3 January period, average precipitation over the IFA was light ( $< 6 \text{ mm day}^{-1}$ , Fig. 7.4) as a consequence of extreme vertical wind shear and low- to midtropospheric drying (Lin and Johnson 1996a). Apart from the abundant mid- and high-level clouds present early in this period (Velden and Young 1994) the predominant cloud type was shallow cumulus, as illustrated in the photograph (Fig. 7.8) from the R/V Vickers at  $2.1^\circ\text{S } 156.3^\circ\text{E}$  on 26 December (one day prior to period of study).

Evidence of this shallow cloud field can be seen in the profiles of mass fluxes, entrainment  $\epsilon$  and detrainment  $\eta$  averaged over the 27 December-3 January period (Fig. 7.9). Large values of cloud environmental mass flux,  $M_c$  and  $\tilde{M}$  can be seen below 900 hPa with the mean mass flux  $\bar{M}$  being a small residual. Entrainment and detrainment both peak near cloud base, but there are secondary peaks between 750 and 820 hPa where clouds lose their buoyancy near the trade inversion. *This result is clear evidence of an active tradewind like cumulus field during the westerly wind bursts.* These findings are very similar to the BOMEX tradewind results of Nitta (1975), except that the detrainment peak for this westerly wind burst over the western Pacific warm pool extends slightly above the inversion whereas the Atlantic peaks (at least for two out of the three cases presented by Nitta) are slightly below. This difference may be a consequence of the much-weaker inversion over the warm pool, which allows for greater cloud-top overshooting and some detrainment above the inversion.

The heat and moisture balances (Fig. 7.10) show cooling and moistening due to evaporation of detrained cloud water ( $-LE_u$ ) near cloud top or 800 hPa. Detrainment of heat or  $\delta(s_u - \bar{s})$  (which is a cooling effect in this case since the virtual temperature excess at cloud base is assumed to be zero) is important in the lowest 50-100 hPa of the cloud layer. These detrainment cooling effects are offset by subsidence warming ( $-M_c \partial \bar{s} / \partial p$ ). Detrainment of water vapor  $\delta(q_u - \bar{q})$  is an important moistening effect near cloud base and cloud top. The combined detrainment moistening effects are offset by subsidence drying ( $LM_c \partial \bar{q} / \partial p$ ). These heat and moisture balance results are qualitatively similar to those of Nitta (1975) and Nitta and So (1980) for other cumulus regimes. They most closely resemble Nitta's (1975) MONEX Periods 2 and 3 when the trades were disrupted by an upper-level

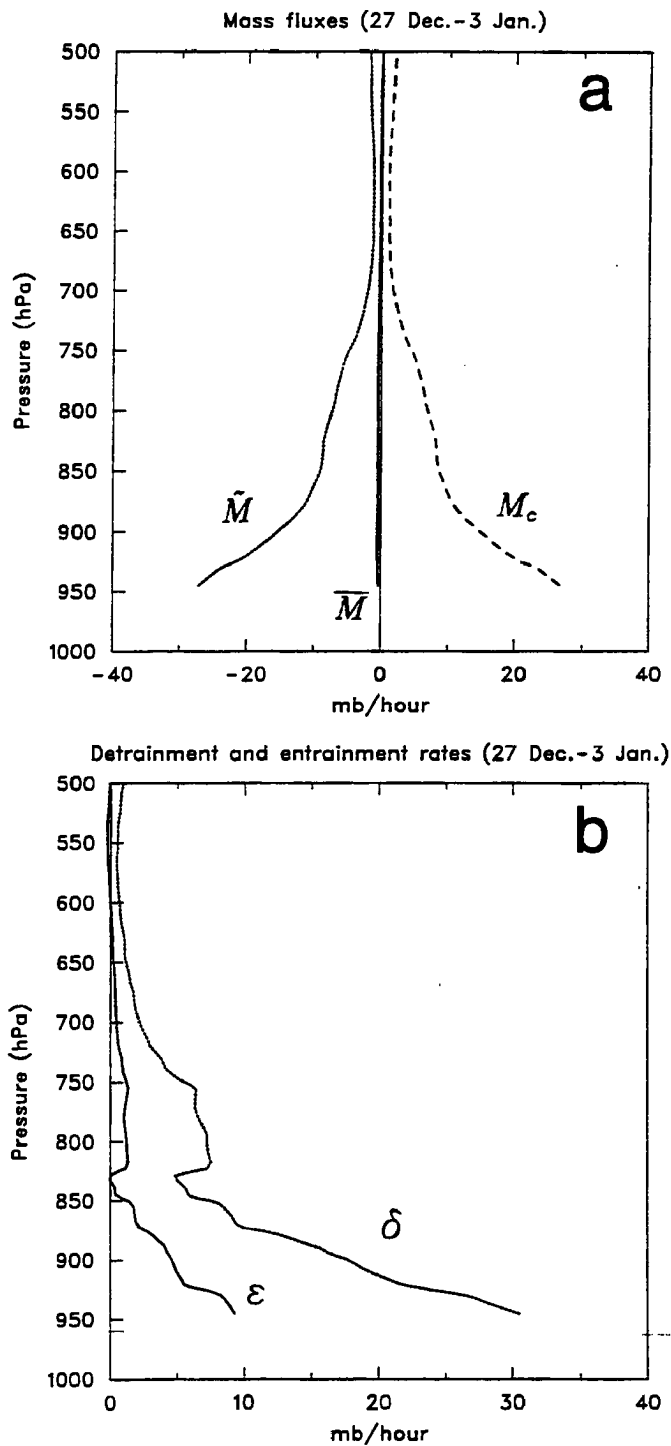


Figure 7.9: (a) Mean, environmental and cumulus mass fluxes and (b) entrainment and detrainment for 27 December-3 January westerly wind burst.

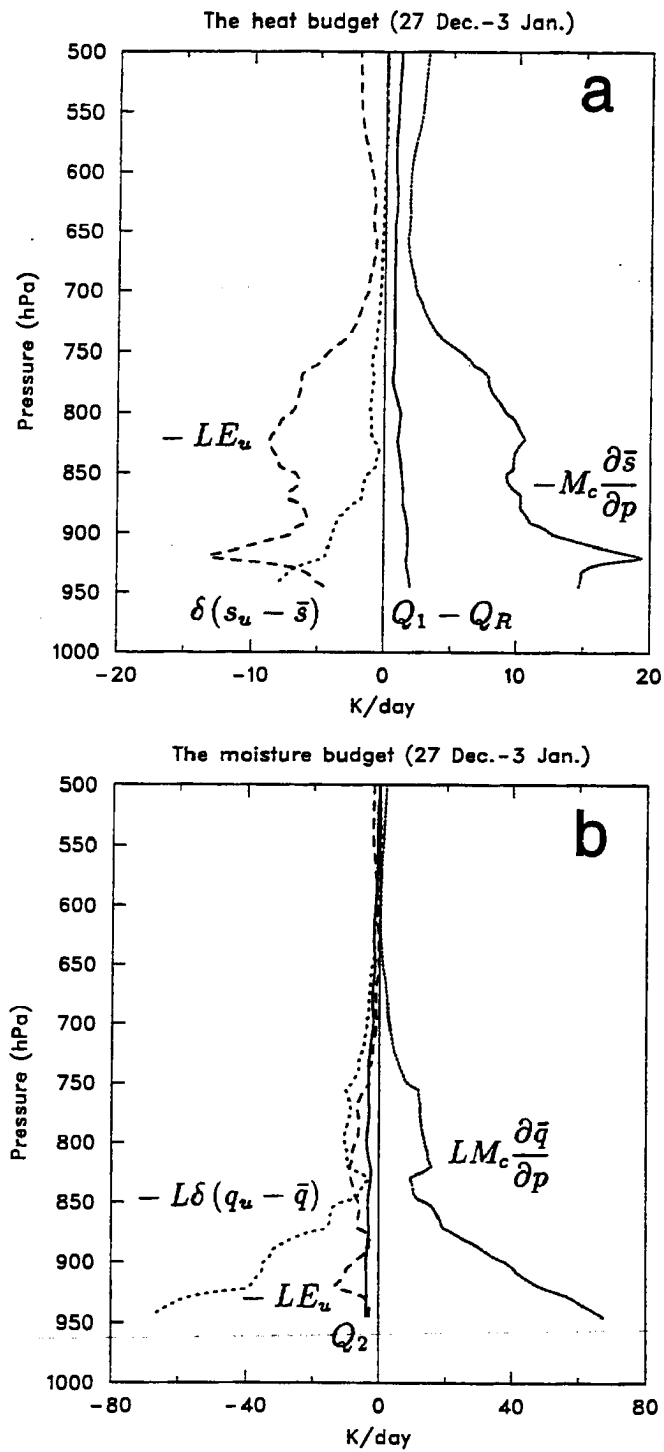


Figure 7.10: (a) Heat and (b) moisture balances for 27 December-3 January westerly wind burst.

trough and an organized cloud cluster, respectively (Nitta's Figs. 13 and 19). During these BOMEX disturbed periods, the trade inversion weakened considerably and some deep convection coexisted with trade cumulus, much as was observed during the COARE westerly wind bursts.

#### 7.4.2 Early-February westerly wind burst

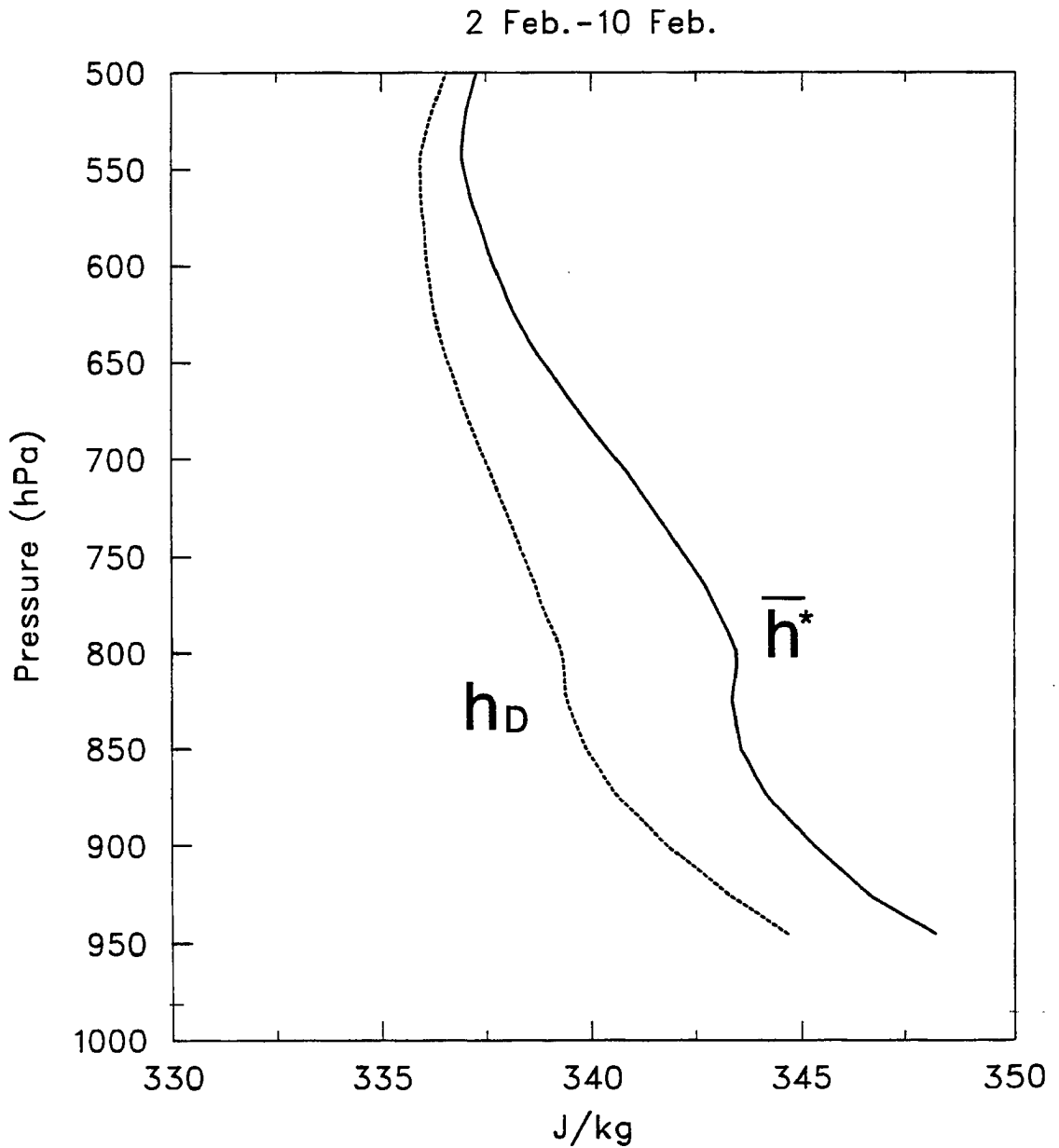


Figure 7.11: As in Fig. 7.7, except for 2-10 February westerly wind burst.

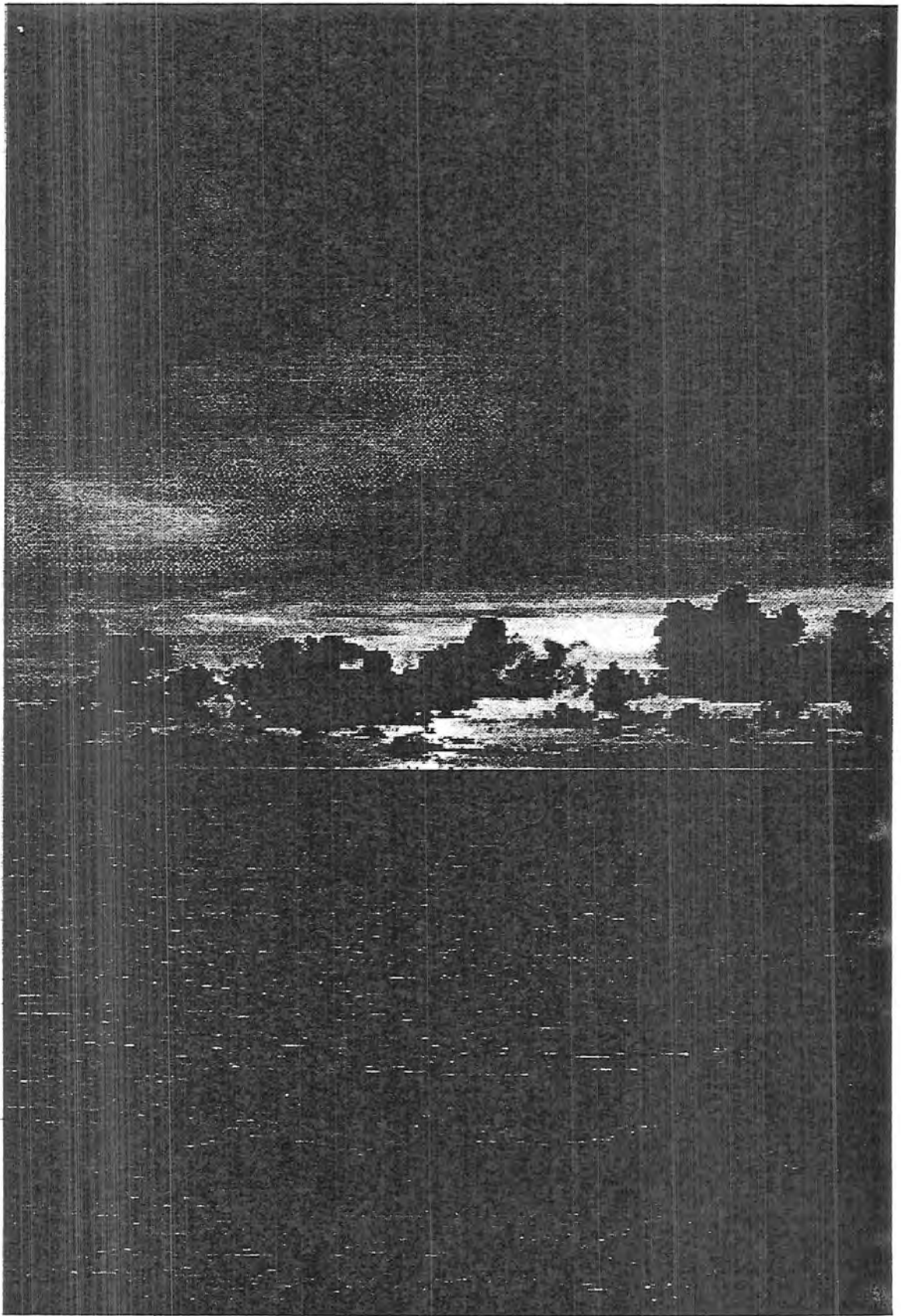


Figure 7.12: A photograph taken from the R/V *Vickers* ( $2.1^{\circ}\text{S}$   $156.3^{\circ}\text{E}$ ) in the evening of 6, 7 or 8 February 1992 (Courtesy Rob Cifelli). The photograph shows shallow cumulus with tops near 1.5 km (assuming a cloud base of  $\sim 0.5$  km).

Mean profiles of  $\bar{h}^*$  and  $h_D$  for the period 2-10 February are shown in Fig. 7.11. Evidence of a trade inversion again appears near 800 hPa, but it is slightly weaker than during the first westerly wind burst (cf Fig. 7.7). Another photograph from the R/V Vickers during the February period illustrates the prevalence of shallow clouds (Fig. 7.12). The mass fluxes, entrainment and detrainment profiles (Fig. 7.13) are similar to those before with a secondary peak in detrainment between 800 and 850 hPa. The detrainment peak is a bit weaker than during the December-January period owing to the slightly weaker inversion. As before, the heat balance (Fig. 7.14) is characterized by cooling effects associated with detrainment (and evaporation) of liquid water and cooler cloudy air offset by subsidence warming. For the moisture balance, moistening from the detrainment of water vapor and evaporation of detrained liquid water are offset by subsidence drying.

For the February westerly wind burst period, there is a peak in low-level moistening (negative  $Q_2$ ) near 900 hPa (Fig. 7.5), as opposed to a very prominent peak near 800 hPa characteristic of the undisturbed Atlantic trades (Nitta and Esbensen 1974, Nitta 1975). The December-January burst has multiple negative  $Q_2$  peaks between 950 and 700 hPa. From Figs. 7.10 and 7.14, these peaks over the warm pool are principally contributed by detrainment of water vapor from updrafts, which is a maximum at lower levels. On the other hand, the undisturbed Atlantic tradewind results show very strong detrainment in the upper part of the cloud layer or near cloud top (Nitta 1975, Figs. 7 and 9). Perhaps the explanation for the different behavior between the undisturbed Atlantic trades and the Pacific westerly wind burst regime is related to strength of the trade stable layer. Specifically, this stable layer is much weaker over the warm pool (note very weak inversions in  $\bar{h}^*$  in Figs. 7.7 and 7.11) such that cumulus detrain less near the warm-pool inversion than in the undisturbed tradewind regime and often penetrate to higher levels (e.g., Williams et al. 1996). However, when the Atlantic trade inversion weakens (e.g., Periods 2 and 3 of Nitta 1975) similar deep convection can occur there and the two regimes are not that distinct.

#### *7.4.3 November-early December undisturbed period*

As discussed in Chapter 5, the period between 14 November and 5 December was characterized by light surface winds and clear skies. Deep convection was generally absent

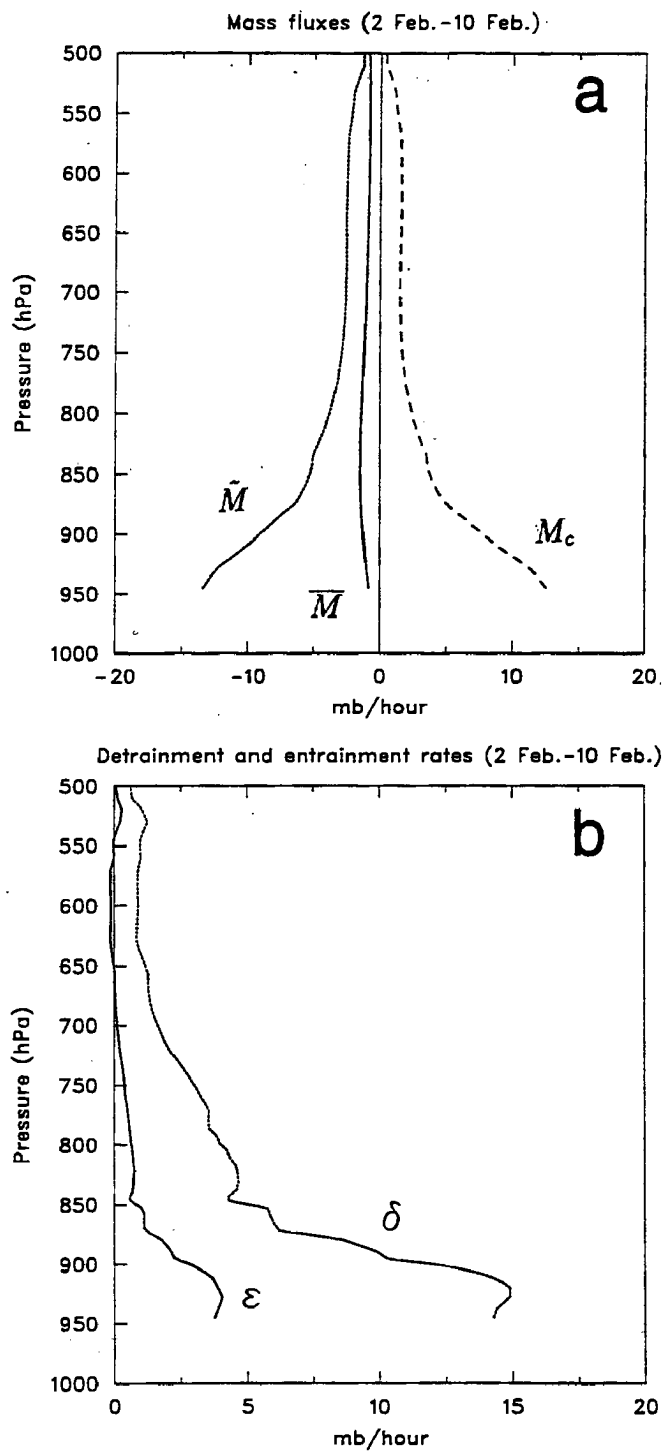


Figure 7.13: As in Fig. 7.9, except for 2-10 February westerly wind burst.

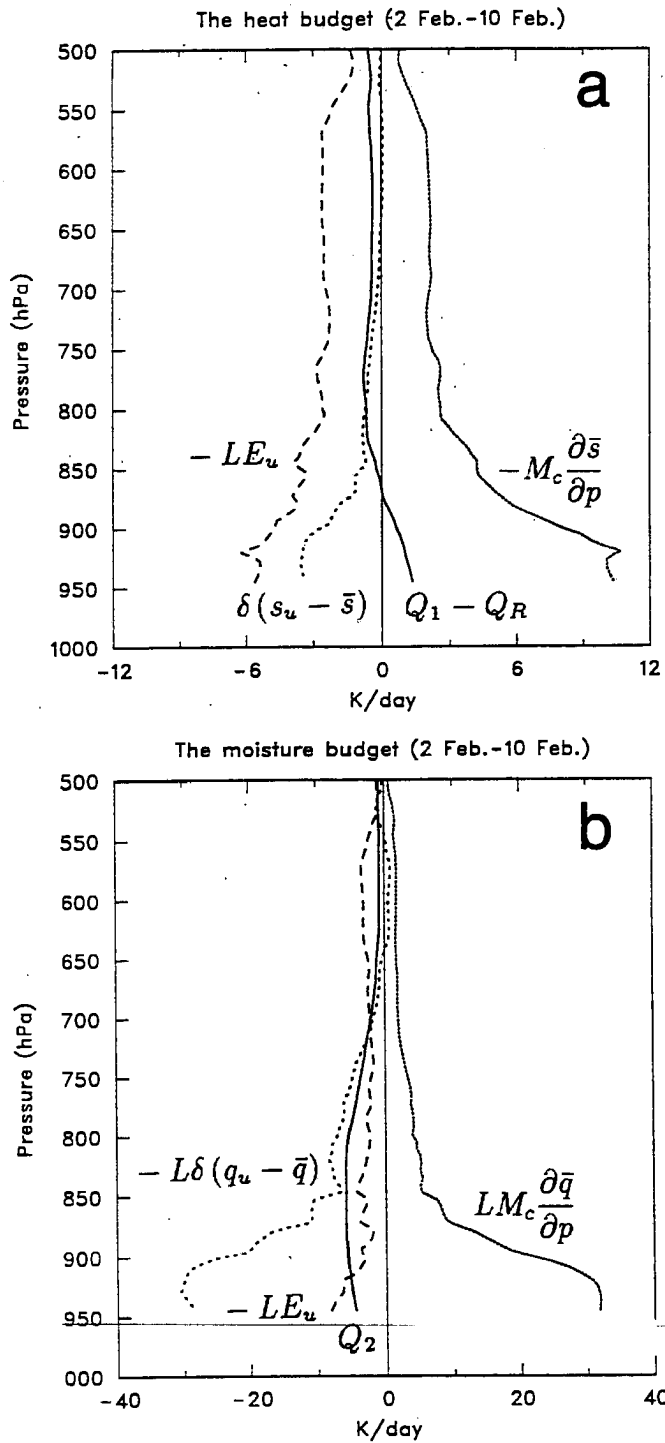


Figure 7.14: As in Fig. 7.10, except for 2-10 February westerly wind burst.

over the IFA. A photograph from the *Xiangyanghong* #5 during this period (Fig. 7.15) clearly shows towering cumulus extending to near the top of the trade stable layer (about 2.5 km) with some evidence of spreading and detrainment near that level (e.g., as in Malkus 1954). The deeper clouds resemble the “inversion-penetrating” cumulus of Esbensen (1978) or “active” cumulus of Stull (1985). Mean profiles of  $\bar{h}^*$  and  $h_D$  for the undisturbed phase of the ISO are shown in Fig. 7.16. A trade inversion, again, can be seen in a 90-hPa layer between 750 and 840 hPa. Not only the trade inversion is much weaker, but also the inversion layer is higher than those during the December-early January and February westerly wind bursts. In addition, below the trade wind inversion, moist static energy at cloud-top level  $h_D$  during the undisturbed period is about 1 K higher than those during two westerly wind bursts. These features are consistent with the  $Q_1$  and  $Q_2$  profiles which indicate a generally more active shallow cumulus and weaker tradewind inversion above a warmer sea surface during the undisturbed period.

The mass fluxes, entrainment and detrainment profiles (Fig. 7.17), as well as the heat and moisture balances (Fig. 7.18) are again similar to those during the westerly wind bursts. The strength of surface winds does not appear to significantly affect the cloud spectral model results, although the development of shallow cumuli during the westerly wind burst events may ultimately be related to the enhanced surface evaporation.

#### 7.4.4 Discussion

The above results for both the westerly wind burst and suppressed, light-wind periods indicate that trade-like cumulus regimes are prevalent over the equatorial western Pacific during the nonprecipitating phases of the 30-60 day intraseasonal oscillation. These findings are consistent with other recent studies (Schubert et al. 1995; Mapes and Zuidema 1996; Johnson et al. 1996) which show trade-stable layers to be commonplace over the equatorial Pacific. Distinctions exist, however, between the shallow cumuli during light- and strong-wind periods. When winds are strong, there is considerable moistening (negative  $Q_2$ ) in the lower part of the cloud layer (Figs. 7.5a and b) where detrainment rates are large (particularly during the December-January burst), presumably in association with many “sub-inversion” or “forced” cumuli that represent upward extensions of boundary-layer

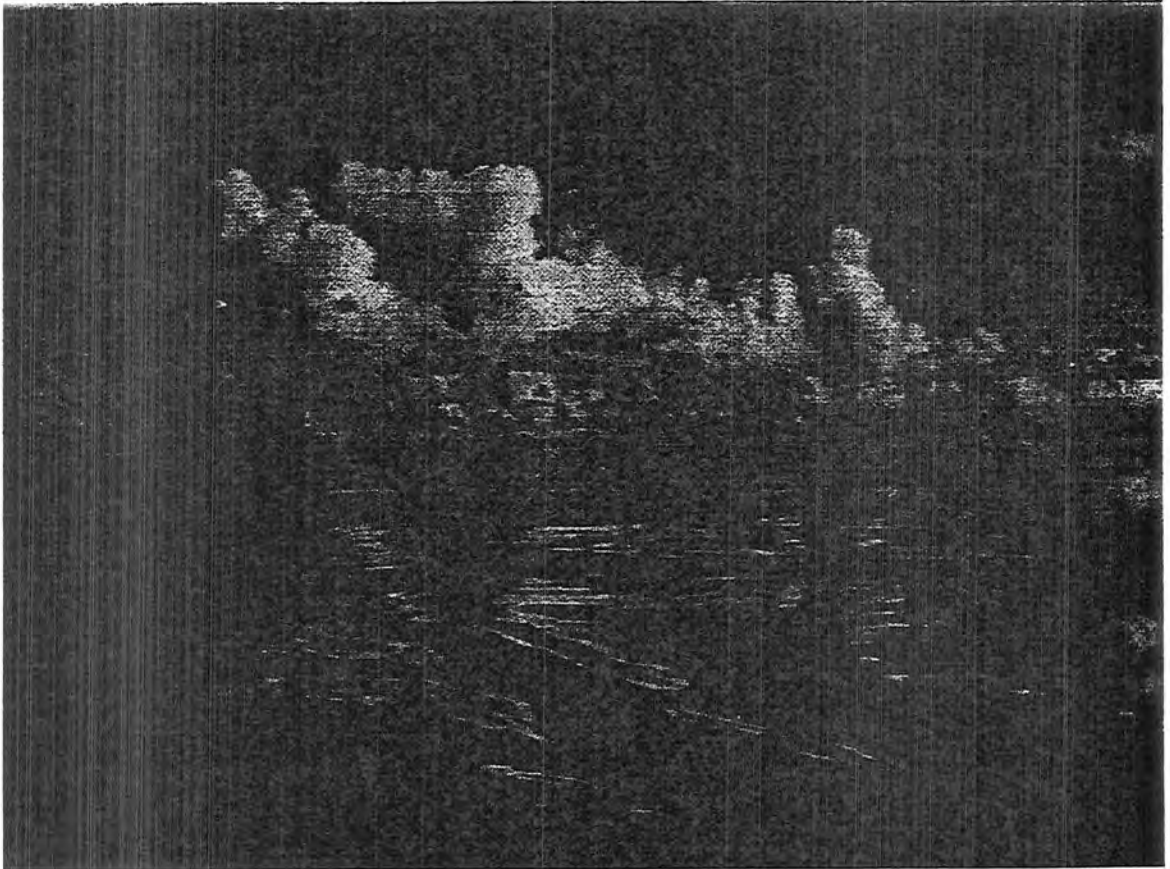


Figure 7.15: A photograph taken from the *Xiangyanghong #5* ( $2.0^{\circ}\text{S}$   $155.8^{\circ}\text{E}$ ) on 21 November 1992). The photograph shows shallow cumulus with tops near 2-2.5 km (assuming a cloud base of  $\sim 0.5$  km).

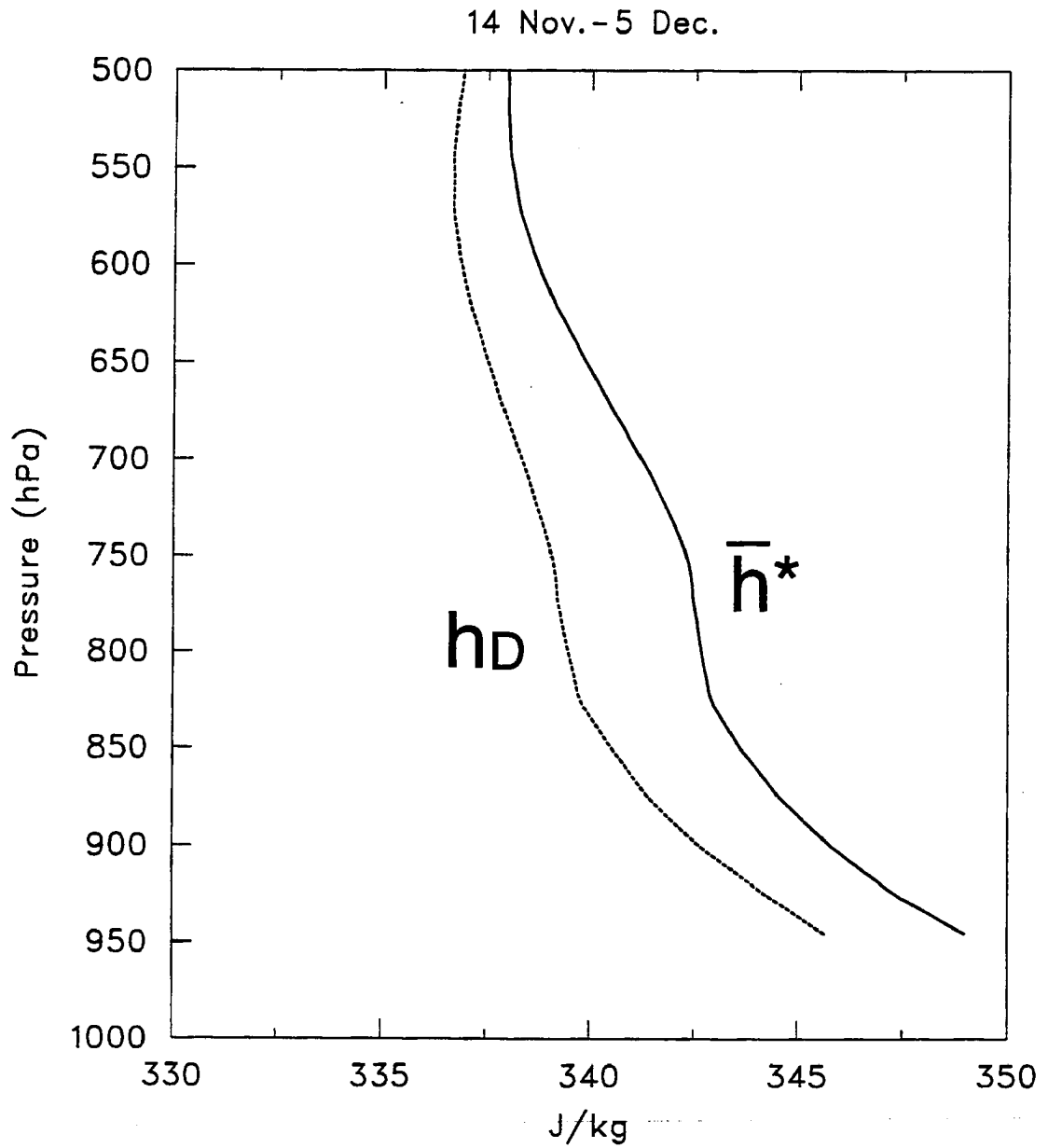


Figure 7.16: As in Fig. 7.7, except for 14 November-5 December undisturbed period.

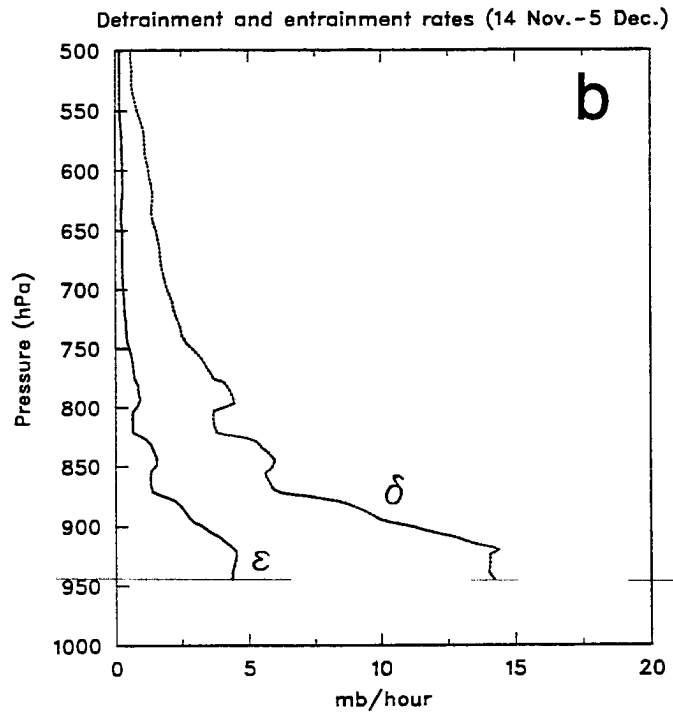
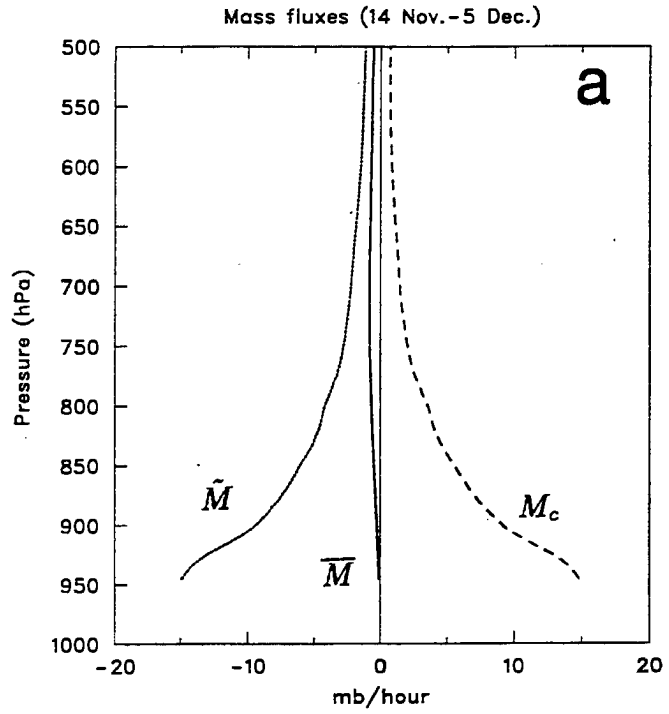


Figure 7.17: As in Fig. 7.9, except for 14 November-5 December undisturbed period.

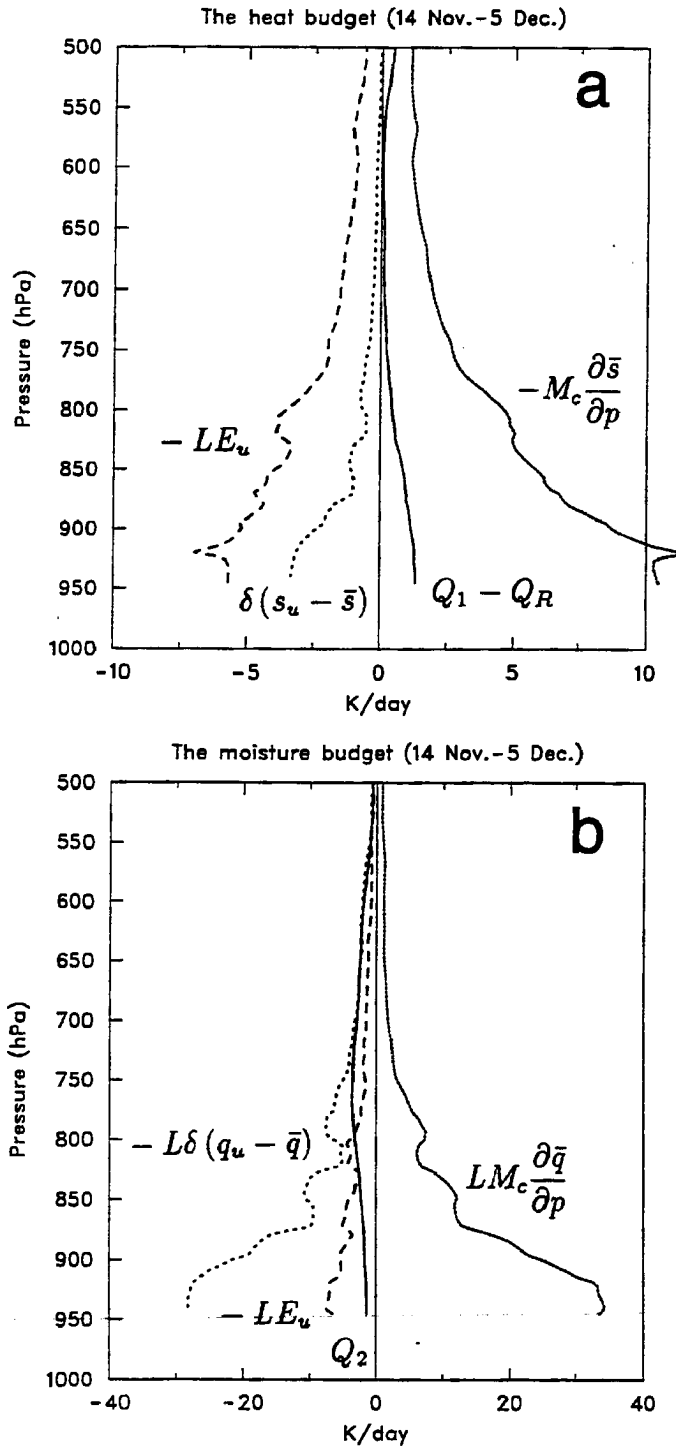


Figure 7.18: As in Fig. 7.10, except for 14 November-5 December undisturbed period.

turbulence (Esbensen 1978; Stull 1985). When winds are light, the cumulus are “active” and extend to a somewhat higher level (as does the trade stable layer), aided by the slightly higher SSTs during light-wind conditions. The profiles of  $Q_2$  during this period shows a peak in the upper part of the cloud layer (Fig. 7.5c), much like the Atlantic trade-wind regime (Nitta and Esbensen 1974).

## 7.5 Summary

Sounding data taken during TOGA COARE reveal a wide range of spatial and temporal variability in the atmospheric heat and moisture budgets. During periods of deep convection, the vertical profiles of the apparent heat source  $Q_1$  and apparent moisture sink  $Q_2$  over the IFA very closely resemble those diagnosed elsewhere in the western Pacific ITCZ regions (e.g., Nitta 1972, Yanai et al. 1973). These profiles are also similar to the four-month mean  $Q_1$  and  $Q_2$  profiles for the extensive area represented by the OSA. However, over the smaller IFA area and on shorter time scales (weeks) the mean  $Q_1$  and  $Q_2$  profiles are strikingly different. In particular, during westerly wind bursts and the undisturbed phase of the ISO, these profiles are characterized by negative  $Q_1$  and  $Q_2$  for a major part of the lowest 2 km. These profiles closely resemble those observed in tradewind cumulus regime of the western Atlantic (Nitta and Esbensen 1974, Nitta 1975) and the convective mixed layer over the East China Sea during cold-air outbreaks (Nitta and So 1980).

However, there are noticeable differences in the shallow cumulus between the strong- and light-wind periods. When winds are strong, there is greater moistening (negative  $Q_2$ ) near cloud base in association with “sub-inversion” (Esbensen 1978) or “forced” (Stull 1985) type cumuli that are in part a manifestation of overshooting boundary-layer eddies. When winds are light, the cumulus are slightly deeper (“inversion-penetrating” after Esbensen 1978 or “active” after Stull 1985) and the moistening peaks in the upper part of the cloud layer (similar to the Atlantic trades, Nitta and Esbensen 1974). Higher SST (by 1 K) and weaker wind shear during the latter period likely contribute to the more active cumuli at that time.

The cloud spectral diagnostic method of Ogura and Cho (1973) and Nitta (1975) has been applied to the study of the shallow cumulus fields during two westerly wind burst periods, 27 December-3 January and 2-10 February, and a suppressed, light-wind period, 14 November-5 December. Computed profiles of mass fluxes, entrainment, detrainment and heat and moisture balances all resemble those for the western Atlantic trades (particularly the somewhat disturbed trades, Nitta 1975) during these periods. This findings leads to the conclusion that *the equatorial western Pacific warm pool boundary layer develops tradewind-like characteristics with abundant shallow cumulus during both westerly wind bursts and suppressed, light-wind periods and these episodic "trade-like" regimes are prominent enough to impact the seasonal (IOP-mean) distributions of boundary-layer heating and moistening.*

## Chapter 8

### SUMMARY AND FUTURE WORK

#### 8.1 Summary

In order to gain a clear understanding of global climate change, the ENSO phenomenon, and the intraseasonal variability of the coupled atmosphere-ocean system, the TOGA COARE experiment was designed to obtain a better specification of the coupling of the ocean and the atmosphere over the tropical western Pacific (Webster and Lukas 1992). In this study, a four-month gridded dataset over the western Pacific warm pool has been generated based on the TOGA COARE rawinsonde data, using the Barnes objective analysis scheme (Chapter 3). This gridded dataset was carefully compared with ECMWF and NCEP operational model analyses. In addition, many other data from satellites, buoys, and ships have also been analyzed, to study multiscale variabilities in connection with the intraseasonal oscillations. These datasets form the base for diagnostic analyses presented in this dissertation, and they are expected to be useful for later observational, theoretical and modeling studies of tropical ocean and atmosphere.

In Chapters 4 and 5, we documented the basic kinematic and thermodynamic features of the atmosphere over the warm pool at different temporal and spatial scales. A descriptive model of a large-scale westerly wind burst was proposed. Distributions of convective heating, moistening, precipitation, and evaporation were investigated. The behavior of the atmosphere and the response of the ocean surface before, during, and after the passages of westerly wind bursts were examined based on various data from rawinsonde, buoys, satellites, Doppler radar, to operational models.

One of achievements of this study is an investigation of the phase relationship among the ISO-related disturbances, surface heat fluxes, SSTs, and westerly winds. The results of this effort can be used to validate ISO theories and model results. Three prominent westerly wind bursts associated with the ISOs occurred over the IFA during the four-month IOP. COARE data reveal that the vertical wind shear (more than  $50 \text{ m s}^{-1}$ ) and the vertical extent of westerlies during the peak westerly wind bursts were far greater than previously recognized. Heavy precipitation usually fell 1 to 3 weeks prior to the peak westerly wind bursts. Subsidence dominated when strong westerly winds prevailed. The tropospheric vertical wind shear associated with tropical low-frequency oscillations strongly modulated convective heating and moistening. SSTs reached their maximum during the undisturbed phase of the ISOs. They gradually decreased as convection intensified, and reached their minimum during the periods of peak westerly winds, when deep convection was generally suppressed over the IFA.

The mean low-level equatorial flow over the western Pacific was westerly, interrupted occasionally by brief periods of easterly flow. The perturbation westerlies to the west of the disturbance associated with the ISO were usually stronger than the perturbation winds to the east. Maximum surface latent heat flux usually occurred during the peak westerlies, whereas the surface sensible heat flux peaked prior to the strongest westerlies. This evidence contradicts the WISHE mechanism (Emanuel 1987; Neelin et al. 1987; Yano and Emanuel 1991), previously used to explain the maintenance and eastward propagation of the ISOs.

IR data for the four-month IOP and vertical motion fields indicate that the intensity of convection, height of maximum upward motion, and SST all increased from west ( $140^\circ\text{E}$ ) to east across the COARE domain. IOP-mean IR data show a double-ITCZ structure north and south of the IFA, although marked variability in the patterns occurred on a month-to-month basis.

The IOP-mean divergence profile over the IFA shows a very weak divergence near the surface and weak convergence at middle and low levels. The ITCZ-band divergence profiles show strong low-level convergence from the surface to about 700 hPa. The striking difference between the divergence profiles along the equator over the IFA and those north and south in

the ITCZ bands suggests that although the divergence and vertical motion profiles tend to look alike whenever and wherever the convection is strong, great care should be exercised in generalizing divergence and vertical motion profiles from one region to another over the western Pacific warm pool.

Correlations between cold clouds and vertical motion indicate that cold clouds are a good indicator of upper-level upward vertical motion, but not low-level vertical motion. In a significant number of cases, low-level downward motion occurred under very cold cloud tops over the warm pool, indicating extensive optically-thick anvil cloud and non-precipitating high cirrus are a common occurrence over the warm pool.

The IOP-mean relative humidity profile over the IFA shows a primary peak at low levels at the top of the mixed layer and a secondary peak near 550 hPa (near the 0°C level). The secondary peak is not present in either ECMWF or NCEP operational analyses, and the midtroposphere is much dryer in the two model-assimilated results.

Surface latent heat fluxes were positively correlated with surface wind speed and varied between 50 and 100 W m<sup>-2</sup> during light winds to more than 200 W m<sup>-2</sup> during strong westerly wind bursts. Surface sensible heat fluxes, however, did not follow the pattern of surface wind speed and usually peaked during organized deep convection over the IFA.

IOP-mean evaporation and sensible heat flux over the LSA were obtained by adjusting the ECMWF fields toward buoy estimates over the IFA. These values were then used to determine IOP-mean rainfall distribution over the LSA from the moisture budget. The results generally compare well with two satellite remote sensing estimations (SSM/I retrievals and GPI), and the ECMWF model forecast. All four methods indicate an east-west zone of minimal rainfall along the equator. Two heavy rainfall bands coinciding with the double-ITCZ structure were located north and south of the equator. The IFA was mainly located within the minimum rainfall band. Budget-diagnosed rainfall rates over the IFA agree with SSM/I retrievals, but the GPI values are excessive, particularly at times of extensive cirrus.

Comparison of the apparent heat source  $Q_1$  profiles suggests that the long-term mean heating rates over the warm pool have large positive values at all levels of the atmosphere and peak between 400 and 450 hPa. In contrast, the apparent moisture sink  $Q_2$  profiles

show distinctly different features over the warm pool. Positive values (indicating drying) exist in the ITCZ bands north and south of the IFA. However, low-level moistening is evident in the profiles over the IFA, probably due to strong evaporation and upward transport of moisture by shallow cumuli during high winds.

In Chapter 6, we investigated diurnal variability of the atmosphere and ocean surface during undisturbed and disturbed phases of the ISOs, namely clear-sky, light-wind, and cloudy-sky, strong-wind conditions. Popcorn-type precipitating cells usually developed over the warm pool in the afternoon in response to strong surface heating under clear-sky, calm wind condition. The diurnal variation in rainfall is similar to the summer diurnal cycle over continents. The precipitating cells were suppressed from late night to early morning, and detrainment from large populations of shallow cumulus clouds tended to moisten middle and lower troposphere, providing a favorable environment for ISO-related deep convection to occur later. Under cloudy-sky, strong-wind condition, diurnal variability in SST was greatly diminished. Organized deep convection tended to occur frequently during the night and rainfall usually had a maximum in the early morning, similar to many previous observational and modeling results.

During westerly wind bursts and the undisturbed phase of the ISO, heating and moistening profiles are characterized by negative  $Q_1$  and  $Q_2$  over the IFA for a major part of the lowest 2 km. These profiles closely resembled those observed in tradewind cumulus regime. In Chapter 7, we tried to further determine populations of shallow cumulus cloud and other cloud properties based on a diagnostic spectral model. Computed profiles of mass fluxes, entrainment, detrainment and heat and moisture balances all resemble those for the western Atlantic trades (particularly the somewhat disturbed trades, Nitta 1975), indicating that the western Pacific warm pool boundary layer can develop tradewind-like characteristics with abundant shallow cumulus during suppressed and undisturbed periods (which may be frequent outside of ITCZ). These episodic trade-like regimes are prominent enough to impact the seasonal distributions of boundary-layer heating and moistening.

## 8.2 Future work

### *8.2.1 Diagnose the effect of a midlevel stable layer*

Besides the wide existence of a trade wind stable layer over the warm pool, a midlevel stable layer can be frequently observed near the 0°C level. Johnson et al. (1996) have recently investigated this feature and related it to melting in precipitating systems. They noticed that the stable layers near the 0°C level can affect tropical cloud populations. Convection impinging upon or penetrating the stable layers may detrain significantly near the 0°C level, thereby contributing to perturbations in the moisture profile there. Interestingly, preliminary cloud spectral results from TOGA COARE data indicate moderate mass detrainment rates near the 0°C level in some of the analyzed cases. Similar features can also be found in studies of tropical eastern Atlantic (e.g., Nitta 1975), but they generally received no attention. The effect of the midlevel stable layer will be further studied by determining the large-scale heat and moisture balances under different conditions associated with the ISO.

### *8.2.2 Compare and validate modeling results*

The 4-month TOGA COARE data are much better than the GATE data because of the additional detailed information on surface fluxes, SSTs, and the ocean mixed layer. This information, along with rawinsonde, satellite and radar data, provide a unique opportunity to better understand the large-scale effects of organized cloud systems, as well as the mechanisms of tropical low-frequency oscillations. The IFA-mean vertical profiles and various time series from observations have been provided to several modeling groups to force cloud resolving models and single column models, and to validate the model results. The preliminary model results are very encouraging. I hope to be able to use both observation and modeling approaches to investigate how cumulus convection, radiation, organizing effect of vertical wind shear, and other related processes can be more physically parameterized in weather prediction and climate models.

## REFERENCES

- Albright, M. D., E. E. Recker, R. J. Reed and R. Dang, 1985: The diurnal variation of deep convection and inferred precipitation in the central tropical Pacific during January-February 1979. *Mon. Wea. Rev.*, 113, 1663-1680.
- Anderson, J. R., and D. E. Stevens, 1987: The presence of linear wavelike modes in a zonally symmetric model of the tropical atmosphere. *J. Atmos. Sci.*, 44 2115-2127.
- Arakawa, A., 1969: Parameterization of cumulus convection. *Proc. WMO/IUGG Symp. Numerical Weather Prediction*. Tokyo, Japan Meteor. Agency, 1-6.
- Arakawa, A., 1972: Design of the UCLA general circulation model. Numerical simulation of weather and climate. Tech. Rep. No. 7, Department of Meteorology, University of California, Los Angeles, 116pp.
- Arakawa, A., and W. H. Schubert, 1974: Interaction of a cumulus cloud ensemble with the large-scale environment. Part I. *J. Atmos. Sci.*, 31, 674-701.
- Arkin, P. A. and B. N. Meisner, 1987: The relationship between large-scale convective rainfall and cold cloud over the western hemisphere during 1982-1984. *Mon. Wea. Rev.*, 115, 51-74.
- Barnes, S. L., 1964: A technique for maximizing details in numerical weather map analysis. *J. Appl. Meteor.*, 3, 396-409.
- Barnes, S. L., 1973: Mesoscale objective map analysis using weighted time-series observations. NOAA Tech. Memo. ERL NSSL-62, Norman, OK, 60 pp.
- Bellamy, J. C., 1949: Objective calculations of divergence, vertical velocity, and vorticity. *Bull. Amer. Meteor. Soc.*, 30, 45-49.
- Betts, A. K., 1975: Parametric interpretation of trade-wind cumulus budget studies. *J. Atmos. Sci.*, 32, 1934-1945.

- Chang, C.-P., 1977: Viscous internal gravity waves and low-frequency oscillations in the tropics. *J. Atmos. Sci.*, 34, 901-910.
- Chang, C.-P., and K.-M. Lau, 1980: Northeasterly cold surges and near-equatorial disturbances over the winter MONEX area during December 1994, Part II: Planetary-scale aspects. *Mon. Wea. Rev.*, 108, 298-312.
- Chang, C.-P., and K.-M. Lau, 1982: Short-term planetary-scale interactions over the tropics and midlatitudes during northern winter, Part I: Contrasts between active and inactive periods. *Mon. Wea. Rev.*, 110, 933-946.
- Chang, C.-P., and H. Lim, 1988: Kelvin wave-CISK: A possible mechanism for the 30-50 day oscillation. *J. Atmos. Sci.*, 45, 1709-1720.
- Chao, W. C., 1987: On the origin of the tropical intraseasonal oscillation. *J. Atmos. Sci.*, 44, 1940-1949.
- Chao, W. C., and S.-J. Lin, 1994: Tropical intraseasonal oscillation, super cloud clusters, and cumulus convective schemes. *J. Atmos. Sci.*, 51, 1282-1297.
- Chen, S. S., R. A. Jouze, Jr., and B. E. Mapes, 1996: Multiscale variability of deep convection in relation to large-scale circulation in TOGA COARE. *J. Atmos. Sci.*, 53, 1380-1409.
- Chen, S. S., and R. A. Jouze, Jr., 1996: Diurnal variation and life cycle of deep convective systems over the tropical Pacific warm pool. *Quart. J. Ry. Meteor. Soc.*, in press.
- Cheng, C.-P., and R. A. Houze, Jr., 1979: The distribution of convection and mesoscale precipitation in GATE radar echo patterns. *Mon. Wea. Rev.*, 107, 1370-1381.
- Cheng, M.-D., 1989: Effects of downdrafts and mesoscale convective organization on the heat and moisture budgets of tropical cloud clusters. Part II: Effects of convective-scale downdrafts. *J. Atmos. Sci.*, 46, 1540-1564.
- Cheng, M.-D., and M. Yanai, 1989: Effects of downdrafts and mesoscale convective organization on the heat and moisture budgets of tropical cloud clusters. Part III: Effects of mesoscale convective organization. *J. Atmos. Sci.*, 46, 1566-1588.

- Cho, H.-R., and Y. Ogura, 1974: A relationship between cloud activity and the low-level convergence as observed in Reed-Recker's composite easterly waves. *J. Atmos. Sci.*, 2058-2065.
- Chong, M., and D. Hauser, 1989: A tropical squall line observed during the COPT 81 experiment in West Africa: Part II: Water budget. *Mon. Wea. Rev.*, 117, 728-744.
- Chu, P.-S., 1988: Extratropical forcing and the burst of equatorial westerlies in the western Pacific: A synoptic study. *J. Meteor. Soc. Japan*, 66, 549-564.
- Chu, P.-S., and J. Frederick, 1990: Westerly wind bursts and surface heat fluxes in the equatorial western Pacific in May 1982. *J. Appl. Meteor.*, 523-537.
- Ciesielski, P. E., L. M. Hartten, and R. H. Johnson, 1996: Impacts of merging profiler and rawinsonde winds on TOGA COARE analyses. *J. Atmos. Ocean. Tech.*, conditionally accepted.
- Davies-Jones, R. P., 1993: Useful formulas for computing divergence, vorticity, and their errors from three or more stations. *Mon. Wea. Rev.*, 121, 713-725.
- Ding, Y. H., and A. Sumi, 1995: Large-scale atmospheric circulation features during TOGA-COARE IOP. *J. Meteor. Soc. Japan*, 73, 339-351.
- Dopplick, T. G., 1972: Radiative heating of the global atmosphere. *J. Atmos. Sci.*, 29, 1278-1294.
- Dudhia, J., and M. W. Moncrieff, 1987: A numerical simulation of quasi-stationary tropical convective bands. *Quart. J. Ry. Meteor. Soc.*, 113, 929-967.
- Emanuel, K. A., 1987: An air-sea interaction model of intraseasonal oscillations in the tropics. *J. Atmos. Sci.*, 44, 2324-2340.
- Emanuel, K. A., 1988: Reply. *J. Atmos. Sci.*, 45, 3528-3530.
- Emanuel, K. A., J. D. Neelin, and C. S. Bretherton, 1994: On the large-scale circulation of the convecting atmospheres. *Quart. J. Ry. Meteor. Soc.*, 120, 1111-1143.
- Esbensen, S. K., 1978: Bulk thermodynamic effects and properties of small tropical cumuli. *J. Atmos. Sci.*, 35, 826-837.

- Esbensen, S. K., and M. J. McPhaden, 1996: Enhancement of tropical ocean evaporation and sensible heat flux by atmospheric mesoscale systems. *J. Climate*, 9, 2307-2325.
- Esbensen, S. K., E. I. Tollerud and J.-H. Chu, 1982: Cloud-cluster-scale circulations and the vorticity budget of synoptic-scale waves over the eastern Atlantic Intertropical Convergence Zone. *Mon. Wea. Rev.*, 110, 1677-1692.
- Esbensen, S. K., J.-T. Wang and E. I. Tollerud, 1988: A composited life cycle of nonsquall mesoscale convective systems over the tropical ocean. Part II: Heat and moisture budgets. *J. Atmos. Sci.*, 45, 537-548.
- Fairall, C. W., E. F. Bradley, D. P. Rogers, J. B. Edson and G. S. Young, 1995: Bulk parameterization of air-sea fluxes for TOGA COARE. *J. Geophys. Res.*, 101, 3747-3764.
- Flatau, M., P. J. Flatau, P. Phoebus, and P. P. Niiler, 1997: The feedback between equatorial convection and local radiative and evaporative processes: The implications for intraseasonal oscillations. *J. Atmos. Sci.*, in press.
- Foltz, G. S., and W. M. Gray, 1979: Diurnal variation in the troposphere's energy balance. *J. Atmos. Sci.*, 1450-1466.
- Frank, W. M., and J. L. McBride, 1989: The vertical distribution of heating in AMEX and GATE cloud clusters. *J. Atmos. Sci.*, 46, 3464-3478.
- Gadgil, S., P. V. Joseph, and N. V. Joshi, 1984: Ocean-atmosphere coupling over monsoon regions. *Nature*, 312, 141-143.
- Garcia, R. R., and M. L. Salby, 1987: Transient response to localized episodic heating in the tropics. Part II: Far-field behavior. *J. Atmos. Sci.*, 44, 499-530.
- Gill, A., 1980: Some simple solutions for heat induced tropical circulations. *Quart. J. Roy. Meteor. Soc.*, 106, 447-462.
- Graham, N. E., and T. P. Barnett, 1987: Sea surface temperature, surface wind divergence and convection over tropical oceans, *Science*, 238, 657-659.
- Grabowski, W. W., X. Wu, and M. W. Moncrieff, 1996: Cloud resolving modeling of tropical cloud systems during Phase III of the GATE. *J. Atmos. Sci.*, 53, 3684-3709.

- Gray, W. M., 1973: Cumulus convection and larger scale circulation. Part I: Broad-scale and mesoscale considerations. *Mon. Wea. Rev.*, 101, 839-855.
- Gray, W. M., and R. W. Jacobson, Jr., 1977: Diurnal variation of deep cumulus convection. *Mon. Wea. Rev.*, 105, 1171-1188.
- Gray, W. M., 1979: Hurricanes: Their formation, structure and likely role in the tropical circulation. *Meteorology over the Tropical Oceans*, D. B. Shaw, Ed., Royal Meteorology Society, 156-218.
- Greenhut, G. K., 1978: Correlations between rainfall and sea surface temperature during GATE. *J. Phys. Oceanogr.*, 8, 1135-1138.
- Gallus, W. A., Jr., and R. H. Johnson, 1991: Heat and moisture budgets of an intense midlatitude squall line. *J. Atmos. Sci.*, 48, 122-146.
- Gamache, J. F., and R. A. Houze, Jr., 1982: Mesoscale air motions associated with a tropical squall line. *Mon. Wea. Rev.*, 110, 118-135.
- Gamache, J. F., and R. A. Houze, Jr., 1983: Water budget of a mesoscale convective system in the tropics. *J. Atmos. Sci.*, 40, 1835-1850.
- Gutzler, D. S., 1991: Interannual fluctuations of intraseasonal variance of near-equatorial zonal winds. *J. Geophys. Res.*, 96, suppl., 3172-3185.
- Gutzler, D. S., 1993: Uncertainties in climatological tropical humidity profiles: some implications for estimating the greenhouse effect. *J. Climate*, 6, 978-982.
- Gutzler, D. S., and R. A. Madden, 1989: Seasonal variations in the spatial structure of intraseasonal tropical wind fluctuations. *J. Atmos. Sci.*, 46, 641-660.
- Gutzler, D. S., G. N. Kiladis, G. A. Meehl, K. M. Weickmann, and M. Wheeler, 1994: Seasonal Climate Summary: The global climate of December 1992 – February 1993. Part II: Large-scale variability across the tropical western Pacific during TOGA COARE. *J. Climate*, 7, 1606-1622.
- Haertel, P. T., and R. H. Johnson, 1997: Two-day disturbances in the equatorial western Pacific. Submitted to *Quart. J. Ry. Meteor. Soc.*

- Harrison, D. E., and P. S. Schopf, 1984: Kelvin-wave-induced anomalous advection and the onset of surface warming in El Niños events. *Mon. Wea. Rev.*, 112, 923-933.
- Hartmann, D. L., and M. Michelsen, 1989: Intraseasonal periodicities in Indian rainfall. *J. Atmos. Sci.*, 46, 2838-2862.
- Hartmann, D. L., H. H. Hendon, and R. A. Houze, Jr., 1984: Some implications of the mesoscale circulations in tropical cloud clusters for large-scale dynamics and climate. *J. Atmos. Sci.*, 41, 113-121.
- Hayashi, Y., 1970: A theory of large-scale equatorial waves generated by condensational heat and accelerating the zonal wind. *J. Meteor. Soc. Japan*, 48, 140-160.
- Hayashi, Y., and D. G. Golder, 1986: Tropical intraseasonal oscillations appearing in a GFDL general circulation model and FGGE data. Part I: Phase propagation. *J. Atmos. Sci.*, 43, 3058-3067.
- Hayashi, Y., and S. Miyahara, 1987: A three-dimensional linear response model of the tropical intraseasonal oscillation. *J. Meteor. Soc. Japan*, 65, 2909-2923.
- Hayashi, Y., and S. Myyahara, 1987: A three-dimensional linear response model of the tropical intraseasonal oscillation. *J. Meteor. Soc. Japan*, 65, 843-852.
- Hayashi, Y., and D. G. Golder, 1993: Tropical 40-50 and 25-30 day oscillations appearing in realistic and idealized GFDL climate model and the ECMWF dataset. *J. Atmos. Sci.*, 50, 464-494.
- Hayashi, Y. Y., and A. Sumi, 1986: The 30-40 day oscillation simulated in an "aqua planet" model. *J. Meteor. Soc. Japan*, 64, 451-467.
- Hendon, H. H., 1988: A simple model of the 40-50 day oscillation. *J. Atmos. Sci.*, 45, 569-584.
- Hendon, H. H., B. Liebmann, 1990a: A composite study of onset of the Australian summer monsoon. *J. Atmos. Sci.*, 47, 2227-2240.
- Hendon, H. H., B. Liebmann, 1990b: The intraseasonal (30-50 day) oscillation of the Australian summer Monsoon. *J. Atmos. Sci.*, 47, 2909-2923.

- Hendon, H. H., B. Liebmann, 1994: Organization of convection within the Madden-Julian oscillation. *J. Geophys. Res.*, 99, 8073-8083.
- Holland, G. J., 1986: Interannual variability of the Australian summer monsoon at Darwin-1952-82. *Mon. Wea. Rev.*, 114, 594-604.
- Holton, J. R., 1972: Waves in the equatorial stratosphere generated by tropical heat sources. *J. Atmos. Sci.*, 29, 368-375.
- Houze, R. A., Jr., 1977: Structure and dynamics of a tropical squall line system. *Mon. Wea. Rev.*, 105, 1540-1567.
- Houze, R. A., Jr., 1982: Cloud clusters and large-scale vertical motions in the tropics. *J. Appl. Meteor.*, 60, 396-409.
- Houze, R. A., Jr., and C.-P. Cheng, 1981: Inclusion of mesoscale updrafts and downdrafts in computations of vertical fluxes by ensembles of tropical clouds. *J. Atmos. Sci.*, 38, 1751-1770.
- Houze, R. A., Jr., and E. N. Rappaport, 1984: Air motions and precipitation structure of an early summer squall line over the eastern tropical Atlantic. *J. Atmos. Sci.*, 41, 553-574.
- Hu, Q., and D. A. Randall, 1994: Low frequency oscillations in radiative-convective systems. *J. Atmos. Sci.*, 51, 1089-1099.
- Jabouille, P., J. L. Redelsperger, and J. P. Lafore, 1996: Modification of surface fluxes by atmospheric convection in the TOGA COARE region. *Mon. Wea. Rev.*, 124, 816-837.
- Janowiak, J. E., 1992: Tropical rainfall: A comparison of satellite-derived estimates with model precipitation forecasts, climatologies, and observations. *Mon. Wea. Rev.*, 120, 448-462.
- Janowiak, J. E., and P. A. Arkin, 1991: Rainfall variations in the tropics during 1986-89, as estimated from observations of cloud-top temperature. *J. Geophys. Res.*, 96, 3359-3373.
- Johnson, R. H., 1976: The role of convective-scale precipitation downdrafts in cumulus and synoptic-scale interactions. *J. Atmos. Sci.*, 33, 1890-1910.

- Johnson, R. H., 1980: Diagnosis of convective and mesoscale motion during Phase III of GATE. *J. Atmos. Sci.*, 38, 733-753.
- Johnson, R. H., 1984: Partitioning tropical heat and moisture budgets into cumulus and mesoscale components: Implication for cumulus parameterization. *Mon. Wea. Rev.*, 112, 1590-1601.
- Johnson, R. H., 1992: Heat and moisture sources and sinks of Asian monsoon precipitating systems. *J. Meteor. Soc. Japan*, 70, 353-372.
- Johnson, R. H., and D. C. Kriete, 1982: Thermodynamic and circulation characteristics of winter monsoon tropical mesoscale convection. *Mon. Wea. Rev.*, 110, 1898-1911.
- Johnson, R. H., and G. S. Young, 1983: Heat and moisture budgets of tropical mesoscale anvil clouds. *J. Atmos. Sci.*, 40, 2138-2147.
- Johnson, R. H., P. E. Ciesielski, and K. A. Hart, 1996: Tropical inversions near the 0°C level. *J. Atmos. Sci.*, 53, 1838-1855.
- Keen, R. A., 1982: The role of cross-equatorial tropical cyclone pairs in the Southern Oscillation. *Mon. Wea. Rev.*, 110, 1405-1416.
- Keen, R. A., 1987: Equatorial westerlies and southern oscillation. Proceedings of the US TOGA Western Pacific Air-Sea Interaction Workshop. R. Lukas and P. Webster Eds., Honolulu, 121-140.
- Kiehl, J. T., J. J. Hack, and B. P. Briegleb, 1994: The simulated Earth radiation budget of the National Center for Atmospheric Research community climate model CCM2 and comparisons with the Earth Radiation Budget Experiment (ERBE). *J. Geophys. Res.*, 99, 20815-20827.
- Kiladis, G. N., G. A. Meehl, and K. M. Weickmann, 1994: Large-scale circulation associated with westerly wind bursts and deep convection over the western equatorial Pacific. *J. Geophys. Res.*, 99, 18527-18544.
- Knutson, T. R., and K. M. Weickmann, 1987: 30-60 day atmospheric oscillations: Composite life cycles of convection and circulation anomalies. *Mon. Wea. Rev.*, 115, 1407-1436.

- Knutson, T. R., K. M. Weickmann, and J. E. Kutzbach, 1986: Global-scale intraseasonal oscillations of outgoing longwave radiation and 250 mb zonal wind during northern hemisphere summer. *Mon. Wea. Rev.*, 114, 605-623.
- Krishnamurti, T. N., and D. Subrahmanyam, 1982: The 30-50 day mode at 850 mb during MONEX. *J. Atmos. Sci.*, 39, 336-360.
- Krueger, S. K., 1988: Numerical simulation of tropical cumulus clouds and their interaction with the subcloud layer. *J. Atmos. Sci.*, 45, 2221-2250.
- Kuma, K., 1994: The Madden and Julian Oscillation and tropical disturbances in an aqua-planet version of JMA global model with T63 and T159 resolution. *J. Meteor. Soc. Japan*, 72, 147-172.
- Kuo, Y.-H., and R. A. Anthes, 1984: Accuracy of diagnostic heat and moisture budgets using SESAME-79 field data as revealed by observing system simulation experiments. *Mon. Wea. Rev.*, 112, 1465-1481.
- Lafore, J.-P., J.-L. Redelsperger and G. Jaubert, 1988: COmparison between a three-dimensional simulation and Dopplar radar data of a tropical squall line: Transports of mass, momentum, heat and moisture. *J. Atmos. Sci.*, 45, 3483-3500.
- Lander, M. A., 1990: Evolution of the cloud pattern during the formation of tropical cyclone twins symmetrical with respect to the equator. *Mon. Wea. Rev.*, 116, 1194-1202.
- Lattau, B., 1974: Pressure-wind relationship in the equatorial surface westerlies. *Mon. Wea. Rev.*, 102, 208-218.
- Lau, K.-M., and P. H. Chan, 1986: The 40-50 day oscillation and ENSO: A new perspective. *Bull. Amer. Meteor. Soc.*, 67, 533-534.
- Lau, K.-M., and L. Peng, 1987: Origin of low-frequency (intraseasonal) oscillations in the tropical atmosphere. Part I: Basic theory. *J. Atmos. Sci.*, 44, 950-972.
- Lau, K.-M., and P. H. Chan, 1988: Interannual and intraseasonal variations of tropical convection: a possible link between the 40-day mode and ENSO. *J. Atmos. Sci.*, 45, 506-521.

- Lau, K.-M., C.-P. Chang, and P. H. Chan, 1983: Short-term planetary-scale interactions over the tropics and midlatitudes: Part II: Winter MONEX period. *Mon. Wea. Rev.*, 111, 1372-1388.
- Lau, K.-M., L. Peng, C.-H. Sui, and T. Nakazawa, 1989: Dynamics of supper cloud clusters, westerly wind burst, 30-60 day oscillation and ENSO: An unified view. *J. Appl. Meteor.*, 67, 205-219.
- Lau, N.-C., 1985: Modeling the seasonal dependence of the atmospheric response to observed El Niños in 1962-76. *Mon. Wea. Rev.*, 113, 1970-1976.
- Leary, C. A., and R. A. Houze, Jr., 1979: The structure and evolution of convection in a tropical cloud cluster. *J. Atmos. Sci.*, 36, 437-457.
- Leary, C. A., and R. A. Houze, Jr., 1980: The contribution of mesoscale motions to the mass and heat fluxes of an intense tropical convective system. *J. Atmos. Sci.*, 37, 784-796.
- Legates, D. R., and C. J. Willmott, 1990: Mean seasonal and spatial variability in gauge-corrected, global precipitation. *Int. J. Climatol.*, 10, 111-127.
- LeMone, M. A., and W. T. Pennell, 1976: The relationship of trade wind cumulus distribution to subcloud layer fluxes and structure. *Mon. Wea. Rev.*, 104, 524-539.
- Lewis, J. M., 1975: Test of Ogura-Cho model on a prefrontal squall line case. *Mon. Wea. Rev.*, 103, 764-778.
- Lim, H., and C.-P. Chang, 1983: Dynamics of teleconnections and Walker circulations force by equatorial heating. *J. Atmos. Sci.*, 40, 1897-1915.
- Lin, X., and R. H. Johnson, 1994: Preliminary heat and moisture budgets and thermodynamic features over TOGA COARE region. Preprint of the *6th Conference on Mesoscale Processes*. Portland, 17-20.
- Lin, X., and R. H. Johnson, 1994: Heat and moisture budgets and circulation characteristics of a frontal squall line. *J. Atmos. Sci.*, 51, 1661-1681.
- Lin, X., and R. H. Johnson, 1996a: Kinematic and thermodynamic features of the flow over the western Pacific warm pool during TOGA COARE. *J. Atmos. Sci.*, 53, 695-715.

- Lin, X, and R. H. Johnson, 1996b: Heat and moisture budgets and rainfall over the western Pacific warm pool during TOGA COARE IOP. *J. Atmos. Sci.*, 53, 3367-3383.
- Lindzen, R. S., 1974: Wave-CISK in the tropics. *J. Atmos. Sci.*, 31, 156-179.
- Liu, C., and M. W. Moncrieff, 1997: A numerical study of the diurnal cycle of tropical oceanic convection. Submitted to *J. Atmos. Sci.*
- Liu, G., and J. A. Curry, 1992: Retrieval of precipitation from satellite microwave measurement using both emission and scattering. *J. Geophys. Res.*, 97, 9959-9974.
- Liu, W. T., 1988: Moisture and latent heat flux variabilities in the tropical Pacific derived from satellite data. *J. Geophys. Res.*, 93, 6749-6760.
- Liu, W. T., and C. Gautier, 1990: Thermal forcing on the tropical Pacific from satellite data. *J. Geophys. Res.*, 95, 13209-13217.
- Liu, W. T., K. B. Katsaros, and J. A. Businger, 1979: Bulk parameterization of air-sea exchanges of heat and water vapor including the molecular constraints at the interface. *J. Atmos. Sci.*, 36, 1722-1735.
- Liu, W. T., W. Tang and P. P. Niller, 1991: Humidity profiles over the ocean. *J. Climate*, 4, 1023-1034.
- Lorenc, A. C., 1984: The evolution of planetary-scale 200-mb divergence flow during the FGGE year. *Quart. J. Ry. Meteor. Soc.*, 110, 427-441.
- Love, G., 1985: Cross-equatorial influence of winter hemisphere subtropical cold surges. *Mon. Wea. Rev.*, 113, 1487-1498.
- Ludlam, F. H., 1980: Clouds and storms: the behavior and effect of water in the atmosphere. *Pennsylvania State University Press*, 405pp.
- Lukas, R., 1990: Freshwater input to the western equatorial Pacific Ocean and air-sea interaction. *Air-Sea Interaction in Tropical Western Pacific, Proc. US-PRC int'l. TOGA Symp.*, Beijing, China, Ocean Press, 305-327.
- Luo, H., and M. Yanai, 1984: The large-scale circulation and heat sources over the Tibetan plateau and surrounding areas during the early summer of 1979. Part II: Heat and moisture budgets. *Mon. Wea. Rev.*, 112, 966-989.

- Luther, D. S., D. E. Harrison and R. A. Knox, 1983: Zonal winds in the central equatorial Pacific and El Niño. *Science*, 222, 327-330.
- Madden, R. A., 1986: Seasonal variations of the 40-50 day oscillation in the Tropics. *J. Atmos. Sci.*, 43, 3138-3158.
- Madden, R. A., and P. R. Julian, 1971: Description of a 30-50 day oscillation in the zonal wind in the tropical Pacific. *J. Atmos. Sci.*, 28, 702-708.
- Madden, R. A., and P. R. Julian, 1972: Description of global-scale circulation cells in tropics with a 40-50 day period. *J. Atmos. Sci.*, 29, 1109-1123.
- Madden, R. A., and P. R. Julian, 1994: Observations of the 40-50 day tropical oscillation -- A review. *Mon. Wea. Rev.*, 122, 814-837.
- Magaña, V., and M. Yanai, 1991: Tropical-midlatitude interaction on the time scale of 30-60 days during the northern summer of 1979. *J. Climate*, 4, 180-201.
- Mapes, B. E., and R. A. Houze, Jr., 1993: Cloud clusters and superclusters over the oceanic warm pool. *Mon. Wea. Rev.*, 121, 1398-1415.
- Mapes, B. E., and R. A. Houze, Jr., 1995: Diabatic divergence profiles in western Pacific mesoscale convective systems. *J. Atmos. Sci.*, 52, 1807-1828.
- Mapes, B. E., and P. Zuidema, 1996: Radiative-dynamical consequences of dry tongues in the tropical troposphere. *J. Atmos. Sci.*, 53, 620-638.
- Matsuno, T., 1966: Quasi-geostrophic motions in the equatorial area. *J. Meteor. Soc. Japan*, 44, 25-43.
- McBride, J. L., and W. M. Gray, 1980: Mass divergence in tropical weather systems. Part I: Diurnal variation. *Quart. J. Ry. Meteor. Soc.*, 106, 501-516.
- McBride, J. L., N. E. Davidson, K. Puri and G. C. Tyrell, 1995: The flow during TOGA COARE as diagnosed by the BMRC tropical analysis and prediction system. *Mon. Wea. Rev.*, 123, 717-736.
- McBride, J. L., B. W. Gunn, G. J. Holland, T. D. Keenan, N. E. Davidson, and W. M. Frank, 1989: Time series of total heating and moistening over the Gulf of Carpentaria radiosonde array during AMEX. *Mon. Wea. Rev.*, 117, 2701-2713.

- McPhaden, M. J., 1993: TOGA-TAO and the 1991-1993 ENSO event. *Oceanography*, 6, 36-44.
- Miller, B. L., and D. G. Vincent, 1987: Convective heating and precipitation estimates for the tropical South Pacific during FGGE, 10-18 January 1979. *Quart. J. Ry. Meteor. Soc.*, 113, 189-212.
- Miller, J., 1976: The salinity effect in a mixed layer ocean model. *J. Phys. Oceanogr.*, 6, 29-35.
- Miller, M. J., A. C. M. Beljaers, and T. N. Palmer, 1992: The sensitivity of of the ECMWF model to the parameterization of evaporation from the tropical oceans. *J. Climate*, 5, 418-434.
- Moncrieff, M. W., and E. Klinker, 1996: Organized convective systems in the tropical western Pacific as a process in general circulation models: A TOGA COARE case study. *Quart. J. Ry. Meteor. Soc.*, 122, in press.
- Murakami, M., 1983: Analysis of the deep convective activity over the western Pacific and Southeast Asia. Part I: Diurnal cycle. *J. Meteor. Soc. Japan*, 61, 60-75.
- Murakami, M., 1987: Intraseasonal atmospheric teleconnection patterns during the Northern Hemisphere summer. *Mon. Wea. Rev.*, 115, 2133-2154.
- Murakami, T., L.-X. Chen, and A. Xie, 1986: Relationship among seasonal cycles, low-frequency oscillations, and transient disturbances as revealed from outgoing longwave radiation data. *Mon. Wea. Rev.*, 114, 1456-1465.
- Nakazawa, T., 1986: Intraseasonal variations in OLR in the tropics during the FGGE year. *J. Appl. Meteor.*, 64, 17-34.
- Nakazawa, T., 1988: Tropical super cluster within intraseasonal variations over the western Pacific. *J. Appl. Meteor.*, 66, 923-839.
- Nakazawa, T., 1995: Intraseasonal oscillations during the TOGA-COARE IOP. *J. Meteor. Soc. Japan*, 73, 305-319.
- Neelin, J. D., 1988: Reply. *J. Atmos. Sci.*, 45, 3526-3527.

- Neelin, J. D., I. M. Held and K. H. Cook, 1987: Evaporation-wind feedback and low-frequency variability in the tropical atmosphere. *J. Atmos. Sci.*, 44, 2341-2348.
- Nitta, T., 1972: Energy budget of wave disturbances over the Marshall Islands during the years of 1956 and 1958. *J. Appl. Meteor.*, 50, 71-84.
- Nitta, T., 1975: Observational determination of cloud mass flux distributions. *J. Atmos. Sci.*, 32, 73-91.
- Nitta, T., 1977: Response of cumulus updraft and downdraft to GATE A/B-scale motion systems. *J. Atmos. Sci.*, 34, 1163-1186.
- Nitta, T., 1983: Observational study of heat sources over the eastern Tibetan Plateau during the summer monsoon. *J. Meteor. Soc. Japan*, 61, 590-605.
- Nitta, T., 1989: Development of a twin cyclone and westerly bursts during the initial phase of the 1986-87 El Niño. *J. Meteor. Soc. Japan*, 67, 677-681.
- Nitta, T., and S. Esbensen, 1974: Heat and moisture budget analyses using BOMEX data. *Mon. Wea. Rev.*, 102, 17-28.
- Nitta, T., and S. S. So, 1980: Structure and heat, moisture and momentum budgets of a convective mixed layer during AMTEX'75. *J. Meteor. Soc. Japan*, 58, 378-393.
- Nitta, T., and T. Motoki, 1987: Abrupt enhancement of convective activity and low-level westerly wind burst during the onset phase of 1986-87 El Niño. *J. Appl. Meteor.*, 65, 497-506.
- Numaguti, A., and Y.-Y. Hayashi, 1991: Behavior of cumulus activity and the structure of circulations in an "aqua planet" model. Part I: The structure of the super clusters. *J. Meteor. Soc. Japan*, 69, 541-561.
- Numaguti, A., R. Oki, K. Nakamura, K. Tsuboki, N. Misawa, T. Asai and Y.-M. Kodama, 1995: 4-5-day-period variation and low-level dry air observed in the equatorial western Pacific during the TOGA-COARE IOP. *J. Meteor. Soc. Japan*, 73, 267-290.
- O'Brien, J. J., 1970: Alternative solutions to the classical vertical velocity problem. *J. Appl. Meteor.*, 9, 197-203.

- Ogura, Y., and H.-R. Cho, 1973: Diagnostic determination of cumulus cloud population from observed large-scale variables. *J. Atmos. Sci.*, 30, 1276-1286.
- Ogura, Y., and H.-R. Cho, 1974: On the interaction between the subcloud and cloud layers in tropical regions. *J. Atmos. Sci.*, 31, 1850-1859.
- Ogura, Y., and Y.-L. Chen, 1977: A life history of an intense mesoscale convective storm in Oklahoma. *J. Atmos. Sci.*, 1458-1476.
- Oort, A. H., 1983: Global atmospheric circulations statistics, 1958-73, NOAA Prof. Paper No. 14.
- Ooyama, K. V., 1971: A theory on parameterization of cumulus convection. *J. Meteor. Soc. Japan*, 744-756.
- Ooyama, K. V., 1987: Scale-controlled objective analysis. *Mon. Wea. Rev.*, 115, 2479-2506.
- Ostapoff, F., Y. Tarbeye, and S. Worthem, 1973: Heat flux and precipitation estimates from oceanographic observations. *Science*, 180, 960-962.
- Parker, D. E., 1973: Equatorial Kelvin waves at 100 millibars. *Quart. J. Roy. Meteor. Soc.*, 99, 116-129.
- Parsons, D., W. Dabberdt, H. Cole, T. Hock, C. Martin, A.-L. Barrett, E. Miller, M. Spowart, M. Howard, W. Ecklund, D. Carter, K. Gage, and J. Wilson, 1994: The Integrated Sounding System: description and preliminary observations from TOGA COARE. *Bull. Amer. Meteor. Soc.*, 75, 553-567.
- Pedigo, C. B., and D. G. Vincent, 1990: Tropical precipitation rates during SOP-1, FGGE, estimated from heat and moisture budgets. *Mon. Wea. Rev.*, 118, 542-557.
- Peixoto, J. P., and Oort A. H., 1992: Physics of climate. *American Institute of Physics*, 520pp.
- Price, J. F., R. A. Weller, and R. Pinkel, 1986: Diurnal cycling: Observations and models of the upper ocean response to diurnal heating, cooling, and wind mixing. *J. Geophys. Res.*, 91, 8411-8427.

- Randall, D. A., Harshvardhan, and D. A. Dazlich, 1991: Diurnal variability of the hydrologic cycle in a general circulation model. *J. Atmos. Sci.*, 48, 40-62.
- Reed, R. J., and E. E. Recker, 1971: Structure and properties of synoptic-scale wave disturbances in the equatorial western Pacific. *J. Atmos. Sci.*, 28, 1117-1133.
- Reed, R. K., 1985: An estimate of the climatological heat fluxes over the tropical Pacific Ocean. *J. Climate Appl. Meteor.*, 24, 833-840.
- Reynolds, R. W. and T. S. Smith, 1994: Improved global sea surface temperature analyses using optimum interpolation. *J. Climate*, 7, 929-948.
- Rickenbach, T. M., S. A. Rutledge, 1996a: Convection in TOGA COARE: Horizontal scale, morphology, and rainfall production. Submitted to *J. Atmos. Sci.*.
- Rickenbach, T. M., S. A. Rutledge, 1996b: The diurnal variation of tropical rainfall: Dependence on convective organization. Submitted to *J. Atmos. Sci.*.
- Riehl, H., 1954: Tropical Meteorology. McGraw-hill, New York, 392pp.
- Riehl, H., and J. S. Malkus, 1958: On the heat balance in the equatorial trough zone. *Geophysica*, 6, 503-538.
- Rui, H. L., and B. Wang, 1990: Development characteristics and dynamic structure of tropical intraseasonal convection anomalies. *J. Atmos. Sci.*, 47, 357-379.
- Salby, M. L., and R. R. Garcia, 1987: Transient response to localized episodic heating in the tropics. Part I: Excitation and short-time near-field behavior. *J. Atmos. Sci.*, 44, 458-498.
- Saxen, T. R., 1996: Surface fluxes and boundary layer recovery in TOGA COARE: Sensitivity to convective organization. *M.S. thesis*, Department of Atmospheric Science, Colorado State University, paper No. 629, 116pp.
- Schmetz, J., and L. Van den Berg, 1994: Upper tropospheric humidity observations from Meteosat compared with short term forecast fields. *Geophys. Res. Lett.*, 21, 573-576.
- Schubert, W. H., P. E. Ciesielski, C. Lu, and R. H. Johnson, 1995: Dynamical adjustment of the trade wind inversion layer. *J. Atmos. Sci.*, 52, 2941-2952.

- Soong, S.-T., and Y. Ogura, 1980: Response of tradewind cumuli to large-scale processes. *J. Atmos. Sci.*, 37, 2035-2050.
- Soong, S.-T., and W.-K. Tao, 1980: Response of deep tropical cumulus clouds to mesoscale processes. *J. Atmos. Sci.*, 37, 2016-2034.
- Spencer, R. W., 1986: A satellite passive 37-GHz scattering-based method for measuring oceanic rain rates. *J. Climate*, 25, 754-766.
- Squires, P., and J. S. Turner, 1962: An entrainment jet model for cumulonimbus updrafts. *Tellus*, 14, 422-434.
- Stull, R. B., 1985: A fair-weather cumulus cloud classification scheme for mixed-layer studies. *Journal of Climate and Applied Meteorology*, 24, 49-56.
- Sui, C.-H., and K.-M. Lau, 1992: Multiscale phenomena in the tropical atmosphere over the western Pacific. *Mon. Wea. Rev.*, 120, 407-430.
- Sui, C.-H., X. Li, and K.-M. Lau, 1997: Radiative-convective processes in simulated diurnal variations of tropical oceanic convection. Submitted to *J. Atmos. Sci.*
- Takahashi, M., 1987: A theory of the slow phase speed of the intraseasonal oscillation using the wave-CISK. *J. Meteor. Soc. Japan*, 65, 43-49.
- Takayabu, Y., 1994: Large-scale cloud disturbances associated with equatorial waves. Part II: Westward-propagating inertio-gravity waves. *J. Meteor. Soc. Japan*, 72, 451-465.
- Takayabu, Y., K. M. Lau, and C. H. Sui, 1996: Observation of a quasi-2-day wave during TOGA COARE. *Mon. Wea. Rev.*, 124, 1892-1913.
- Tao, W.-K., and S.-T. Soong, 1986: A study of the response of deep tropical clouds to mesoscale processes: Three-dimensional numerical experiments. *J. Atmos. Sci.*, 43, 2653-2676.
- Taylor, R., 1973: An atlas of Pacific rainfall. Rep. HIG-73-9, Hawaiian Inst. of Geophys., Honolulu, Univ. Hawaii, 7pp, 13 figures.
- Thompson, R. M., Jr., S. W. Payne, E. E. Recker, and R. J. Reed, 1979: Structure and properties of synoptic-scale wave disturbances in the intertropical convergence zone of the eastern Atlantic. *J. Atmos. Sci.*, 36, 53-72.

- TOGA COARE Intensive Observing Period Operations Summary, 1993, TOGA COARE International Project Office, University Corporation for Atmospheric Research.
- Trier S. B., W. C. Skamarock, M. A. LeMone, D. B. Parsons, and D. P. Jorgensen, 1996: Structure and evolution of the 22 February 1993 TOGA COARE squall line: Numerical simulations. *Mon. Wea. Rev.*, 53, 2861-2886.
- Velden, C. S., and J. A. Young, 1994: Satellite observations during TOGA COARE: Large-scale descriptive overview. *Mon. Wea. Rev.*, 122, 2426-2441.
- Waliser, D. E., and N. S. Graham, 1993: Convective cloud systems and warm-pool sea surface temperatures: Coupled interactions and self-regulation. *J. Geophys. Res.*, 98, 12881-12893.
- Waliser, D. E., N. S. Graham, and C. Gautier, 1993: Comparison of the highly reflective cloud and outgoing longwave data sets for use in estimating tropical deep convection. *J. Climate*, 6, 331-353.
- Wallace, J. M., 1975: Diurnal variations in precipitation and thunderstorm frequency over the conterminous United States. *Mon. Wea. Rev.*, 103, 406-419.
- Wallace, J. M., and V. E. Kousky, 1968: Observational evidence of Kelvin waves in the tropical stratosphere. *J. Atmos. Sci.*, 25, 900-907.
- Wang, B., 1988a: Dynamics of tropical low-frequency waves: An analysis of the moist Kelvin wave. *J. Atmos. Sci.*, 45, 2051-2064.
- Wang, B., 1988b: Comments on "An air-sea interaction model of intraseasonal oscillation in the tropics." *J. Atmos. Sci.*, 45, 3521-3525.
- Wang, B., and J. Chen, 1989: On the zonal-scale selection and vertical structure of equatorial intraseasonal waves. *Quart. J. Roy. Meteor. Soc.*, 115, 1301-1323.
- Wang, B., and H. Rui, 1990: Synoptic climatology of transient tropical intraseasonal convection anomalies. *Meteor. Atmos. Phys.*, 44, 43-61.
- Weare, B. C., P. T. Strub, and M. D. Samuel, 1981: Annual mean surface heat fluxes in the tropical Pacific Ocean. *Mon. Wea. Rev.*, 115, 2687-2698.

- Webster, P. J., 1983: Mechanisms of monsoon low-frequency variability: Surface hydrological effects. *J. Atmos. Sci.*, 40, 2110-2124.
- Webster, P. J., 1991: Ocean-atmosphere interaction in the tropics. ECMWF Seminar Series: Interaction of the Mid-latitudes and the tropics. European Centre of Medium-Range Weather Forecasting, Reading, U.K., 67-116.
- Webster, P. J., 1994: The role of hydrological processes in ocean-atmosphere interactions. *Rev. Geophys.*, 32, 427-476.
- Webster, P. J., and L. C. Chou, 1980: Low frequency transitions of a simple monsoon system. *J. Atmos. Sci.*, 37, 368-382.
- Webster, P. J., and G. L. Stephens, 1980: Tropical upper-tropospheric extended clouds – inference from winter MONEX. *J. Atmos. Sci.*, 37, 1521-1541.
- Webster, P. J., and R. Lukas, 1992: TOGA COARE: The Coupled Ocean-Atmosphere Response Experiment. *Bull. Amer. Meteor. Soc.*, 73, 1377-1416.
- Webster, P. J., C. A. Clayson, and J. A. Curry, 1996: Clouds, radiation, and the diurnal cycle of sea surface temperature in the tropical western Pacific. *J. Climate*, 9, 1712-1730.
- Weickmann, K. M., G. R. Lussky, and J. E. Kutzbach, 1985: Intraseasonal (30-60 day) fluctuations of outgoing longwave radiation and 250 mb stream function during northern winter. *Mon. Wea. Rev.*, 113, 941-961.
- Weisman, M. L., J. B. Klemp, and R. Rotunno, 1988: A theory for strong, long-lived squall lines, *J. Atmos. Sci.*, 45, 463-485.
- Weller, R. A., and S. P. Anderson, 1996: Surface meteorology and air-sea fluxes in the western equatorial Pacific warm pool during the TOGA Coupled Ocean-Atmosphere Response Experiment. *J. Meteor.*, 9, 1959-1990.
- Williams, A. G., H. Kraus, and J. M. Hacker, 1996: Transport processes in the tropical warm pool boundary layer. Part I: Spectral composition of fluxes. *J. Atmos. Sci.*, 53, 1187-1202.

- Wyrтки, K., 1965: The average annual heat balance of the North Pacific Ocean and its relation to ocean circulation. *J. Geophys. Res.*, 70, 4547-4559.
- Xu, K.-M., D. A. Randall, 1995: Impact of interactive radiative transfer on the macroscopic behavior of cumulus ensembles. Part II: Mechanisms for cloud-radiation interactions. *J. Atmos. Sci.*, 800-817.
- Xu, K.-M., D. A. Randall, 1996: Explicit simulation of cumulus ensembles with the GATE phase III data: Comparison with observations. *J. Atmos. Sci.*, 53, 3710-3736.
- Xu, K.-M., A. Arakawa, and S. K. Krueger, 1992: The macroscopic behavior of cumulus ensembles simulated by a cumulus ensemble model. *J. Atmos. Sci.*, 49, 2402-2420.
- Yamagata, T., and Y. Hayashi, 1984: A simple diagnostic model for the 30-50 day oscillation in the tropics. *J. Meteor. Soc. Japan*, 62, 709-717.
- Yanai, M., and T. Maruyama, 1966: Stratospheric wave disturbances propagating over the equatorial Pacific. *J. Meteor. Soc. Japan*, 44, 291-294.
- Yanai, M., and R. H. Johnson, 1993: Chapter 4: Impacts of cumulus convection on thermodynamic fields. AMS Monograph. The representation of cumulus convection in numerical models. Ed. K. A. Emanuel and D. J. Raymond.
- Yanai, M., S. Esbensen and J. H. Chu, 1973: Determination of bulk properties of tropical cloud clusters from large-scale heat and moisture budgets. *J. Atmos. Sci.*, 30, 611-627.
- Yanai, M., J.-H. Chu, T. E. Stark, and T. Nitta, 1976: Response of deep and shallow tropical maritime cumuli to large-scale processes. *J. Atmos. Sci.*, 33, 976-991.
- Yano, J. I., and K. A. Emanuel, 1991: An improved model of the equatorial troposphere and its coupling with the stratosphere. *J. Atmos. Sci.*, 48, 377-389.
- Yasunari, T., 1979: Cloudiness fluctuations associated with the Northern Hemisphere summer monsoon. *J. Appl. Meteor.*, 57, 227-242.
- Yasunari, T., 1980: A quasi-stationary appearance of 30 to 40 day period in the cloudiness fluctuation during the summer monsoon over India. *J. Meteor. Soc. Japan*, 58, 225-229.

- Yasunari, T., 1981: Structure of an Indian summer monsoon system with around 40-day period. *J. Meteor. Soc. Japan*, 59, 336-354.
- Yoneyama, K., and T. Fujitani, 1995: The behavior of dry westerly air associated with convection observed during TOGA-COARE R/V Natsushima cruise. *J. Meteor. Soc. Japan*, 73, 291-304.
- Zhang, C., 1996: Atmospheric intraseasonal variability at the surface in the tropical western Pacific Ocean. *J. Atmos. Sci.*, 53, 739-758.
- Zhang, G. J., and M. J. McPhaden, 1995: The relationship between sea surface temperature and latent heat flux in the equatorial Pacific. *J. Climate*, 8, 589-605.
- Zipser, E. J., 1977: Mesoscale and convective-scale downdrafts as distinct components of squall line structure. *Mon. Wea. Rev.*, 105, 1568-1589.